To the Graduate Council:

I am submitting herewith a dissertation written by Jason Fowlkes entitled "Laser – Induced Nanostructures in Silicon". I have examined the final electronic copy of this dissertation for form and content and recommend that it be accepted in partial fulfillment of the requirements for the degree of Doctor of Philosophy, with a major in Materials Science and Engineering.

Dr. A. J. Pedraza

Anthony J. Pedraza, Major Professor

We have read this dissertation

and recommend its acceptance:

Dr. D. Joy

Dr. R. Buchanan

Dr. M. McCay

Dr. C. McHargue

Dr. D. Lowndes

Accepted for the Council:

Dr. Mayhew

Vice Provost and Dean of

Graduate Studies

(Original signatures are on file with official student records.)

Laser – Induced Nanostructures in Silicon

A Dissertation

Presented for the

Doctor of Philosophy

Degree

The University of Tennessee, Knoxville

Jason Fowlkes

December 2002

Dedication

Dedicated to Robert, Vicky, and Robin Fowlkes

Acknowledgements

I would like to thank first and foremost, Dr. Antonio J. Pedraza, for his patience, insights, and guidance over the duration of this work. Dr. Pedraza's criticism was always constructive as to aid my learning experience and for this I am very thankful. A special thanks to Steven Jesse, Daryl Smith, and Yingfeng Guan whom each had a hand in the eventual success of this work. Finally, I would like to thank Dr. Mary McCay, Dr. David Joy, Dr. Carl McHargue, Dr. Ray Buchanan, and Dr. Douglas Lowndes for serving on my dissertation committee.

Abstract

This dissertation addresses the formation of nanostructures induced by the laser irradiation of silicon. A KrF (248 nm) pulsed excimer laser was used as the irradiation source. Irradiating micro – structured substrates in a reactive O_2 atmosphere produced SiO nanostructures. Si nanoparticles were formed by irradiating both flat and micro – structured silicon surfaces in an inert gas ambient. On flat surfaces, low energy density irradiation ($E_d < 1$ J/cm^2) induces the formation and clustering of a thin silicon film pulsed – laser deposited on silicon into nanoparticles that grow to 2 – 80 nm in diameter. Control over the Si nanoparticle diameter to within ± 1 nm could be obtained by optimizing the laser beam energy density, the inert gas pressure, and the number of laser pulses. The nanoparticles in the surface plane will self – organize into periodically spaced lines, if a periodic or quasi – periodic, microstructure is present at the surface.

A film of silicon nanoparticles was formed on the surface of a silicon target following pulsed laser irradiation in an inert, background gas. Silicon species generated during laser ablation were backscattered by the background gas and re – deposited on the target. Polished and micro – structured silicon targets were used to study the re – deposited films. The nanoparticle film was formed *outside* the laser – irradiated area but on the same substrate from which the silicon species were ablated. The film consisted of a dispersion of very small nanoparticles between 1 and 100 nm. The diameter of the nanoparticles comprising the film is a function of the distance from the laser – irradiated area at which the film is collected, the gas pressure present during irradiation, and the surface topography of the target prior to irradiation.

The effect of a micro – structured target was to significantly shift the mean nanoparticle diameter of the film to smaller values. Moreover, the FWHM of the nanoparticle diameter distributions increases 2 – fold for films prepared with micro – structured target surfaces. This is a direct result of the increased clustering observed when using micro – structured targets. The optimal size distribution is one with a narrow FWHM, a minimal mean nanoparticle diameter, and a nanoparticle distribution fit to a single Gaussian peak. Size – selected nanoparticle films of this quality are attractive for potential device applications where the nanoparticles would be deposited at a specific location and their collective optoelectronic operation would require them all to be of a specific size for proper device operation.

The minimum mean nanoparticle diameter and minimum FWHM were achieved by

1 Increasing the linear distance from the irradiated area, on the substrate, where the nanoparticle are collected.

2 Reducing the total pressure of UHP Ar present over the surface during nanoparticle formation.

3 Irradiating a rough target surface as opposed to a flat target surface all over variables constant.

A model was composed to correlate target roughness and processing pressure with the nanoparticle size distribution of Si nanoparticle films.

The irradiation of a micro – structured Si target in a reactive atmosphere induces the formation of a silicon oxide nanostructure. The micro – structured target surface contains an array of silicon microcones, also produced by pulsed laser irradiation. The microcone morphology is produced by pulsed laser irradiation of silicon in the presence of

SF_6 gas. The SiO nanostructure is produced by a second, subsequent pulsed laser irradiation in an O_2 atmosphere.

The SiO nanostructure is formed by the reaction of laser ablated Si species with O_2 molecules in the gas phase. The Si species are ablated from the trench pits surrounding the Si microcones. Si species diffuse out of the confined vapor cloud and react with O_2 in the gas atmosphere to produce SiO nanoparticles. The SiO nanoaggregates cluster by collisions with the background gas and other SiO species and some of these aggregates re – deposit on the microcone walls forming Si microcones sheathed in the SiO nanostructure.

Visible, bright – to – the – eye, room temperature photoluminescence was observed from Si microcones embedded in the SiO nanoaggregate sheath. Two main, prominent photoluminescence peaks located at 420 nm (3.0 eV) and 500 nm (2.5 eV) in the photoluminescence spectra provide most of the photoluminescence observed. Photoluminescence intensity was enhanced by a 900 ^{o}C thermal anneal which reduced the contribution of non – radiative defects to emitted light absorption from the SiO.

Irradiating a flat Si substrate produces ablated Si species that are backscattered by the ambient gas and re – deposited onto the surface in the form of a thin ~ 1 nm Si film. If the background pressure is lower than 250 mTorr of UHP He not enough material is backscattered to form a continuous surface film. The laser fluence must be larger than 0.6 J/cm^2 to produce enough ablated material, but lower than 1.3 J/cm^2 to avoid the fusion of the film with the substrate. The Si film clusters on the surface to form Si nanoparticles. These nanoparticles scatter light in the surface plane and the superposition of the incoming light from the laser pulse plus the scattered component produces an interference pattern at the substrate surface. The clustering process is influenced by this intensity pattern and

individual clusters have spacings on the surface a distance λ apart, where λ is the incident laser beam wavelength.

The scattering of the incident laser beam and the interaction of this scattered light with the incident light, at the surface of the irradiated substrate, is required to induce the self – organization of Si nanoparticles on the substrate surface. The light scattering event can take place in the beam path in route to the substrate by an obstacle in the beam path or at a pre – existing micro – roughness, present on the surface prior to the laser pulse. However, the interference pattern resulting from the interaction between the incident beam and scattered beam must be located at the substrate surface. Moreover, it appears that the intensity modulation in the surface region, set up by the linear nanoparticle arrays there, is responsible for driving the alignment event over many laser pulses!

Laser – induced periodic surface structures (LIPSS) form simultaneously, in the surface plane, with the nanoparticle – ordering phenomenon. LIPSS were found to lie beneath the nanoparticles only when they were self – organized. Moreover, the nanoparticles lie always in the periodic depressions of the LIPSS. P – polarized light was required to induce the formation of LIPSS and the self – organization of Si nanoparticles. The beam need be only partially polarized but it must contain a substantial portion, at least 50%, p – polarized light. The LIPSS formation and nanoparticle alignment seemed to be intimately related.

A very important result of this work was the achievement of a pulsed laser deposition (PLD) system capable of ordering nanoparticles on substrates using a separate target. In this configuration, it is proposed that multi – material, nanoparticle – substrate, self – organized, linear nanoparticle arrays could be produced. Further, an additional

technique, laser – induced chemical vapor deposition (LICVD) was used to deposit ordered nanoparticle line arrays spaced $\lambda/2$ apart, where λ is the laser beam wavelength. A minimum line spacing of 124 nm was achieved using this approach.

Table of Contents

List of Tables

Table **Page**

List of Figures

Figure **Page**

Chapter 1

Literature Review

1.1 Introduction

The irradiation of a polished, atomically flat silicon wafer with a pulsed excimer laser beam induces the formation of a wide variety of micro- and nano-structures on the wafer surface. The energy density of the laser beam is the key variable in determining the feature size of surface morphology. For example, irradiation at energy densities higher than 1.0 J/cm^2 induces the formation of micrometer scale morphologies in the surface layer. Nanoscale features are produced on the surface using laser beam energy densities lower than 1.0 J/cm^2. Moreover, by irradiating a silicon surface at high energy followed by irradiation at lower energy produces a surface consisting of both micro- and nano- scale surface features.

The evolution of surface morphology in laser-irradiated silicon occurs by the rearrangement of silicon species on the surface. Over the entire range of energy densities used in this research the surface experiences both melting and vaporization during laser irradiation. These phase changes make possible a variety of pathways for silicon atoms or species to relocate on the surface.

Inherent to the laser-surface interaction is the spatially non-uniform deposition and absorption of laser beam energy. This leads to surface tension gradients in the melted layer; the driving force for mass transport in the liquid.

Vaporized silicon species recondense on the silicon surface if an adequate vapor pressure exists at the surface during irradiation. A background gas pressure of several mTorr is adequate to induce silicon re-deposition on the surface. A percentage of the

vaporized species are redirected back to the surface via momentum exchange with the background gas through collisions. The species can either reincorporate by depositing at liquid portions of the surface thereby epitaxially recombining with the target or by cluster deposition at both liquid and/or solid regions of the target. Species chemistry and cluster size depend strongly on the reactivity of silicon with the background gas and the pressure of the background gas, respectively.

Vaporized silicon species were also collected on substrates located at various positions with respect to the irradiated target. Specifically, nanoscale species varied in diameter, distribution, and number density based on the location of the substrate, the background gas pressure, fluence, and the number of laser pulses applied to the target.

The aim of this research is to study the mechanisms of micro- and nano- structures that can be produced during the pulsed laser irradiation of silicon. The above mentioned variables were varied over a wide range and in various combinations to fully characterize the extent of morphologies. The various morphologies were studied as a function of laser energy density, the number of laser pulses, background gas pressure and reactivity, angle of incidence, laser beam polarization, and target surface roughness. Paramount to the study was to develop *controllable*, processes and techniques to generate nanostructures, and self – organized nanostructures, of specific diameters, and with narrow size – distributions and sub-irradiation wavelength feature spacings, respectively. Emphasis was placed on research into growth of nanostructures via the laser irradiation of microstructures. For example, surface cone *microstructures were used* as ablation targets to take advantage of their ability to promote species clustering and the resulting nanoparticle formation in the gas phase.

In order for nanotechnology to find a useful niche in the existing technological infrastructure will require significant advances in the isolation of nanostructures and the self – assembly of applicable nanostructures to engineering. The ability to control nanoparticle size and distribution is required, from a scientific point of view, to better isolate nanostructures so that they can be studied independently, or as collective networks, to determine their unknown chemical, structural, and physical properties as individual particles or networks, respectively. Self – organization is important from the standpoint of engineering. Self – assembly of nanostructures on the surface plane removes the difficulties associated with external techniques, such a lithography, to pattern such small – scale elusive features. Both cost of facilities and fundamental scientific, physical limitations impede the application of lithography to patterning nanostructures.

High-resolution scanning electron microscopy (HRSEM), high-resolution transmission electron microscopy (HRTEM), Auger electron spectroscopy (AES), atomic force microscopy (AFM), and energy dispersive spectroscopy (EDS) were used to characterize the laser-irradiated surfaces in terms of their chemistry, crystal structure, and morphology.

1.2 Pulsed Laser Irradiation

1.2.1 Excimer Lasing

An excimer laser emits monochromatic pulsed, coherent photons at ultraviolet wavelengths. The excimer lasing process occurs by excitation of rare gas halide molecules through an electric discharge. Voltages of 13 – 20 kV can produce a pulse, for example, of ~ 700 mJ. Table 1.1 lists rare gas halide molecules and their highest gain transitions from

electric discharge excitation. The laser transitions occur 10 – 50 ns after the electrical discharge excitation [1]. High powers of ~ 700 mJ / 25ns = 30 MW are produced per pulse due to the nanosecond laser pulse width. For focused laser beams of 0.2 cm x 0.5 cm dimensions, power densities on the order of ~ 300 MW/cm^2 are obtained.

The pulse profile has a full-width, half maximum in emission wavelength of ~ 0.050 nm due to Doppler broadening [1]. The transition products are an unbound ground state molecule and an energetic photon, hν. The unbound ground state dissociates in less than 1 ps, thus providing an excitation to ground state lifetime ratio of ~ 1x10^4 making rare gas halide excitation an efficient source of ultraviolet pulses.

1.3 Laser – Material Interactions

1.3.1 Material Optical Properties

The optical properties of a material determine the amount of electromagnetic radiation it absorbs. The refractive index of a material quantitatively describes the absorption of incident radiation. The frequency dependent, complex dielectric constant has a real and an imaginary part [1]

$$\varepsilon(\omega) = \varepsilon'(\omega) + i\varepsilon''(\omega) \qquad 1.1$$

where ω is the frequency of the radiation.

Both the real and imaginary parts of the dielectric constant can be determined through the experimental determination of the real n(ω) and imaginary κ(ω) parts of the complex, refractive index, N(ω) [1]

$$N(\omega) = n(\omega) + i\kappa(\omega) \qquad 1.2$$

Table 1.1 Rare gas halide molecules and their highest gain transitions for laser action. [1, 2]

RGH Molecule	Wavelength (nm)
F_2	157
ArCl	175
ArF	193
KrCl	222
KrF	248
XeBr	282
XeCl	308
I_2	342
XeF+	351, 353

Sources:

[1] W. W. Duley, p. 6 and 36 in UV Lasers : Effects and Applications in Materials Science, Cambridge University Press, 1996

[2] D. J. Eliot, p. 48 in Ultraviolet Laser Technology and Applications, Academic Press, Inc., San Diego, 1995

The complex dielectric function is related to the complex refractive index through the relationship [3].

$$N(\omega) = \sqrt{\varepsilon(\omega)} \qquad 1.3$$

Excimer optical wavelengths are four orders of magnitude larger than the lattice constant of an arbitrary solid material. This large difference allows the use of a macroscopic quantity, such as the complex refractive index, to describe matter's response to ultraviolet light [4] The reflectivity, R, at normal incidence, derived from the material's refractive properties, provides the amount of coupling between laser light and material [4]

$$R(\omega) = \frac{(n(\omega)-1)^2 - (i\kappa(\omega))^2}{(n(\omega)+1)^2 - (i\kappa(\omega))^2} \qquad 1.4$$

Jellison et al. found the reflectivity of Si, under 248 nm irradiation, to be 0.63 and 0.70 in the solid and liquid, respectively [5]. The solid reflectivity measurement of 0.63 for Si is an average from room temperature to the melting point.

The absorption of the incident radiation as a function of depth can be calculated using the Beer – Lambert law

$$I(x) = I_o e^{-\frac{4\pi kx}{\lambda}} \qquad 1.5$$

where I_o is the incident light intensity and λ is the wavelength of the radiation. The attenuation coefficient is defined as

$$\alpha = \frac{4\pi k}{\lambda} \qquad 1.6$$

and the penetration depth of the radiation into the material is α^{-1} [1]. Aspnes et al. found that the absorption coefficient of Si at 300 K, exposed to 248 nm radiation, is 1.81×10^6

Table 1.2 Non-thermal, electronic excitations resulting from laser – light and semiconductor target interactions.

Interband excitations
Excitation of electron-hole pairs with energy greater than the band gap energy, $h\nu > E_g$.
Intraband excitations
Excitation of conduction band electrons to higher energy levels within the same band. [5]
Defects and impurities
Defects and impurities make it possible for photons of energies less than the band gap to excite electrons from the valence band to conduction band. These disruptions of the crystal lattice form permissible states in the forbidden gap by which sub-gap energies can produce a conducting electron-hole pair.
Multiphoton Excitations
High power laser pulses can produce multiphoton excitations. These excitations create virtual states in the forbidden gap, creating more paths for exciting electrical carriers. The efficiency of a given wavelength laser-material interaction is increased via these pathway. [8]

Sources:

[6] D. E. Aspnes and A. A. Studna, *Phys. Rev. B* **27**, 985 (1985)

[9] D. Bauerle, p. 15 – 28, 173 – 190, 251 – 254, and 262 – 264 in Laser Processing and Chemistry, 2nd Ed., Springer – Verlag, Berlin, Heidelburg, 1996

cm^{-1} [6]. For multiphoton excitations, which occur at high incident photon energies; the attenuation coefficient becomes intensity dependent. The above mathematical equations give quantitative results concerning the amount of radiation absorbed, yet carry no information regarding the mechanisms of absorption.

1.3.2 Mechanisms of Absorption

The primary interactions of ultraviolet laser light and material are non – thermal. Examples of non – thermal, electronic state transitions are listed in Table 1.2. In semiconductors, electrons are excited to the conduction band from the valence band by absorption of a photon with an energy, $h\nu$, greater than the band – gap energy, E_g. This process is termed interband absorption. Intraband absorption occurs when free electrons in the conduction band absorb a photon and are increased to greater energy states *within* the band.

The absorption of radiation is increased as electronic defect states are introduced into the band – gap. Defects located within the bulk, as well as at a material's surface, introduce available electronic states into the band – gap region. Electrons trapped in these defect states can be excited into the conduction band with incident photon energies less than the band – gap energy. Hence, the number density of defects in a material greatly influences the absorption efficiency.

Electron – electron interactions occur within ~ 10^{-14} s of laser excitation [7]. Electron plasmas form in the conduction band when high densities of free carriers occupy similar energy states within the band. Electron – electron and electron – plasma

interactions establish an effective carrier temperature that is far greater than the lattice temperatures [8].

Electron – phonon collisions occur 10^{-11} – 10^{-12} s after photon absorption [7]. The electron interacts with the lattice generating heat and leaving the free carriers with energies just above the conduction band. Electrons still have energies greater than the band gap energy when they are located just above the conduction band. This energy is lost when the electron recombines with a hole in the valence band. The recombination energy transfers to a free carrier in the conduction band [7].

Electron – hole recombination is not the only available pathway for energy relaxation. A thermal, i.e., non – radiative, process provides an additional relaxation conduit. The energy relaxation pathway is determined by comparing the rate constants for the radiative and non – radiative events. At the end of the process most of the absorbed laser energy is transferred as heat to the lattice.

1.3.3 Laser Melting & Ablation

The ablation process occurs either by a photochemical, or photothermal, mechanism, or via a combination of the two means. The laser ablation process can be modeled for a specific material based on the characteristic time for both routes of excitation [9]. The time required for the thermalization of excited species is characterized by τ_T. Similarly, τ_R is the time required for ablation by direct photon – chemical bond interaction.

Consider the irradiation of a semiconductor material with photons of energy less than the band – gap but of sufficient energy *density* to induce the vaporization of species

from the solid – gas interface. Clearly, only intraband excitations can take place under these irradiation conditions and hence the thermalization of electron energies will lead to the desorption of species due to the inherent temperature rise associated with *nanosecond* pulsed laser irradiation. For example, a maximum surface temperature of ~10^3 K can be achieved during nanosecond irradiation. Thus, in the case of semiconductor materials, photochemical ablation is restricted to situations for which irradiation is performed with visible/ultraviolet wavelengths, i.e., for energies greater than the band – gap energy. Moreover, the thermalization rate in the uv irradiated material must be slow relative to the rate of coupling between the incident photons and chemical bonds/defects for purely photochemical ablation.

If adequate laser energy density is supplied to a target, both photochemical and thermal processes can yield material removal. This being the case even though heat conduction in the bulk dissipates a significant amount of the absorbed energy. Excimer laser processing can produce temperatures as high as 10^4 K in shallow absorption depths [9]. Shinn estimated the surface temperature of Si irradiated with 248 nm radiation and a fluence of 1.3 J/cm^2 to be 2700 ^{o}C [10].

Wood et al. developed a melting model for the pulsed laser processing of silicon [11]. De Unamuno and Fogarassy computed the melt depth in crystalline silicon (c-Si) as a function of time for a laser pulse duration of 50 ns and a laser wavelength of 193 nm (figure 1.1) [12]. Figure 1.2 shows the melt penetration depth as a function of laser energy density for a 248 nm, 32 ns laser pulse [12].

De Unamuno and Fogarassy also calculated the c-Si melting threshold as a function of the FWHM pulse duration [12]. Both the simulated and experimental data are presented

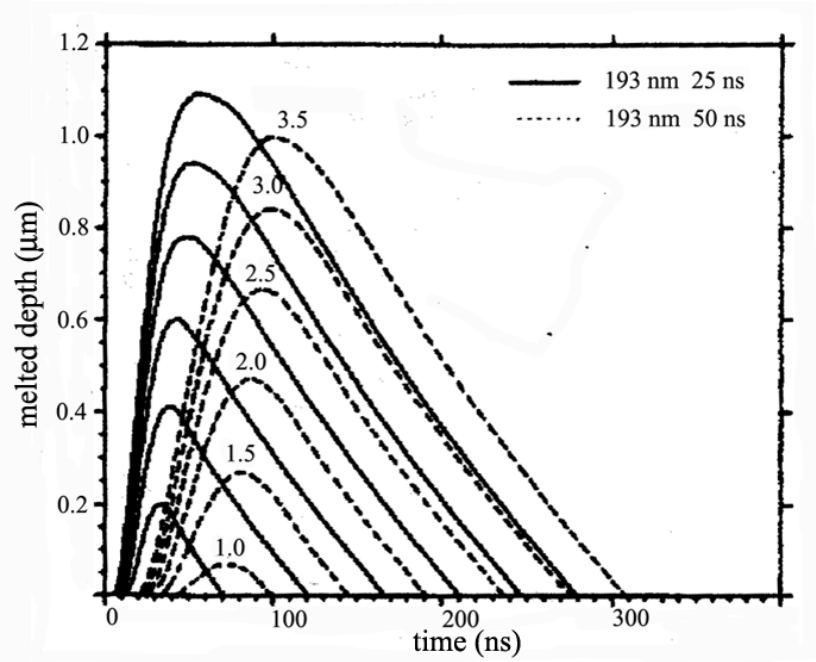

Figure 1.1 The simulated melt penetration as a function of time for c-Si melted with 193 nm laser pulses at various energy densities. The pulse width of the dashed plot was 50 ns and the pulse width of the solid line was 25 ns. [12]

Source:

[12] S. De Unamuno and E. Fogarassy, *Appl. Sur. Sci.* **36**, 1 (1989)

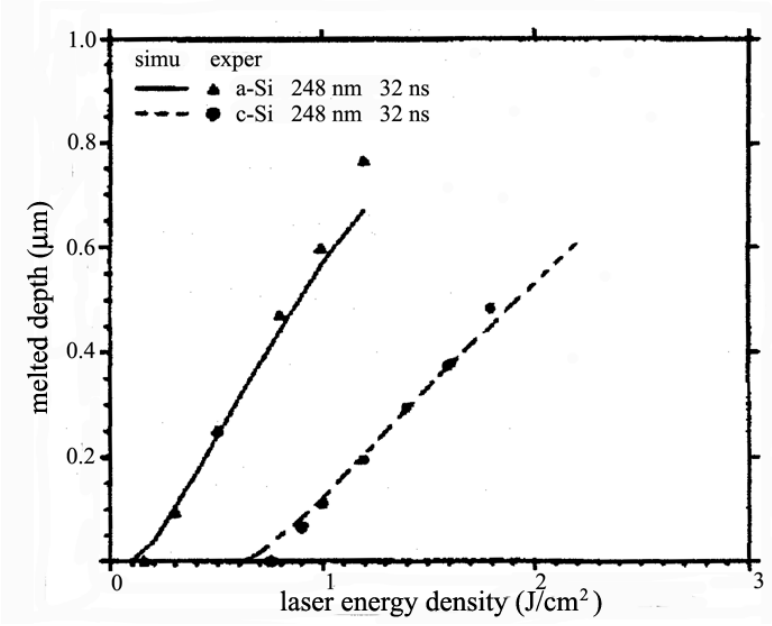

Figure 1.2 The simulated melt penetration depth plotted against the laser energy density for 248 nm, 32 ns laser irradiation of both a-Si and c-Si. Experimental data points are also included in the plot. [12]

Source:

[12] S. De Unamuno and E. Fogarassy, *Appl. Sur. Sci.* **36**, 1 (1989)

in figure 1.3. The simulated curve for 248 nm laser irradiation gives a c-Si melting threshold value of ~ 0.55 J/cm^2 for a pulse duration of 25 ns [12].

Shinn et al. reported ablation, i.e., material removal, of silicon at an energy density as low as ~ 1 J/cm^2 when irradiated with a 14 ns ArF pulse in 1000 Torr of He. In contrast, to these results, Wood and others calculated no vaporization at fluences up to 5 J/cm^2 for 41 ns XeCl radiation. Even considering the longer pulse duration and longer wavelength of a 41 ns XeCl pulse yielding a lower power density, it is hard to imagine such a discrepancy in vaporization energy density for the same material.

Heating rates up to 10^{15} K/s can be generated over a pulse width at FWHM of 20-50 ns [9]. The result of such heating rates is vaporization of the target, expulsion of liquid, thermal shock, and modified microstructure and surface morphology. However, the response to a laser pulse and the form in which that material changes is predominantly dictated by the material's properties. Thus, it is a material's properties that ultimately determine the active laser sputtering mechanism.

1.4 Laser-Induced Vapor Plume

1.4.1 Nanocluster Formation

Nanoclusters are produced in a laser generated vapor and/or plasma plume following deceleration of the plume via an attenuating background gas. Neutrals, ions, and excited atoms/molecules are the initial components of the laser generated vapor plume prior to interaction with the background gas. The background gas acts to decelerate, attenuate, and aid in the condensation of these active species within the plume. Nanoscale clusters form as a result of silicon species condensation.

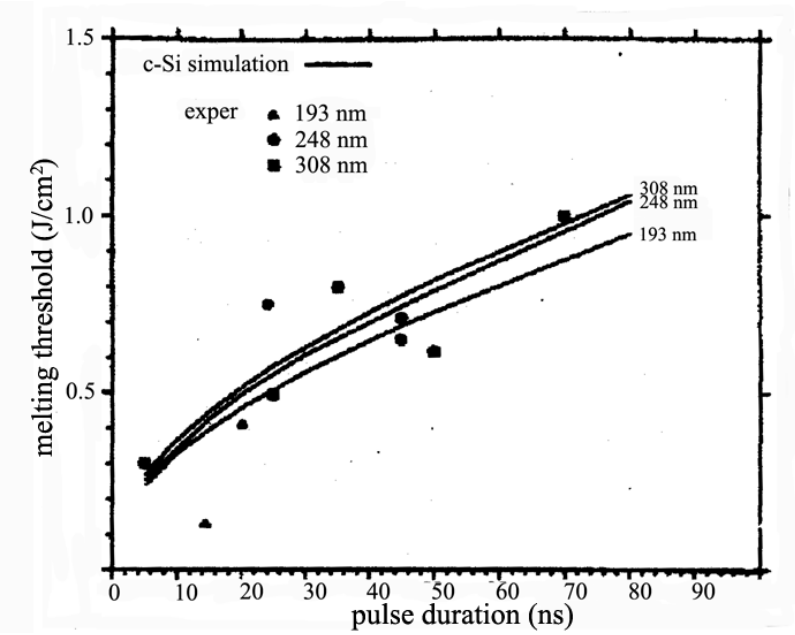

Figure 1.3 The c-Si melting threshold as a function of pulse duration for three different excimer laser wavelengths. Both simulated and experimental data are included in the plot. [12]

Source:

[12] S. De Unamuno and E. Fogarassy, *Appl. Sur. Sci.* **36**, 1 (1989)

Cluster size can be controlled by adjusting variables such as background gas pressure and flow rate, the atomic mass ratio of the background gas to the vapor species, the fluence of the laser pulse, i.e., the plume density and kinetic energy, and the type of background gas, either non-reactive or reactive. These variables ultimately determine the plume density and the kinetic energy of species in the plume, and the types of species.

Irradiating in reactive background gases can produce clusters of modified chemical composition, relative to the initial target composition. For example, TiN nanoparticle films can be deposited in a conventional pulsed laser deposition experiment by ablating a Ti target into nitrogen – containing atmosphere [13]. Thus, the expanding vapor plume – background gas system can be used to control the cluster composition as well as cluster size.

1.4.2 A Qualitative description of Vapor Plume Generation and the Plume – Background Gas Interaction

Fluences in the range of 1 – 10 J/cm^2 will ablate an enormous amount, ~ 10^2 nm/pulse, of material, for most materials systems, such that a luminescent plasma/vapor plume is ejected from the irradiated surface. Laser beam power densities on the order of MW/cm^2 can be produced at ultraviolet wavelengths and nanosecond pulse – widths. Moreover, the optical penetration depth at, for example 248 nm, is roughly $1/\alpha = 5.5$ nm, where α is the frequency dependent absorption coefficient [14]. Thus, an enormous power density is delivered in a very shallow region of the target. The result is the ejection from the surface of highly excited species and neutrals in the form of a vastly non – equilibrium energetic, dense vapor plume that travels at roughly 10^6 cm/s with

temperatures in the plasma of ~ 10^1 eV, e.g., roughly 10^4 K! Pressures in the range 10^1 – 10^2 atm are generated within the plume. [15]

Figure 1.4 shows a schematic sequence of the propagation of a laser – generated plume into a confining background gas. Figure 1.4a shows a focused laser beam generating a luminescent vapor plume over the target surface. The luminescence arises from several sources in the vapor/plasma plume. Bremsstrahlung radiation from free electron – free electron transitions produces a broad spectrum of radiation spanning the visible range. Superimposed on the Bremsstrahlung spectra are atomic, ionic, and molecular transition lines from excited species in the plume [9].

A typical beam profile at the target surface of 0.5 cm x 0.5 cm will produce a roughly spherical plume of ~ 10^1 cm^3. On the *nanosecond* time scale, the plume will approximately freely expands into a background gas of ~ 10^1 mbar (figure 1.4b). Anisimov [16] described this expansion as adiabatic, i.e., the temperature drops in the plume and it expands to occupy more volume;

$$T_2 = \left(\frac{V_1}{V_2} \right)^{\gamma - 1} T_1 \qquad 1.7$$

where V is volume of the plume, T is the plume temperature, and γ is the ratio of heat capacity at constant volume to the heat capacity at constant pressure. This analysis clearly ignores non-equilibrium effects present in confined plasmas.

Vapor plume – background gas interactions begin following the free expansion of the plume up to ~ 10^2 μs. Initially, the plume compresses the background gas as it expands outward. At the plume – gas interface the rapid expansion leads to local compression of the background gas at this interface. As a result, a shockwave develops at the leading edge

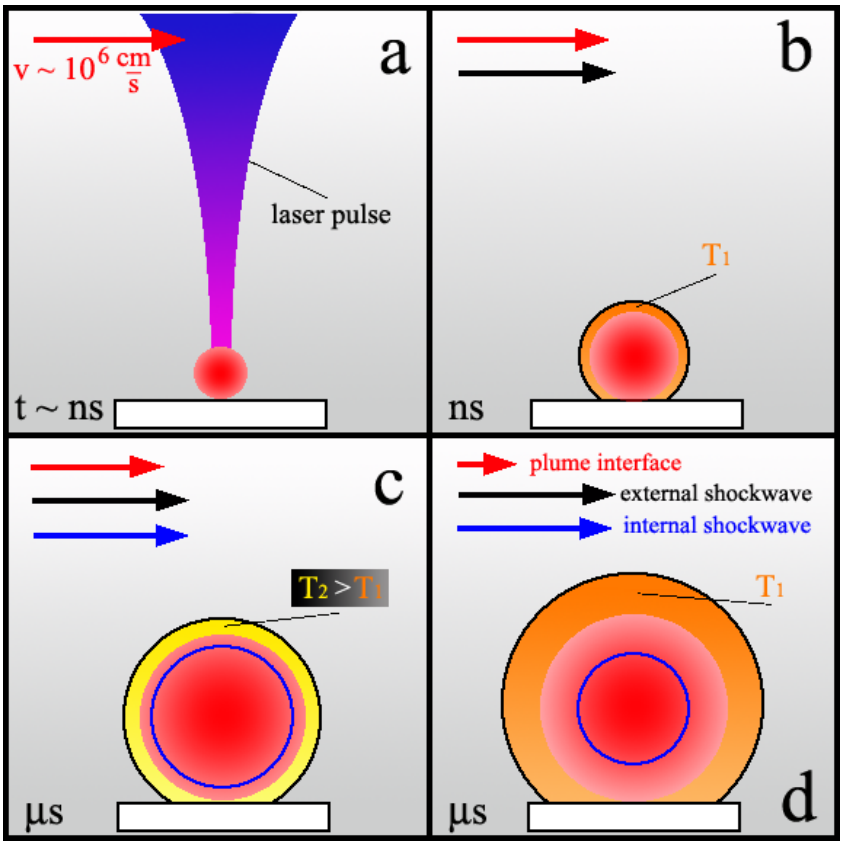

Figure 1.4 Schematic representation (cross – section) of the temporal history of a propagating laser – induced, vapor plume. *a*) the initial laser pulse generates a freely expanding, roughly spherical vapor plume. The free expansion velocity of the plume is ~ 10^6 cm/s. *b*) the plume maintains its free expansion on the nanosecond time scale and a shock wave develops at the plume/background gas interface. *c*) microseconds after the initial pulse, the free propagation condition deteriorates as the plume exchanges energy with the background gas (the interface heats up to T_2). An internal shockwave develops within the plume and thermalizes the plume species as it propagates. *d*) the vapor plume expansion has all but ceased whilst the shock waves continue to propagate. Nanoparticle condensation occurs milliseconds after the initial pulse when the species of the plume diffusively propagate into the background gas!

of the plume (figure 1.4c).

The velocity of the species within the plume decreases at the leading edge due to the transfer of their momentum to the background gas. The interface continues to heat up and the plume begins to decelerate as its kinetic energy is dissipated. A reverse pressure gradient develops at the leading edge interface. Hence, an internal shockwave develops within the plume itself that propagates inward towards the geometric center of the roughly spherical plume (figure 1.4d). Moreover, during laser-induced vapor expansion, cooling rates as high as 10^{10} K/s, are achieved within the plume. As a result, strong non-linearities in temperature and density develop and these non-linearities are inevitably responsible for the wide, size – distributions of nanoparticles produced on substrates in conventional pulsed – laser deposition (PLD) experiments to deposit nanoclusters. The condensation of species and nanoparticle formation takes place milliseconds (ms) after the initial laser pulse.

The internal shockwave contained within the plume, cycles between reflecting off the plume – vapor interface and propagating in the plume volume. Thermalization, i.e., a uniform distribution of energy over a spatial dimension, of the plume components occurs as a result of this process. The completion of thermalization in the vapor plume and the total deceleration of the plume occur in approximately the same temporal increment. Nanocluster *formation* takes place during the thermalization cycle *and* the subsequent *diffusive dissipation* of the plume into the background gas.

Once the plume has lost all forward velocity, the transport of species is driven by the concentration gradient existing at the plume – gas interface and diffusion takes place. Condensation and clustering occurs in the gas phase spanning the time from deceleration

of the plume until the point of substantial background gas – plume species mixing. However, the thermalization process does not provide an adequate homogenization of species, i.e., less than desirable cluster and nanocluster size distributions result when cluster species are collected on a suitable substrate. Cluster size distributions collected from conventional PLD experiments follow the relationship;

$$\Delta r \approx 0.3 r_{\max} \qquad 1.8$$

where Δr is the full – width half – maximum (FWHM) of the "Gaussian – like" size distribution shape [9].

Hydrodynamic models predict accurately vapor plume position as a function of time in the presence of a background gas. At t < μs, a classic drag force model best describes plume propagation as a function of time,t;

$$r = r_f (1 - e^{-at}) \qquad 1.9$$

where r_f is the maximum distance the leading edge of the plume propagates and *a* is a constant. A blast wave model, formulated by Zel dovich et al., best describe the relationship between leading edge displacement and time at longer times, i.e., t > μs;

$$r = \xi_o \left(\frac{E_o}{\rho} \right)^{\frac{1}{5}} t^{\frac{2}{5}} \qquad 1.10$$

where ξ_o is a constant and E_o is energy confined prior to an explosion at t = 0 s [17]. The blast wave model assumes an energy E_o is released in an initial explosion that propagates as an expanding, spherical plasma into a high pressure surrounding gas. The schematic of propagation provided in figure 1.4 was drawn following the assumptions of this model.

1.4.3 Experiments in Cluster Formation

1.4.3.1 Temporal Studies of Nanoparticle Evolution

Time-resolved photoluminescence emission, measured in situ, during vapor plume evolution and propagation is used to determine *when* nanoparticles form in the gas phase with respect to the initial laser pulse. Photoluminescence is the emission of light quanta from the nanoparticles following the radiative recombination of an electron – hole pair within the particle. The electron – hole pair is created by a probe pulse that illuminates the vapor plume in flight. The energy of the emitted light is related to the luminescent nanoparticle's diameter.

Luminescence bands with maxima at 1.4 – 1.72, 1.7, 1.8, 1.9, 2.15, 2.5, and 3.2 eV [18 – 22] are attributed to the emission from oxidized, i.e., passivated, nanocrystalline silicon (nc-Si) based on the quantum confinement theory [23 – 25] of luminescence in semiconductor crystals. The quantum confinement theory and the photoluminescence of silicon nanostructures will be described in a later section.

In laser ablation experiments, silicon nanoparticle luminescence begins when plasma luminescence is quenched, i.e., following thermalization of the plasma! Geohegan et al. observed photoluminescence 3 ms after the initial ablation pulse (λ = 248 nm) when Si was ablated, E_d = 5 – 8 J/cm^2, into 1 Torr argon gas [26]. Photoluminescence was observed after only 0.15 ms for ablation into a helium background gas, P_{He} = 10 Torr. Makimura observed photoluminescence emission to begin at 1.2 ms following silicon ablation (λ = 532 nm Nd-YAG) into 5 Torr argon gas [27]. These results agree well with those of Geohegan. Moreover, the emission was observed by a different experimental process, e.g., Makimura et al. used a second laser pulse to *decompose* nc-Si and imaged the

luminescence from the decomposed clusters. Geohegan observed directly luminescence from the nanoparticles without nanoparticle decomposition. The excited silicon nanoparticle remnants, produced via the decomposition, were responsible for the detected emission. Figure 1.5 shows the plasma and nanoparticle emission as a function of time for experiments performed by Makimura et al [27].

The background gas type strongly affects the hydrodynamic interaction of the gas and vapor plume during PLA into an ambient gas [26]. Argon gas is significantly heavier than helium gas. Hence, the plume is totally "braked" and reflected by 1 Torr of argon (figure 1.6). A static, uniform cloud of nanoparticles forms by condensation of the plume species. In the case of ablation into 10 Torr of helium gas, a spatially "smoke – like" – nanoparticle ensembles that luminesce is produced that propagates throughout the chamber, eventually reflecting off the walls (figure 1.7) [26]

1.4.3.2 The Spatial Distribution of Nanoclusters in the Chamber Space

Nanoparticle diameter and distribution are strongly a function of the position where they are collected with respect to the maximum distance the leading edge plume propagates. For example, Makimura et al. placed substrates at various distances from the target during pulsed laser ablation (λ = 532 nm, E_d = 10 J/cm^2) into helium (P_{He} = 500 mTorr) [28]. Nanoparticles were *formed only* at *distances greater* than the maximum distance the plasma plume was observed to propagate into the background gas.
The nanoparticle size distribution depends also on the specific position of the substrate, at a given target – to – substrate distance. For example, Wu et al. found that the mean nanoparticle diameter decreases as the distance from the plume center increases on a

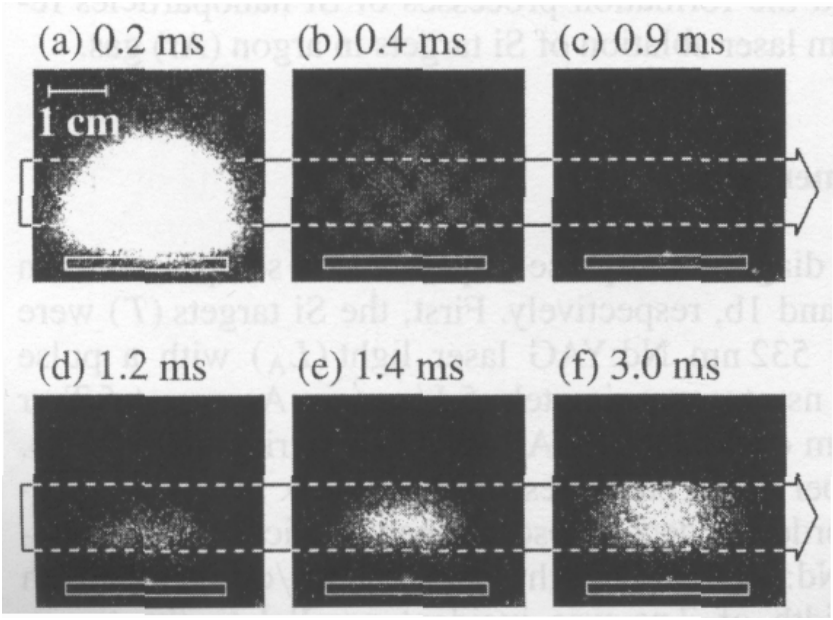

Figure 1.5 Nanoparticle photoluminescence is observed at times > 1.2 ms relative to the initial ablation pulse. A second laser pulse decomposes, and excites, the nanoparticles inducing light emission. A 532 nm Nd:YAG laser with a pulse width of 7 ns and an E_d = 5 J/cm^2 was used to produce the initial flux of silicon. Nanoparticle formation occurred by the interaction of the ablated Si species with the 5 Torr Ar background gas. A 7 ns, 355 nm Nd:YAG pulse (E_d =2 J/cm^2) was passed through the plume at a) 0.2, b) 0.4, c) 0.9, d) 1.2, e) 1.4 and f) 3.0 ms delay after the initial laser pulse to induce nanoparticle emission. [27]

Source:

[27] T. Makimura, T. Mizuta, and K. Murikami, *Appl. Phys. Lett. A* **69**[Suppl], S213 (1999)

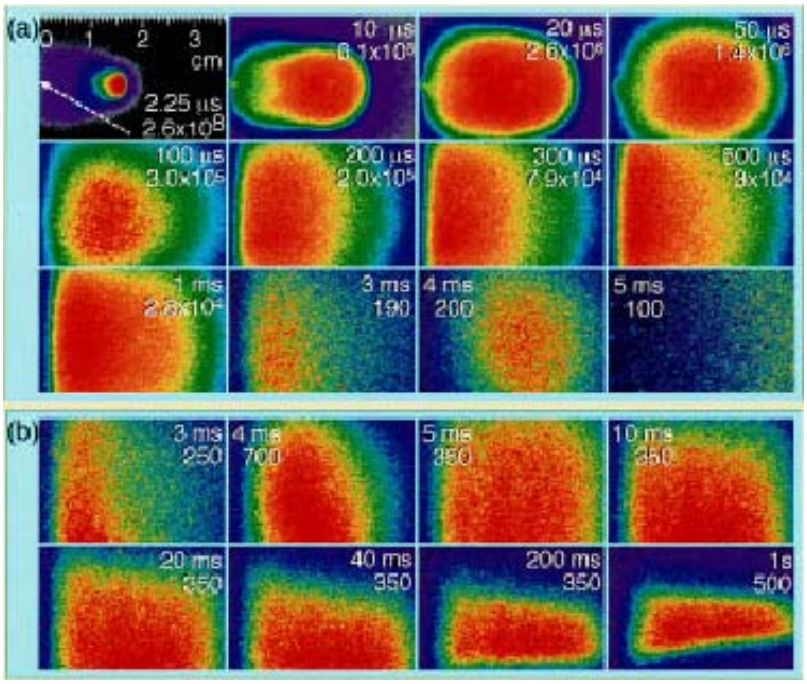

Figure 1.6 a) Visible plasma luminescence from a plume generated by 248 nm (E_d = 5 – 8 J/cm^2) laser illumination of a silicon target into 1 Torr Ar gas. The plume is totally reflected by the background gas after 100 μs! b) A XeCl probe (λ = 308 nm, E_d ~ 0.2 J/cm^2) pulse induces photoluminescence from Si nanoparticles at delay t > 3 ms, following the pump laser pulse (exposure times = 3 μs. [26]

Source:

[26] D. B. Geohegan, A. A. Puretsky, G. Duscher, and S. J. Pennycook, *Appl. Phys. Lett.* **72**(23), 2987 (1998)

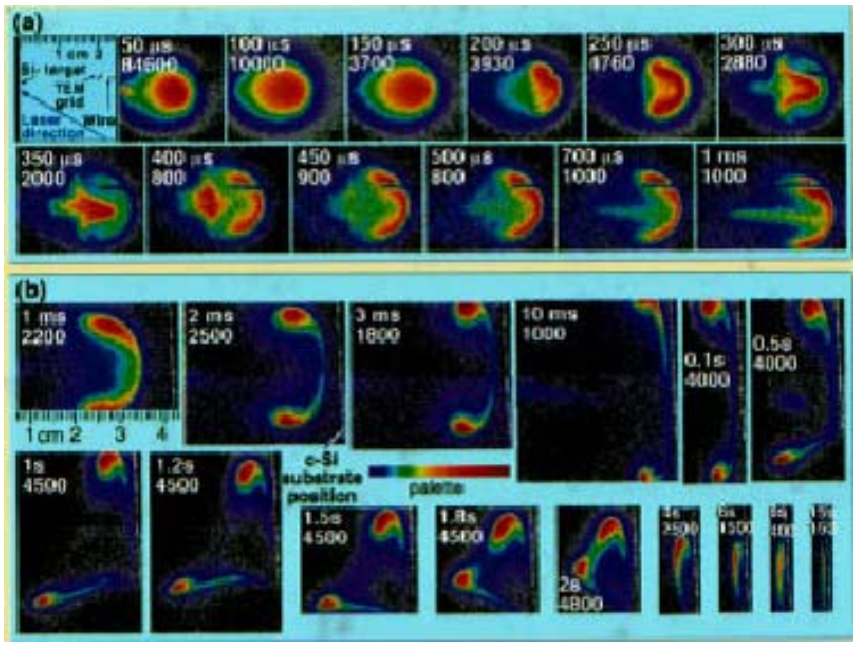

Figure 1.7 a) Visible plasma luminescence ($\Delta t < 400$ µs) superimposed with photoluminescence ($\Delta t > 200$ µs) from silicon ablation ($\lambda = 248$ nm, $E_d = 5 - 8$ J/cm^2) into 10 Torr He gas. b) Photoluminescence, induced by a ($\lambda = 308$ nm, $E_d \sim 0.2$ J/cm^2) probe pulse, of Si nanoparticles for $t > 1$ ms relative to the initial pump laser pulse. In the presence of 10 Torr He gas, the plume propagates completely through the chamber space, as opposed to the case of complete plume "braking" by heavier (1 Torr) Ar gas. [26]

Source:

[26] D. B. Geohegan, A. A. Puretsky, G. Duscher, and S. J. Pennycook, *Appl. Phys. Lett.* **72**(23), 2987 (1998)

given substrate [29]. Using 1000 Nd:YAG (λ = 355 nm), 30 ps pulse – width, pulses (E_d = 0.25 J/cm^2), at 4 cm target – to – substrate distance they found the average Si nanoparticle diameter to decrease from ~ 6 to 2 nm from plume center to 5 mm laterally on the substrate [29].

Lowndes et al. characterized nanoparticle mean diameter and distribution as a function of the target – to – substrate distance under ultraviolet (λ = 193 nm) pulsed laser deposition conditions. Figure 1.8 shows a plot of the nanoparticle number density vs. mean height for several target – to – substrate distances and at constant helium pressure (P_{He} = 1.5 Torr) [30]. The negative slope of the line for a 40 mm target – to – substrate distance is much steeper than the line for 10 mm target – to – substrate separation. This reflects a narrower size distribution at larger target – to – substrate distances.

Moreover, the line plot for the 40 mm distance is shifted to smaller mean diameters by an order of magnitude relative to the 10 mm line plot. This reflects a smaller, average nanoparticle diameter for larger target – to – substrate distances [30]. It is desirable for technological applications to have narrow size distributions of photoluminescent nanoparticles, i.e., nanoparticles (d < 30 nm) exhibiting the quantum confinement effect. These requirements are met at large target – to – substrate distances under ultraviolet PLD into low pressures, ~ 1 Torr, of inert gases.

Lowndes et al. [30] also found that nanoparticles are collected only outside the propagating plasma plume, in agreement with Makimura's results [28]. Thus, it has been confirmed that nanoparticle condensation occurs during the diffusive expansion of the plume remnant.

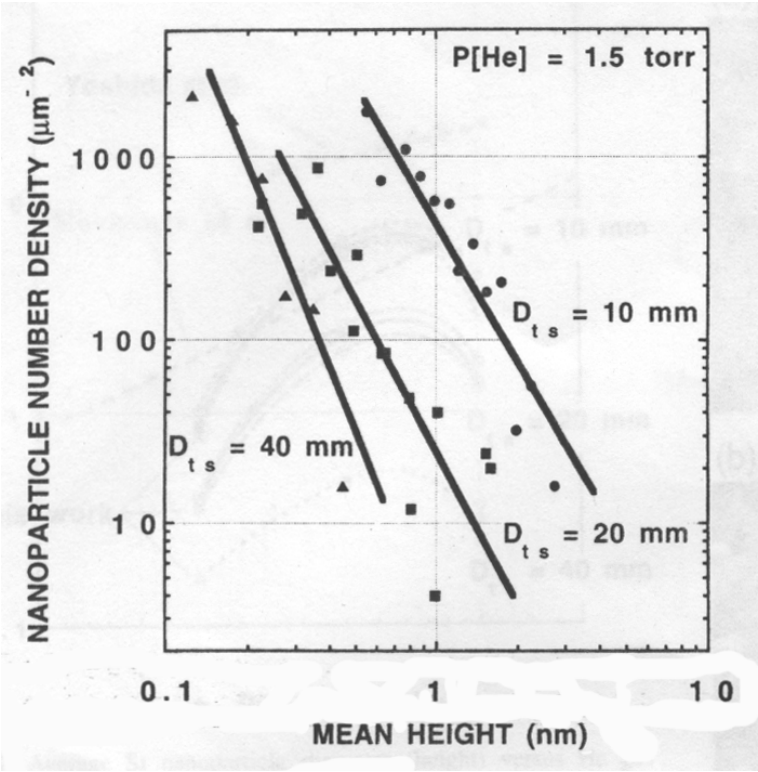

Figure 1.8 Si nanoparticle number density vs. the mean diameter (nm) of the nanoparticles for various target – to – substrate distances, D. The nanoparticles were produced by 500, ArF (λ = 193 nm, E_d = 1.04 J/cm^2) laser pulses into 1.5 Torr, static He gas. The nanoparticles were collected on silicon substrates and the mean diameter was determined by measuring the z – height of the nanoparticles relative to the substrate surface in an AFM. [30]

Source:

[30] D. H. Lowndes, C. M. Rouleau, T. G. Thundat, G. Duscher, E. A. Kenik, and S. J. Pennycook, *J. Mater. Res.* **14**(2), 359 (1999)

1.4.3.3 The Fluence Dependence of Nanocluster Formation

Patrone et al. found the nanoparticle average diameter and the FWHM of the size distribution to increase as the fluence was increased from 1 to 3.9 J/cm^2 (P_{He} = 4 Torr) [31] (figure 1.9). The substrate distance was fixed for each experiment and the cluster size and distribution were characterized using an AFM. In fact, the target acted as the substrate, with the nanoparticles collected being those reflected from the gas phase back toward the target.

Patrone et al. generated ideal, narrow nanoparticle size distributions [31]. For example, the average Si nanoparticle diameter was ~ 1.2 nm at 1 J/cm^2 with a FWHM of 0.5 nm. At 3.9 J/cm^2, the average diameter increased to ~ 3.5 nm and the FWHM increased to > 2 nm.

1.4.3.4 The Pressure Dependence of Nanocluster Formation

The average nanoparticle diameter increases as the total pressure of inert gas increases up to ~ 7 Torr helium for a fixed target – to – substrate distance [30]. The trend reverses for pressures greater than 7 Torr. A possible explanation for this trend is that initially, as the pressure is increased, at *low pressures*, the mean free path of Si species decreases and thus they experience more collisions prior to their deposition at the substrate surface. More collisions translate to more condensation, i.e., nanoparticle size increases.

However, at *higher pressures*, these larger clusters experience too many collisions, lose their momentum and cannot reach the substrate. Only nanoparticles experiencing fewer collisions can reach the substrate, i.e., nanoparticle size decreases with increasing pressure at total pressures > 7 Torr.

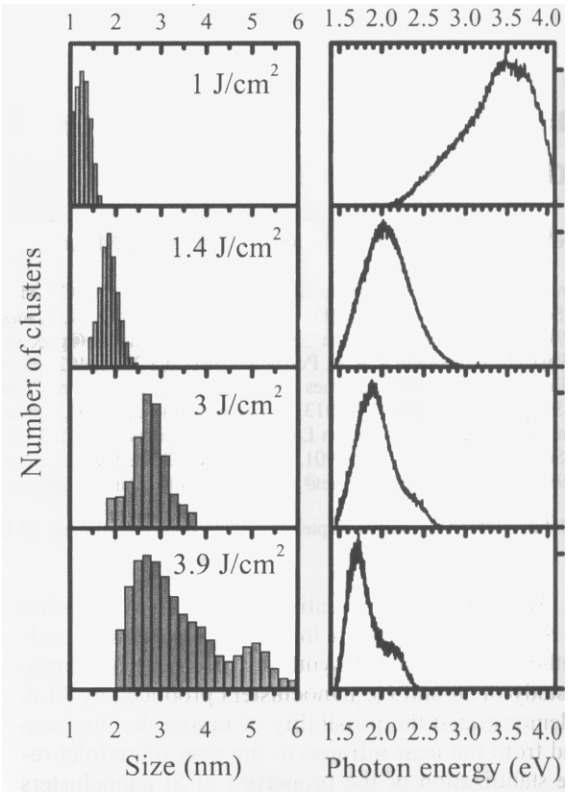

Figure 1.9 Cluster size distributions prepared by PLD at various energy densities. The background gas pressure was 4 Torr He. The corresponding photoluminescence spectra are shown to the right of each cluster size distribution. [31]

Source:

[31] L. Patrone, D. Nelson, V. I. Safarov, S. Giorgio, M. Sentis, and W. Marine, *Appl. Phys. A* **69**[Suppl], S217 (1999)

1.4.3.5 Size – Selected Nanoparticle Collection

Nanoparticles can be size – separated from a pulsed – laser ablation (PLA) generated vapor based on their charge. A flux of silicon species is produced by PLA as discussed in sections 1.4.3.1 – 1.4.3.4. The silicon species, in the form of nanoparticles, are passed through an alpha radiation source ^{241}Am that ionizes the carrier gas, e.g., He or Ar [32]. The nanoparticles are charged by collisions with the ionized gas. The charged nanoparticles enter a differential mobility analyzer (DMA) [32].

The nanoparticles are forced to flow between two charged plates, parallel to the plate surface, by a sheath gas flowing orthogonal to their initial direction (figure 1.10a). An inlet located in one plate accepts nanoparticles of a specific size based on their horizontal velocity and the electric – field between the plates. The size – selected nanoparticles emerge from a nozzle and deposit on a biased substrate [32]. The bias on the substrate is optimized to collect the most nanoparticles.

This technique is a leading candidate for technological applications where the size – selection of nanoparticles is important. The DMA technique has several advantages. In situ, temporal monitoring of the size distribution is possible by inserting an electrometer above the substrate. Figure 1.10b shows the fair agreement of nanoparticle size distribution measured in situ with an electrometer and ex situ with an AFM.

Flow rates and voltages can be tuned, during continuous nanoparticle production, to obtain the desired size – distribution. The shutter can then be removed over the substrate to collect the nanoparticles. Narrow size distributions are obtained, e.g., d_{max} = 6.4 nm and FWHM = 3 nm [32], comparable to distributions by the standard PLD techniques aforementioned.

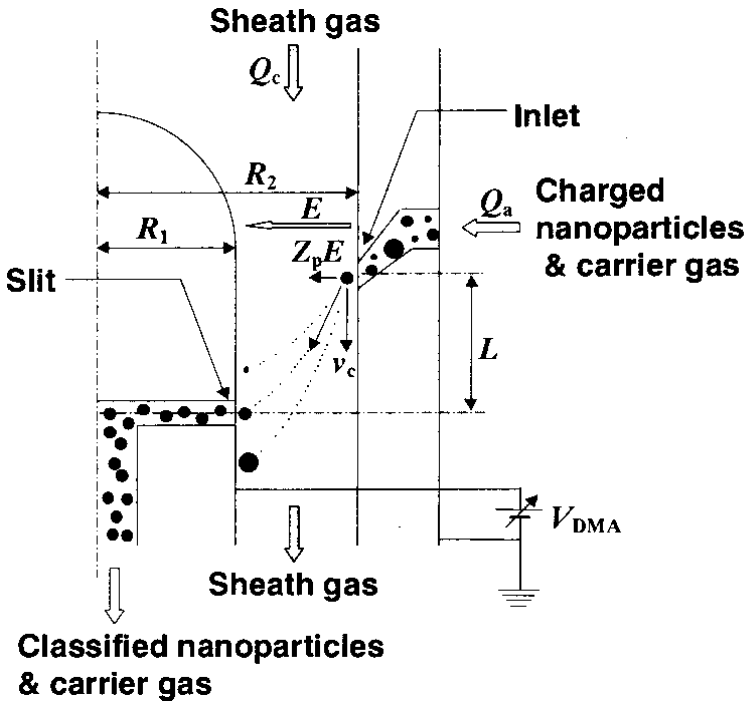

Figure 1.10 A schematic illustration showing the size selection of nanoclusters by a differential mobility analyzer. (a) Charged nanoparticles and the carrier gas emerge from an inlet into an electric field between two plates. A sheath gas, flowing between the plates, gives the nanoclusters a velocity component orthogonal to their initial direction. The charged clusters exhibit different trajectories based on their mass. A small aperture located in one plate collects nanoparticles of a specific size. [32]

Source:
[32] M. H. Wu, R. Mu, A. Ueda, and D. O. Henderson, *Mater. Res. Soc. Symp. Proc.* **638**, F13.2.1 (2001)

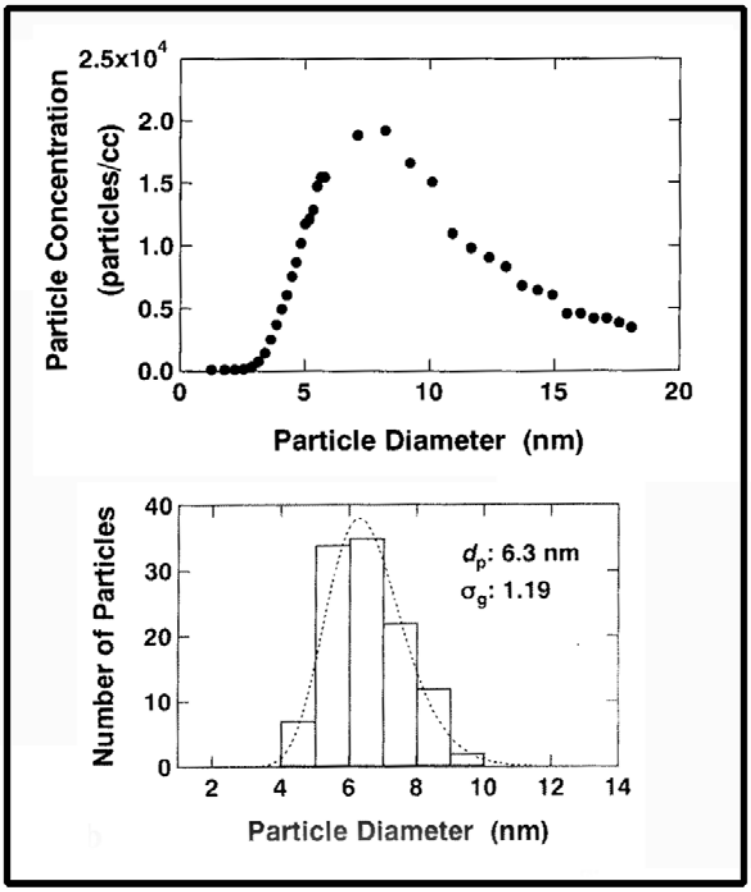

Figure 1.10 (cont'd) (b) The nanoclusters emerging from the DMA deposit as a film on an appropriately chosen substrate. An electrometer placed just above the substrate provides in situ information on the size distribution of a film as it is being deposited. Ex situ measurements of the film size distribution with an AFM reproduces closely the distribution obtained from the electrometer measurement. [32]

Source:

[32] M. H. Wu, R. Mu, A. Ueda, and D. O. Henderson, *Mater. Res. Soc. Symp. Proc.* **638**, F13.2.1 (2001)

Two major disadvantages of the process arise due to the long path that the nanoparticles must navigate prior to deposition. There is more time available, relative to the PLD technique where oxidation is already a problem, for the contamination of the particles through gas phase collisions with oxygen. Thus, high – vacuum environments ~ 10^{-10} Torr are required. Moreover, the Brownian motion of the nanoparticles in the low pressure ambient, ~ 10 Torr, is increased [32]. Thus, nanoparticles with diameters roughly < 5 nm will deposit in significant amounts on walls and tubes while traveling through the system reducing their contribution to the size – distribution at the substrate.

Nanoclusters were size – selected based exclusively on their velocity [33]. A highly directional, nanocluster beam was generated by directing a diffuse nanoparticle cloud into a supersonic nozzle. The nozzle collimates the beam and projects its into a specific direction and accelerates the nanoparticles. A high-speed, rotating disk, with a thin, radial slit was placed in the path of the beam to select nanoparticles based on their speed. Low mass nanoparticles will travel faster in the beam relative to higher mass particles comprised in the beam. Hence, nanoparticles were size – selected by controlling the frequency of rotation of the disc. A substrate was placed beyond the disc to collect nanoparticles that emerge from the rotating slit [33].

The minimum, average nanoparticle diameter that can be collected by this technique is roughly 3 – 6 nm [33]. A Gaussian nanoparticle distribution of ~ 2 nm FWHM is typical. The FWHM is related to both the rotating disc frequency and the nanoparticle distribution present in the vapor that passes through the slit [33].

Ledoux et al. produced patterned islands of nanostructures by placing a mask in front of the substrate during deposition [34]. The pattern of the mask is reproduced on the

substrate surface. A nanoparticle film deposits for each perforation in the mask with the same dimension of the mask feature down to perforation sizes of 10 μm x 10μm [34].

1.4.4 Alternative Processes to Produce Nanoclusters

The focusing of laser light at a scanning tunneling microscope (STM) tip has been used to deposit volatile species, from the probe tip to the scanned surface, with feature dimensions < 1 nm [35]. The transfer of tip atoms occurs preferentially at the sharp, STM tip where the optical field is locally enhanced and enormous coupling ensues between objects of spatial dimensions << than the laser wavelength, e.g., species at the precise tip. However, this process is limited to conducting materials and results are irreproducible from experiment – to – experiment due to the complexity of the experiments.
Ion sputtering, chemical vapor deposition (CVD) and laser – assisted chemical vapor deposition (LACVD) have been used to deposit nanoclusters from a thermally activated vapor phase.

Radio – frequency, magnetron sputtering followed by high – temperature annealing treatments, have been used to generate superlattices of alternating layers of amorphous silicon – dioxide (a-SiO_2) and nanocrystalline silicon (nc-Si) [36]. The thickness of the silicon layer defines the minimum dimension of silicon nanostructure. High strain fields in the SiO_2 layers prohibit crystallization in the silicon layers for layer widths less than ~ 4 nm. However, rf – magnetron sputtering is a highly reproducible, clean sputtering technique. Both nanocrystalline blocks and particles can be grown in the oxide confined silicon layers. [36]

In a similar process, plasma – enhanced chemical vapor deposition (PECVD) and excimer laser annealing have been used to produce a sandwich of nc-Si embedded between two layers of amorphous silicon nitride (a-SiN_x:H) [37]. Hydrogen was present in all precursor compounds, e.g., SiH_4 and NH_3, and hence was a component in all the deposited layers. The a-SiN_x:H layer was transparent to the laser (λ = 248 nm) wavelength so the incident energy coupled only with the a-Si:H layer. A 2 μm grating was placed in front of the laser beam to crystallize the a-Si:H layer in a striped geometry [37]. Only in regions of constructive interference does the crystallization phenomenon take place. The technique produces precise micro – scale organization. However, intraband crystallite size is extremely erratic in size distribution. Also, diffraction effects inherent to lithographic processes limit the minimum lateral dimension.

1.4.5 Photoluminescence from Si & SiO_x Nanostructures

1.4.5.1 Quantum Confinement

Silicon is an indirect band – gap semiconductor. In indirect band – gap materials, the conduction band minimum, in Fourier space, and the valence band maximum occur at different wave vector values. Luminescent transitions in silicon, via electron – hole recombination, have low quantum efficiencies ~ 10^{-6}, due to the misaligned bands. Phonon (lattice vibration quantum) absorption, or emission, is required to drive the radiative transition in indirect gap materials. Consequently, a phonon must be available to assist the transition and also it must have the proper wave vector to conserve momentum for the transition. This limits the number of transitions per absorbed photon and leads to an inefficient radiative process relative to a direct band – gap semiconductor.

In direct band – gap semiconductors, the minimum of the conduction band, in Fourier space, and the maximum of the valence band have the same wave vector value. Hence, momentum is conserved via a *direct*, electron – hole recombination. Phonon assistance is not required for these transitions. Direct band – gap materials, e.g., GaAs are most often used for optoelectronic applications based on their high quantum efficiency ~ 10^2 relative to indirect band – gap materials. However, most electronic devices, i.e., integrated circuits, are mostly composed of silicon or silicon oxide. If silicon could be rendered "optically efficient" complete optoelectronic integration with only silicon components could be realized. A reduction in the number of materials in a particular device correlates to easier thermal management and to reductions in production costs.

Quantum efficiencies of ~ $10^1 – 10^2$ can be realized in silicon taking advantage of the quantum confinement effect in nanostructures. Quantum confinement effects arise in silicon structures confined to dimensions < 50 nm. The luminescence efficiency of nanoscale silicon features increases due to the halting of Auger non – radiative recombination and the overlap of the electron and hole wavefunctions of an exciton (an electron – hole pair). Nanoscale silicon, exhibiting quantum confinement effects, is described as having a quasi direct band – gap.

Auger non – radiative recombination is the dominant electron – hole recombination process in bulk Si

$$(e^- + h^+) + e^- \rightarrow e^- + 1.1 \text{ eV (K.E.)}$$

where the 1.1 eV is dissipated as kinetic energy in the silicon [36]. This Auger recombination process is quenched in Si nanostructures. Moreover, the wave functions of electrons and holes comprising bound excitons overlap in quantum – confined dimensions.

This renders the nanostructure's band – gap quasi direct. To understand how the band – gap is "engineered" to a direct state, analogies have been made to the band – bending process that takes place in superlattice structures with nanoscale layers [36].

The optical emission and absorption properties of superlattices can be understood in the context of Brillioun zone folding of the original band structure [37]. Figure 1.11 shows the indirect band – structure in silicon (001) (the dotted lines in the figure) [37]. The folded zone structure is shown superimposed on the indirect band – structure. The Brillioun zone boundary is folded upon itself in submultiples to produce the final folded bands. Physically, as material boundaries approach the nanoscale, the coupling between the conduction band minimum and the valence band maximum increases. The band – gap is effectively reshaped by this change in band – coupling [37].

Gnutzmann et al introduced the concept of zone folding. [38]. Takagahara and Takeda applied the zone – folding concept to quantum – confined excitons in Si and germanium (Ge) nanocrystals [39]. They found the exciton energy and exciton binding (figure 1.12) energy to increase exponentially as nanocrystal size decreases for nanocrystal sizes less than roughly 60 nm [39]. The calculated values for exciton binding energy resemble closely the values determined experimentally for the activation energy of temperature dependent photoluminescence from Si nanocrystals [40].

In a photoluminescence experiment, the luminescent material is "optically pumped", via a flash lamp or laser beam, producing bound electron – hole pairs. The radiative recombination (luminescence) of these carriers is measured with a spectrometer – photomultiplier configuration. Decay rates from milliseconds (ms) to nanoseconds (ns) are observed for photoluminescence experiments on optically – pumped silicon nanoclusters

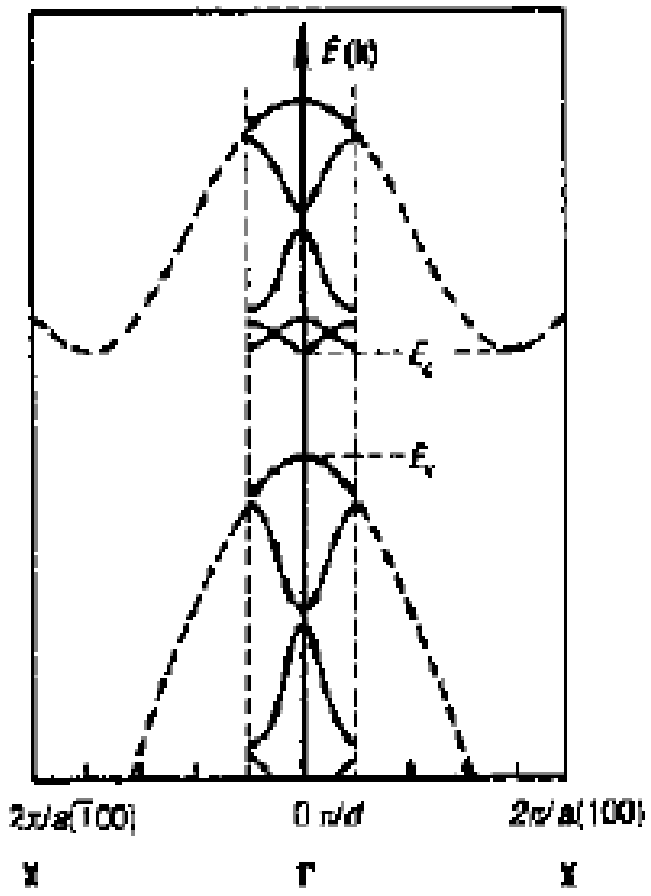

Figure 1.11 The Si(001) indirect band – gap for bulk silicon is shown as the perforated shape in the figure. Si nanostructures exhibit quasi – direct band gap behavior for nanoparticle d < 50 nm. Brillioun zone folding is one theory that has been proposed to account for the quasi – direct optical behavior. Folding the Brillioun zone in submultiples of 1/5 produces the direct band structure shown above. [37]

Source:
[37] S. S. Iyer and Y. –H. Xie, *Science* **260**, 40 (1993)

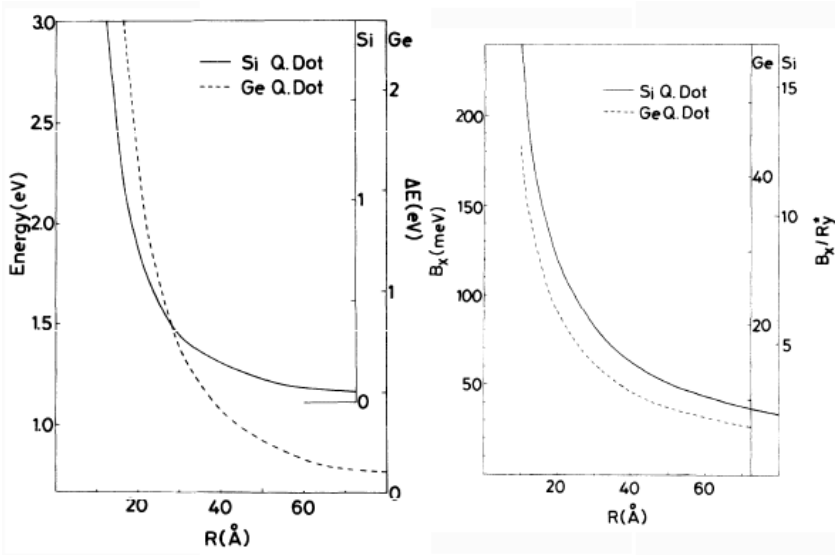

Figure 1.12 The calculated exciton energy (left) and exciton binding energy (right) for silicon nanocrystals of various diameters. The calculated values for exciton binding energy resemble closely the values determined experimentally for the activation energy of temperature dependent photoluminescence from Si nanocrystals. [39]

Source;

[39] T. Takagahara and K. Takeda, *Phys. Rev. B* **46**, 15578 (1992)

[41]. Photoluminescence experiments have produced results that are predicted by the quantum confinement theory. Most notably, quantum confinement theory predicts a relationship between nanoparticle diameter and emission quanta,

$$E_\lambda = E_o + \frac{3.73}{d^{1.39}} \qquad 1.11$$

where E_λ is the energy (eV) of the emitted quanta, E_o is the indirect band – gap energy of silicon (1.17 eV), and *d* is the silicon nanoparticle diameter in nanometers (nm) [42]. Bulk silicon inefficiently emits 1.17 eV photons when optically pumped.

Figure 1.13 shows a plot of experimental photoluminescence data, extracted from several sources, superimposed with equation 1.11 [43 – 46]. A reasonable fit of experimental data to theoretical predictions results, suggesting the quantum confinement model is responsible for the blue – shift of photoluminescence as nanoparticle diameter increases (figure 1.13). However, several other sources of luminescence have been identified for silicon nanoclusters.

A passivation layer exits on the surface of a silicon nanoparticle even in a high – vacuum environment, i.e., 10^{-9} Torr. A thin oxide layer, hydroxide bonds, and/or hydrogen bonds commonly terminate dangling surface bonds on Si nanoparticles. These terminating layers introduce interface and/or defect states that can radiatively emit discrete quanta.

Several sources of radiation emitters are now identifiable;

1 Si nanoclusters themselves, i.e., quantum confinement

2 Defects within the passivation layer encompassing the nanoparticle

3 Interface states between the Si nanoparticle and the passivating layer

Moreover, several contributors to non-radiative recombination can be identified which would detract from photoluminescence efficiency;

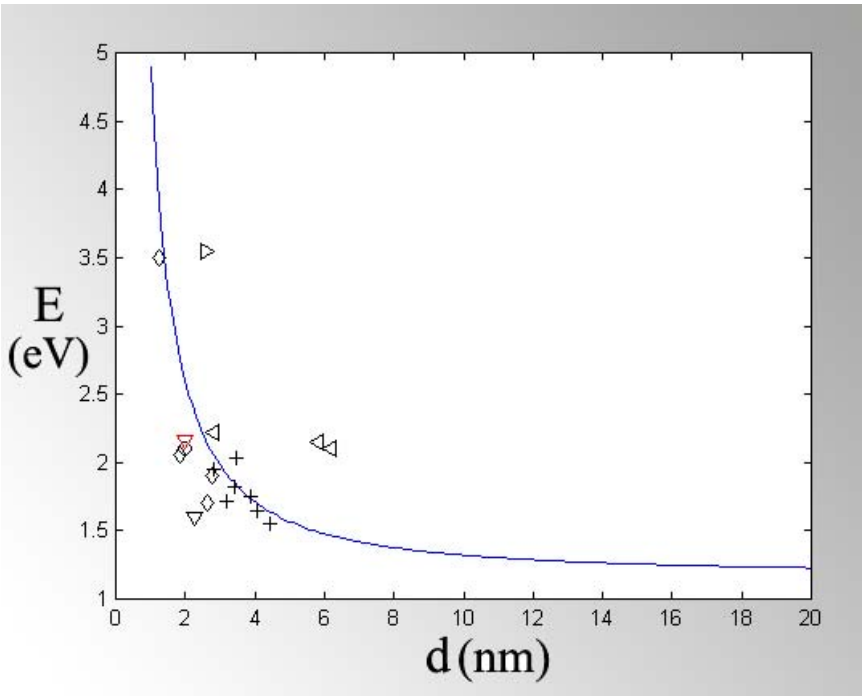

Figure 1.13 A survey of experimentally obtained photoluminescence maxima (eV) vs. Si nanocrystal diameter (data points). Quantum confinement theory predicts the relationship represented by the bold line. O Wolkin [43], + Ledoux [33], ◇ Patrone [47], ▽ Makimura [44], ◁ Botti [45], ▷ Li [46]

Sources;

[33] G. Ledoux, O. Guillous, D. Porterat, C. Reynaud, F. Huisken, B. Kohn, and V. Paillard, *Phys. Rev. B* **62**(23), 15942 (2000)

[43] M. V. Wolkin, J. Jorne, P. M. Fauchet, G. Allan, C. Delerue, *Phys. Rev. Lett.* **82**, 197 (1999)

[44] T. Makimura, Y. Kunii, and K. Murakami, *Jpn. J. Appl. Phys.* **35**, 4780 (1996)

[45] S. Botti, R. Coppola, F. Gourbilleau, and R. Risk, *J. Appl. Phys.* **88**(6), 3396 (2000)

[46] X. J. Li and Y. H. Zhang, *Phys. Rev. B* **61**(19), 12605 (2000)

[47] L. Patrone, D. Nelson, V. I. Safarov, M. Sentis, and W. Marine, *J. Appl. Phys.* **87**(8), 3829 (2000)

1 Absorption by dangling bonds at the Si nanoparticle surface

2 Auger recombination (only active in the bulk dimension)

3 Absorption by non – radiating defects

A review of experimental work now follows that addresses these radiative and non – radiative absorption mechanisms and which are present in Si nanoclusters.

A strong argument is presented in the literature for quantum confinement as the active photoluminescent mechanism in Si nanoparticles. [47 – 48, 21] In order to achieve *detectable* luminescence, *films* of Si nanoparticles, with "Gaussian – like" nanoparticle distributions, are optically pumped to generate intense luminescence, visible to the eye. This is the case in all the following works cited, *unless otherwise stated*. Moreover, the nanoparticles are formed by the PLA method via condensation of species to clusters in low pressures of inert background gas.

In a most *thorough* and *insightful* work, Marine et al. provide strong results, in the form of a discrete size model, that photoluminescence occurs through the quantum confinement of carriers [47]. They found *all* their photoluminescence spectra could be deconvoluted into a set of Gaussian emission bands from nanoparticles of *discrete* diameter, only nanoclusters with complete outer atomic layers emit radiation. Therefore, Si nanoclusters of diameter, d_2,

$$d_2 = d_1 + 2a \qquad 1.12$$

where d_1 is the nanoparticle diameter prior to the addition of one atomic monolayer a. Auger non – radiative recombination at the defects associated with nanoparticles of incomplete outer layers prevented these nanoparticles from contributing to experimental photoluminescence spectra [47] The photoluminescence efficiency of bulk c-Si has been

found to scale inversely with the non – radiative defect density for densities between 10^8 – 10^{12} cm^{-2} [49]. Moreover, the photoluminescence was tunable, via decreasing the nanoparticle diameter, over the range from the near – infrared to near – ultraviolet, respectively.

Ledoux et al. found their experimental photoluminescence results at various Si nanoparticle diameters to follow *precisely* equation 1.11 when narrow size distributions, e.g., $\Delta d = 0.44$ nm, of nanoparticles were illuminated [21]. Significant data scatter, relative to equation 1.11, occurs for Si nanoparticle distributions exceeding this value.

Si nanoparticles that condense in low oxygen pressure ambients, e.g., $p_{Ox} = 10^{-7}$ Torr, will have a thin, ~ 1 nm, SiO_x passivating layer on their outer surface. The photoluminescence from a film of these passivated particles is blue shifted if the film is annealed in an O_2 environment as a second process step [49]. The SiO_x passivating layer thickens at the expense of the Si core, i.e., the silicon core diameter decreases, during the annealing treatment. The luminescence blue shift observed is consistent with that expected, according to the quantum confinement model [49]. One could argue that the luminescence is due to defects in the oxide or at the interface. However, the luminescence maximum would not be expected to shift following nanoparticle oxidation because the electronic nature of the defect does not change with oxidation, only number density of defects. Thus, defects in the oxide, and/or at the interface, can be excluded as the luminescent center in a Si nanoparticle.

Morisaki et al. have attributed the photoluminescence from oxide – passivated, Si nanoparticles to a defect center within SiO_2. However, the explanation provided by the authors is not entirely consistent. For example, Si nanoparticles prepared by thermal

evaporation in 20% O_2 had ~ 10 times the luminescence of nanoparticles prepared in 1% O_2. They attributed the increase in luminescence to an increase in the number of defects in 20% O_2 relative to the number density in 1% O_2 yet no mention is made of the difference in particle density or morphology between the two films [50]. Moreover, the nanoparticle film formed in 20% O_2 is blue – shifted, as predicted by the quantum confinement model, relative to the film generated in 1% O_2. Thus, one could argue that quantum confinement induces the luminescence and the intensity increase is due to a *higher density* of collected particles. Figure 1.13 shows that the single data point (nanoparticle size vs. photoluminescence quanta) that they provide falls along the line (the red triangle data point) predicted by the quantum confinement theory [50].

Strong, visible room temperature photoluminescence has also been observed from nano – sized SiO_x agglomerate chains by [51]. They observed blue light emission at 2.7 eV for oxygen deficient, SiO_x nanostructures. The observed photoluminescence was attributed to radiative recombination at oxygen vacancies [51].

Si – OH (silanol) complexes terminating SiO_2 nanotubes have PL maxima at 2.7 eV [52]. Photoluminescence has been observed at 2.65 eV in oxygen deficient SiO_2 [53] and Tohman et al. have reported similar results [54]. Geohegan et al. observed violet PL (3.2 eV) from a film of average composition $SiO_{1.4}$ [18].

1.5 0 – D & 1 – D Si Quantum Dot (Nanocluster) Devices

Active electronic and optoelectronic devices have been fabricated taking advantage of the modified band structure of 0 & 1 – D silicon nanostructures and the tunneling capability of electrons through these nanoscale features [55 – 58] Historically, optical

devices have been fabricated with direct band – gap materials, e.g., gallium arsenide (GaAs) and these devices have been integrated with silicon – based microelectronics to assemble complete optoelectronic devices. However, a reduction in the number of materials in a particular device correlates to easier thermal management and to reductions in production costs. Nanoscale silicon features have "quasi – direct" electronic band – gaps and thus provide a way to engineer optically efficient, all silicon, devices.

The Bohr radius, the equilibrium spacing for an electron – hole pair, is ~ 5 nm in silicon. The electron and hole wave functions spread out and overlap when confined to spatial dimensions, within silicon, less than the Bohr radius. The band – gap is effectively rendered quasi – direct as a result of the overlap. Quantum size effects arise in silicon structures for feature widths of roughly < 50 nm. Hence, the radiative recombination efficiency of silicon is drastically increased, e.g., ~ 10^{-1} to 10^{1}.

A Si – based electroluminescent LED has been fabricated with an electroluminescent (EL) efficiency greater than 0.1% [55]. The LED produced red photon emission at 1.1 eV. Silicon grains ~ 100 nm in diameter, embedded in SiO_x, were responsible for the luminescence. A schematic of the device structure is shown in figure 1.14. The optically – active nanograins of silicon were formed by anodization of a p^+ doped region embedded in an n-type substrate. The anodization process interacts chemically with the hole majority in the p^+ region leaving the n – type region effectively undamaged. Luminescence was observed for forward bias > 1 V and at current densities < 10 mA/cm^2 [55].

Electroluminescent silicon pillars, d = 10 nm and L = 400 – 600 nm, have been fabricated using a combination of deep – uv lithography and highly anisotropic silicon

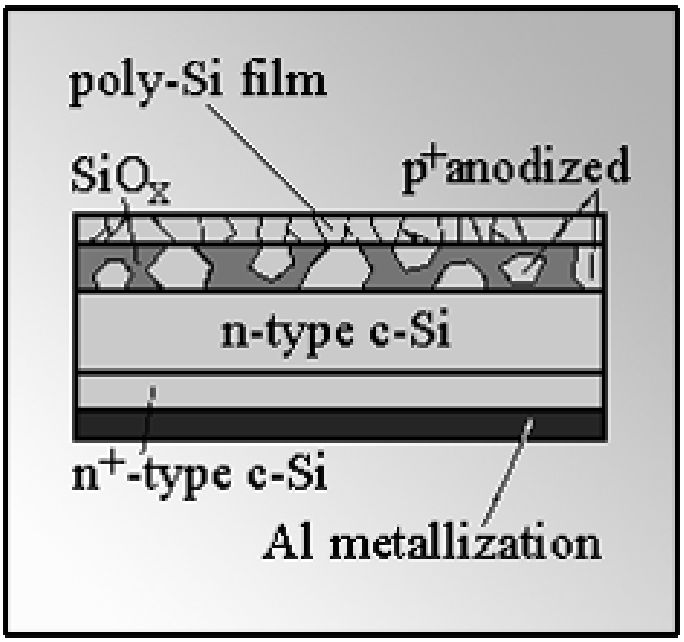

Figure 1.14 A schematic diagram (cross – sectional view), by the author, of Tsybeskov's electroluminescent LED. The LED had a quantum efficiency greater than 1%. The active region of the device contains Si grains, ~ 100 nm in diameter, embedded in an SiO_x matrix. [55]

Source:

[55] L. Tsybeskov, K. L. Moore, S. P. Duttagupta, K. D. Hirschman, D. G. Hall, and P. M. Fauchet, *Appl. Phys. Lett.* **69**(22), 3411 (1996)

reactive ion etching (RIE) [56]. Figure 1.15 shows the top – down, step – by – step procedure to generate the nanopillars. Figure 1.16 shows a SEM image of the nanopillars embedded in an electrically insulating layer of poly – methyl methacrylate (PMMA). Visible, room – temperature electroluminescence was observed from the device at forward voltages > 10 – 12 V [56].

A quantum dot transistor has been fabricated based on electron tunneling from quantum dot – to – quantum dot (QD) in a self – assembled quantum dot array [57]. Sharp metallic pads placed 30 nm apart were used as the source and drain for a QD device consisting of ~ 3 QDs located between the source and drain. A third conducting pad was deposited to supply a gate voltage.

The current – voltage characteristics of the QD transistor exhibited periodic plateaus. Such electrical behavior is consistent with single electron, quantum tunneling from dot – to – dot between the source and drain electrodes [57].

Arrays of silicon nanocrystals are also used in memory storage applications [58]. The nanocrystals are embedded in a control oxide, and store charge when active, in an n-type silicon – based, field – effect transistor (figure 1.17) A single – electron is stored per nanocrystal when the gate is forward biased with respect to the source and drain. Coulomb blockade limits the injection of additional carriers into the crystal [58]. Write – and – read times are on the order of 10^2 ns for these devices. Nanocrystal densities as high as ~ 10^{12} cm^{-2} are present in the oxide providing high storage densities. The oxide thickness between the gate control and the nanocrystal array *strongly* determines the "write" voltage. A thinner oxide layer corresponds to lower charge storage voltages. For example, charging is activated at 1.25 V for a tunnel oxide barrier of 1.6 nm thickness and a QD diameter of 5

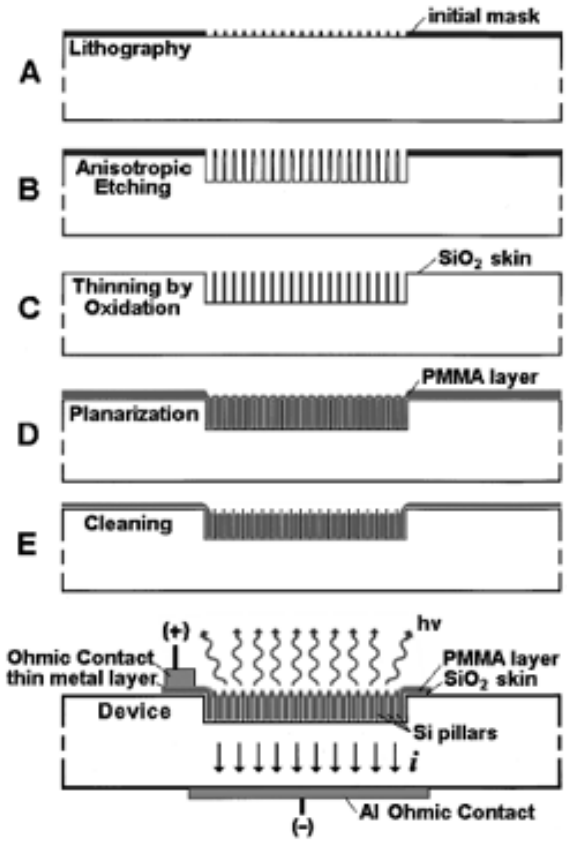

Figure 1.15 The step – by – step procedure to form electroluminescent Si pillars. A) An initial mask is generated on the surface by photolithography. B) High aspect ratio Si pillars are generated by anisotropic etching. The initial photolithography mask is removed. C) The pillars are thinned by oxidation to form SiO_2. Approximately 40% of the thickness of the new SiO_2 skin was previously Si pillar. D) The empty space surrounding the pillars is filled with PMMA to give additional structural stability to the Si pillars. E) A cleaning step ensures the tips of the pillars protrude from the PMMA layer. The device is completed when thin, metal layer contacts are deposited on the front and back surfaces. [56]

Source:

[56] A. G. Nassiopoulos, S. Grigoropoulos, and D. Papadimitriou, *Appl. Phys. Lett.* **69**(15), 2267 (1996)

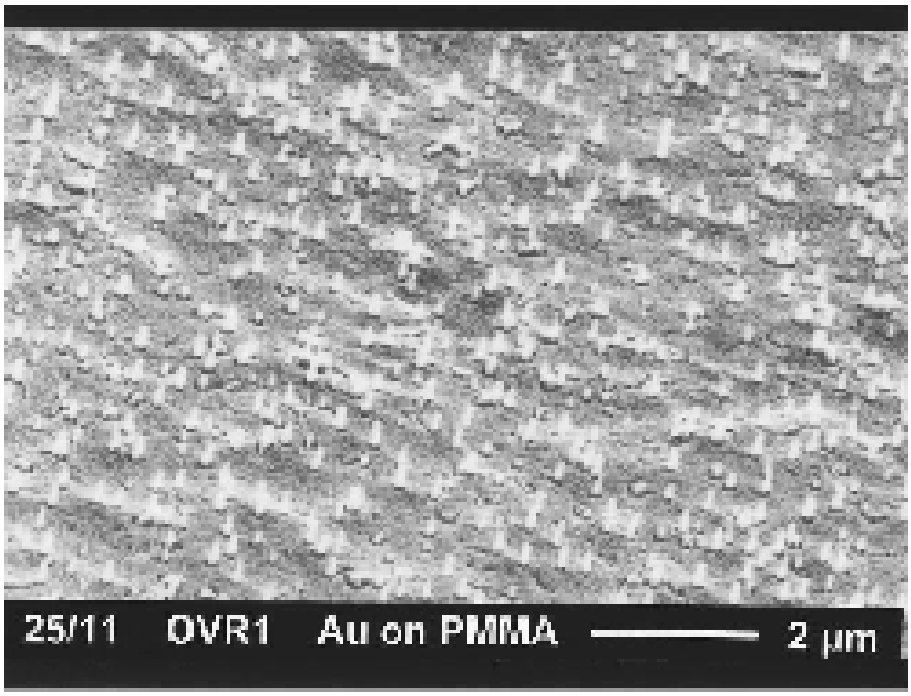

Figure 1.16 An SEM image, at oblique incidence, of the Si nanopillar tips protruding from the PMMA film. A thin, gold film is present on the surface to form the top surface metal contact. [56]

Source:
[56] A. G. Nassiopoulos, S. Grigoropoulos, and D. Papadimitriou, *Appl. Phys. Lett.* **69**(15), 2267 (1996)

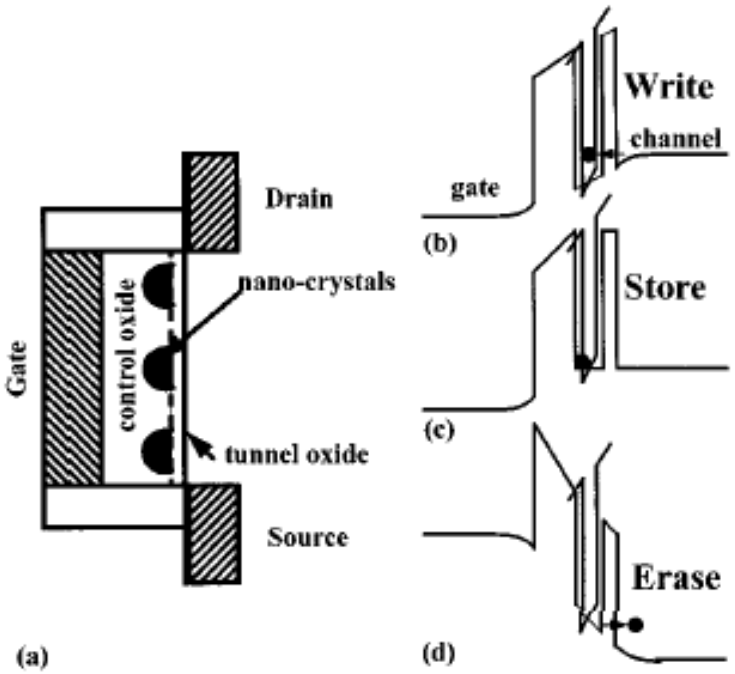

Figure 1.17 a) A silicon – based memory device. One electron is stored per Si nanocrystal when the control gate is forward biased (b) ~ 1.2 V with respect to the drain – source. The electron directly tunnels through an ultrathin SiO_2 layer 1.1 – 1.8 nm thick to store (c) in the nanocrystal. d) A reverse bias induces the stored electrons to tunnel across the oxide layer and to be carried away by the drain. [58]

Source:

[58] S. Tiwari, F. Rana, H. Hanafi, A. Hartstein, E. F. Crabbe', and K. Chan, *Appl. Phys. Lett.* **68**(10), 1377 (1996)

nm [58]. The low gate voltage and high charge storage density make these devices extremely attractive for memory storage applications.

1.6 Laser – Induced Target Morphologies

1.6.1 Laser-Induced Periodic Surface Structures

1.6.1.1 Introduction

The optical interaction of a pulsed laser beam with the near surface region of a material produces a stable, periodic grating pattern on the surface of the material [59]. The permanent damage on the surface has the form of a frozen, plane wave of a discrete spatial frequency (figure 1.18). An energy density approximately equal to the fluence required to melt the material is necessary to generate the surface damage. The periodic pattern is produced on the irradiated surface in as few as 1 – 10 laser pulses.

The periodic damage pattern has been indicated by various names prior to the establishment of the currently accepted designation, laser-induced periodic surface structures or LIPSS. Other names used to identify the damage pattern are; periodic surface damage, surface gratings, irreversible gratings, ripples, and periodic fringes. The LIPSS phenomenon has been studied extensively both theoretically and experimentally and several generalizations have been established relating the morphology of these structures intimately to the laser beam characteristics and sample orientation.

The generation of LIPSS structures depends on the polarization of the pulsed-laser beam and the plane of incidence of the laser beam with respect to the surface of the sample to be irradiated. Three relationships have been experimentally determined and theoretically derived that provide the wavelength of the LIPSS as a function of the angle of

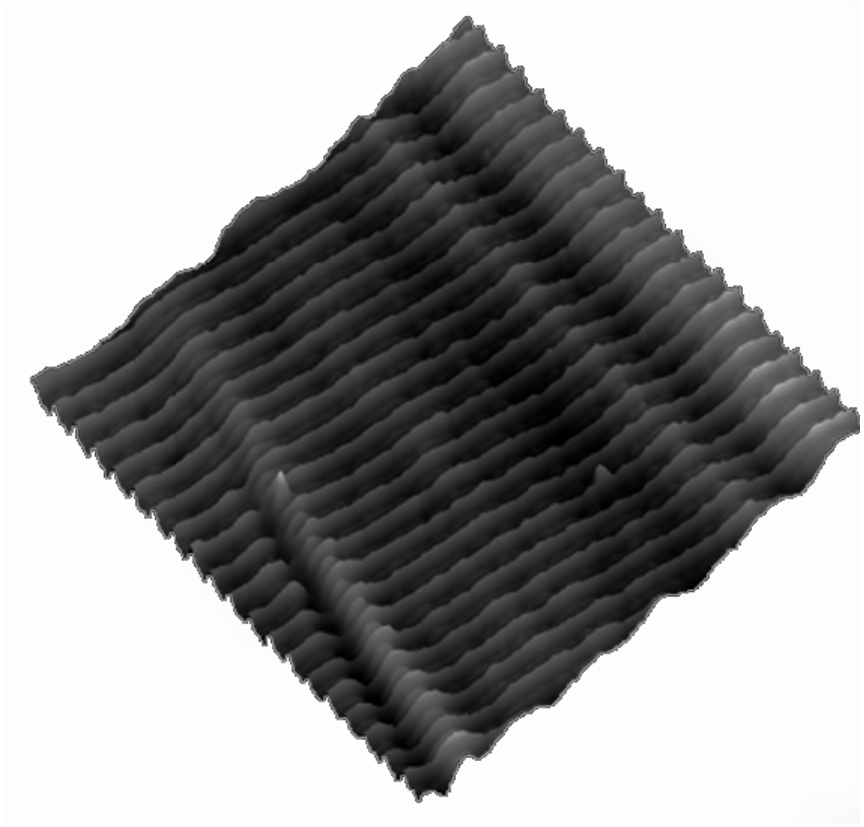

Figure 1.18 An AFM image of laser – induced periodic surface structures (LIPSS) on the surface of a c-Si substrate. The LIPSS waves formed following 400 pulses of 248 nm irradiation in 100 Torr He (E_d = 0.8 J/cm^2).

incidence of the laser beam. Linearly polarized light of the p-type, incident on the surface at an angle of incidence, θ, will induce a ripple pattern of wavelength;

$$\Lambda = \frac{\lambda}{1 \pm \sin\theta} \qquad 1.13$$

where λ is the laser beam wavelength. If the linearly polarized beam is of the s-type, the LIPSS spacing could also be determined by the relation;

$$\Lambda = \frac{\lambda}{\cos\theta} \qquad 1.14$$

In some instances results of experiments have been reported where deviations from these relationships have been observed [60 – 61] but the majority of data on LIPSS in the literature adheres to the abovementioned mathematical relationships. The orientation of the wave vector, **k**, of the LIPSS is governed by the polarization of the laser beam. In most instances the wave vector of the LIPSS runs parallel to the projection of the s- or p-polarized electric field vector.

The LIPSS spatial frequency depends exclusively on the frequency of the laser light used to generate them and the spatial orientation of the sample. Thus, it may appear that the phenomenon is material insensitive, i.e., the bulk properties of the underlying material have no effect on LIPSS formation. In fact, LIPSS obeying equations (1.13 – 1.14) have been observed in a variety of materials, i.e., metals [62 – 65], semiconductors [66 – 67], dielectrics [68 – 69] and polymers [70 – 75]. However, one requirement of the bulk is to absorb at the laser beam wavelength, and the energy density of the beam must be above the melting threshold. As reviewed in section 1.6.2, LIPSS waves can be initiated in the surface plane *either* by optical excitation of surface electromagnetic waves, i.e., surface polaritons , *or* by mass transport via surface tension gradients.

1.6.1.2 Review of LIPSS Studies

Birnbaum first identified the existence of a periodic grating in the surface layer of ruby laser-irradiated germanium [59]. He attributed the evolution of the grating pattern to inhomogeneous energy deposition in the surface layer. In 1976, Temple and Soileau found that the ripples were most easily promoted by defects spaced distances apart approximately equal to the laser beam wavelength [76].

By the early 1980's a number of processes to describe ripple evolution and growth were emerging in the literature. Brueck et al. observed the scattering of the incident light pulse, from surface microroughness and/or surface contamination, into surface plasmon modes that oscillate transversely and propagate in the surface plane [77]. The surface grating (LIPSS) formed when the surface plasmon condensed in the surface layer. In semiconductors and dielectrics the condensation of surface polaritons was responsible for the observation of stable ripple patterns in these materials [78 – 79].

Maracas et al. postulated that the nonlinear interaction of oscillating axial modes of the laser itself were responsible for ripple formation [80]. In a thorough analysis, Guosheng et al. proposed a growth model whereby scattered light, nearly along the surface, interferes with the incident pulse that ultimately modulates the light absorbed in these regions [81]. A feedback process between the optical interference pattern and the modulated surface was indicated as the driving force for ripple growth.

From a similar point-of-view to the Guosheng work [81], Young et al. also attributed the initial evolution to light propagating approximately along the surface but criticized the "surface scattered wave model". They proposed the existence of a selvedge region of thickness $<< \lambda$, the wavelength of the laser light, containing a vertical roughness

in the layer such that the optical properties of the selvedge region change in the vicinity of the scattering center. Theoretically, they found certain specific Fourier components of the selvedge to be especially effective at creating electric fields [82]. Radiation remnants are scattered electromagnetic waves, traveling parallel to the surface, that are coupled into these Fourier modes. Scattering was especially effective in certain directions along the surface.

In 1983, Sipe et al. proposed a comprehensive theory to describe LIPSS evolution and growth [83]. The theory detailed exactly how the light distributed over the surface plane as a result of scattering in the selvedge. A follow up paper was written to detail the experimental characteristics of LIPSS growth and evolution [84]. In 1984 Young et al. published a third paper in a series "Laser-induced periodic surface structures", to address the mechanism for mass transport required to transform the surface region into a grating morphology [85]. They found that, depending on the incident fluence, the necessary mass transport could be attributed to either partial melting or capillary waves.

The equations giving the spatial frequency of LIPSS waves as a function of the angle of incidence and the polarization of the laser beam are derived in this section. The derivation is carried out in Fourier space and the surface scattered waves, required for LIPSS formation, are generated via laser beam scattering by preexisting surface relief. Relationships for both s- and p-polarized light are derived. The derivation follows closely that as provided by Akhmanov et al. [86]. This derivation closely adheres to the "surface-scattered wave" development of spatial period vs. angle of incidence equations provided by Guosheng et al. [81].

The electric field vector of a traveling electromagnetic wave can be decomposed into two orthogonal components. The two components lie in a plane orthogonal to the propagation direction of the wave. A laser pulse emanating from a gas laser contains un-polarized light. If the light pulse is made to interact with an interface oriented in space such that the normal to the interface lies at an angle with respect to the incident laser pulse wave vector, the electric field vector can be decomposed into s- and p- components, indicated in figure 1.19.

Figure 1.19 shows a schematic diagram of a laser pulse striking an interface oriented at some arbitrary angle θ. Due to the tilting of the substrate it is possible to define a plane of incidence as the plane containing the surface normal of the interface and the incident wave vector. The electric field vector is shown in the diagram at some time, t, and it is assumed this field is interacting with the surface with the magnitude and direction as shown. It is then possible to decompose this vector into s- and p- components. The p-component lies in the plane of incidence and s- component is orthogonal to the plane of incidence.

A laser beam that encounters an interface is partially reflected and partially absorbed. A diffracted wave is also produced as a result of the laser – interface interaction if a roughness is present on the surface. Diffraction from a grating is described quantitatively by the grating equation;

$$\vec{k} = \vec{k}_i \pm n\vec{q} \qquad 1.15$$

where **k** is the reflected/refracted (diffracted) wave vector, $\mathbf{k_i}$ is the incident wave vector, and **q** is the grating vector in the surface plane. This equation holds for all reflected and refracted waves into the ambient and bulk, respectively.

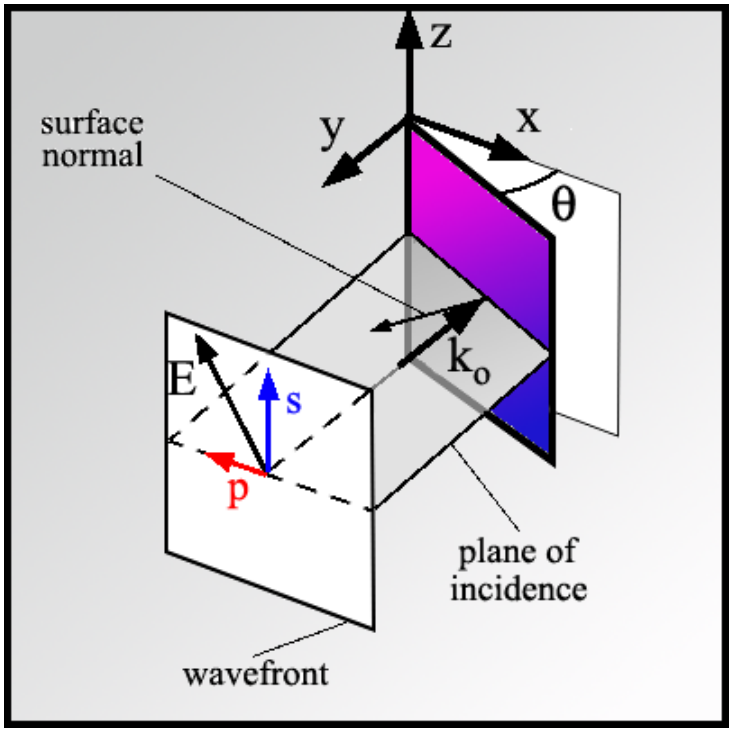

Figure 1.19 A schematic representation of a coherent, planar wave front parallel to the x – z plane approaching a substrate parallel to the z – axis, tilted with respect to the x – axis by θ. An electric field vector lying in the wave front plane can be decomposed into s- and p- components with respect to the surface. The plane – of – incidence is defined as the plane containing the wave front wave – vector and the substrate surface normal. The p-component of the electric field lies in the plane – of – incidence and s- component of the electric field lies orthogonal to the plane – of – incidence.

The diffracted wave travels in specific modes, (n) in equation 1.15, the modes being differentiated by the angle their wave vector makes with the interface normal. The periodicity and roughness of the surface relief, **q**, determines the magnitude and direction in which the modes propagate. Two particular modes will propagate parallel to the interface. A Stokes and Anti-Stokes wave propagate in opposite directions along the surface and are contained in the plane of incidence, as shown in figure 1.20.

Diffracted waves in the surface plane must satisfy the grating equation. The grating spacing for the Stokes (q_+) and anti-Stokes (q_-) scattered components respectively are;

$$\vec{q}_+ = \vec{k}_t + \vec{k}_s \qquad 1.16$$

$$\vec{q}_- = -(\vec{k}_t - \vec{k}_{as}) \qquad 1.17$$

where $\mathbf{k_t}$ is the projection of the incident laser wave vector in the surface plane. The vector diagrams in the bottom portion of figure 1.20 show the Stokes and anti-Stokes grating vectors for a particular angle of incidence θ. It should be noted that the magnitude of the Stokes and anti-Stokes waves are equal in magnitude in the diagram. This is the *degenerate* case for the conservation of momentum. Under degenerate conditions, the projection of the incident wave vector in the surface plane is directed *parallel* to the grating wave vector. Experiments in this work were conducted under these conditions.

The magnitude of the Stokes/anti-Stokes wave vector is;

$$\left|\vec{k}_{s/as}\right| = \frac{\omega}{c}\left(\frac{|\varepsilon'|}{|\varepsilon'|-1}\right)^{\frac{1}{2}} \qquad 1.18$$

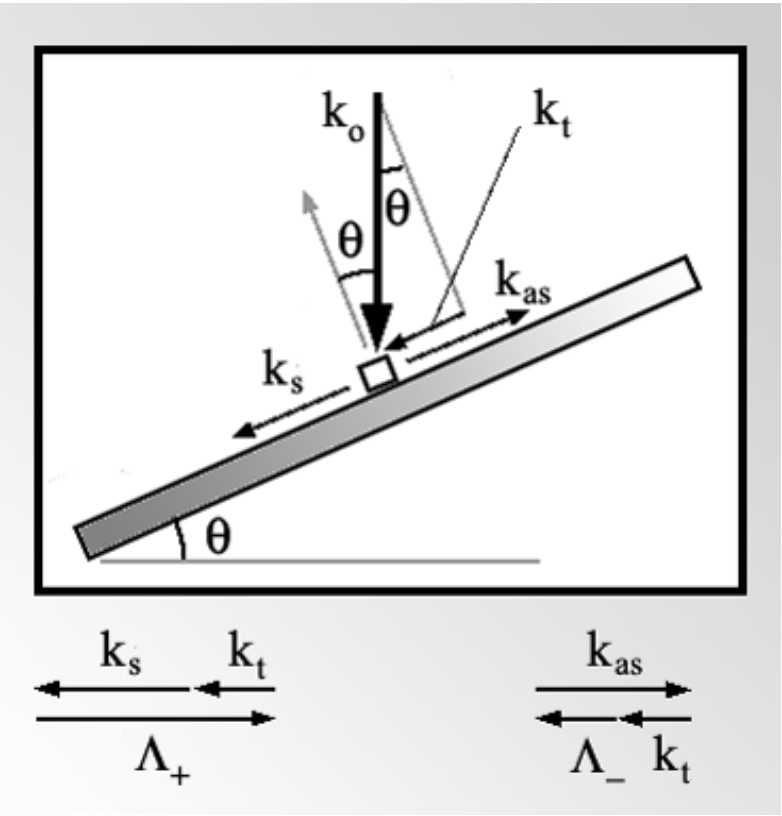

Figure 1.20 A schematic, cross – section view through a substrate being irradiated by a coherent, ***p – polarized*** wave front with wave vector $\mathbf{k_o}$ incident at an angle θ with respect to the surface normal. The wave is diffracted by a surface roughness and certain orders of the scattered wave propagate roughly parallel to the substrate surface. A Stokes wave propagates down the substrate surface and an anti – Stokes wave propagates up the substrate surface. The interaction between the surface scattered waves and the incident wave front produces an interference pattern in the surface plane. Both the Stokes and anti – Stokes waves can each be added, individually, to the projection of the incident wave vector, in the surface plane. The resulting two vectors, Λ_+ and Λ_- give the wavelength of the inhomogeneous intensity distribution (the interference pattern) on opposing sides of the surface roughness.

where ε' is the real part of the frequency dependent dielectric constant, c is the speed of light, and ω is the frequency of the laser light. For crystalline silicon, c-Si, ε' = 11.9 and substituting this is equation 1.18 gives;

$$\left|\vec{k}_{s/as}\right| = 1.045\frac{\omega}{c} = 1.045\left|\vec{k}_o\right| \approx \left|\vec{k}_o\right| \qquad 1.19$$

where k_o is the incident laser light wave vector. The projection of the incident light wave vector, incident at an angle θ with respect to the surface, in the surface plane is;

$$\left|\vec{k}_o\right|\sin\theta = \left|\vec{k}_t\right| \qquad 1.20$$

Substituting 1.19 in 1.20 and then filling 1.20 into 1.16 & 1.17 gives;

$$\left|\vec{q}_+\right| = \left|\vec{k}_o\right|\sin\theta + \left|\vec{k}_o\right| \qquad 1.21$$

$$\left|\vec{q}_-\right| = -(\left|\vec{k}_o\right|\sin\theta - \left|\vec{k}_o\right|) \qquad 1.22$$

The relationship between wavelength and wave vector is;

$$\left|\vec{k}_o\right| = \frac{2\pi}{\lambda_o} \qquad 1.23$$

and substituting 1.23 into 1.21 & 1.22 gives equation 1.13 which is rewritten here;

$$\Lambda_+ = \frac{\lambda_o}{1+\sin\theta} \qquad 1.24$$

$$\Lambda_- = \frac{\lambda_o}{1-\sin\theta} \qquad 1.25$$

Λ is the grating spacing and λ_o is the incident laser pulse wavelength.

In the case of s-polarized light the incident laser light wave vector is orthogonal to the LIPSS wave vector and both vectors lie in the surface plane. In figure 1.21 both vectors are shown schematically; the plane of the page is parallel to the surface being

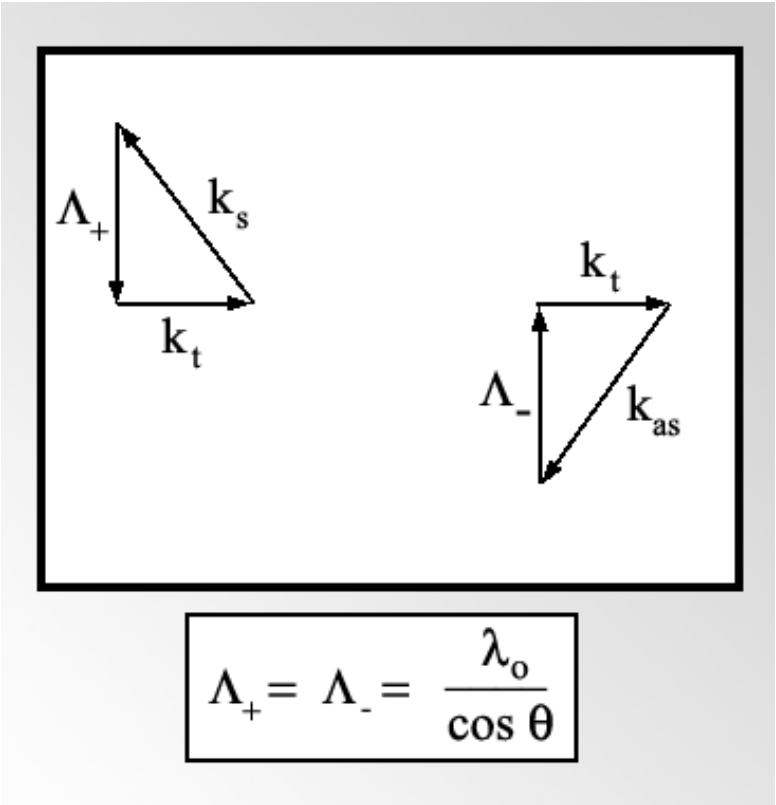

Figure 1.21 The interference pattern (surface scattered wave + incident wave) produced on opposite sides of the surface roughness during ***s – polarized***, coherent source irradiation *has the same wavelength* because the surface is not tilted along the direction of propagation of the Stokes and anti – Stokes waves (which, in this case, can not be differentiated from one another).

irradiated. If the same analysis, as applied to the p-polarized case in the previous section, is used to derive the grating spacing equation for the s-polarized case, the following expression is obtained;

$$\Lambda_+ = \Lambda_- = \frac{\lambda_o}{\cos\theta} \qquad 1.26$$

The Stokes and anti-Stokes components are indistinguishable.

1.6.2 Mechanisms of LIPSS Growth

LIPSS structures can develop from an active, optical surface *polariton*. A polariton is the quantum unit of energy associated with a resonant, coupled phonon-photon wave field. The polariton is excited if the frequency of the laser light is at or near the oscillating frequency of the polariton. This is termed resonant transverse phonon – transverse photon coupling and occurs predominantly in semiconductor or dielectric materials. In metallic materials surface *plasmons* couple with the incident photons *if* LIPSS waves are formed via the SEW pathway [77].

The electric field of the photon couples with the dielectric polarization of the *surface* ions that make up the transverse, optical (TO) phonon mode. At ultraviolet wavelengths silicon attenuates the incident, oscillating field quickly; the absorption coefficient $\alpha = 1.83 \times 10^6$ cm^{-1} and thus, 0.63 of total absorption has occurred at a depth of 5.5 nm below the surface. A dispersion relation results in the coupled system as a result of the quantum nature of the phonons. For example, in c-Si, forbidden frequencies of coupled fields thus exist for frequencies around ~ 20 μm. Thus, for the ultraviolet irradiation of single-crystal silicon substrates, the propagation of polaritons is allowed and *could* be the active pathway for LIPSS growth.

The grating spacing for polaritons, as a function of incidence angle, is similar to those equations (24) & (25) for LIPSS formation,

$$\Lambda_{SEW} = \frac{\lambda}{\frac{c}{\nu_{ph}} \mp \sin\theta} \qquad 1.27$$

where n is the index of refraction of the material [78]. Keilmann et al. generated LIPSS on the surfaces of both quartz and Suprasil [78]. LIPSS initiated at preexisting surface microroughness. Figure 1.22 shows LIPSS of spacing Λ_+ and Λ_- propagating in opposing directions away from the microroughness [78]. They attributed ripple formation to the holographic recording of propagating surface polaritons.

Erlich et al. also attributed ripple evolution to scattering of incident laser light by cracks and surface defects [79]. They laser irradiated germanium with 533 nm laser pulses and described ripple formation assisted by feedback occurring through the modulation of the liquid/solid interface by the interference of the incident beam and the scattered components of the beam. Scattering by a surface polariton wave increased with the number of pulses as a result of the periodic surface modulation and index of refraction gradient increase. In metals, surface plasmon propagation can also lead to LIPSS generation [77]. In this case, the LIPSS wave vector was also parallel to the grating wave vector in cadmium, zinc, and aluminum thin films. The spatial period of the ripples was equal to the surface plasmon wavelength.

Young et al. conducted a series of experiments at various fluences around the melting threshold of germanium [84]. They found two distinct formation mechanisms for LIPSS depending on the fluence. LIPSS formed by partial surface melting in the fluence range of 120 – 200 mJ/cm^2 [84]. Long, thin equally – spaced strips of germanium were

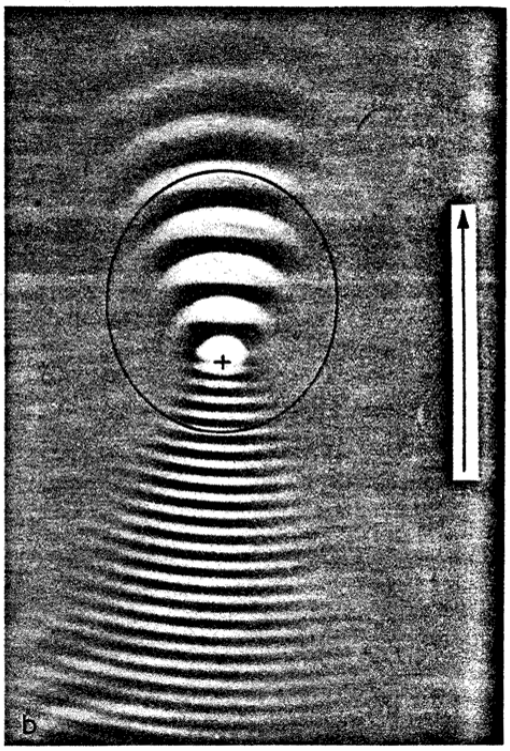

Figure 1.22 A SEM micrograph of the interference phenomenon illustrated schematically in figure 1.20. An inhomogeneous intensity distribution was produced on Suprasil by the interference of surface scattered waves, propagating in opposite directions from roughness at (+), with incident p – polarized laser light. The scattered light was absorbed into surface polariton modes, during the molten state during and immediately following irradiation, and these oscillating modes were "frozen" into the near surface region when the surface resolidified. [78]

Source:
[78] F. Keilmann and Y. H. Bai, *Appl. Phys. A* **29**, 9 (1982)

melted during each laser pulse cycle forming the LIPSS morphology. For 1.06 μm CO_2 beam irradiation, strips ~ 0.25 μm wide and spaced ~ 1 μm apart are produced on the surface [84]. At higher fluences, in the range 220 – 450 mJ/cm^2, they found the LIPSS morphology to develop by the freezing of oscillating capillary waves.

Oscillating, capillary waves are launched by surface tension gradients in the near surface region. A non-uniform surface temperature induces the surface tension gradient as the surface tension decreases with temperature;

$$\frac{d\sigma}{dT} < 0 \qquad 1.28$$

where σ is the surface tension and T is the temperature. The spatially non-uniform heating during laser annealing results in the following equation describing the temperature along the surface as;

$$T(x, z=0, t) = \left[\left(A_1 - \frac{g v_o}{x} \right) \xi - q A_2 \varphi_o - i q A_3 a_{oo} \right] e^{-iqx + i\Omega t} \qquad 1.29$$

where φ is scalar potential of the velocity, g is the acceleration due to gravity, ξ is a Fourier component of the surface relief, and Ω is the surface roughness frequency [86].

If a perturbation of a discrete period is present in a liquid layer and if the wavelength of the perturbation is << $(\gamma/\rho g)^{1/2}$, the force acting to restore equilibrium is the surface tension, γ and where ρ is the liquid density. A dispersion relationship exists for thermocapillary waves and is of the form;

$$\omega_c = \left(\frac{\gamma}{\rho} \right)^{\frac{1}{2}} k_c^{\frac{3}{2}} \qquad 1.30$$

where k_c is the wave vector of the liquid surface perturbation, ω_c is the capillary wave oscillation frequency, and ρ is the liquid density. Figure 1.23 shows a plot of the capillary wave oscillation frequency excited at ultraviolet/blue electromagnetic wavelengths. The perturbation wavelength is assumed to be equal to the incident light wavelength. This is indeed the case for LIPSS waves produced on surfaces oriented at normal incidence with respect to the incident laser beam. The oscillation frequency of the liquid perturbations increases rapidly for spatial periods equivalent to ultraviolet, electromagnetic wavelengths.

Viscous forces damp the capillary waves as

$$e^{-\left(\frac{2\eta}{\rho}\right)k_c^2 t} \qquad 1.31$$

η is the shear viscosity of the liquid. The damping expression, equation 1.31, is plotted vs. time in figure 1.24 for an excitation wavelength of 248 nm. The initial amplitude is reduced to 10% of its initial value after only ~ 5 ns. This time is extremely short compared to melt times in silicon at fluences conducive to the development of LIPSS, i.e., under an irradiation fluence of 0.8 J/cm^2 the melt duration is ~ 60 ns in Si under 248 nm illumination. Figure 1.25 shows the damped, oscillation cycle vs. time for an excitation wavelength of 248 nm.

Stable, LIPSS structures have been observed when semiconductor materials were irradiated under ultraviolet wavelengths [87]. An essentially flat substrate surface should have been produced by the processing conditions used, based solely on the high damping rate calculated in the previous section. Thus, an additional variable must be acting during irradiation and melting to stabilize the LIPSS morphology.

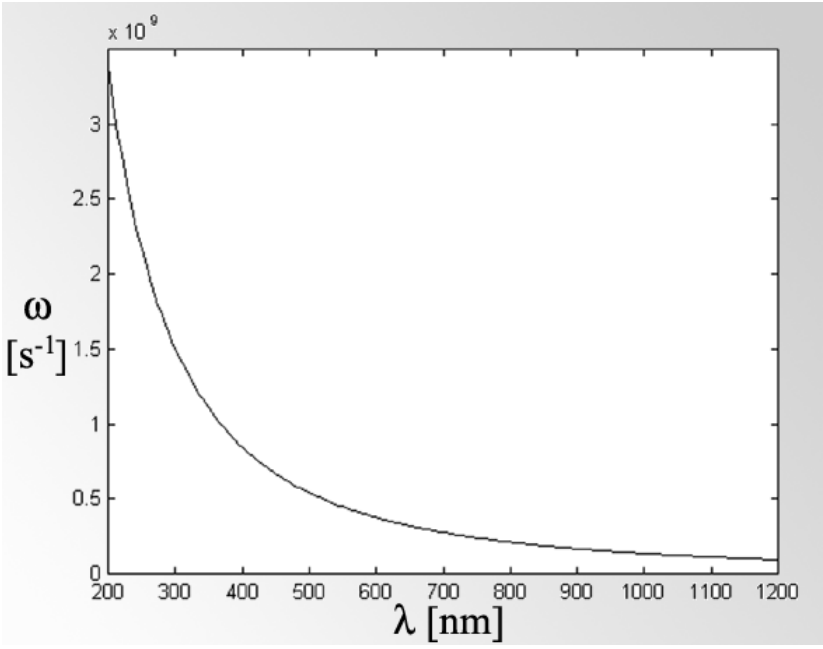

Figure 1.23 The calculated dispersion relationship for the oscillation frequency of capillary waves in silicon for excitation wavelengths ranging from 200 – 1200 nm.

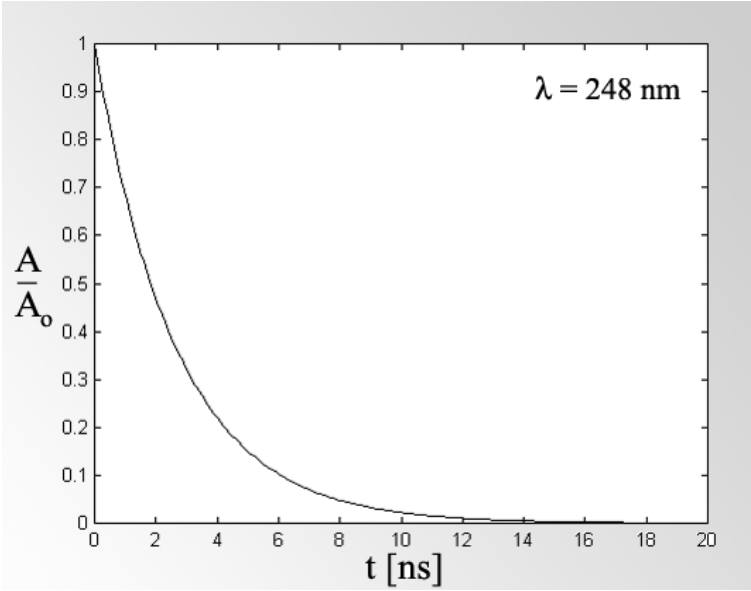

Figure 1.24 The normalized value of the calculated damping coefficient of capillary waves excited at 248 nm in c-Si as a function of time. The damping force is the surface tension gradient in the liquid layer for the laser – induced oscillating capillary waves. The damping of the oscillation is roughly complete after only 12 ns.

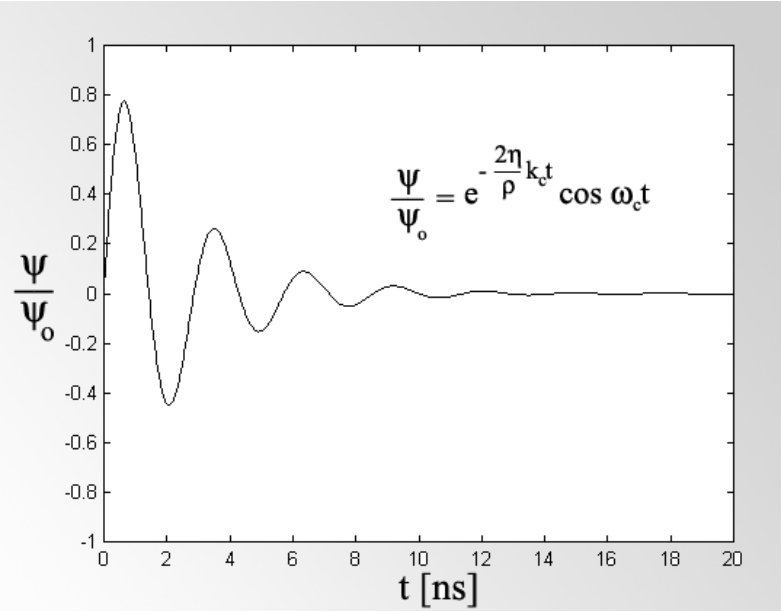

Figure 1.25 The calculated amplitude of a uv – laser (248 nm) excited, surface tension damped, capillary wave oscillating in a thin melted region present on the surface of a c-Si substrate.

Chapter 2

Experimental Procedure

2.1 Sample Preparation Procedure

Test grade silicon wafers of (001) orientation were used in the ablation/surface modification experiments. The wafers were four inches in diameter, n – type, phosphorous doped, and were purchased from Transition Technology International (TTI). The specified thickness range of the wafers was 475 – 525 μm. The resistivity range for the (001) wafers was 1.0 – 6.2 Ω cm.

The wafers were cut to sizes of ~ 1 x 2 cm^2 prior to introduction into the irradiation chamber. The wafers were scribed on their unpolished surface using a sharp edged diamond knife. Each scribe was made along a <100> direction. A light load was then applied to the unpolished face to cleave the wafer along the scribe. This procedure ensured a sharp, cleaved wafer edge.

The native oxide was removed, in some cases, from the surface by a 5 minute dip in 10:1 HF dilute in distilled and de – ionized H_2O. The HF dip was bought from J. T. Baker inc, in order to have a consistent, uniform oxide removal process from sample – to – sample. Following the HF dip the surface was immediately rinsed in methanol in order to stabilize the hydrogen bonds terminating the Si surface (these H – bonds were formed during the oxide removal dip) for time > 2 minutes. This ensured that no oxide reformed on the surface in the time it took to introduce the sample into the high vacuum chamber.

Following the methanol rinse, the sample was rinsed with distilled H_2O, blown dry with Ar/ 5% - H_2 gas and introduced into the sample chamber. The sample chamber was pumped to roughly $1x10^{-2}$ Torr with a mechanical pump and then backfilled with UHP He

or UHP Ar. This procedure was performed to remove residual oxygen from the chamber introduced during sample insertion from the air, and the pump and backfill procedure was also repeated three times prior to high vacuum pumping to $1x10^{-7}$ Torr via a turbomolecular pump.

2.2 Laser Irradiation Procedure

A Lambda Physik LPX – 305i excimer laser producing KrF (248 nm) wavelength radiation was used to irradiate the single – crystal Si (001) wafers. Figure 2.1 shows a schematic diagram of the beam delivery pathway from the excimer laser output window to the fused silica entrance window to the high vacuum, stainless steel chamber. An aperture was used to trim the unwanted, low energy Gaussian tail from the emitted laser beam to ensure a more uniform laser pulse, in energy, irradiated the substrate.

The excimer laser produces un – polarized laser pulses. A ultraviolet light beam – splitting cube, purchased from Newport, was introduced into the path of the beam for experiments that required either p – or s – polarized laser beams (figure 2.1). A beam attenuator, purchased from the Acton Research Company (ARC), with variable attenuation, as a function of tilt angle of the attenuator, was used to aide in controlling the beam energy. The laser beam energy density was most often controlled by varying the laser beam spot size on the sample surface using converging fused silica optics. The output energy of the laser beam was controlled by varying the high voltage discharge in the excimer gas tube over a range of 13 – 23 kV (0.1 J – 1.1 J).

The sample chamber is shown in the digital photograph provided in figure 2.2. The picture was taken looking at the chamber from the laser beam entry port. The focused

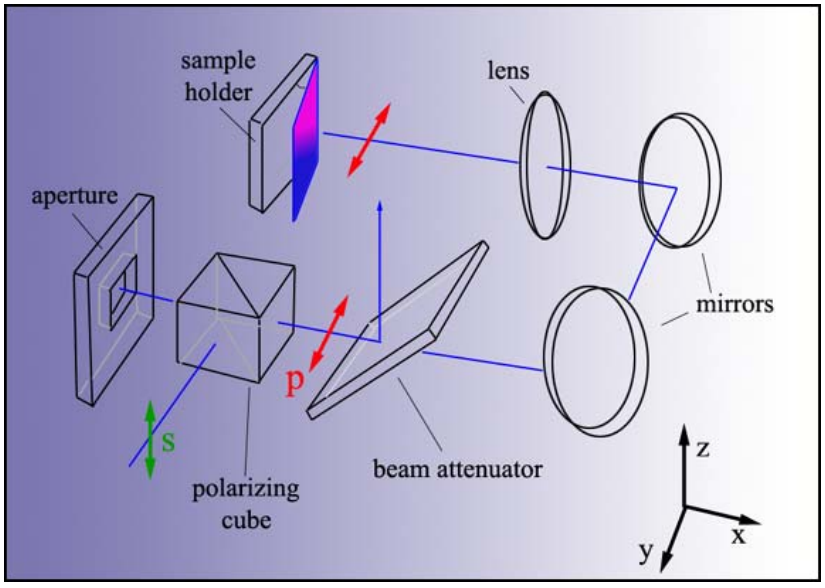

Figure 2.1 A schematic diagram of the laser beam path from the excimer laser output window to the sample. The sample was always irradiated in a high vacuum, stainless steel chamber, however the chamber was left out of the above schematic to reduce clutter.

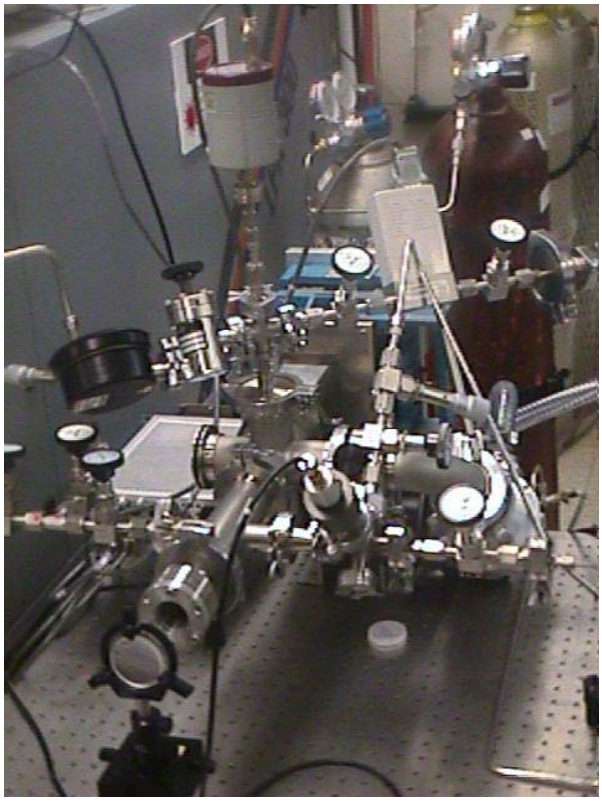

Figure 2.2 The stainless steel, chamber used to house Si samples under either vacuum conditions of $1x10^{-7}$ Torr or for a specific gas type with both pressure and flow control available.

laser beam entered the chamber via a 2" fused – silica window. The energy of the beam entering the chamber was measured with a Scientech Astral AD30 volume absorber calorimeter. The calorimeter was placed in front of the window to measure the energy and was removed prior to laser treatment. The energy density reaching the target was determined by measuring the laser spot mark produced on target after irradiation and dividing this number by the energy that was obtained using the calorimeter. Thus, the energy density values reported in this work are average values because the energy profile of the laser beam was not completely homogeneous, ever after passing through the aperture.

A wide – range of irradiation conditions were investigated to determine their affects on Si wafer surface morphology and Si nanoparticle formation. The laser fluence range investigated was 0.5 – 4 J/cm^2. Laser pulse repetition rates of 1 to 10 Hz were used. The number of laser pulses spanned three orders of magnitude from 1 to 4000 laser pulses.

The laser treatments were carried out in a number of different atmospheres including air, UHP Ar, UHP He, SF_6, $O_2 – N_2$, O_2 – Ar, and vacuum. The gases were pure to two decimal places 99.95%, except for the ultra – high purity gases (UHP) which had a purity to four decimal places, 99.9995%. MKS brand mass flow controllers were used to regulate the flow of gas into the chamber. An MKS pressure controller coupled to MKS pressure transducer allowed for feedback control of the pressure from 1 – 10^2 Torr. The pressure in the chamber was also measured using both a Varian ionization gauge at low pressure ($1x10^{-3}$ – $1x10^{-7}$ Torr) and a Boc dial gauge (50 – 760 Torr). Figure 2.3 shows a digital image of the chamber configuration with all the important attachments indicated and listed in the figure.

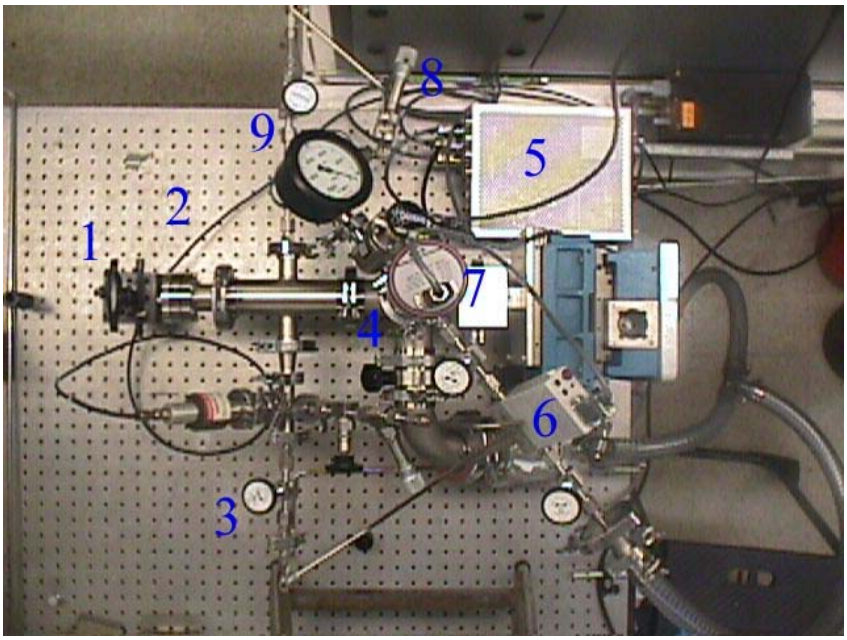

Figure 2.3 A top – down view of the sample chamber with all the main chamber components labeled. 1) beam focusing optic, 2) chamber entrance window, 3) inert gas entry for venting, 4) sample location (in chamber), 5) mass flow and pressure control box, 6) pressure controller, 7) capacitance manometer, 8) needle value for gas flow regulation, and 9) reactive gas inlet port.

A Pascal series mechanical pump and an Alcatel turbomolecular pump were attached in series to lower the pressure in o – ring sealed, vacuum chamber. Prior to each experiment the chamber was pumped to base pressure of $1.2x10^{-7}$ Torr to remove gaseous impurities present in the chamber.

2.3 Post – Irradiation Morphology and Microstructure Characterization Techniques

2.3.1 Scanning Electron Microscopy and Transmission Electron Microscopy

Following laser processing, the Si nanostructures were analyzed in a Hitachi 4700 scanning electron microscope. The microscope utilizes secondary electron emission form a sample irradiated with 5 – 20 keV electrons to produce high magnification viewing of the irradiated surface. The electron emission filament was operated at ~ 10 μA and at an extraction voltage of 5 keV to produce high resolution images of nanostructures in silicon. The smallest working distance possible of 2 – 4 mm was used during SEM imaging to produce an image of the highest possible resolution. Si samples were viewed at angles ranging from 0^o to 90^o in the microscope.

Transmission electron microscopy (Hitachi 2000) was utilized to determine the crystalline nature of the as – processed Si and SiO nanostructures. Electrons penetrate and interact with a thin specimen, no thicker than 50 nm (to ensue ample electron penetration through the sample in order to form a signal of adequate intensity to interpret). The SiO nanostructures analyzed in this work were thin enough to use in the microscope as – processed, so sample preparation was minimal. The emerging electrons contain information on the crystalline nature of the specimen and this information can be expressed

in visual form as an electron diffraction pattern or as a "semi – real" image of the specimen's electron density. The images produced from a well – aligned microscope have angstrom scale resolution.

2.3.2 Auger Electron Spectroscopy

To determine the surface composition of the irradiated sample, down to a depth of roughly 5 nm into the surface, Auger electron microscopy (AES), coupled with ion sputtering, was used. An electron of sufficient energy can strike an atom of the bulk material such that an orbital electron is ejected. An outer shell electron will fall into this vacant shell and simultaneously an Auger electron, or x – ray, is ejected. The Auger electron ejected has a characteristic energy that depends on the excited electronic shell, the electronic level of the excited Auger electron, and the nature and chemical environment of the atom in question.

Auger electrons ejected from atoms located over a few monolayers from the material's surface are absorbed. To determine composition changes with depth into the bulk material requires periodically alternating AES and ion sputtering. Ar^+ ions were used to sputter the modified silicon target. AES followed the Ar^+ sputtering to determine the chemical composition of the exposed Si surface.

2.3.3 Atomic Force Microscopy

TappingMode AFM operates by scanning a tip attached to the end of an oscillating cantilever across the sample surface. A tip of radius ~ 100 nm lightly "taps" on the sample surface during scanning, contacting the surface at the bottom of its swing. The tip is

attached to a cantilever that oscillates at or near its resonance frequency with an amplitude ranging typically from 20 nm to 100 nm. A feedback loop maintains a constant oscillation amplitude by maintaining a constant RMS of the oscillation signal acquired by a split photodiode detector.

The vertical position of the scanner, i.e., the tip, at each data point of the surface required to maintain the constant RMS amplitude is recorded during a surface scan. This ensures a constant tip – sample force is maintained during oscillation. The output image provides quantitative surface roughness information, in a direction orthogonal to the surface, with a resolution of angstroms. Due to tip – sample convolution, the lateral, or (x,y) resolution of the image, is accurate only to 10^2 nanometers.

Chapter 3

Results

3.1 Formation of SiO_x in Micro - Structured Substrates

An atomically flat Si target was pulsed laser irradiated in an SF_6 atmosphere to produce an array of microcones with a surface density of $1x10^5$ microcones/cm^2. Figure 3.1 shows a scanning electron microscope (SEM) image of the Si microcone network produced on the surface of laser – irradiated silicon in SF_6 gas. Figure 3.2 shows a high – resolution scanning electron microscope (HRSEM) image of a cross – section through the microcone morphology.

The microcone morphology occupies only the irradiated region of the Si target. Each Si microcone protrudes above the initial surface by 50 – 60 μm and is surrounded by several deep, steeply sloped microholes (figure 3.2). The microholes extend down to 120 μm below the initial surface. The evolution and growth mechanism of the microcones has been discussed elsewhere [88].

Subsequent irradiation of the single – crystal, silicon microcones in a reactive atmosphere of oxygen – argon and oxygen – nitrogen resulted in the formation of a dense, web-like nanostructure that sheathed the microcones. Under continuous, ultraviolet irradiation at 351 nm, this nanostructure exhibited intense, visible room – temperature photoluminescence. Efficient photoluminescence from *silicon*, or silicon – containing, *nanostructures* is important since bulk silicon is a poorly efficient emitter of visible light due to its indirect band gap. The nature of this nanostructure and its photoluminescence is the topic of the next section.

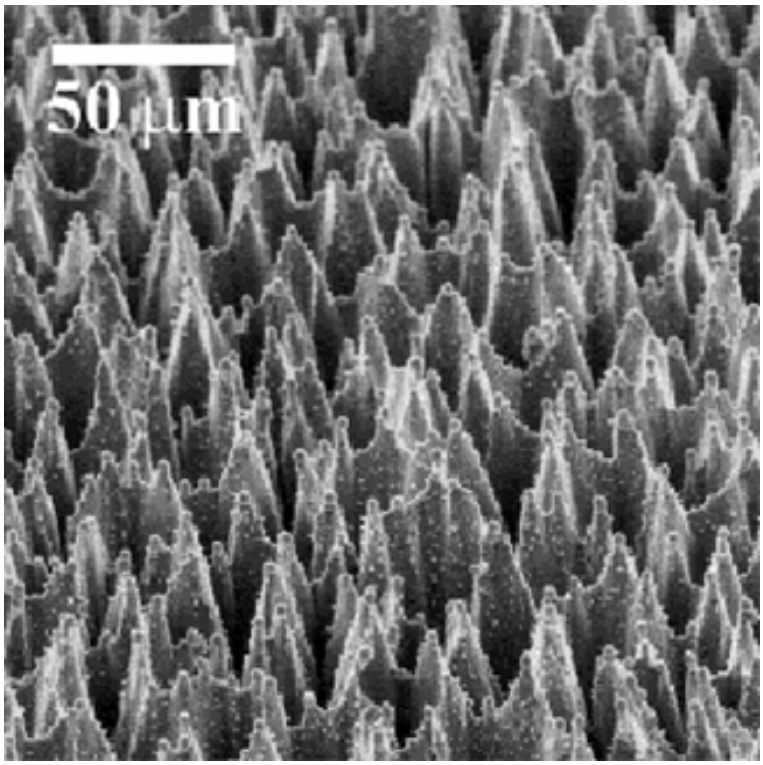

Figure 3.1 An array of Si microcones tilted at oblique incidence (~25^{o}) to better illustrate the microcone morphology. The microcones were grown in 1 atm SF_6 gas with 2000, E_d = 2.9 J/cm^2, laser pulses.

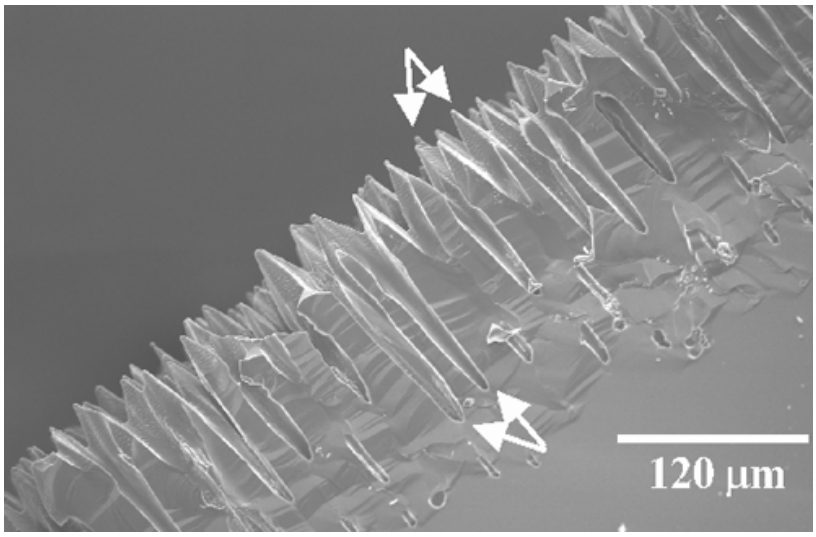

Figure 3.2 A cleaved Si substrate along the substrate surface normal. The sample was cleaved through the microcone morphology to illustrate the long, deep trenches (~ 100 μm) surrounding the Si microcones. The microcones were grown with 7500 laser pulses (E_d = 3 J/cm^2) in P_T = 0.25 atm SF_6 gas.

Silicon *micro*cones sheathed in a web – like, SiO_x *nano*structure exhibit intense, visible room – temperature photoluminescence. The formation of the SiO_x nanostructure, via pulsed laser irradiation, requires an initially rough target surface. An array of silicon microcones (figure 3.1), also produced by pulsed laser irradiation, provides this required initial roughness. The microcone morphology is produced by pulsed laser irradiation of silicon in the presence of SF_6 gas. The SiO_x nanostructure is produced by a second, subsequent pulsed laser irradiation in an O_2 atmosphere.

Figure 3.3 shows the SiO_x nanostructure produced on the microcone bodies by 1300 pulses with an $E_d = 1.4$ J/cm^2 in an atmosphere of 5% O_2 – Ar. The view in the image is down the axis of the microcone bodies. The nanostructure consists of an entanglement of high – aspect ratio strings that sheath the microcone bodies circumferentially (figure 3.4). The tips of the microcones (figure 3.3) protrude up and beyond the location of the sheathing nanostructure with no trace of the nanostructure on their spherical surface.

The annular thickness of the nanostructure layer decreases with distance from the microcone tips to the trenches surrounding each cone. Figure 3.5 shows a HRSEM image of a microcone body sheathed in the nanostructure. The thickness of the nanostructure layer surrounding the microcones clearly decreases progressing down the cone body toward the trench as indicated by the arrows in the figure. In fact, the thickness of the sheath layer is a maximum just below the uncovered microcone tip. Moreover, little or no nanostructure is seen at the microcone base.

An abrupt boundary exists between the microcone tip and the nanostructure sheathing the microcone body. Figure 3.6 shows a HRSEM image of this boundary. The

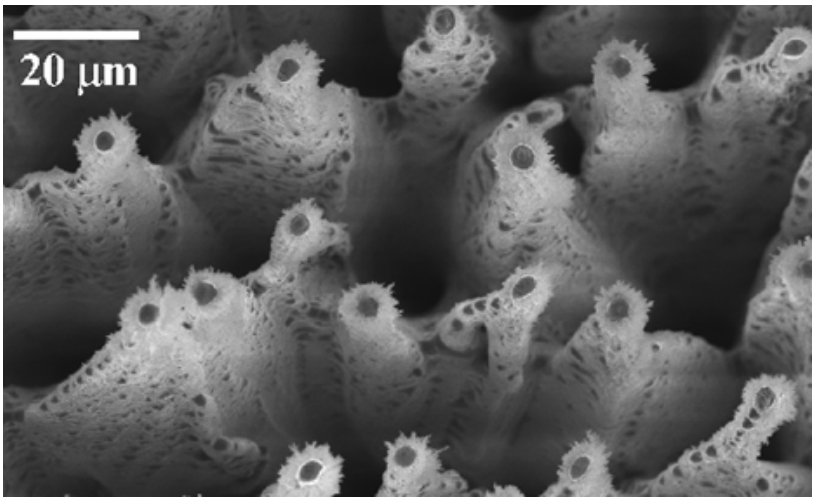

Figure 3.3 Subsequent irradiation in 5% O_2 – Ar, following Si microcone growth, induces the formation of a nano – scale morphology that covers the surface of the microcones. The nanostructure shown in this figure was produced with 200 pulses (E_d = 1.4 J/cm^2) in the O_2 – Ar ambient (P_T = 1 atm). The Si microcone morphology was produced with 1300 laser pulses (E_d = 2.1 J/cm^2) in ½ atm SF_6 gas.

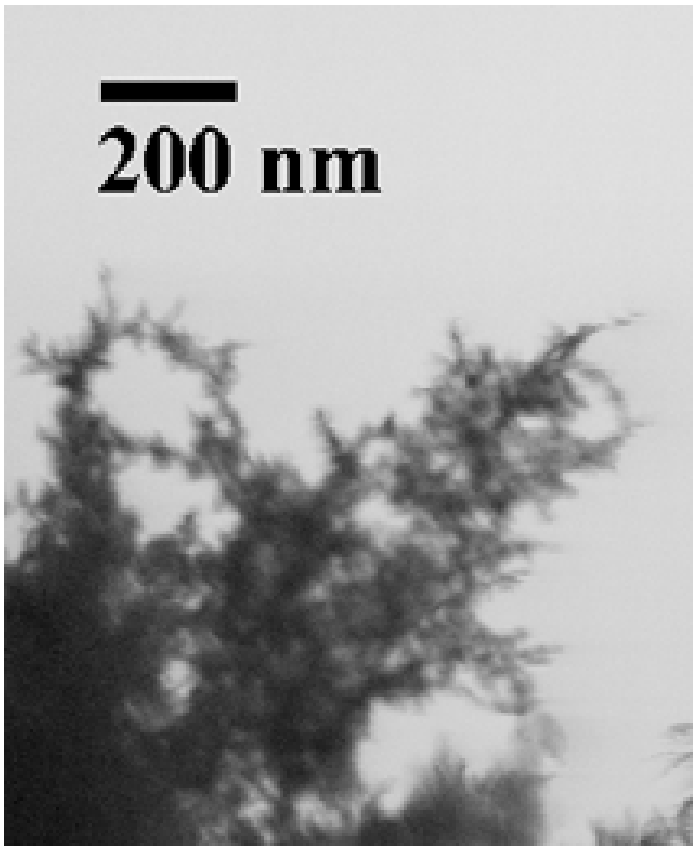

Figure 3.4 A HRSEM image of the nanoscale material shown in figure 3.3. The nanoscale material protrudes from the outer diameter of a Si microcone.

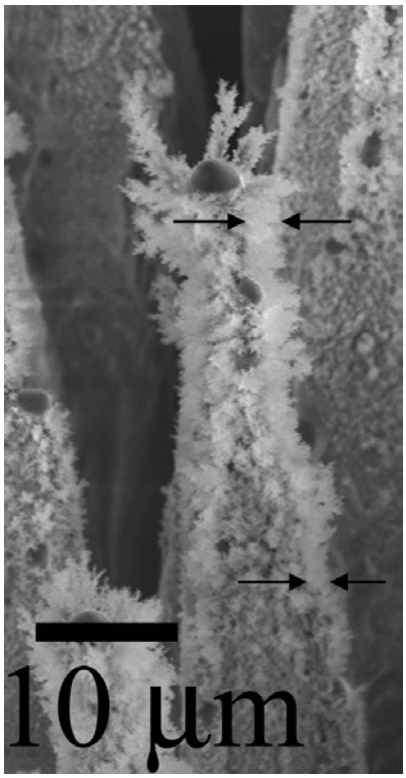

Figure 3.5 The annular thickness of the sheathing microstructure located around the microcone bodies, decreases in thickness from a maximum just below the microcone tip to a minimum of zero coverage at the base of the trenches surrounding the microcone.

\

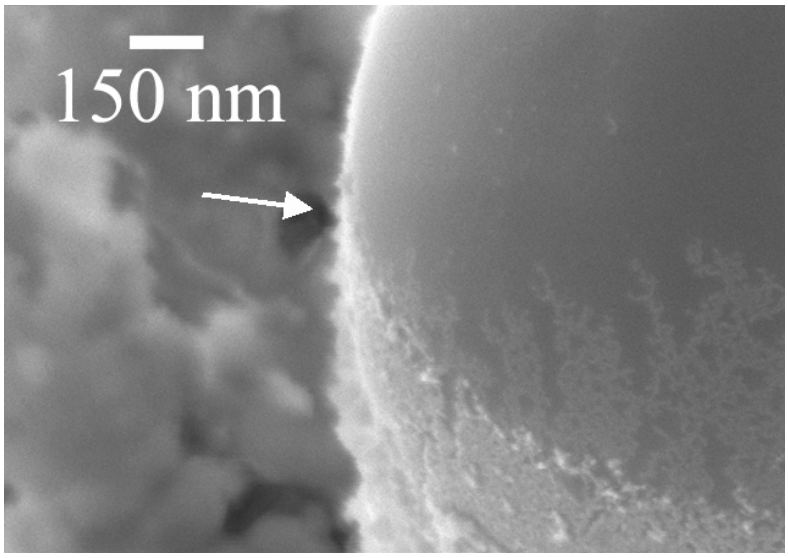

Figure 3.6 An oblique incidence HRSEM image (~25^{o}) of the tip of a Si microcone sheathed in the nano – scale material. The very tip of the Si microcones, i.e., the first 2 – 3 μm of the cone from the tip, down, is not coated with the nanoscale material. Shown here, and indicated by the arrow, is the boundary between the microcone tip and microcone body. The nano – scale material was produced with 400 pulses (E_d = 3.1 J/cm^2) in 20% O_2 – N_2 (P_T = 1 atm).

image shows only the side of a microcone body with the boundary between the microcone tip and the microcone body indicated by an arrow. The nanostructure layer is very thin, roughly 70 nm, and in this case has not formed the string type morphology shown in figure 3.4. A high, laser beam energy density of 3.1 J/cm^2 was used to generate the nanostructure shown in figure 3.6. This is in contrast to the low energy density used to produce the sheathing nanostructures shown in figures 3.3, and 3.4.

Figure 3.7 shows two superimposed of SEM images of the same Si microcone that exemplify the growth of Si microcones, sheathed in SiO nanoaggregate, as a function of the number of laser pulses. SiO that strikes the molten tip decomposes there to deposit Si [88]. The evidence for the re – deposition process is the linear growth process itself since no other plausible source of growth for the microcones is present during processing other than the flux of Si provided by the trench "guns" surrounding each microcone.

This nanostructure has been observed in the 1 – 3.1 J/cm^2 energy density range. An energy density of 3.1 J/cm^2 not only induces the formation of the nanostructure but erodes it as well. For the sample shown in figure 3.3 (E_d = 1.4 J/cm^2, fewer numbers of shots and a lower oxygen partial pressure, produces a *thicker nanostructure sheath* relative to the sheath shown in figure 3.6 (E_d = 3.1 J/cm^2). As will be shown in the following paragraphs, both of these trends in variables, i.e., fewer numbers of laser pulses and lower partial pressures of O_2, tends to *shrink* the thickness of the nanostructure layer. The thickness of the sheath in figure 3.3 is of roughly 40x the thickness of the sample shown in figure 3.5 for half the number of pulses and ¼ the partial pressure of oxygen. Hence, the E_d increase of ~ 2 times has significantly retarded the evolution of the nanostructure.

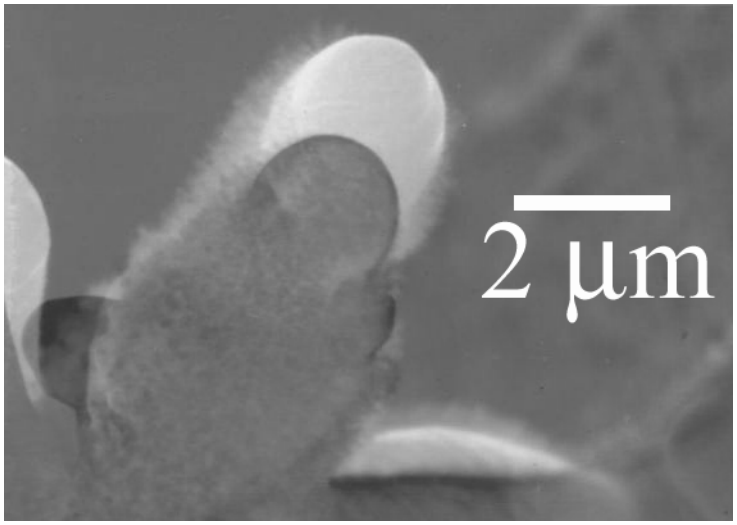

Figure 3.7 Two superimposed images illustrating the linear growth of a Si microcone, away from the initial surface. The microcone after 50 laser pulses (bright) has grown 1/3 longer than its previous length (dark). SiO nanoaggreagate surrounds the microcone in an annular fashion.

The thickness of the nanostructure increases as the number of laser pulses increases up to 600 laser pulses (figure 3.8a – 3.8c). However, the thickness of the nanostructure decreases at numbers of pulses greater than 800. The images in figures 3.8a – 3.8c each show one microcone tip surrounded by an annular nanostructure layer. The viewing axis is straight down the microcone symmetry axis. The microcone shown in figure 3.8a is from a sample irradiated with 200 laser pulses. If irradiation ensues with an additional 200 pulses the sheath thickness increases by 3 – fold (figure 3.8b). A thick sheath of average thickness of 4.5 μm is formed with 600 laser pulses.

Between 600 and 800 laser pulses microrods 15 – 20 μm in length are formed. These rods grow in the radial direction forming bridges between microcones (figure 3.9). A HRSEM image of one individual microrod showed that they are an entanglement of 20 to 50 nm diameter strings (figure 3.10). However, it is possible that the string diameter is significantly smaller because objects that appear focused at 20 nm could in fact be smaller than 20 nm. In fact, TEM images (shown later) indicate feature dimensions of these wires as small as 5 nm in width.

Nanostructure sheath thickness increases as the partial pressure of oxygen in the chamber is increased. Figure 3.11a – d shows images of nanostructure sheaths formed with 600 laser pulses at 20, 15, 10, and 5 Torr O_2 in P_T = 740 Torr O_2 – Ar. In a 3% O_2 – Ar ambient the average sheath thickness is 1.9 μm ± 0.4 μm (figure 3.11a). The average sheath thickness in a 2% O_2 – Ar ambient (figure 3.11b) is reduced to 1.3 μm ± 0.4 μm. This value drops below 1 μm for oxygen partial pressures less than 2% (see figures 3.11c – d). In fact, a sheath is barely observable after 1000 laser pulses for a sample irradiated in a 0.3% O_2 – Ar ambient.

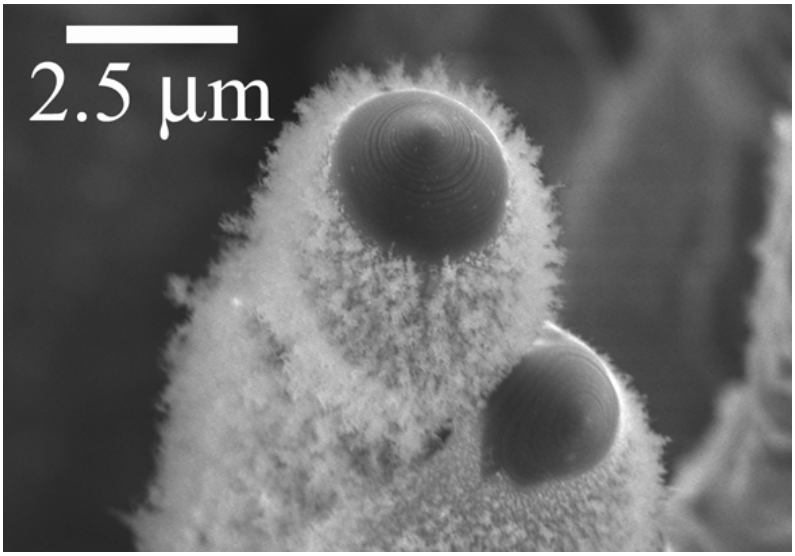

Figure 3.8 The annular thickness of nano – scale material increases as the number of laser pulses increases. (a) 200 laser pulses (E_d = 1.4 J/cm^2) in 5% O_2 – Ar produced the sheath thickness shown above.

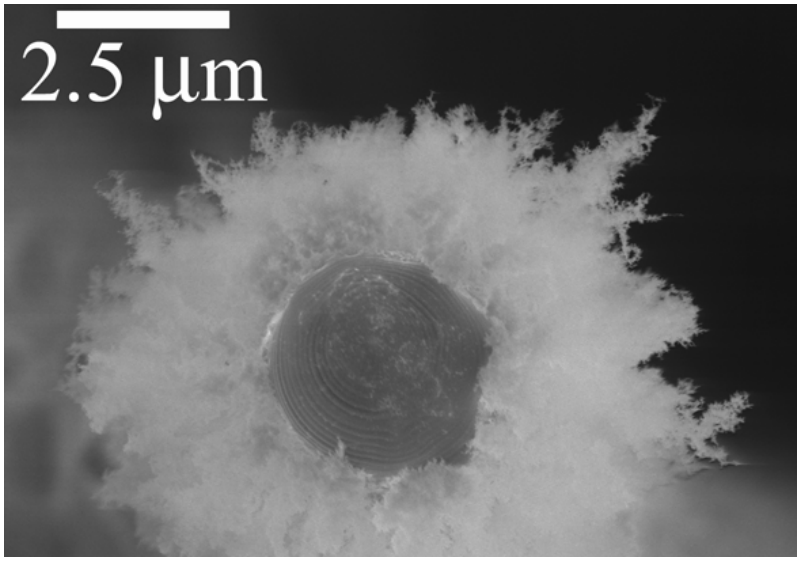

Figure 3.8 (cont'd) (b) Following 400 laser pulses (E_d = 1.4 J.cm^2) in 5% O_2 – Ar, the sheath thickness around the microcone circumference has clearly increased relative to the thickness shown in figure 3.7(a) that was produced with only 200 pulses.

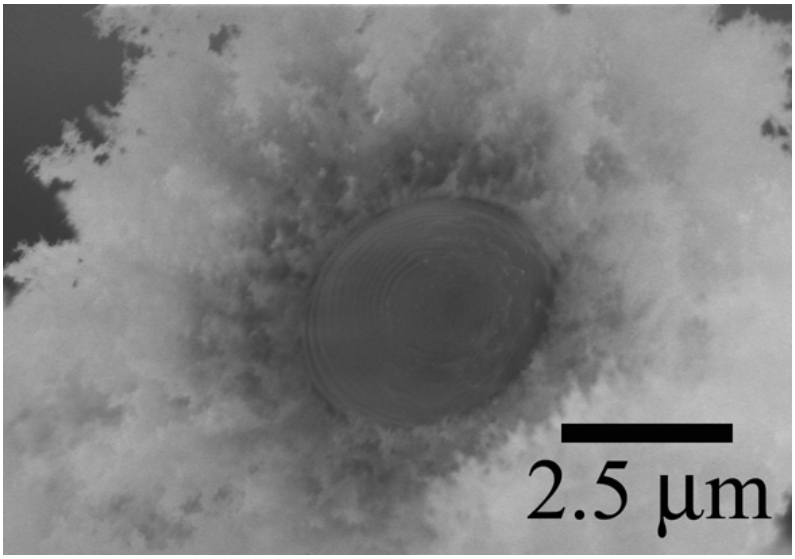

Figure 3.8 (cont'd) (C) The microcone tip is nearly hidden after 600 pulses (E_d = 1.4 J/cm^2) in 5% O_2 – Ar!

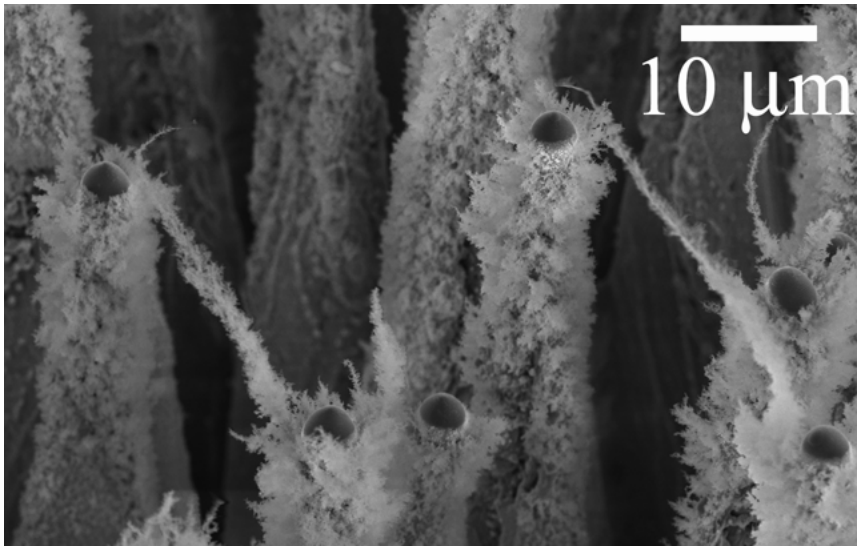

Figure 3.9 Long, entangled tendrils of nanoscale material interconnect adjacent Si microcones after 800 laser pulses (E_d = 1.4 J/cm^2) in 5% O_2 – Ar.

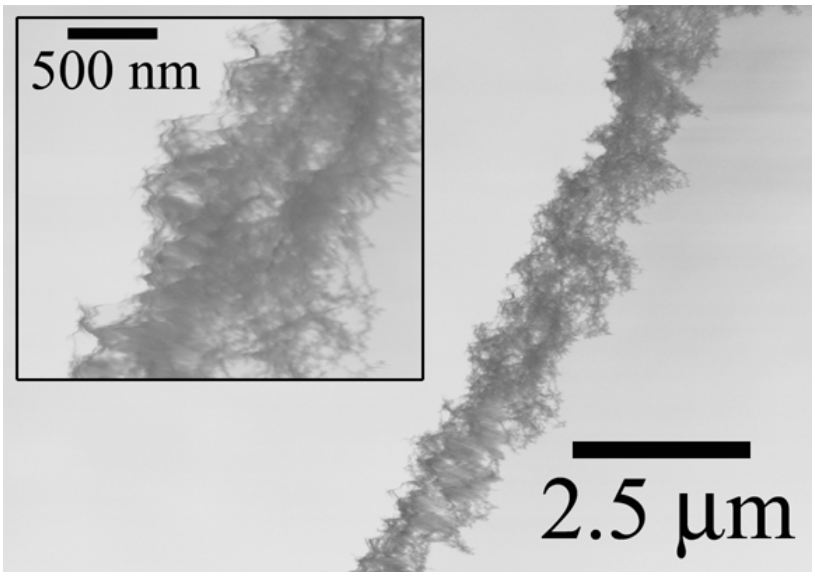

Figure 3.10 A HRSEM image of the entangled tendrils of nanoscale material indicates that each tendril consists of long, high – aspect ratio strings which are entangled to produce the microscopic tendril. The strings that make up the tendril are roughly 20 – 50 nm in diameter and over $1x10^2$ nm long!

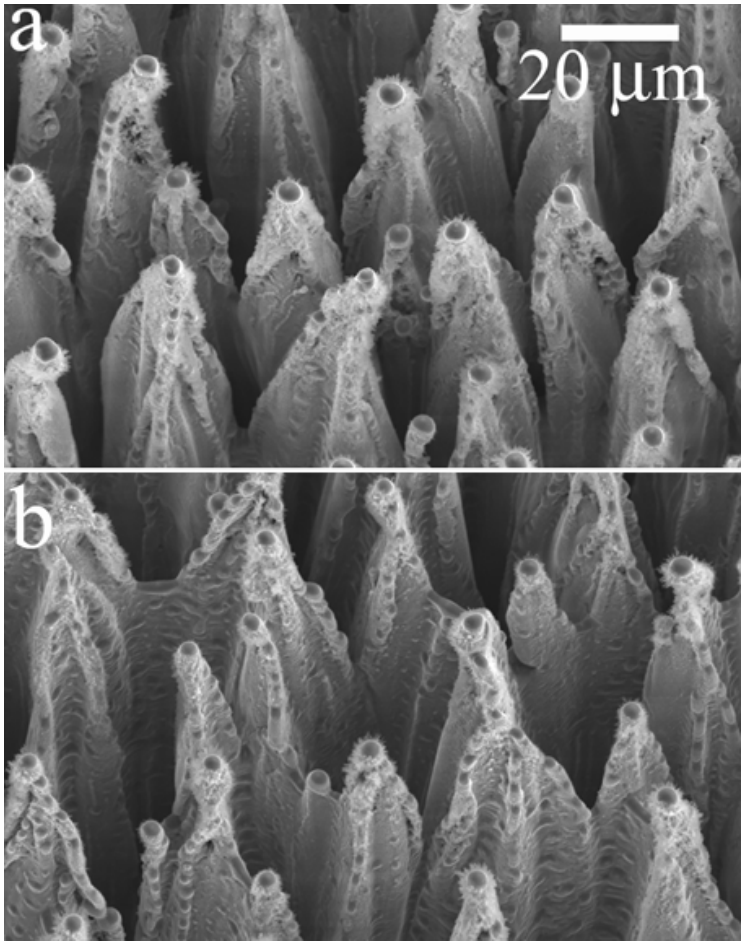

Figure 3.11 Increasing the partial pressure of O_2 in Ar has the affect of increasing the thickness of sheathing nanoscale product at a constant number of laser pulses (600) and laser energy density (1.4 J/cm^2). (a) the sheath thickness is the largest for nanoscale product generated in P_{O2} = 20 Torr, P_T = 740 Torr Ar relative to product generated in lower partial pressures of O_2 in Ar, i.e., (b) 15 Torr, (c) 10 Torr and (d) 5 Torr.

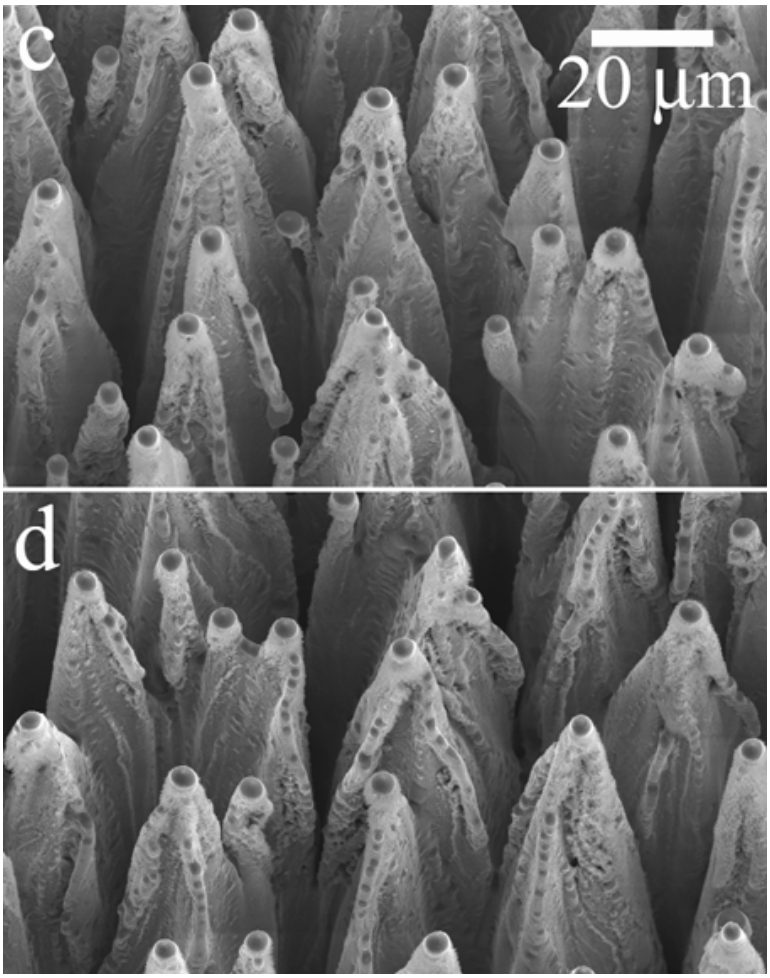

Figure 3.11 (cont'd) Nanoscale product formed in (c) 10 Torr O_2 and (d) 5 Torr O_2, P_T = 740 Torr (E_d = 1.4 J/cm^2, 600 pulses).

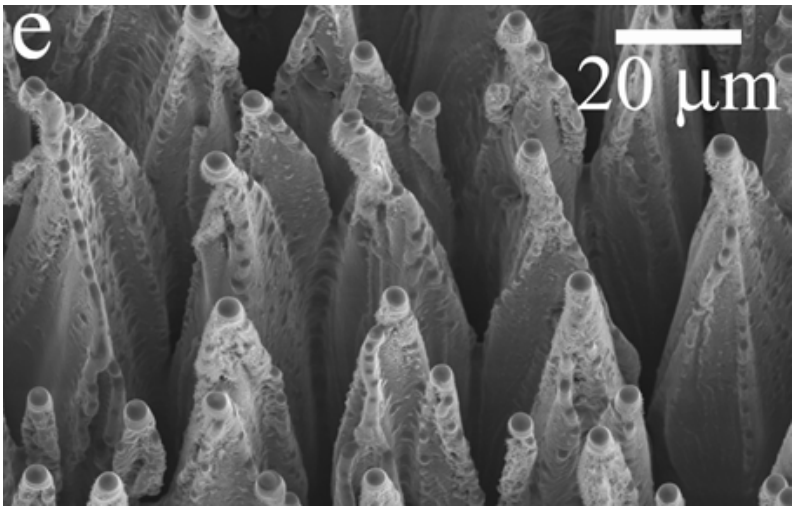

Figure 3.11 (cont'd) (e) The nanoscale aggregate is barely, visually detectable, sheathing the microcones, after 1000 pulses (E_d = 1.4 J/cm^2) in 2 Torr O_2 – Ar, P_T = 740 Torr (0.3% O_2 – Ar) The aggregate appears as the brightly, contrasting region located just below the tips of the microcones in the SEM image above.

The oxygen partial pressure also affects the fine structure of the morphology within each nano – string comprising the sheath volume. Figure 3.12 shows a HRTEM image of the terminating end of the sheath, i.e, nano – strings protruding from the external surface of the sheath, for nanostructure product formed in 5% O_2 – Ar with 600 pulses. It should be noted that the sheath was observed still connected to the base of a microcone, i.e., no mechanical polishing technique was required to transfer the nanostructure to the TEM grid. A holey carbon grid was used to support the microcone body and the nanostructure.

Figures 3.12 and 3.13 show HRTEM images of nanoparticle agglomerates formed under laser irradiation in 5% O_2 – Ar and 25% O_2 – Ar, respectively. The individual strings of the nanostructure (figure 3.12) consist of aligned nanoparticles of various diameters. In other words, each string observed at high resolution does not have a constant diameter but rather an oscillating diameter along its length. A mean nanoparticle diameter was calculated from several TEM images. The diameter of each nanoparticle was measured and the average nanoparticle diameter was determined for two different oxygen partial pressures. The number of nanoparticles having a diameter within ± 1 nm is plotted in figure 3.14. The data was fit to a Gaussian curve

$$f(x) = \frac{S}{\sqrt{2\pi}\sigma} e^{-\frac{(x-\mu)^2}{2\sigma^2}} \qquad 3.1$$

where $(2\pi)^{1/2}\sigma$ is the full – width half maximum (FWHM) of the distribution, S is the total number of particles, and μ is the diameter at the maximum of the distribution. The values of S, σ, and μ were determined by minimizing the function

$$\left\{\sum^{n} |y_n - f(x_n)|\right\}. \qquad 3.2$$

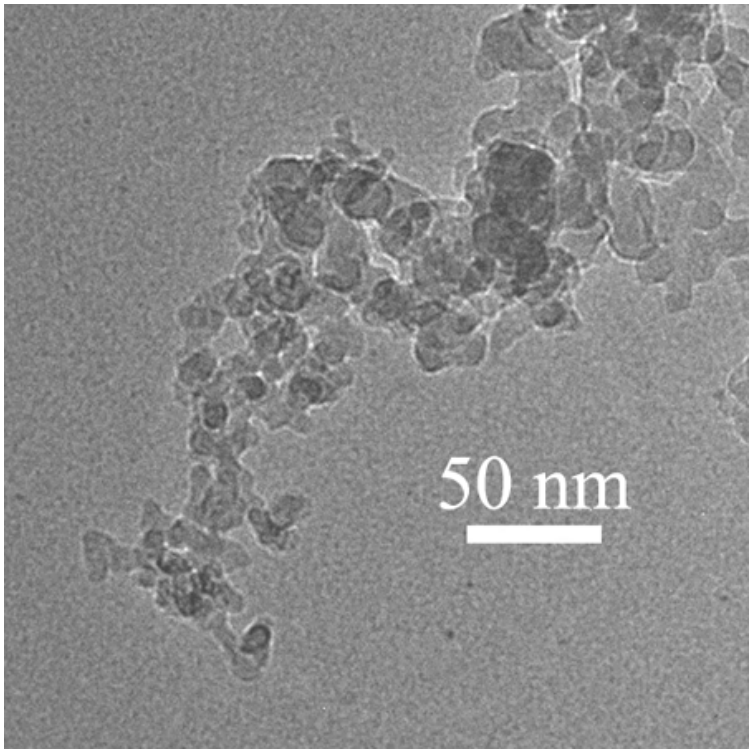

Figure 3.12 A TEM image of the tip of an entanglement of nanoscale strings protruding from the surface of a Si microcone. The image shows that the strings are in fact an agglomerate of small nanoparticles that modulate in diameter along the length of the strings that make up an entanglement. The aggregate was produced with 600 laser pulses in 5% O_2 – Ar (E_d = 1.3 J/cm^2). The aggregate was introduced to the holey carbon grid for TEM microscopy by mechanically fracturing microcones, sheathed in aggregate, off the Si substrate and onto the TEM grid. The macroscopic damage induced to remove the microcones induced very little microscopic damage to the microcones and hence the aggregate + microcones was transferred to the grid with little to no post – processing damage.

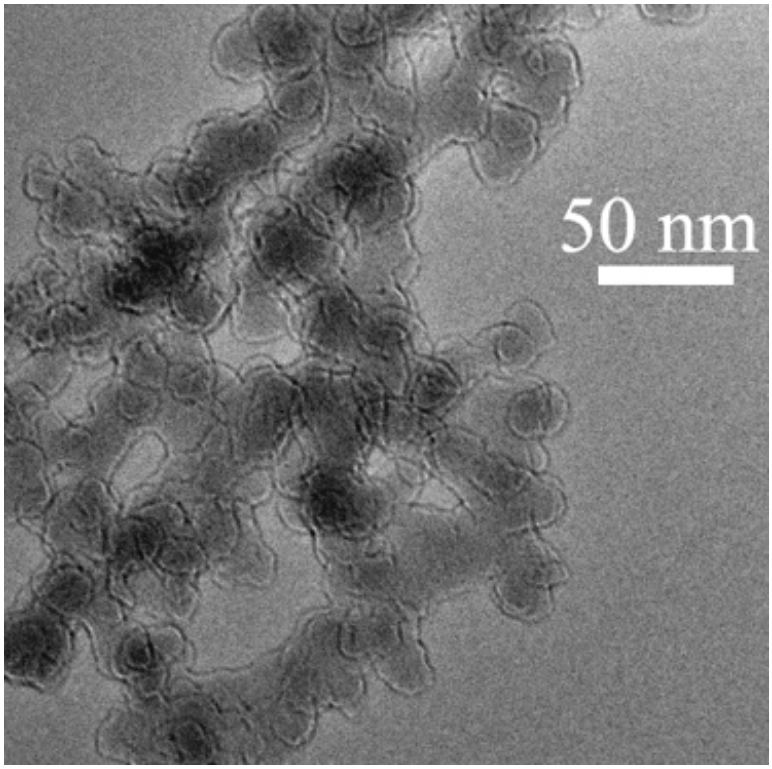

Figure 3.13 A TEM image of nanoscale aggregate generated with 1.9 J/cm^2, 500 laser pulses in 25% O_2 – Ar, P_T = 1 atm. The average diameter of the small nanoparticles that make up each nanoscale string for aggregate processed in 25% O_2 – Ar is larger than the corresponding average for the small nanoparticles produced during irradiation in 5% O_2 – Ar (figure 3.13).

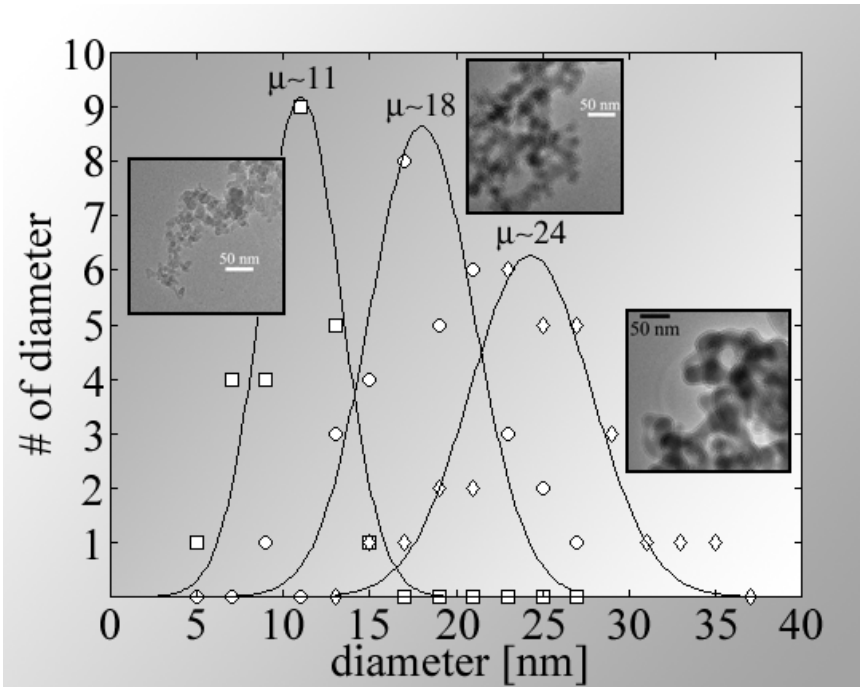

Figure 3.14 A plot of the # of nanoparticles falling in a particular nanoparticle diameter range ($\Delta d = 2nm$) over a domain of 0 – 40 nm for nanoscale aggregate produced under laser illumination in 5% O_2 – Ar and 25% O_2 – Ar. The experimental data, as measured from TEM images, fits well to a distribution of the Gaussian type. The fits yield mean nanoparticle diameters of ~ 11 nm (5% O_2) and ~ 18 nm (25% O_2). The sample produced in 25% O_2 – Ar (and superimposed with the plot in figure 3.13) was annealed for 30 min. at 900 ^oC and the diameter distribution was remeasured. In this case, a Gaussian fits yields a mean nanoparticle diameter, for the sample, of ~ 24 nm, an increased of x1.3 the value prior to annealing.

where y_n is the number of nanoparticles of diameter x_n. The mean nanoparticle diameter at 5% O_2 – Ar was 11 nm, less than the mean for the nanoparticle agglomerates formed at 25% O_2 – Ar, 18 nm (figure 3.14).

A nanoparticle size analysis was performed on the HRTEM images shown in figure 3.14 and figure 3.15 to determine the affect of annealing on nanostring component particle size. The average nanoparticle size for the pre – annealed SiO aggregate formed with 500 pulses in 25% O_2 – Ar was ~ 18 nm. The average nanoparticle diameter increased to ~ 24 nm after annealing at 900 ^{o}C for 30 minutes.

The affect of oxygen partial pressure on the post – annealed photoluminescence was investigated. Photoluminescence spectra were taken from annealed samples prepared with 500 pulses in 0%, 25%, 50%, and 75% O_2 – Ar. The maximum intensity was found for the sample produced in 50% O_2. It exhibited a photoluminescence intensity 2x greater than any other sample examined. Figure 3.16 shows two photoluminescence spectra for samples irradiated in 50% O_2 and 75% O_2.

3.1.2 Chemical Composition of the Nanoparticle Sheath

EDS was used to determine the chemical composition of the nano – aggregate sheath surrounding microcone bodies. The sample examined for chemical composition was prepared in 5% O_2 – Ar with 400 laser pulses. Figure 3.17 shows an EDS spectrum obtained from the just the sheath volume surrounding a microcone. Only silicon and oxygen signals were present in all spectra taken on the nano – aggregate sheath.

A quantitative value for the atomic concentration in the aggregate of silicon oxide was determined by referencing the sheath spectrum to one from a SiO_2 standard. A

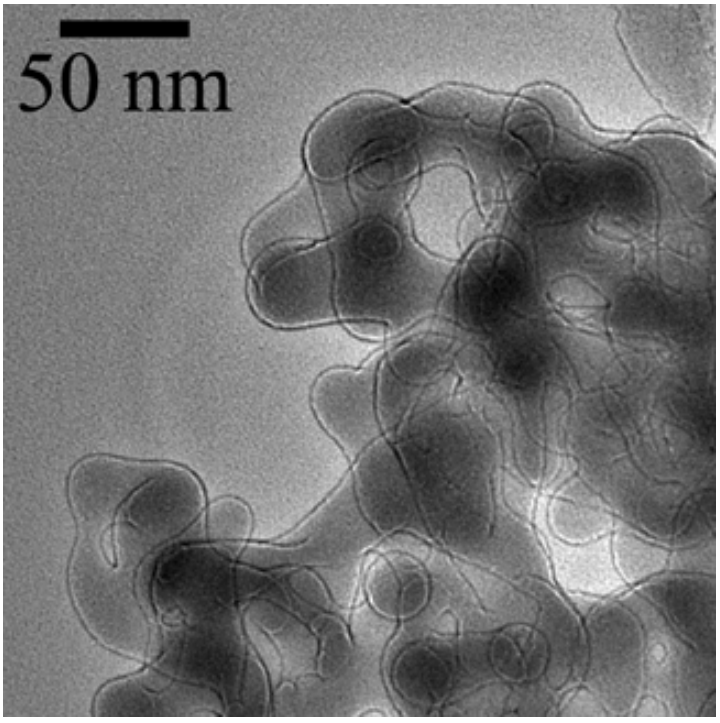

Figure 3.15 A TEM image of the nanostructure comprising the nanoscopic, high – aspect ratio strings (refer to figure 3.12 for nanostructure morphology prior to annealing) following the annealing treatment at 900 ^{o}C for 30 minutes in UHP Ar. The edges of the nanostructures are smoother than their prior configuration (figure 3.12) due to the minimization of surface energy driven by the thermal treatment cycle.

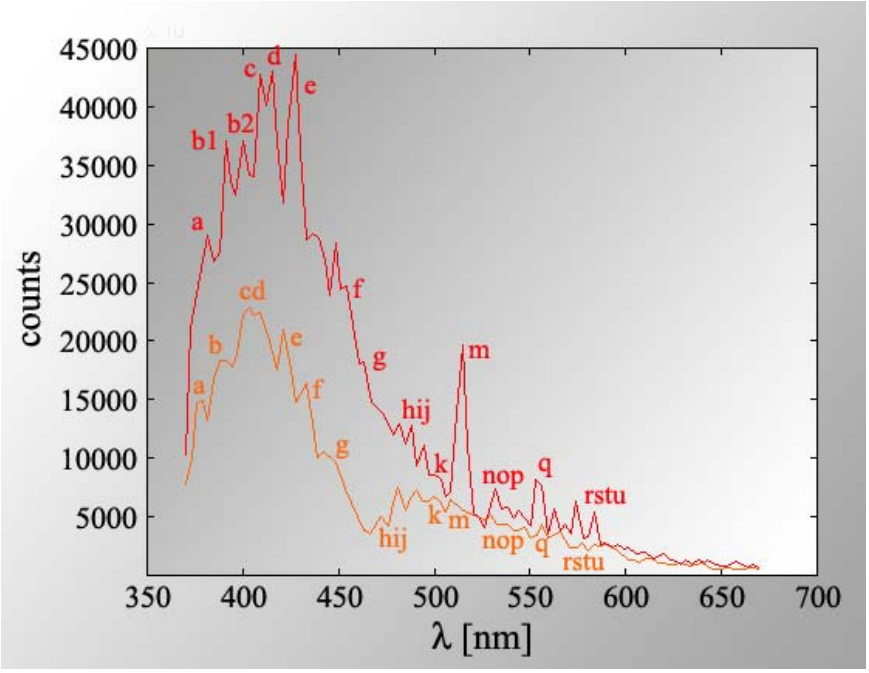

Figure 3.16 Total photoluminescence intensity, over the wavelength range 350 – to – 700 nm, was found to be a maximum for an oxygen partial pressure of 50% in an O_2 – Ar mixture relative to photoluminescence from aggregate prepared in 25% O_2 and 75% O_2 in Ar. For example, the higher total intensity curve shown above is the photoluminescence spectrum for SiO aggregate prepared in 50% O_2 – Ar, P_T = 1 atm, with 500 laser pulses (E_d = 1.9 J/cm^2) The other photoluminescence spectrum was obtained from aggregate prepared in 75% O_2 – Ar, P_T = 1 atm, with 500 laser pulses (E_d = 1.9 J/cm^2). The letters listed above each spectrum indicate fine structure that was present in all spectra obtained. The fine structure is not a material's property but rather noise associated with the light collection system (excepting point (m)).

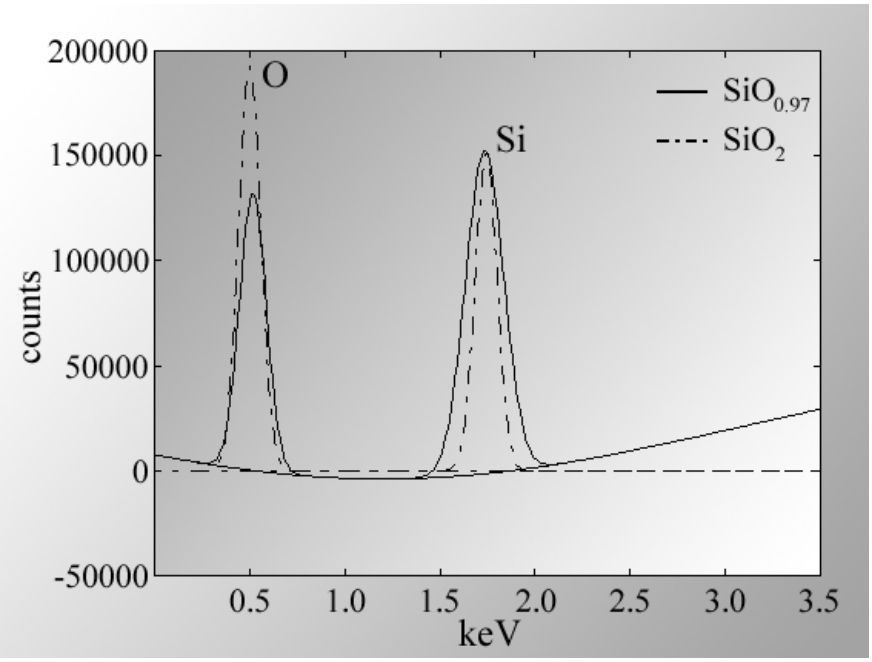

Figure 3.17 Energy dispersive spectrum (EDS) for the nanoscale aggregate material sheathing the Si microcones. The bold spectrum in the figure is the actual experimental spectrum obtained during electron beam exposure. The background has been subtracted from the spectrum. The dotted spectrum was experimentally obtained from an SiO_2 standard. The quantitative composition of the Si_xO_y aggregate was determined by referencing the nanoscale material spectrum to the standard, reference specimen. The nanoscale aggregate had an atomic composition of $SiO_{0.97}$ for a sample produced with 400 pulses in 5% O_2 – Ar (E_d = 1.4 J/cm^2)

spectrum was obtained for the SiO_2 standard and the integrated intensity of both the oxygen and silicon peaks was calculated. The ratio of the peak intensities leads to an atomic concentration of 2:1 oxygen. Hence, by calculating this intensity ratio for the sheath silicon and oxygen peaks, the ratio of atomic oxygen to silicon;

$$\frac{\frac{I_{O(SiO_2)}}{I_{Si(SiO_2)}}}{\frac{I_{O(SiO_x)}}{I_{Si(SiO_x)}}} = \frac{\frac{2_O}{1_{Si}}}{\frac{x_O}{1_{Si}}} \qquad 3.3$$

could be determined for the sheath. Figure 3.17 shows both a spectrum from the SiO_2 standard and the nano – aggregate sheath. The integrated intensities of all the peaks was determined by first fitting the peaks to appropriate Gaussian profiles (the method as described in the previous section) and then the profiles were integrated using a numerical technique exploiting the trapezoid rule to numerically determine the area under each peak. Background subtractions were made for both spectra shown in figure 3.17 to obtain the best possible comparison among the spectra for SiO_2 and, as determined, the $SiO_{0.97}$ sheath. EDS spectra taken for SiO nanoaggregate formed in 25% O_2 – Ar confirmed a roughly SiO composition as well. Hence, the SiO composition was not a function of oxygen pressure from 5% - 75% O_2 in Ar.

3.2 Nanoscale SiO Photoluminescence

3.2.1 Un – annealed SiO Photoluminescence

Brightly visible, room temperature photoluminescence was observed from microcones embedded in the SiO nanoscale – aggregate. Photoluminescence measurements were taken on the SiO nanomaterial to determine if Si nanoparticles embedded in the aggregate, or SiO related defects, were responsible for the emitted radiation. The SiO aggregate was also annealed at high temperature, 900 ^{o}C, to induce the formation of Si nanoparticles:

$$2SiO \rightarrow SiO_2 + Si$$

Figure 3.18 shows the photoluminescence spectrum from microcones embedded in SiO nanomaterial prepared with 500 pulses in 25% O_2 – Ar (E_d = 1.9 J/cm^2). The luminescence was very intense to the naked eye and appeared visibly whitish – blue. The photoluminescence spectrum in figure 3.18 indeed falls over the visible range with higher luminescence intensity at smaller visible wavelengths. For example, the most intense luminescence occurs at 427 nm, the blue portion of the visible spectrum, and it is reduced by 4 – fold at the orange – red end of the visible spectrum relative to the blue luminescence at 427 nm. The region shown in figure 3.13 is a good representation of the morphology present throughout the irradiated area.

The photoluminescence data in figure 3.18 was fit to a smooth continuous curve by the superposition of several Gaussian curves. The smooth curve following the raw data is the superposition of the 5 Gaussian profiles shown as hatched lines in the figure. Table 3.1 shows the wavelength representing the maximum intensity for each Gaussian peak for the peaks used to fit the raw data. The Ar continuous laser beam had a spot size of 1 mm x

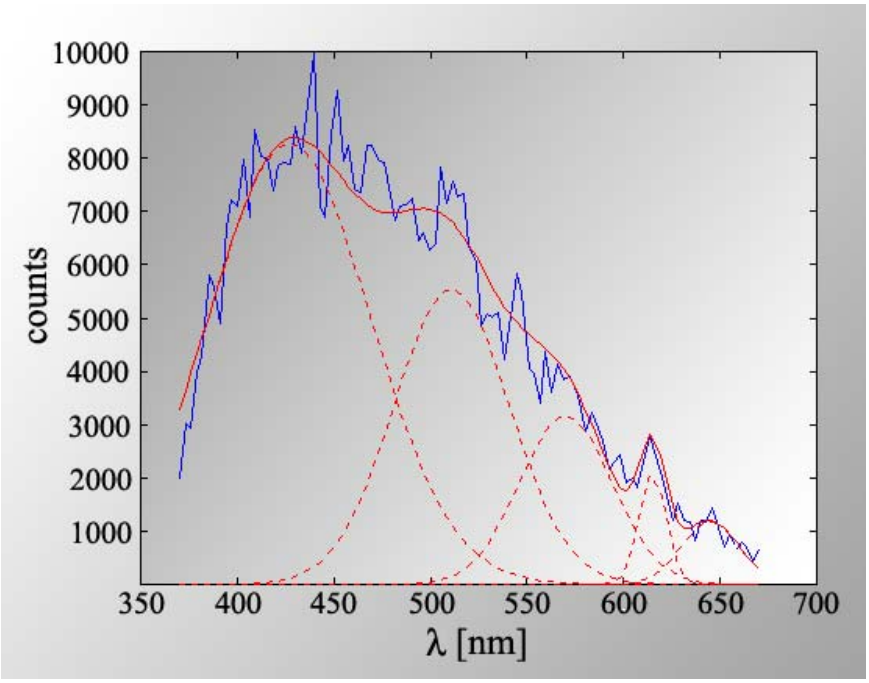

Figure 3.18 Photoluminescence spectrum from SiO nanoaggregate over the emission wavelength range of 350 to 700 nm for aggregate formed with 500 pulses in 25% O_2 – Ar (E_d = 1.9 J/cm^2). The excitation source for photoluminescence was an Ar^+ laser operating continuously at 351 nm, 4mW power. The raw spectrum is fit by a series of 5 Gaussian peaks whose superposition closely resembles the experimental data. The maxima of the 5 Gaussian peaks, from left – to –right is 427 nm (2.91 eV), 512 nm (2.43 eV), 570 nm (2.18 eV), 615 nm (2.02 eV), and 644 nm (1.93 eV).

Table 3.1 The following table lists the mean wavelength for each Gaussian curve used to form a superposition curve that fits the experimentally obtained photoluminescence spectra for spectra taken from 3 different samples. The visible spectrum and the color associated with each wavelength is also listed since the photoluminescence from SiO falls within the visible portion of the electromagnetic spectrum.

Unannealed SiO

500 pulses, 25% O_2

eV	nm
1.93	644
2.02	615
2.18	570
2.43	512
2.91	427

Annealed SiO

500 pulses, 50% O_2

eV	nm
2.00	622
2.18	570
2.24	555
2.33	534
2.41	516
2.52	493
2.99	416

Annealed SiO

500 pulses, 75% O_2

eV	nm
2.12	586
2.31	538
2.52	493
3.05	408

Visible Spectrum

color	nm
red	700
orange	630
yellow	590
green	520
blue	460
violet	390

1mm. Hence, roughly 10^3 microcones sheathed in SiO, contributed to the collected photoluminescence signal.

3.2.2 Annealed Silicon Oxide Photoluminescence

A 4 – fold increase in photoluminescence intensity is observed on the nanoscale SiO aggregate after annealing at 900 ^oC for 30 minutes in UHP Ar gas. Figure 3.19 shows the un – annealed photoluminescence spectrum superimposed with the spectrum obtained from annealed SiO aggregate. The two spectra shown in figure 3.19 were taken from samples processed under similar conditions except for the oxygen content in the atmosphere during irradiation.

The unannealed sample was prepared in 25% O_2 – Ar whilst the annealed sample was prepared in 50% O_2 – Ar. *However, photoluminescence spectra taken from unannealed samples prepared in 25%, 50%, and 75% O_2 – Ar after 500 pulse show no, significant difference in peak positions*. Hence, most probably the difference in intensity shown in figure 3.19 is due to the annealing process.

Photoluminescence maxima at 427 nm and 512 nm are clearly discernable from the background of the spectrum. No observable shift in maximum peak intensity position is observed when comparing the annealed and unannealed samples (figure 3.19). A fine structure, indicated with letters in figure 3.19, is present in both spectra with positions that are not shifted following annealing. This structure that was present in all spectra taken is most probably an artifact of the photoluminescence system used.

The effect of annealing on morphology is exhibited in figures 3.20 and figures 3.21. Figure 3.20 shows the SiO sheath morphology prior to annealing and figure 3.21

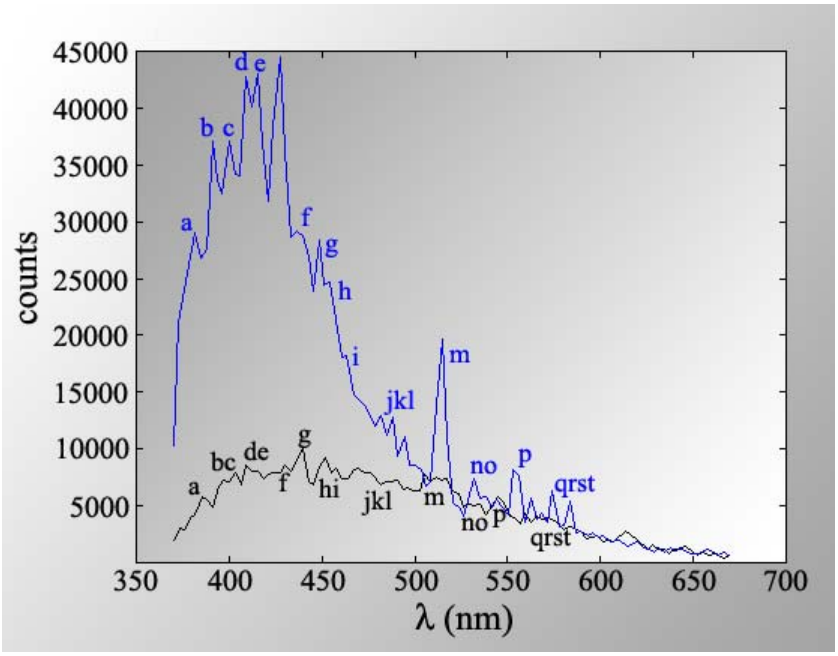

Figure 3.19 Photoluminescence spectra for both annealed and unannealed SiO. The curve of highest maximum intensity shows the photoluminescence behavior of the annealed SiO. The maximum intensity is x4 greater at the ~ 425 nm wavelength for the annealed SiO relative to the unannealed specimen.

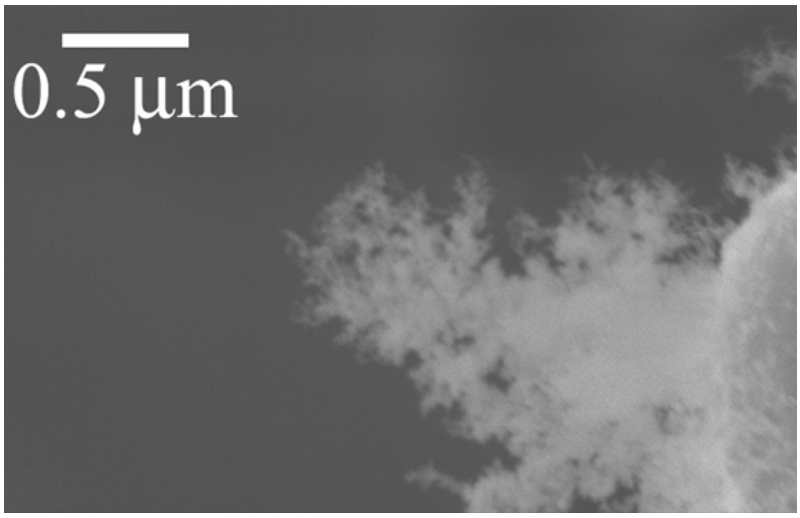

Figure 3.20 A HRSEM image of the SiO aggregate prior to annealing. The SiO was formed with 500 pulses (E_d = 1.9 J/cm^2) in 25% O_2 – Ar, P_T = 1 atm.

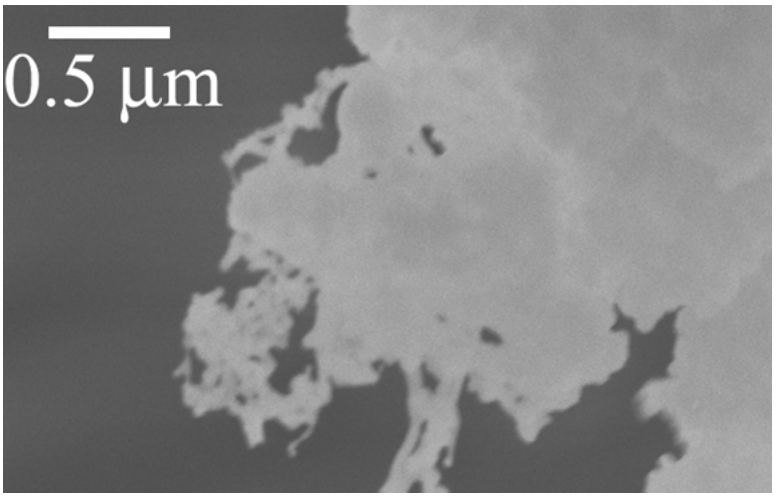

Figure 3.21 A HRSEM image of the SiO aggregate following annealing at 900 ^{o}C for 30 minutes in UHP Ar (the same sample as is shown in figure 3.17).

shows the same sample following annealing. The samples were annealed in a vacuum tube furnace and backfilled with Ar during the thermal treatment cycle. The width of the nanostrings, comprising the fine structure of the SiO nanoscale aggregate, increased as measured following the annealing treatment. Moreover, the post – annealed morphology exhibits increased curvature due to the surface energy minimization that took place during the high temperatures thermal treatment cycle. The heat treatment at 900 ^{o}C promoted diffusion and hence the minimization of the surface area of the SiO aggregate.

To better understand the morphology transition from the micro – scale to the nano – scale for the annealed aggregate, a sequence of HRSEM and HRTEM images is provided (figures 3.21, 3.22, and 3.15), that exhibit this transition in terms of magnification. A huge cluster of SiO sheath protruding from the side of a microcone is shown in figure 3.21. An individual nanostring from this sheath is shown in the HRSEM image provided in figure 3.22. This HRSEM image was taken from the same region shown in figure 3.21. Figure 3.15 shows a HRTEM image of a cluster of intertwined nanostrings. Clearly evident in the figure is the spherical nature of the nanostring components and the enlargement of these components relative to the pre – annealed aggregate shown in figure 3.13.

Two main, broad photoluminescence peaks were observed for all the spectra obtained from annealed SiO aggregate. The most intense peak was centered at roughly 420 nm (3.0 eV) and a less intense peak at roughly 500 nm (2.5 eV) was also observed. In addition, Table 3.1 shows the centered positions of the Gaussian peaks used to construct fits to the raw data shown in figure 3.16. For example, figure 3.23 shows the array of

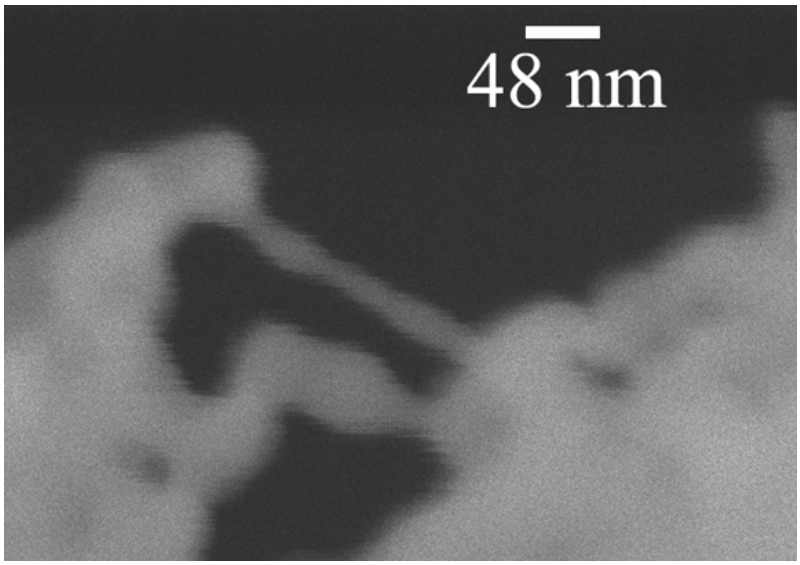

Figure 3.22 A HRSEM image of a straight, 100 nm long SiO rod found within the aggregate shown in figure 3.17 following the annealing heat treatment.

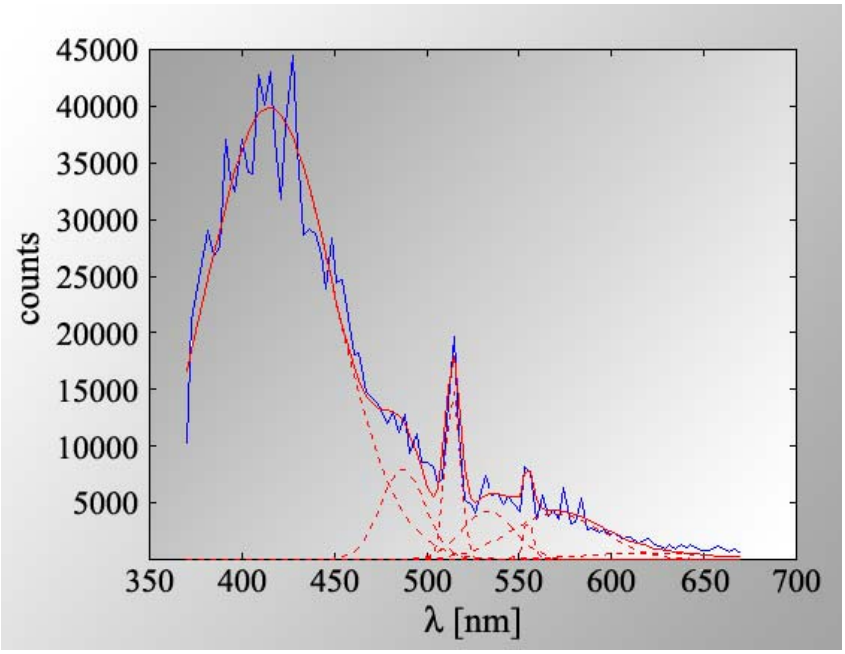

Figure 3.23 The photoluminescence spectrum, shown in figure 3.21 for the 50% O_2 – Ar sample, fit to a series of Gaussian curves. A total of seven Gaussian curves were found to best fit the experimental data.

Gaussian peaks as a result of the fit for the 50% O_2 data (hatched curves), their superposition (solid, smooth curve), and the raw data.

Figure 3.24 shows an electron diffraction pattern, produced by using the HRTEM in diffracting mode, from the region of SiO entanglement shown in figure 3.15. The observation of a diffuse, continuous ring (the dark ring shown that just fits inside the square formed by the image itself) *without diffraction spots*, indicates no crystalline component is present in the region shown, in image mode, in figure 3.15. The HRTEM was also used in image mode to check for lattice fringes at high resolution in many samples.

In summary :

1. Annealing the SiO nanostructure greatly increases its photoluminescence intensity.
2. The maximum intensity of photoluminescence is observed for SiO sheath produced in 50% O_2 – Ar.
3. The two broad peaks (2.5 & 3.0 eV) clearly discernable as components in the photoluminescence spectra, obtained for the SiO sheath, are consistent with luminescence from oxide related defects (see Table 3.2).
4. No crystalline structure was detectedin the unannealed and annealed SiO. SiO and SiO_2 are amorphous and any detection of crystallinity would be necessarily attributed to Si.

These points suggest that the nanoscale silicon aggregates are not present in the SiO aggregate (as, for example, nanoparticles embedded in the sheath) and that the luminescence is due exclusively to oxygen – related defects.

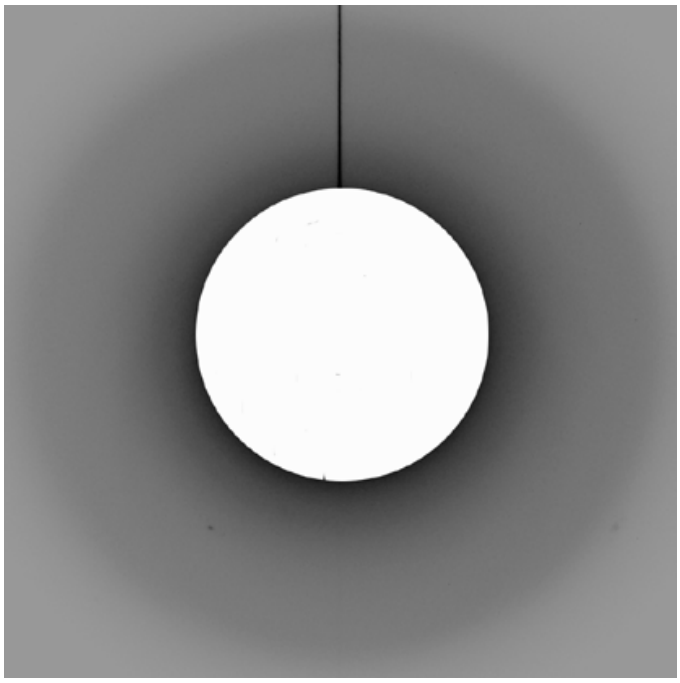

Figure 3.24 The electron diffraction TEM (EDTEM) image shown above contains only symmetric, diffuse rings (the dark bands surrounding the central, bright region; this is the transmitted central beam which has been subtracted out of the image) indicating that there is no crystallinity present in the nanostructured aggregate sheathing the Si microcones. The electrons collected for the diffraction pattern shown above interacted only with the SiO aggregate on passing through the grid supported aggregate sample. The presence of discrete streaks or spots in the dark rings would suggest the presence of crystalline, nano – sized components. The SiO aggregate was prepared in 25% O_2 – Ar gas with 500 laser pulses (E_d = 1.9 J/cm^2). The sample was then annealed at 900 ^oC for 30 minutes in flowing, UHP Ar to induce the transformation of amorphous Si (a – Si) to crystalline Si, if any a – Si was present at all in the samples.

Table 3.2 A list of photoluminescence peaks characteristic of various defects in SiO

Defect related luminescence in SiO

2.7 & 4.4 eV [a]
A triplet-to-singlet transition associated with an oxygen defect. The transition is from an excited state ≡ Si - x - Si ≡ to a ground state ≡ Si — x — Si ≡

2.5 eV +/- 0.3 eV [b]
Radiative recombination at an oxygen-induced defect state.

2.3 eV [c]
Self-trapped exciton

1.8 eV [d]
Red luminescence due to non - bridging oxygen

[a] R. Tohman, Y. Shimogaichi, H. Mizuno, Y. Ohki, K. Nagasawa, and Y. Hama, *Phys. Rev. Lett.* **62**(12), 1388 1989
[b] P. O Keefe, S. Komuro, T. Morikawa, and Y. Aoyagi, *Appl. Sur. Sci.* **113/114**, 135 1997
[c] A. N. Trukhin, M. Goldberg, J. Jansons, H. -J. Fitting, and I. A. Tale, *J. Non-Cryst. Solids* **223**, 114 1998
[d] L. N. Skuja, A. R. Silin, and A. G. Bogarov, *J. Non-Cryst. Solids* **63**, 431 1984

3.3 Si Nanoparticle Formation from Laser – Irradiated Smooth and Rough Silicon Targets

3.3.1 Nanoparticle Diameter as a Function of Laser Processing Variables

A film of silicon nanoparticles was formed on the surface of a silicon target following pulsed laser irradiation in an inert, background gas. Silicon species generated during laser ablation were backscattered by the background gas and redeposited on the target. Polished and microstructured silicon targets were used to study the redeposited films. The targets considered "flat" were atomically flat, pre – polished silicon wafer. Pulsed laser irradiation of silicon wafer in an SF_6 ambient was used to generate the pre – existing target microroughness.

The microstructure consists of an array of microcones produced by laser irradiating in SF_6 atmospheres (figure 3.1). The evolution and characteristics of this microstructure have been presented in section 3.1. However, it should be noted that the rough microstructure greatly affects the nanoparticle formation process and thus changes the morphology and characteristics of the nanoparticle film. In fact, under identical irradiation conditions, i.e., fluence, background gas pressure, and number of pulses, two different types of nanoparticle films were produced on the target surface depending on whether the initial target surface was flat or rough. It is the purpose of this section to characterize these differences.

Figure 3.25 shows the edge of a laser spot generated by irradiating at 3.5 J/cm^2 a previously flat silicon target. A line running through the central, largest image in the figure designates the laser spot edge. Roughly 20 μm of the 2 mm edge of the laser spot is shown in the figure. Melting is observed just inside (upper right image) of the laser spot

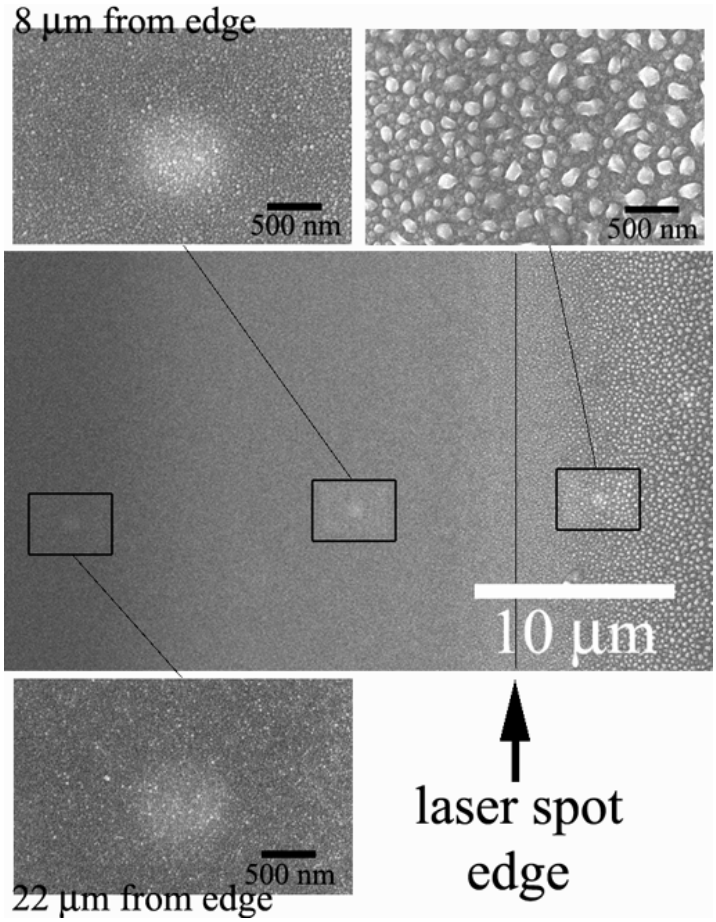

Figure 3.25 The spatial distribution, directly adjacent to the laser irradiation region, of Si nanoparticles produced by an irradiation of 500 pulses in 100 Torr Ar (E_d = 3.5 J/cm^2). Some Si species, produced during laser ablation and ejected from the surface, cluster in the Ar atmosphere as nanoparticles and redeposit on the surface following backscattering collisions.

boundary. A thin layer of the surface melted during the laser pulse and resolidified as ~ 100 nm droplets. The surface free energy of the film was minimized when the film drew – up into the 100 nm droplets by surface tension forces.

A nanoparticle film was formed *outside* the laser – irradiated area. The film consists of a dispersion of very small nanoparticles and of such a density that they are piled on top of one another, (upper left and lower left images in figure 3.25) with diameters < 100 nm. The diameter of the nanoparticles comprising the film is a function of the distance from the laser irradiated area at which the film is collected, the gas pressure present during irradiation, and the surface topography of the target prior to irradiation.

Figure 3.26 shows a plot of the nanoparticle diameter distribution for the specimen irradiated at 3.0 J/cm^2 under 100 Torr UHP Ar with 100 pulses. The nanoparticle diameters were measured from AFM images taken at 1 mm from the laser spot edge. The plot shows the number of nanoparticles falling in a range of 2 nm, from a size range of roughly 35 to 110 nm. The large peak evident in the plot yields a mean nanoparticle diameter of roughly 50 nm. A small peak in the curve represents a larger nanoparticle component with an average diameter of ~ 90 nm. However, the maximum intensity (number of silicon nanoparticles per range) of this Gaussian component at 90 nm is 1/3 the maximum of the main contributing peak. Thus, a nanoparticle film consisting of nanoparticles with mean diameters of ~ 50 nm are embedded around a fine dispersion of larger, ~ 90 nm, nanoparticles.

The nanoparticle size distribution from a film prepared under 500 mTorr UHP Ar is also shown in figure 3.26. This sample was prepared under similar irradiation conditions; E_d = 3.0 J/cm^2 and the film was collected at a distance of 1 mm from the laser spot edge

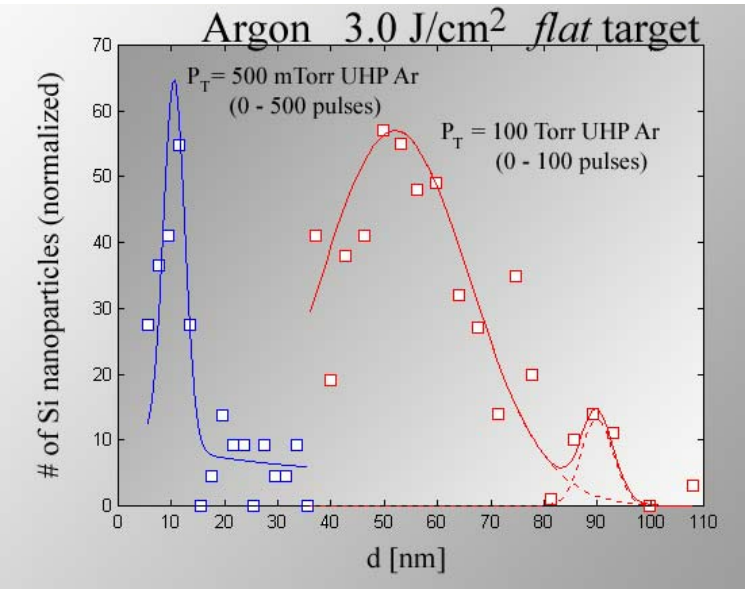

Figure 3.26 Si nanoparticle diameter distributions collected at a distance of 1 mm from the edge of the laser spot from which they were derived. Si nanoparticle diameter distributions are shown for collections made in 500 mTorr and 100 Torr Ar.

after 500 laser pulses. *However, the "number of pulses" variable does not influence the nanoparticle size distribution but rather affects only the number of particles per film*. A lower surface density of nanoparticles is produced at lower values of inert gas total pressure for a constant number of laser pulses.

The mean diameter of the nanoparticle film decreases by a factor of 5 when the total inert gas pressure is reduced by a factor of 200 (figure 3.26). Also, the FWHM of the distribution generated at 500 mTorr UHP Ar is much narrower (by a factor of 7) than the FWHM of the distribution generated under 100 Torr UHP Ar. A small FWHM is desirable since this indicates a nanoparticle film with a small standard deviation in diameter. This is attractive in technological applications where a film consisting of a specific nanoparticle diameter, and with a small standard deviation, is required.

The data fit for the nanoparticle diameter distribution for the P_T = 500 mTorr UHP is also shown in figure 3.26. The tail of the distribution indicates a substantial portion of nanoparticles have diameters ranging from 20 to 40 nm in the film. A HRSEM image of the nanoparticle film formed with 500 laser pulses in 500 mTorr UHP Ar is shown in figure 3.27a. The presence of the "larger" nanoparticles is clearly evident in the figure as is the small spatial dispersion of these particles.

The nanoparticle diameter distribution also changes as a function of distance from the laser spot edge and whether the initial target surface is rough or flat. Figure 3.27b shows a HRSEM taken at 5 mm from the laser spot for the sample irradiated in 500 mTorr Ar. The nanoparticle surface density and mean diameter have both clearly decreased as the distance from the laser spot edge to the film collection point has increased. This is evident, in a more quantitative way, in figure 3.28. A silicon target was laser irradiated under 100

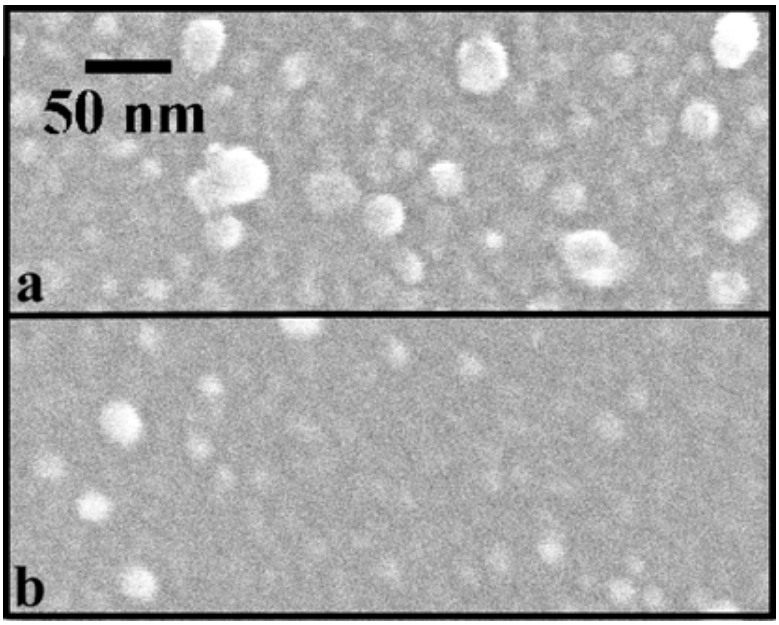

Figure 3.27 Si nanoparticles located (a) 1 mm and (b) 5 mm from the edge of a laser spot that was produced with 500 laser pulses in 500 mTorr Ar (E_d = 3.0 J/cm^2).

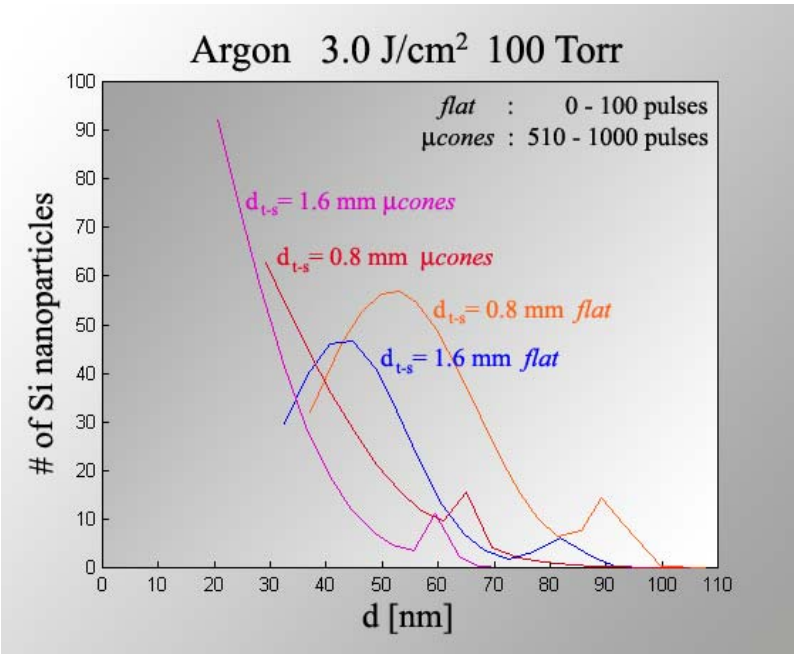

Figure 3.28 Gaussian fits to experimental data of the # of Si nanoparticles per nanoparticle diameter for nanoparticles 20 – 110 nm in diameter. Distributions are shown for nanoparticles collected at 0.8 and 1.6 mm and derived from both rough and flat surfaces. The "roughness" was pulsed laser induced Si microcones (figure 3.1) and the nanoparticles were collected from irradiating these structures only after they had fully developed on the surface, i.e., after 500 laser pulses and up to 1000.

Torr UHP Ar (E_d = 3.0 J/cm^2) and with 100 laser pulses. A nanoparticle film was observed in the HRSEM at 0.8 mm and 1.6 mm from the laser spot edge. The mean diameter of nanoparticles of the film collected at 1.6 mm (blue curve in figure, ~ 43 nm) is reduced by 17 % from ~ 53 nm, the value found for the film collected at 0.8 mm (orange curve in figure).

The surface density of the "larger" nanoparticles (the sharp spike in the tails of the fitted distributions shown in figure 3.28) decreases with distance from the laser spot. *This is an important result considering that these larger nanoparticles particles should be removed completely from the film in order to generate films containing only nanoparticles of diameters centered about one mean diameter, i.e., a film whose distribution can be mathematically represented by one discrete Gaussian profile*. In fact, when nanoparticles were collected at 7.5 mm from the laser spot edge *no large nanoparticles were found in* the nanoparticle film. Figure 3.29 shows a film of nanoparticles ranging from ~ 2 – 6 nm in diameter with a surface density much less than the surface density evident in the films collected closer to the laser spot (figure 3.28) for 100 laser pulses. Moreover, the FWHM of the nanoparticle diameter distribution is at least equal to, or less than, the distribution at 1.6 mm (blue curve, figure 3.28). A quantitative plot of the nanoparticle diameter distribution was not generated for the film collected at 7.5 mm since the small number of particles collected was not sufficient enough to generate a representative plot of the actual distribution. However, it was inferred from several images that the distribution would be at least equal to, or less than, the distribution obtained at 1.6 mm.

The effect of a microstructured target was to significantly shift the mean nanoparticle diameter of the film to smaller values. Figure 3.28 also shows the

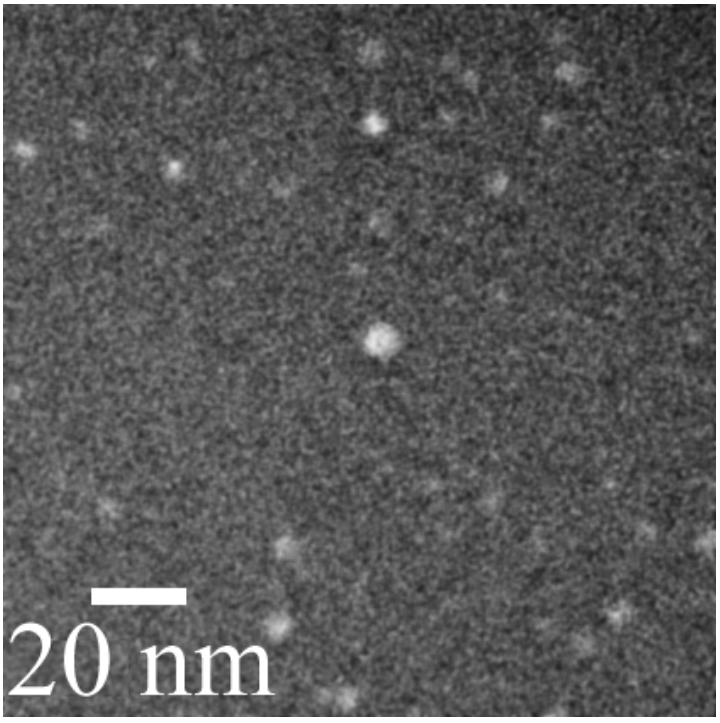

Figure 3.29 A TEM image showing nanoparticles collected on a holey carbon grid that was located 7.5 mm form the laser spot edge during a laser irradiation cycle of 100 pulses on an initially flat Si surface with an energy density of 3.0 J/cm^2 in 500 mTorr UHP Ar. The nanoparticles shown in the image, range in diameter from 2 – 10 nm.

nanoparticle diameter distribution for films produced from rough target surfaces as well as from flat surfaces *at the same position from the laser spot*. The figure shows the fitted data up to only $d_{particle}$ = 20 nm for data collected on films from rough surface irradiation. *The nanoparticle films generated from rough surfaces exhibited large degrees of clustering relative to films produced from flat surfaces*. This made measuring particles of diameters less than 20 nm very difficult. If we assume the distribution to be Gaussian in nature then, we can infer, approximately, the mean nanoparticle diameter from the Gaussian fits to the data. The mean nanoparticle diameter for films collected at 0.8 mm (red curve in figure 3.27) and 1.6 mm (violet curve in figure 3.28) from a Gaussian extrapolation is roughly 5 nm. Clearly, a drastic reduction in mean diameter has occurred just by modifying the pre – irradiation target surface roughness.

The FWHM of the nanoparticle diameter distributions increases 2 – fold for films prepared with pre – roughened target surfaces. This is a direct result of the increased clustering observed when using pre – roughened targets. For example, figure 3.30 shows a SEM image of the film collected from rough surfaces at 1 mm (figure 3.30a) and 5 mm (figure 3.30b) from the laser spot edge. These images are directly comparable (based on the fact that they were prepared under identical experimental conditions) with the images shown in figure 3.27 of films produced in the same locations from flat surfaces. By comparing the images one can clearly see the increased degree of clustering of individual nanoparticles to form "clouds" of nanoparticle agglomerates (figure 3.30a).

Figure 3.30b shows irregularly shaped, less dense nanoparticle aggregates, at 5 mm from the laser spot edge, that are more discernable to the eye compared to the dense nanoparticle cloud formed at 1 mm from the laser spot edge. The decrease in nanoparticle

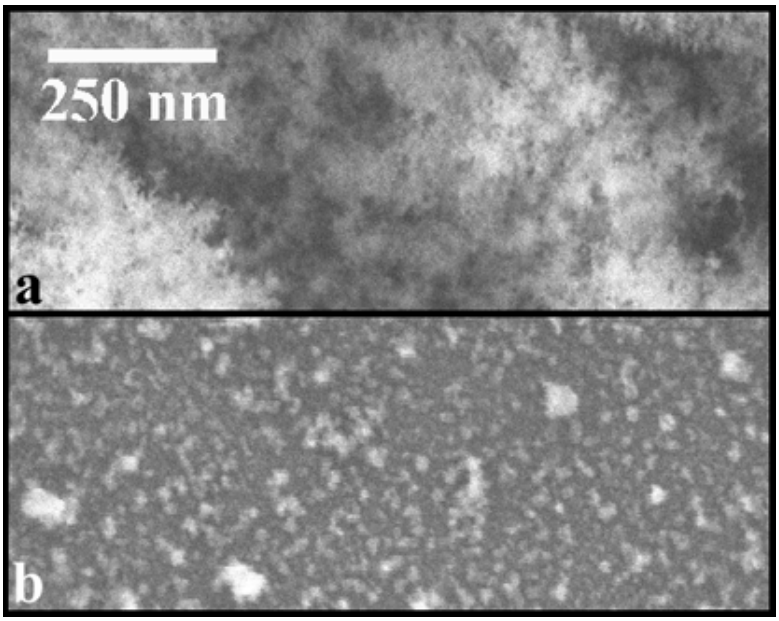

Figure 3.30 Si nanoparticles collected at (a) 1mm and (b) 5 mm from the laser spot edge during the laser irradiation of Si microcones, i.e., a rough target surface, with 500 laser pulses in 500 mTorr Ar (E_d = 3.0 J/cm^2)

density with distance from the laser spot edge is clearly evident from Figure 3.30. The irregularly shaped aggregates shown in figure 3.30b consist of attached collections of spheres that cluster *randomly*. Hence, the aggregates have irregular shapes as opposed to ordered clustering. Ordered clusters would yield a common shape from cluster – to – cluster.

3.3.2 Nanoparticle Crystallinity

A substantial portion of the nanoparticles comprising the films characterized in the previous section were found to be single crystal spheres. For example, all the nanocrystals shown in the HRTEM image in figure 3.29 are single crystal spheres. Figure 3.31 shows a HRTEM of one such nanoparticle. The lattice fringes of the nanoparticle are discernable as the periodic lines, inside the outlined sphere, running from the upper left – to – lower right areas of the 2D projection of the 3D spherical nanoparticle. The circle approximates the diameter of the nanoparticle as determined from fine structure in the HRTEM image that is now covered up by the circle.

The diameter of the nanoparticle is roughly 12 nm. The diffraction pattern created by the interaction of the electron beam with the periodic lattice of the spherical nanoparticle is shown in the lower – left corner of figure 3.31. The intense spot in the diffraction pattern bordered by the square box is characteristic of the (111) lattice plane spacing of bulk silicon. The value obtained for the spacing between the planes shown was 0.313 A in consistency with the (111) lattice plane spacing in bulk silicon that is 0.315 A.

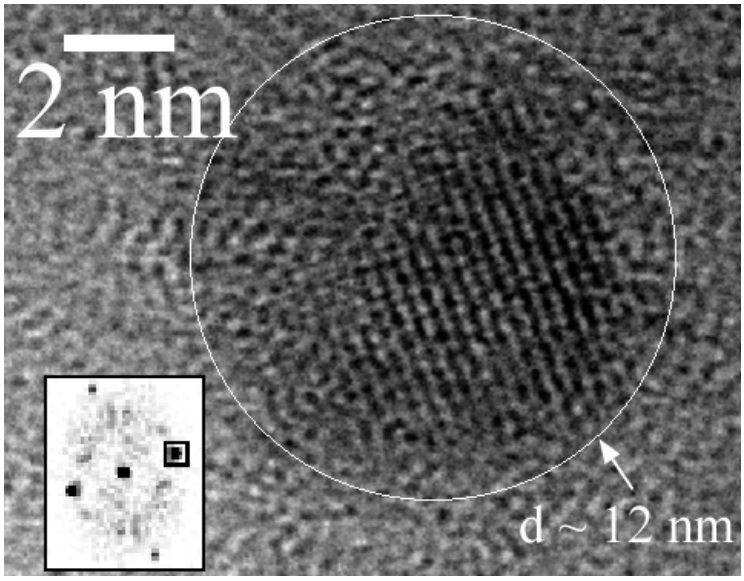

Figure 3.31 A HRTEM image of one crystalline Si nanoparticle collected on a holey carbon grid during the laser irradiation of atomically flat Si with 100 laser pulses in 500 mTorr UHP Ar (E_d = 3.0 J/cm^2).

3.3.3 The PLD of Silicon Nanoparticles onto a separate Substrate

Nanoparticle films were also deposited on substrates separate from, and located at some distance normal to, the target surface. The target was irradiated with many laser pulses prior to the deposition of nanoparticles on the substrate. The laser pulses were used to develop the microcone morphology on the target surface. A shutter was placed in front of the substrate to block ejected species and contaminants during the pre – roughening treatment. Once the microcone morphology developed on the target surface the shutter was removed and nanoparticles were allowed to contact and deposit on the substrate surface.

The evolution of the microcones on the target surface is accompanied by the appearance of a bright, orange vapor plume over the target surface. In fact, the development of the plume is crucial to the evolution of the microcone structures; the vapor plume supplies the silicon necessary to grow each individual microcone away from the target surface.

At a fluence of 2.5 J/cm^2 the vapor plume evolved over the target surface after roughly 700 – 1000 laser pulses and changed in shape over this 300 pulse range. The plume is initially less than 1 cm in diameter (the plume is roughly spherical) and grows continuously in diameter up to roughly 100 laser pulses. Over the next 200 pulses the plume changes shape subtly. The plume flickers over these 200 pulses with bright white momentary luminescence occurring in and around the plume. After 300 pulses (E_d = 2.5 J/cm^2) the plume reaches a steady – state spatial profile of 4 cm in diameter and a light orange hue.

The best nanoparticle films, devoid of larger 30 – 100 nm aggregates, are produced when particles are collected only after the vapor plume attains its spatially steady – state behavior. Figure 3.32 shows a Si nanoparticle film collected over 2000 pulses (steady – state plume) for ablation (E_d = 2.5 J/cm^2) into 100 mTorr UHP Ar. Pressures in the 10^2 mTorr range are just high enough to promote clustering in the gas phase to generate only nanoparticle formation while low enough to allow the nanoparticles to maneuver the distance from the target – to – substrate. The target – to – substrate distance was 4 cm.

The film consists of a fine distribution of nanoparticles devoid of large nanocluster aggregates (figure 3.32, right image). The nanoparticle diameter distribution for the film shown in figure 3.32 is provided in figure 3.33. The mean nanoparticle diameter is roughly 2.2 nm. Moreover, the FWHM of the distribution is ~ 2 nm. This is a very attractive distribution with a very small nanoparticle diameter and a tight standard deviation (relative to nanoparticle films generated from flat surfaces and mentioned in the Literature Review portion of this work). This is also a technologically attractive distribution because it falls within the quantum confinement regime of silicon (quantum confinement effects are prominent at spherical d < 5 nm. The fluence used to generate this nanoparticle film was the minimum fluence possible to generate such a film density in so few number of laser pulses.

A fluence of 2.45 J/cm^2 was not high enough to promote the evolution of microcones up to ~ 3000 laser pulses. The resulting, approximately flat target surface changed drastically the nature of the nanoparticle film collected under exactly the same experimental conditions to generate the film at 2.5 J/cm^2. The film has a nanoparticle diameter distribution shifted to a d_{mean} < 1nm and a FWHM of < 1nm. However, the

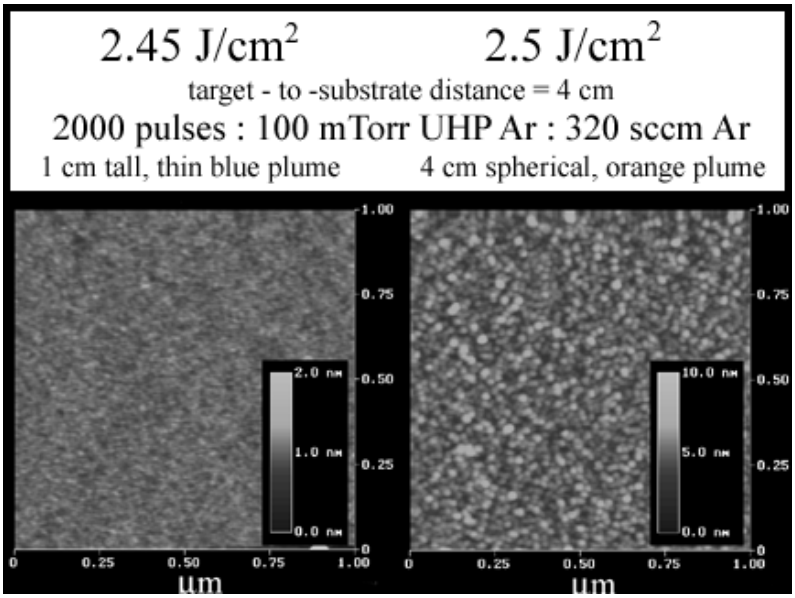

Figure 3.32 AFM images of two Si substrates containing Si nanoparticles collected during a pulsed laser depositon (PLD) experiment. For the left most image, a fluence of 2.45 J/cm^2 was used to irradiate, an initially flat, Si substrate with 2000 laser pulses in 100 mTorr UHP Ar flowing at 320 sccm Ar. A higher fluence of 2.5 J/cm^2 was used to irradiate the target surface and produce the nanoparticles that were collected on the right most substrate shown above. The substrates were located in the path of the laser induced vapor plume, 4 cm from the target surface.

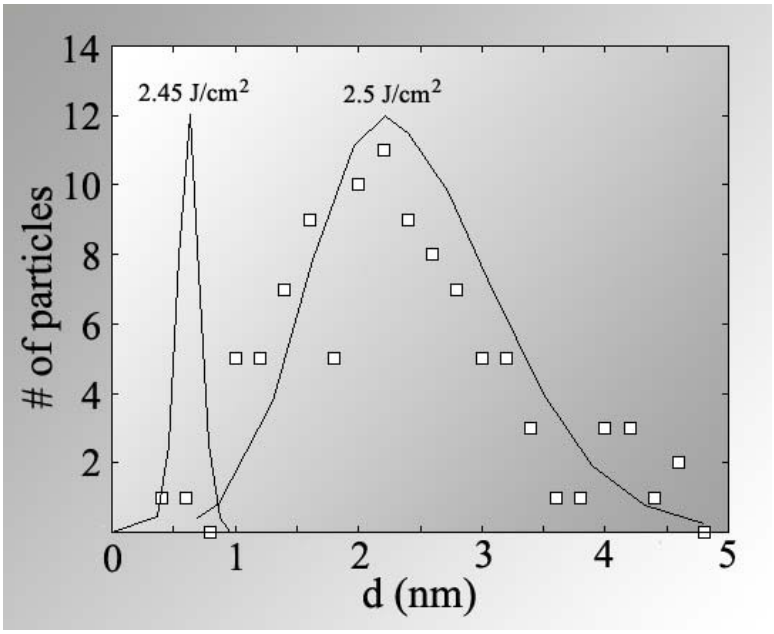

Figure 3.33 Nanoparticle size distributions for nanoparticles collected during PLD experiments at two different target irradiance of 2.45 and 2.5 J/cm^2. Experimental data points are shown as squares in the figure and Gaussian fits to data are also shown. The fit to the data collected for a fluence of 2.45 J/cm^2 has been normalized to the 2.5 J/cm^2 curve in order to compare the mean diameter for each distribution. The mean nanoparticle diameter is ~ 0.6 nm and 2.2 nm for the 2.45 J/cm^2 and 2.5 J/cm^2 case, respectively.

density of the film was drastically reduced. During the deposition, a thin 1 cm, blue plume was present over the target surface. In fact, using a fluence of 2.4 J/cm^2 no plume at all was observed over the target surface and no nanoparticles were collected on the substrate. A fluence of 3.0 J/cm^2 induces more ablation of the target and a more dense film at fewer numbers of pulses relative to the sample produced with E_d = 2.5 J/cm^2. However, the film is contaminated with nanoparticles of sizes greater than 30 nm and hence film quality is degraded. Thus, a narrow fluence range exists over which to generate nanoparticle films, from PLD experiments, possibly capable of exhibiting quantum confinement affects, under photoluminescence excitation, without the notorious large particle contamination inherently associated with PLD.

3.4 LINO (Laser – Induced Nanoparticle Ordering)

3.4.1 Linear Self – Organized Arrays of Si Nanoparticles

Figure 3.34 shows a substrate surface containing periodic rows of Si nanoparticles with a lateral spacing between rows of a discrete spatial frequency. The SEM image was taken with the electron beam aligned along the substrate surface normal vector. The network of arrays extends continuously over a roughly 12 μm x 8 μm surface area. *However, these arrays extend uninterrupted over the surface millimeter distances with little change in morphology from that shown in figure 3.33*. The only disturbance present in the organized network are small, localized cells where the nanoparticles have failed to form into linear chains but rather exhibit a spatially random distribution within the cell. The arrow in figure 3.34 points to one such cell. Two laser irradiation steps are required to generate the nanostructures shown in figure 3.34.

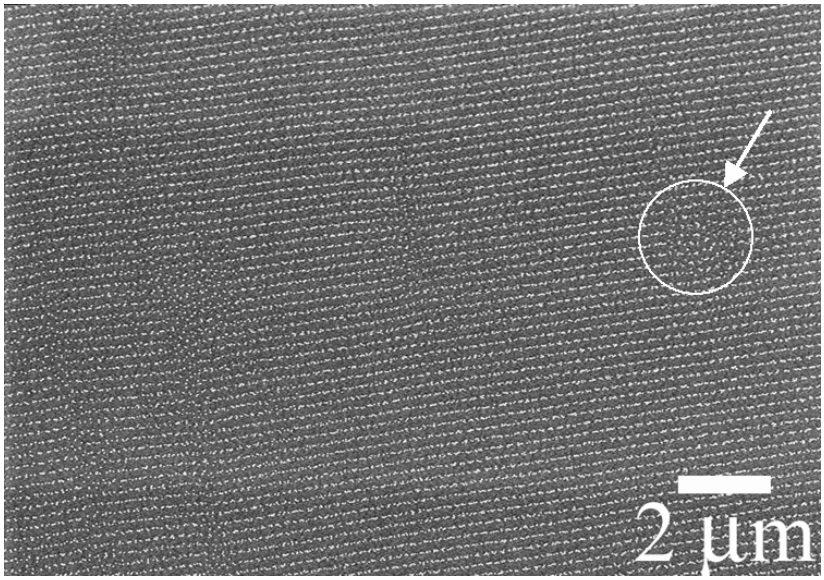

Figure 3.34 Self – organized, linear arrays of Si nanoparticle spaced 248 nm apart on a partially undulating, underlying Si substrate. The nanoparticles lie in the trenches of a periodically undulating surface shaped mostly like a sine wave. The maximum amplitude of the surface wave lies exactly between the nanoparticle lines. A disruption in the linear network is indicated by an arrow in the figure. The nanoparticle arrays formed on the Si surface following 200 pulses in 500 mTorr UHP He each pulse having a fluence of 1 J/cm^2. A pre – existing surface roughness of Si microcones, produced with 1500 laser pulses in ½ atm SF_6 (E_d = 3.9 J/cm^2), located adjacent to the region shown above, and also irradiated in He, is indirectly responsible for the evolution of the linear Si nanoparticle arrays.

Prior to laser irradiation, substrates were emersed in hydrofluoric acid 5%, in distilled H_2O, for 5 minutes in order to remove the passivating, thin (~ 1 nm) SiO_2 layer from the silicon substrate surface. The substrates were rinsed in methanol and distilled H_2O, post – HF etch, to halt the etching process. The substrate was blown dry with UHP N_2 to remove the HF 5%, methanol, and distilled H_2O completely from the substrate surface.

A passivating layer of hydrogen – terminated silicon is left on the surface as a result of this etch and clean surface treatment cycle. Hydrogen radicals, produced during the SiO_2 etch, react with the dangling silicon surface bonds to form a Si – H bond at the surface. This bond is stable during the methanol + distilled H_2O rinse and remains on the silicon wafer surface for up to 5 minutes, if air is present over the wafer surface, after the etch treatment is finished [89]. Hence, the substrate is loaded into a high – vacuum, stainless steel chamber within this 5 minute time window and pumped to 10^{-7} Torr in order to prevent the re – oxidation of the surface prior to laser – irradiation of the surface. It is important to have a relatively oxide free surface during laser processing to prevent oxide incorporation into silicon nanoparticle films.

The substrate was first exposed to 1500, 248 nm laser pulses (E_d = 3.9 J/cm^2), in an atmosphere of 0.5 bar SF_6 in order to generate a microcone morphology on the wafer surface. These laser – processing conditions ensure that the microcones will protrude roughly 30 – 60 μm above the initial wafer surface. The morphology produced on the wafer surface is very similar to that shown in figure 3.1.

The formation of the nanostructures takes place when a larger region, that encompasses the microstructure previously formed, is irradiated at 1 J/cm^2 with 200 pulses

in 500 mTorr UHP He. This second low irradiation process does not produce significant changes in the microcone structure but promotes the formation and ordering of the nanostructure as shown in figure 3.34

Figure 3.35 shows a low magnification view of the substrate surface following both the irradiation in SF_6 and He gas. There are three discrete regions in figure 3.35 and these can be differentiated based on the variation in image contrast of these regions.

1 The region first irradiated to produce the microcone structure showing a very strong contrast

2 The larger irradiated region that includes the microstructure and whose boundary is marked by the arrow pointing horizontally

3 The unirradiated region at the bottom of the image

The very tip of the arrow in the figure indicates where exactly the image shown in figure 3.34 was taken.

The morphology change induced during each laser – processing step is illustrated in the diagram of figure 3.36. The first irradiation treatment in SF_6 is responsible for the formation of the silicon microcones. The second irradiation cycle in He forms a thin, ~ 1 – 8 nm thick film on the surface, in the previously un – exposed, adjacent Si surface to the microcones, after roughly 0 – 100 laser pulses. Additional laser pulses in He induce the clustering of this film into the linear arrays of nanoparticles observed in figure 3.34. *The microcone morphology triggesr the alignment process in the adjacent film during the laser irradiation of both regions*.

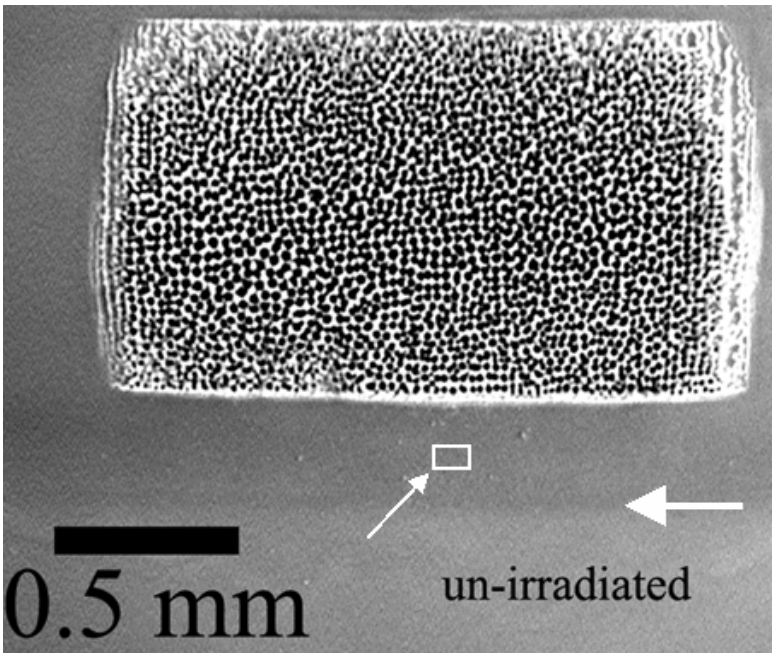

Figure 3.35 The box in the figure indicates the region on the Si substrate where the image shown in figure 3.33 was taken. This region, minus the high contrast (whitish) region located below the horizontal arrow and the laser spot shown in the upper right had corner of the image, are the areas where the formation of Si nanoparticles takes place and also where the self – organization takes place. However, in order to induce nanoparticle alignment, the laser spot (containing Si microcones) and region containing the Si nanoparticles must be simultaneously irradiated.

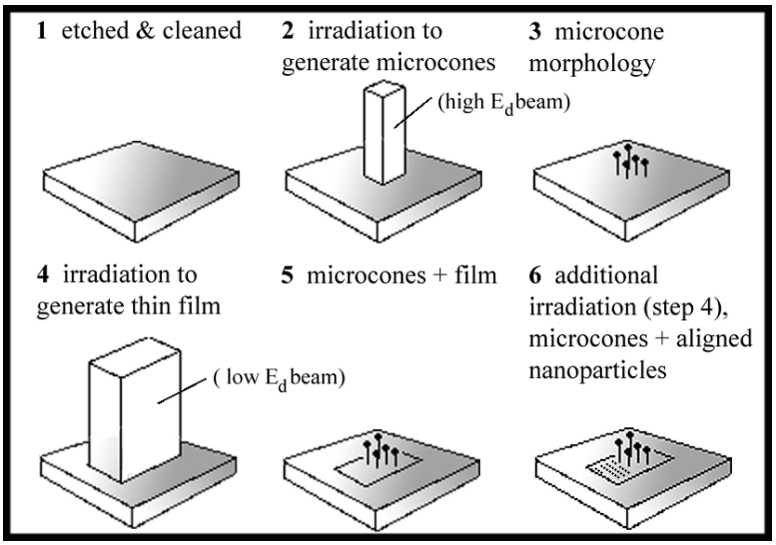

Figure 3.36 A schematic diagram of the pulsed laser irradiation cycle required to produce self – organized Si nanoparticle arrays. (1) atomically flat Si was etched in 10:1 HF, dilute in distilled H_2O, for 5 min., prior to laser irradiation to remove the native oxide layer from the Si wafer, (2 &3) laser irradiation in SF_6 gas with sufficient energy density (~ 3 J/cm^2) and laser pulses (10^3) to induce the formation of Si microcones exclusively in this irradiated region, (4&5) a roughly x2 larger spot, at the expense of beam energy (E_d ~ 1 J/cm^2), irradiates both the Si microcones and the surrounding flat Si wafer in ~ 10^1 Torr UHP He to produce a thin Si film ~ 1 nm thick in both regions. The film develops in as few a number of pulses as 30! (6) the film begins to cluster into Si nanoparticles and begins to align if the flat substrate and Si microcones are simultaneously irradiated for number of pulses > 50 nm.

3.4.2 Silicon Film Formation and Clustering

The Si nanoparticle arrays are completely aligned, and film clustering is complete, after 200 laser pulses in 10 Torr He (E_d = 1 J/cm^2). Figure 3.37 shows a HRSEM image of the aligned and clustered film of Si nanoparticles. The periodic lines of nanoparticles can be characterized by a wave vector orthogonal to the direction of the lines and with a magnitude equal to 2π / 248 nm, i.e., the lines are spaced 248 nm apart. This is exactly the wavelength of the pulsed, ultraviolet radiation used to irradiate the substrate to form the film and that aides in driving the alignment process!

Each line of nanoparticles is shown to consist of regions, or zones, of nanoparticles (figure 3.37). Each zone of nanoparticles is separated from adjacent regions, *along the line of nanoparticles it belongs to*, by roughly 60 – 100 nm. The nanoparticle zones contain, on average, 1 – 12 nanoparticles. The spacing between nanoparticles, within each zone, is roughly 5 – 30 nm. This value is small relative to the spacing between individual neighboring zones mentioned above.

An additional 200 pulses applied to the region on the Si substrate shown in figure 3.37 induces *no noticeable change,* in the morphology seen at high resolution, relative to that shown at 200 pulses. However, very significant changes occur during the first 200 pulses that generated the morphology shown in figure 3.37. Figure 3.38 shows the morphology of the Si film after only 100 laser pulses. Some clustering has occurred though because the film shows tears and fissures (the dark contrast regions in the shapes of high – aspect ratio wiggles) that are not present in the film (the film referenced here is the bright white region in the image) after roughly 1 – 50 laser pulses. HRSEM imaging of films at numbers of pulses less than 100 was cumbersome and for the most part

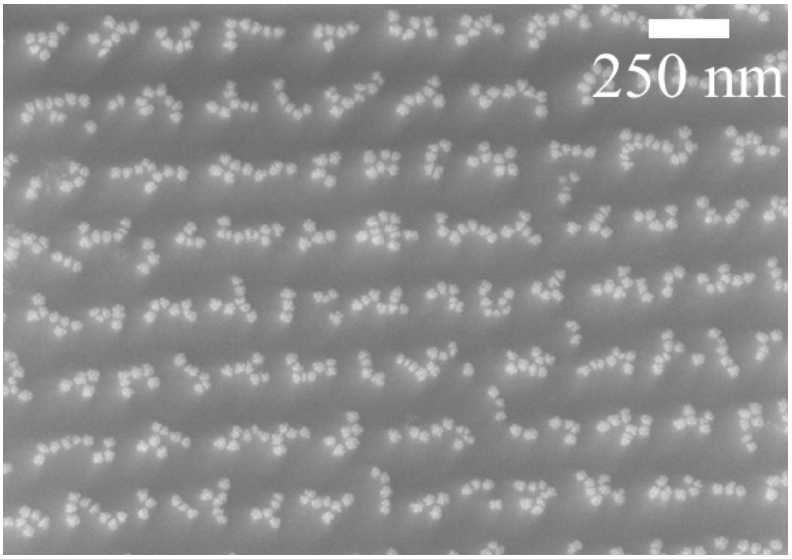

Figure 3.37 A HRSEM image showing the self – organized arrays of Si nanoparticles. Each line of nanoparticles actually contains zones, or regions, of Si nanoparticles separated from adjacent regions by 30 – 60 nm. The arrays were formed during the simultaneous irradiation of Si microcones and atomically flat Si surface in 10 Torr UHP He with 200 laser pulses (E_d = 1 J/cm^2).

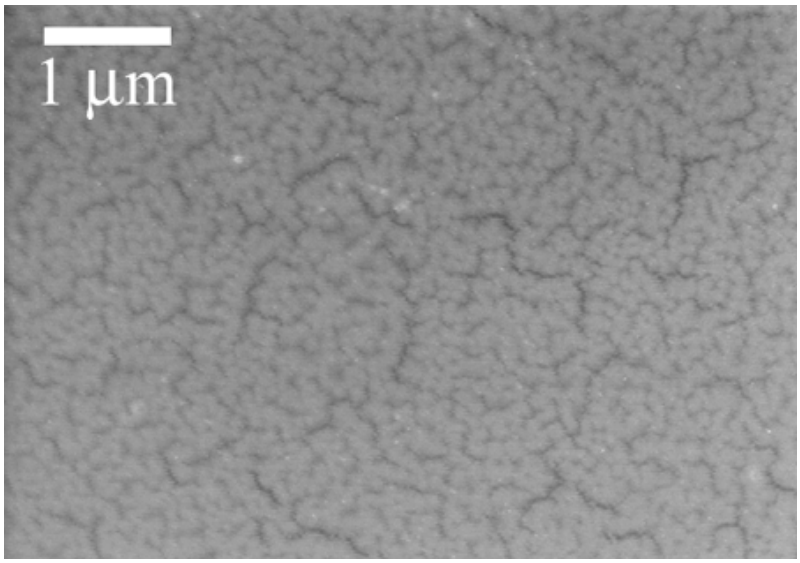

Figure 3.38 Si film, ~ 1 nm thick, formed on a Si substrate following 100 laser pulses (E_d = 1 J/cm^2) in 10 Torr UHP He. The image was taken at the inside edge of the laser spot where the E_d < 1 J/cm^2 due to the Gaussian distribution in intensity of the laser beam. In the central portion of the laser irradiated area the film had already clustered into nanoparticles after 100 laser pulses.

unsuccessful due to a lack of contrast present in the film structure, i.e., the film is of a roughness < 1 nm, the resolution limit of the microscope (HRSEM), and hence beyond the capability of the microscope to image. The fissures and tears in the film at 100 pulses made it possible to image the Si film.

In a few cases, Si films were observed in the HRSEM for number of pulses in He (E_d = 1 J/cm^2) less than 100 pulses. A region was observed in the film after 30 laser pulses where the clustering of nanoparticles had begun (figure 3.39). The nanoparticles observed in figure 3.39 (left image) have diameters < 5 nm, as determined by atomic force microscopy (AFM). A film sample was also prepared under the same irradiation conditions plus an additional 30 pulses and a second HRSEM image was taken to view the clustering process as a function of time. The degree of clustering was observed to increase after 30 additional pulses (figure 3.39, right image). The two images presented in figure 3.39 are from two different specimens.

AFM images were derived from tapping mode scans made on several film samples. Highly accurate (~ angstrom) film thickness values could be derived from these images because the z – resolution of the microprobe is sub – angstrom. It was found that the film had a thickness of no more than 8 nm up to 200 laser pulses. However, this is an upper limit in film thickness, the average film thickness observed over all experiments performed was ~ 1 nm. The film thickness does not appear to accumulate much from pulse – to – pulse. This value could not be directly measured because it was impossible to probe the same region with the AFM from pulse – to – pulse. However, a film thickness that changes very little from 50 pulses to 200 pulses seems to suggest that very little film accumulation takes place. *This is direct consequence of the simultaneity of film formation*

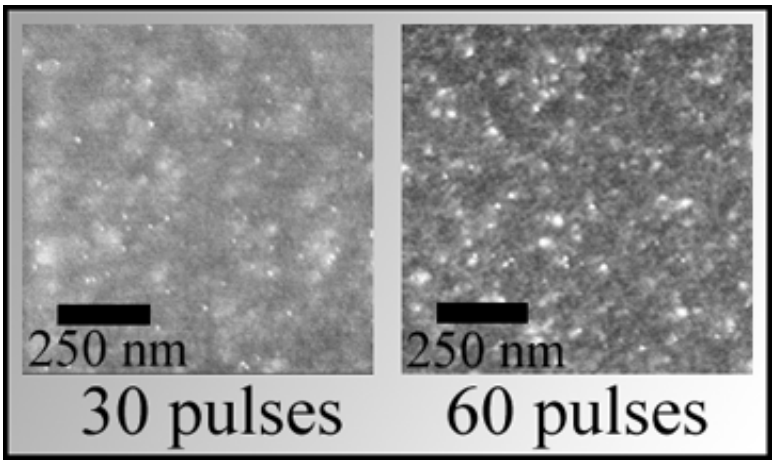

Figure 3.39 Some nanoparticle clustering takes place after only 30 laser pulses (E_d = 1 J/cm^2, P_T = 10 Torr UHP He, left – most image). The average nanoparticle diameter in the image is roughly < 10 nm. Additional clustering takes place with 30 extra laser pulses increasing the diameter of already present nanoparticles and new nanoparticles nucleate having the affect of increasing the density of nanoparticles per unit area.

and film clustering. Consumption by clustering appears to deplete film from adjacent regions and later pulses provide fresh film for redistribution, to these depleted regions.

Figure 3.40 shows the replenishment of film in flat, adjacent regions to clustering centers. The left – most image in figure 3.40 shows a Si surface with a random network of cluster chains, or zones, and very little film remaining between the zones. However, 50 additional pulses to this same area generated fresh film in the region between cluster zones (figure 3.40, right most image). It is interesting to note that the bit of film that *was* present after 450 pulses remains after 50 additional pulses. It is possible that the exposure of the film to air and to the electron beam changes its nature and hence its ability to cluster. This presumption is based on the observation that the film region charges significantly when viewed at magnifications greater than 25 kX in the HRSEM and this charging is still present after the sample has been removed from the HRSEM, laser – processed, and re – introduced into the HRSEM to observed the previously observed region!

The laser – generated Si film is confined to the irradiated region. Very little film deposits in regions far removed from the laser – irradiated area. For example, figure 3.41 shows a low magnification image of a Si substrate irradiated with 4000 laser pulses (E_d = 1.1 J/cm^2) in 100 Torr He. The film is confined to the laser spot size used to illuminate the substrate and it is seen in figure 3.41 as the brightest rectangular region at the center of the image.

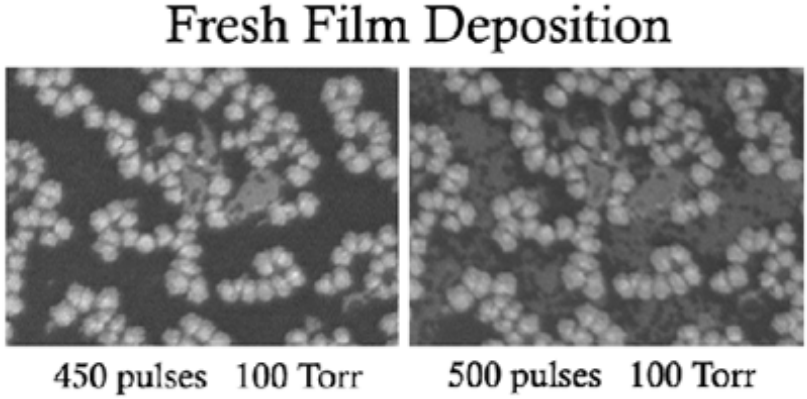

Figure 3.40 The replenishment of exhausted film has been directly viewed from pulse – to – pulse by monitoring the exact same region of the Si target during the sample pulse history. The left most image above shows a region of the laser irradiated surface after nanoparticle generation has occurred, but the linear alignment process has not yet taken place on the surface. The interchain substrate areas contain no Si film, it has been consumed to form the adjacent nanoparticles. However, after 50 additional laser pulses new film has evolved in the interchain locations but has yet to cluster into nanoparticles.

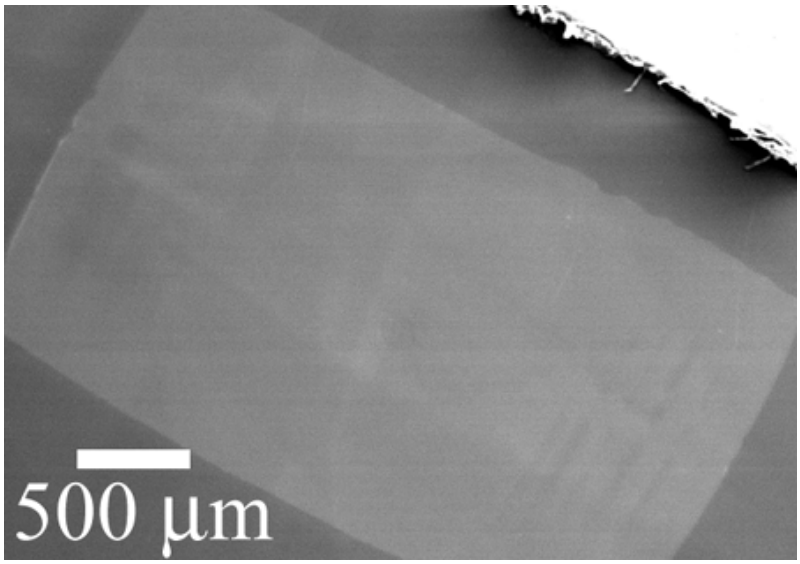

Figure 3.41 The Si film forms only in the laser irradiated surface region. The above low magnification SEM image shows this confinement to the irradiated region as the bright rectangle. The use of a light polarizer (p – polarized transmission) retards the clustering phenomena of the film on the surface but not the film formation process. Hence, after 4000 pulses the film completely fills the irradiated region (enough pulses have been provided to the low energy Gaussian tail region to induce film formation after 4000 pulses) and is clearly evident in the above SEM image.

3.4.3 The Chemical Composition of the Silicon Film

The film initially formed on the surface (from 0 to 200 laser pulses) inevitably clusters to form the nanoparticles that reside on that surface. Hence, the composition of the film will dictate the composition of the nanoparticles. Thus, to determine the composition of the precursor film is fundamental to determining the composition of the nanoparticles.

Depth profiling chemical analysis was performed in a precursor film by Auger electron spectroscopy (AES). The precursor film was formed with 200 laser pulses in 500 mTorr He with each pulse having an energy of 1 J/cm^2. SEM analysis of the film in-situ, prior to AES measurements, revealed that clustering had taken place on some regions of the surface while other regions, close to the edge of the laser spot, had yet to cluster into nanoparticles. It was the region close to edge that was chosen to perform the AES measurements since the film was continuous in this region.

AES measurements were first taken on the surface on the film. Sputtering was performed in increments of 0.6 nm and at each increment AES spectra were taken. The atomic concentration of species in the film was derived from the AES spectra and plotted as a function of sputter depth to a depth of 5 nm from the film surface (figure 3.42).

The first nanometer of the film was found to be thoroughly oxidized, i.e., 55 at% oxygen at the surface. This oxide layer is characteristic of a film exposed to air following laser processing and indeed this film was exposed to ambient on removal from the laser – processing chamber. For a reference, the same plot of atomic concentration vs. sputter depth was generated from data collected on a region outside the un – irradiated region. A

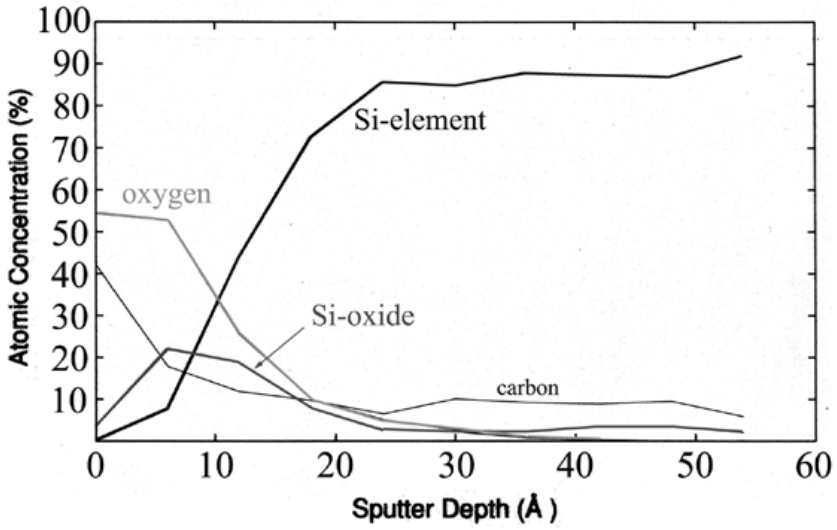

Figure 3.42 Auger electron spectrum (AES) of a Si film deposited with 200 pulses (E_d = 1J/cm^2) in 10 Torr UHP He. The spectrum shows the atomic concentration of oxygen, carbon, and silicon as a function of depth into the film. Different layers of the film were exposed by Ar ion sputtering through the film to the depth of interest. The "Si – oxide" peak shows the atomic concentration of Si tied up in Si – O bonds down to ~ 1 nm below the surface.

thin, passivating oxide layer also existed in this region. Moreover, the profile of the oxygen concentration as a function of depth was the same as that shown in figure 3.42.

At a depth of 1.5 nm below the film surface, the composition of the film is the same as the bulk silicon wafer substrate. Figure 3.43 shows a nanoparticle that has clustered at the expense of the surrounding film. The spherical volume of the nanoparticle is $4/3*\pi*(2.5\ nm)^3$. The silicon for this particle came from the missing cylinder of film surrounding the particle that is 13.2 nm in diameter. A rough estimation of the film thickness is given by setting the volume of the cylinder of missing material, $\pi(13.2/2\ nm)^2*h$, equal to the volume of the nanoparticle, and solving for h, the height of the cylinder. For the HRSEM image shown in figure 3.43; h ~ 1.1 nm (the film thickness calculation was performed on the same sample used to collect the AES data from!). *Hence, the nanoparticles should contain only silicon, assuming the exposure to air after laser – processing oxidized the silicon film present on the substrate surface. This would seem to be a logical extrapolation from the AES results considering the neighboring, un – irradiated silicon, had the same oxygen concentration profile as a function of depth. However, to completely characterize the film and nanoclusters, AES + Ar^+ ion sputtering was performed only on the nanoparticles to directly measure their chemical composition*.

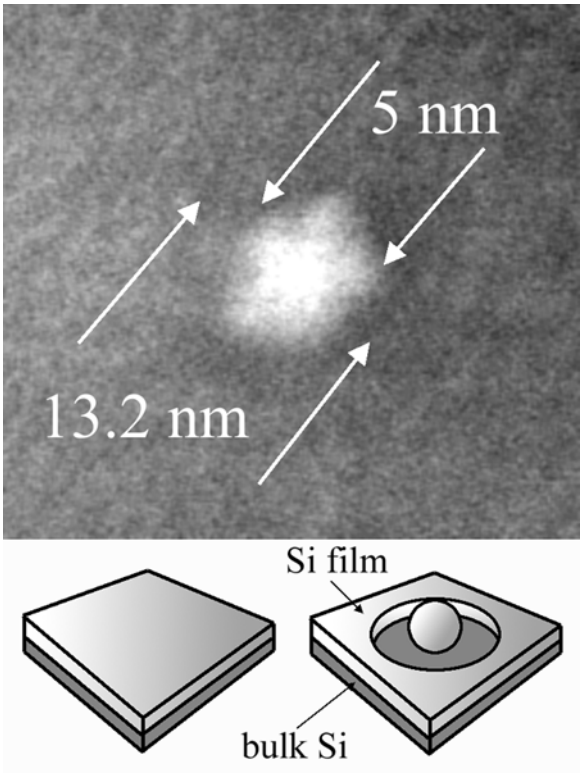

Figure 3.43 A SEM image, saturated in contrast, of one Si nanoparticle embedded in a Si film. The dark ring around the particle is the film – denuded region that was depleted in film to fed the adjacent nanoparticle's growth.

3.4.4 **The Chemical Composition of the Nanoparticles**

The substrate containing the nanoparticle arrays was tilted at an extreme angle in the AES system so that the electron beam irradiated only the nanoparticles on the substrate surface. The substrate orientation inside the microscope is shown schematically in figure 3.44. The substrate is shown in cross – section where the wave vector of the nanoparticle arrays lies in the plane of page running along the tilted surface, i.e., the observer to the page is viewing down along the lines of nanoparticles.

The sample shown in figure 3.44 has been tilted such that the electron beam can irradiate only nanoparticles. Moreover, Ar^+ ion sputtering was used to probe the chemical composition of the nanoparticles to their cores. The sputtering beam was oriented 45^o off the substrate surface normal when the sample is oriented flat in the microscope. Thus, for each sputtering cycle the sample had to be tilted back to a flat orientation to sputter. Figure 3.44 shows the orientation of the sputtered "flat" on each particle and the orientation of this flat with respect to the electron beam when Auger spectra were taken.

Auger spectra taken from the nanoparticles prior to sputtering showed an oxygen atomic concentration of 26 at% at the surface of the nanoparticles. The silicon peak in the N(E)*E vs kinetic energy spectra was shifted to 73 eV, a peak energy characteristic of Si bonded to oxygen in SiO_2. Sputtering into the nanoparticles 1 nm deep produced an Auger spectra far different from the one obtained from the surface. The oxygen atomic concentration dropped to 3 atomic percent and the Si peak was located at 90 eV (figure 3.45). This position indicates Si – Si bonds predominate in the nanoparticle.

Figure 3.46 shows two Auger electron spectra, one from a sample of un – sputtered nanoparticle arrays oriented with the sample surface normal parallel to the electron beam

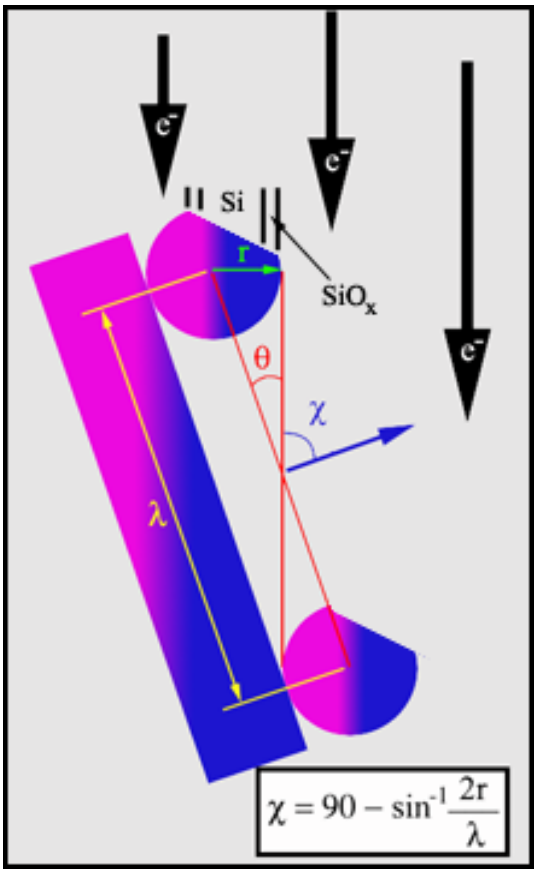

Figure 3.44 A schematic diagram showing how the Si nanoparticles were prepared for AES spectroscopy to elucidate the chemical composition of the nanoparticle cores. The nanoparticles' surfaces were sputtering at 45^{o} with respect to the substrate surface normal. The substrate was then tilted to a sufficient angle in order to irradiate only the nanoparticles with the incident electron beam. This steep angle irradiation ensures that only Auger electrons are generated from the nanoparticles. The nanoparticles were sputtered through their thickness to determine the chemical composition of the nanoparticles as a function of intraparticle radius. It was found that nanoparticles of d > 5nm had an encapsulating layer of silicon oxide that surrounded a silicon core.

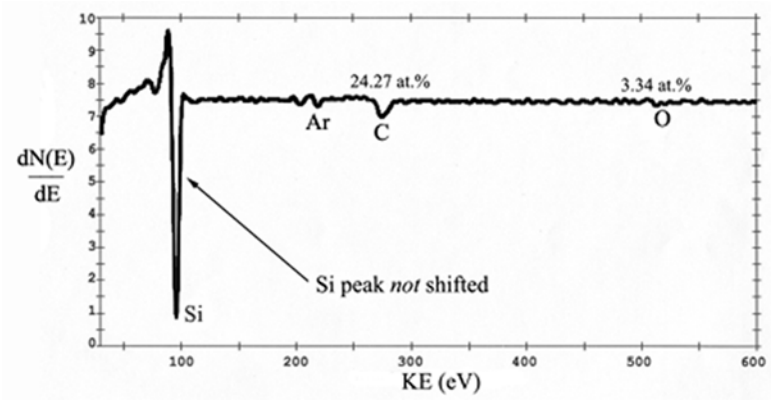

Figure 3.45 AES spectrum from a nanoparticle core, i.e., at a depth below the nanoparticle surface > 1 nm. The nanoparticle chemical composition resembles a spectrum taken from bulk Si (pre – sputtered, bulk Si to remove surface contamination and hence, obtain the true chemical composition of the bulk Si).

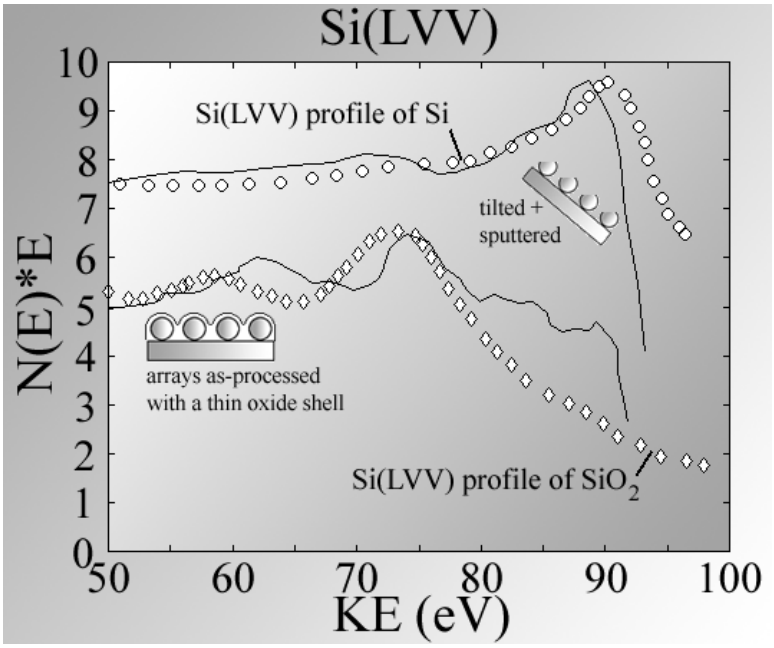

Figure 3.46 Experimentally obtained AES spectra from oxide sheathed Si nanoparticles and Si nanoparticles with their silicon cores exposed. Superimposed on these spectra are Si(LVV) profiles for Si in bulk Si and Si in silicon oxide. The experimentally generated data points for the nanoparticle cores closely fit the Si(LVV) profile for bulk Si. In contrast, the oxide coated nanoparticles produce a Si(LVV) Auger signal representative of Si tied up in SiO_2.

and another spectra from sputtered and tilted nanoparticle arrays such that only nanoparticles are irradiated by the electron beam. In the aforementioned sample the Si peak is shifted characteristic of predominantly Si – O bonds whilst the later spectra contains a Si peak characteristic of predominantly Si – Si bonding.

3.4.5 Direct Evidence of the Clustering of Si Film and the Collective Motion of Nanoparticles on the Surface

Figure 3.47 shows a HRSEM image of the discrete boundary between a region of fresh Si film and arrays of Si nanoparticles. The sample was prepared by first irradiating at a fluence of 3.9 J/cm^2 in SF_6 gas with 1500 laser pulses to produce microcone protrusions in the wafer surface layer. A second irradiation cycle of 200 pulses in 500 mTorr He with 1 J/cm^2 overlapped the first laser spot and fresh, un – irradiated Si adjacent to the first laser spot containing the microcones. The microcone morphology induced nanoparticle ordering in the adjacent, un – exposed Si surface during the second irradiation cycle. The Si film was also produced in this region by the second laser treatment cycle but the film formation is unrelated to the microcone morphology.

Several nanoparticles have begun to cluster in the Si film seen as the bright, smooth region in the left portion of the image in figure 3.47. A film – denuded region surrounds each nanoparticle embedded within the film. These denuded regions appear as dark rings surrounding each nanoparticle. Figures 3.48a and 3.48b present HRSEM images that show the clustering process.

The remnant annular ring of Si film in figure 3.48a was formed in the following way. A large, ~ 2 μm micron particle of silicon was initially present on the surface,

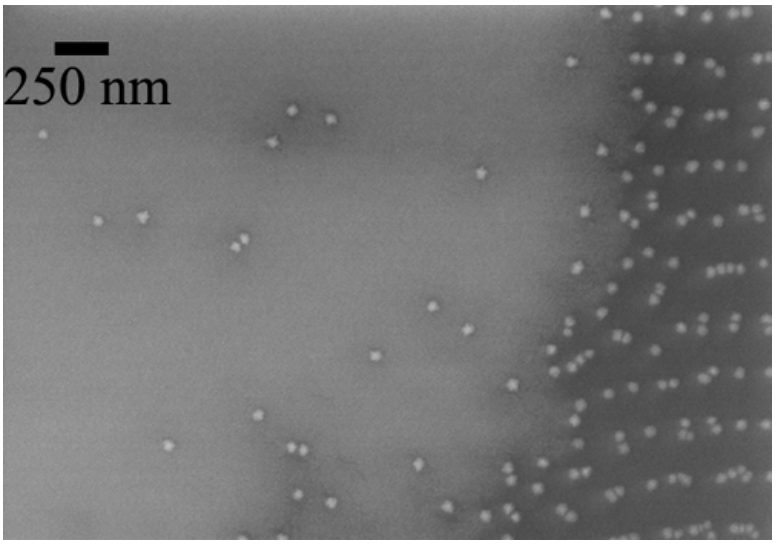

Figure 3.47 An abrupt boundary between a region of nearly completely clustered Si nanoparticles and a region completely covered in Si film. The boundary marks a region between low energy density (the film) and higher energy density (the nanoparticles) relative to the average, incident laser intensity of 1 J/cm^2 (P_T = 500 mTorr, 200 laser pulses).

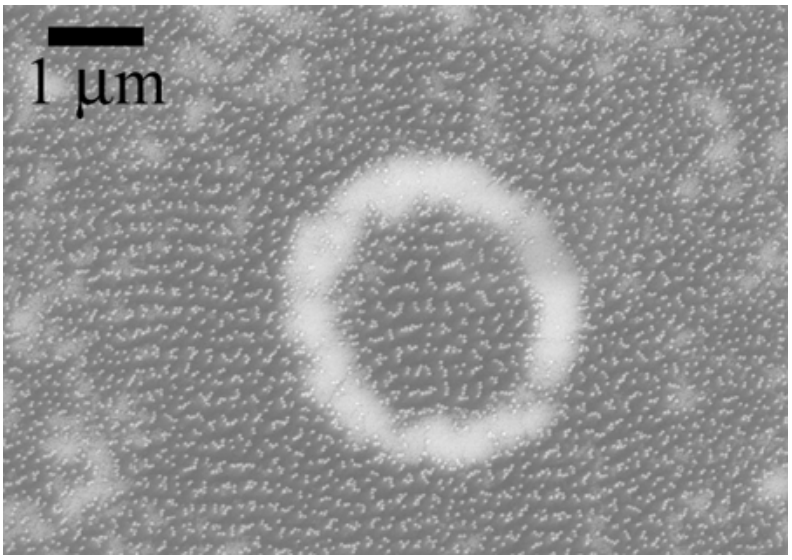

Figure 3.48 A microparticle, 2 μm in diameter was present on the surface during the laser pulse cycle to produce a film of Si on the surface. (a) Film was produced in the shadow of the microparticle but received no radiation there. The microparticle was subsequently removed at some point during the 200 pulse laser treatment cycle. The clustering of the film in the former shadow is retarded in its evolution into nanoparticles relative to adjacent regions (E_d = 1 J/cm^2, P_T = 10 Torr).

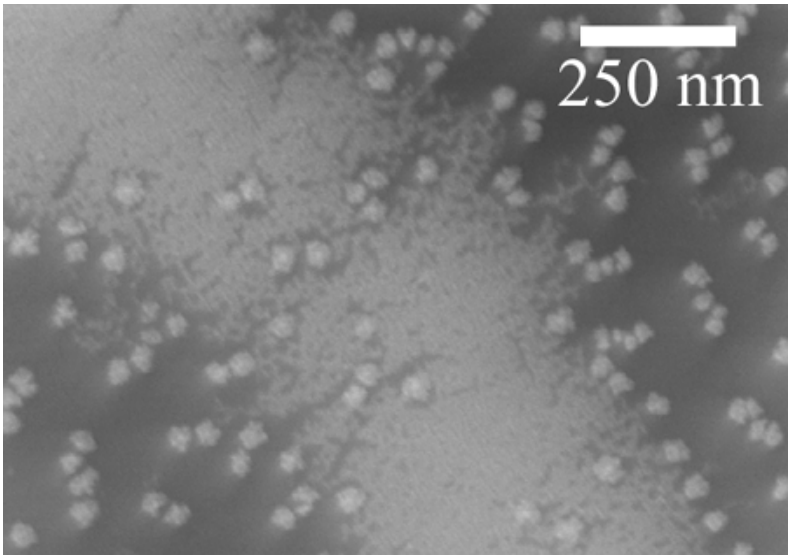

Figure 3.48 (cont'd) (b) A HRSEM image of the annular ring of the Si film shown in figure 3.47a. Partial clustering of the annular ring section is clearly evident based on the evolution of nanoparticles there at the expense of the adjacent film in the ring.

centered about the symmetry axis of the annular ring prior to the formation of the silicon film, i.e., the second irradiation cycle in He had not been performed. The particle was produced during the microcone growth process, ejected from the region between microcones and deposited on the surrounding, un – irradiated silicon. The particle remained during some range of pulses during the second irradiation cycle because film formed in the shadows of the particle but did not cluster because the material was shielded from the laser energy.

The particle was ejected sometime during the last series of laser pulses the substrate received. It had to be during the last laser pulses because the annular film remains on the surface, it did not receive enough pulses to cluster the film contained within its boundaries completely.

The above rationalization based on the image in figure 3.48a makes clear that;

1 The clustering process occurs over more than one pulse however the exact number of pulses is unclear.

2 The clustering process requires direct laser light energy to occur.

3 A film is clearly the source for nanoparticle mass.

Figure 3.48b shows a high magnification HRSEM image of one small portion of the annular ring. This photo establishes clearly that each nanoparticle is formed of Si film that was in closest proximity to the particle's present position prior to its nucleation and growth. Clearly each nanoparticle embedded in the annular ring has a film – denuded region directly adjacent to it.

The self – organization process begins at a point on the surface and spreads outward radially, consuming Si film as a function of the number of laser pulses (figure

3.49). Nucleation was assumed to occur in the central region of the nanoparticle region because the largest nanoparticles are there, i.e., they have existed the longest in the surface plane and, as a result, have had more time to consume surface migrating Si. Moreover, nanoparticles at the film boundary are very small because they are the newest nanoparticles to nucleate.

The actual relative motion of nanoparticle chains, with respect to one another, has been observed on a Si substrate from one series of laser pulses to another. Figure 3.50 shows an image of a Si surface containing a series of randomly oriented nanoparticle chains. These nanoparticles are located on a substrate with no alignment launching roughness, i.e., no microcone structures are present in the surface region. Hence, the nanoparticle chains have no means to align but rather are observed to continuously move on the surface without achieving an observable steady – state, linear spatial configuration. Three regions are boxed in the figure to monitor the relative to motion of the nanoparticles, contained within the regions bounded by the boxes, to their surroundings following an additional 50 laser pulses.

Figure 3.51 shows the same region in the sample surface layer after 50 additional laser pulses. It is clear that nanoparticle motion has taken place, within the regions denoted by boxes, observing closely the two figures. For example, in the left most boxes, labeled 1 in both figures, two spatially separated nanoparticle chains (figure 3.50) have linked up to form one continuous chain after the 50 laser pulses (figure 3.51). In the boxes labeled 2, three spatially separate nanoparticle chains have linked up to form one continuous chain after 50 laser pulses. In box 3 it appears that the packing density of the individual nanoparticles has increased after 50 laser pulses.

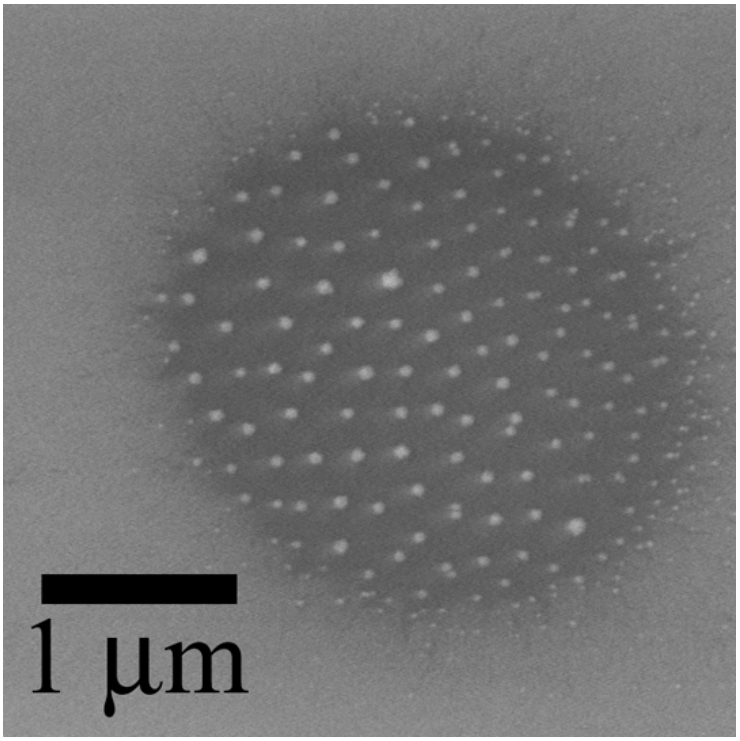

Figure 3.49 Nanoparticles alignment appears to begin as the clustering of a nanoparticle of a critical size ~ 1 nm. For example, and shown above, the nucleation of clustering spreads from a point source, a point at which film consumption begins. Film consumption spreads out to the point surface condition shown above (as a function of the number of laser pulses). Notice the inter – particle spacing is ~ 248 nm, the wavelength of the laser light used to induce clustering. After an additional 20 – 50 laser pulses the self – organization of nanoparticles into linear arrays will begin here.

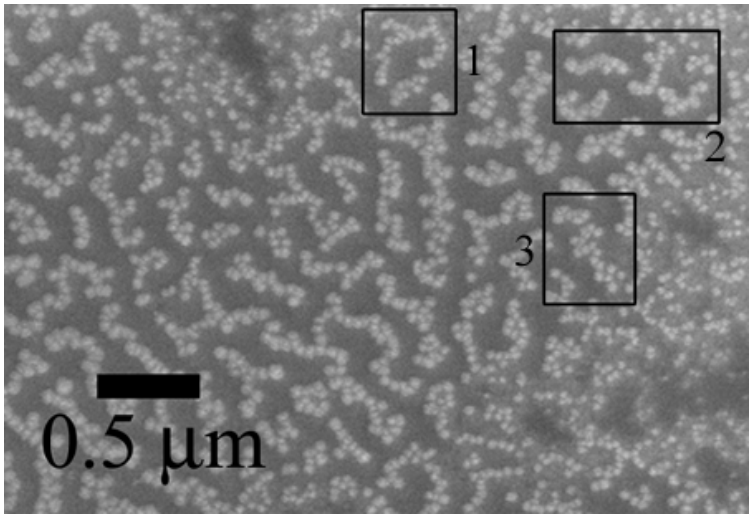

Figure 3.50 The self – organization of Si nanoparticles on the surface has been observed by following the motion of individual nanoparticle chains as a function of the number of laser pulses. Boxes 1, 2 and 3 will be redisplayed following 50 additional laser pulses in figure 3.50 to show the displacement of nanoparticle chains with respect to their position shown here. These nanoparticle chains were produced with 450 pulses in 100 Torr UHP He with laser pulses of fluence 0.6 J/cm^2.

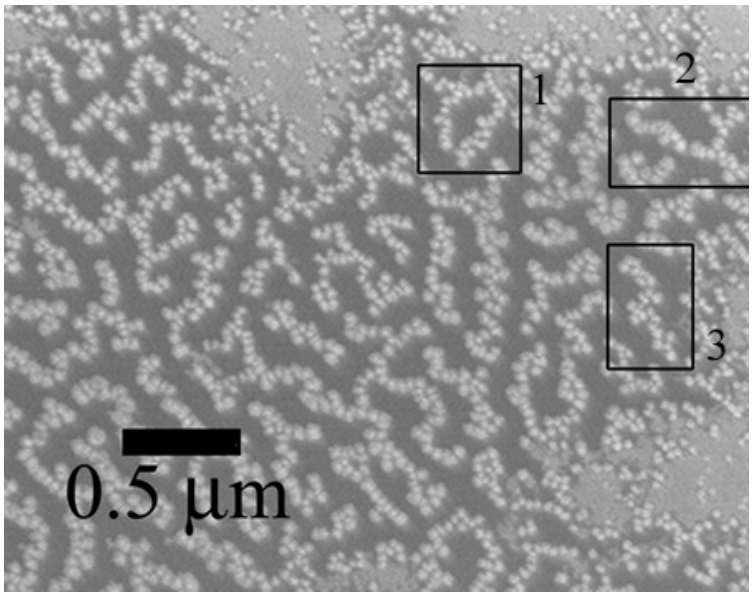

Figure 3.51 Nanoparticle chain motion has taken place on the Si target in the regions indicated by boxes in the image above, relative to their positions 50 pulses previously (figure 3.48).

Nanoparticle chains have also been observed to move, in the HRSEM, under even higher resolution conditions relative to the resolution of the images shown in figures 3.50 and 3.51. The nanoparticle chains shown in figure 3.52 are aligned on the substrate surface in the direction indicated by the arrow superimposed on the image. The alignment was induced by the presence of a microcone morphology, in the surface layer, that was partially irradiated during the laser treatment cycle to produce the Si film, clustering to form nanoparticles, and the alignment of the nanoparticles. The image shown in figure 3.50 was taken after the Si substrate had received 200 laser pulses in 100 Torr He (E_d = 0.9 J/cm^2).

Figure 3.53 shows an image of the same region of the substrate after 50 additional pulses. The resolution of the second image is slightly less than the resolution of the image in figure 3.52. The slow, electron beam scan rate used to capture the HRSEM image in figure 3.52 led to the cracking and deposition of hydrocarbons in this region during the scan. The slow scan rate translates to increased beam residence time per unit area on the sample and hence more time for the cracking of hydrocarbons to occur. The deposited carbon film appears as a rectangular, dark region when viewed at lower magnification following the scan procedure to acquire the image. Fewer secondary electrons are received by the Everhart – Thornley detector in the SEM, from the film – coated region, explaining the dark appearance of this region relative to surrounding regions. This region is charged positively with respect to the E – T detector. Hence, the ability to produce an image of equal quality was degraded when the same region was imaged later. In fact, even after 50 additional laser pulses the carbon layer remained on the substrate surface. Nonetheless, the nanoparticle chains can still be resolved in the image and their relative motion observed!

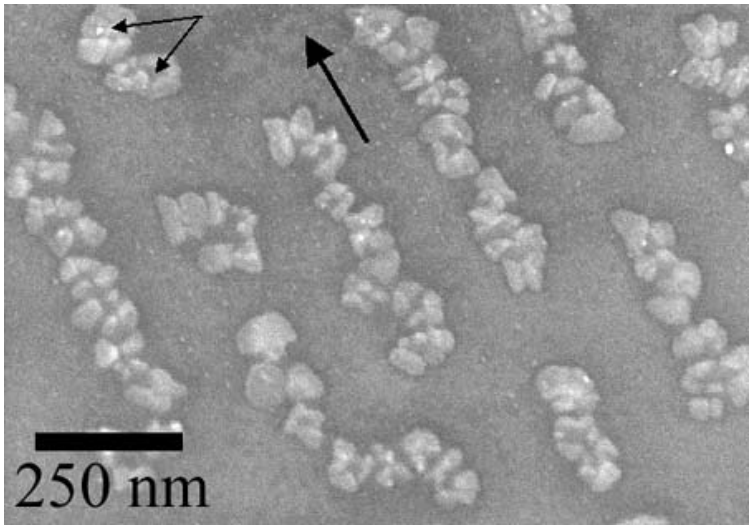

Figure 3.52 Nanoparticle chain motion was also monitored, as a function of the number of laser pulses, at a significantly higher magnification relative to the same experiments performed and shown in figures 3.48 & 3.49. A high magnification was chosen to determine how far the chains move on the surface in response to a specific number of laser pulses. The nanoparticle chains shown above were generated with 225 laser pulses in 100 Torr UHP He. The arrow superimposed on the image indicates the reference point for nanoparticle chain motion measurements.

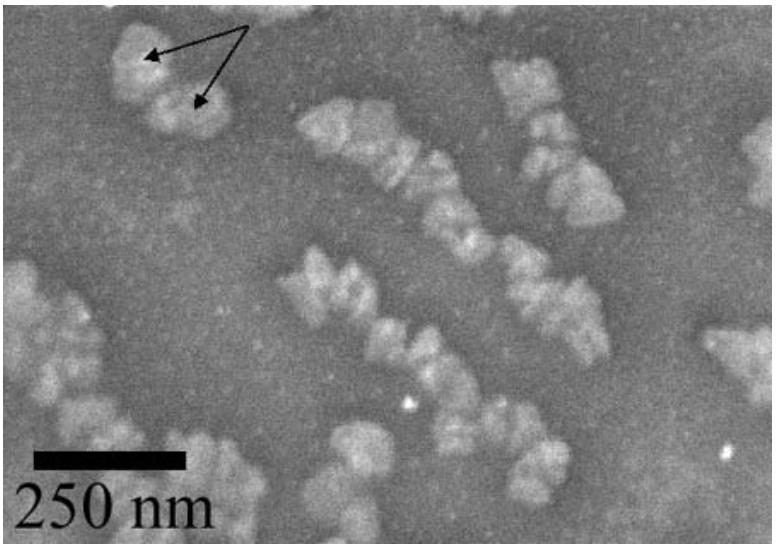

Figure 3.53 Nanoparticle chain locations in the surface plane after 50 additional laser pulses. Clearly, nanoparticle chain motion has taken place by comparing this image and the image shown in figure 3.50.

Images 3.52 and 3.53 were overlapped to reconcile clearly the relative motion amongst nanoparticle chains on the surface after 50 laser pulses (figure 3.54). The two large, elliptical agglomerates, indicated by arrows in the figures 3.52 and 3.53, were chosen as the reference point to track the relative motion of the nanoparticle chains. An arrow in figure 3.54 also indicates this agglomerate's position. The nanoparticle chains that appear white in the image in figure 3.54 are their positions after 225 pulses and the new positions of the chains after 50 pulses are shown in black. The scale bar has been left out of the image on purpose so that the image space is not cluttered (refer to figures 3.52 or 3.53 to determine the scale of the features in the image). Small vectors in the image indicate the magnitude and direction of motion of the ends of nanoparticle chains after 50 laser pulses. Both translation and rotational motions are evident in the figure. For example, a cluster of three nanoparticles has translated 130 nm on the surface after 50 pulses and the entire cluster has rotated ~ 30^{o} CCW also. The maximum translation measured in the image was 250 nm. Moreover, relative to the arbitrary pivot point chosen, the collective motion on the surface had no preferred direction but rather appeared, for the most part, random. However, the nanoparticle chains did appear to remain aligned!

3.4.6 **The Surface Topography of the Aligned Nanoparticle Chains**

Atomic force microscopy (AFM) was utilized to determine the characteristics of the surface topography for the nanoscale – aligned rows of nanoparticles. Figure 3.55 shows an AFM image of the nanoparticle arrays with the surface normal of the substrate parallel to the normal vector of the page the image is printed on. The arrays are spaced exactly 248 nm apart in the surface layer. Moreover, each line of nanoparticles consists of

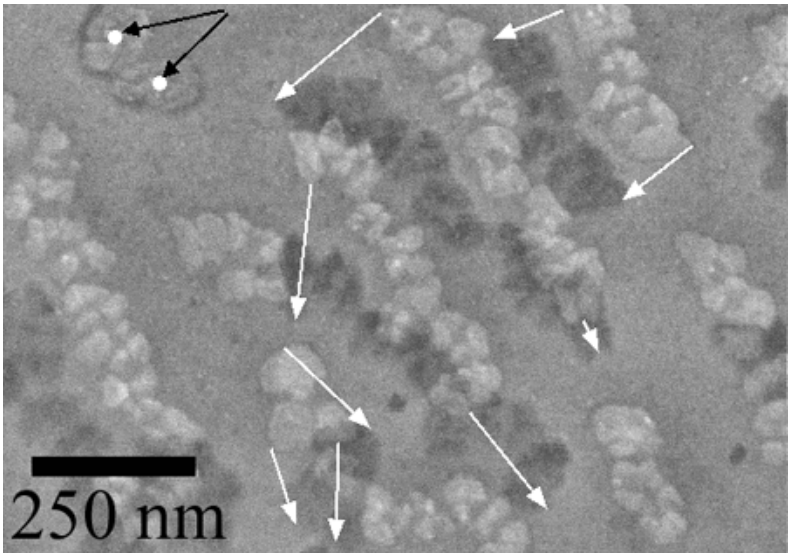

Figure 3.54 A superposition of images taken after 225 laser pulses and 275 laser pulses with the images overlapped such that the two nanoparticles in the upper left portion of the images exactly overlap. Nanoparticle chain positions after 225 pulses are shown as white chains and positions after 275 pulses are shown as black. A maximum chain translation of 250 nm was measured after 50 laser pulses.

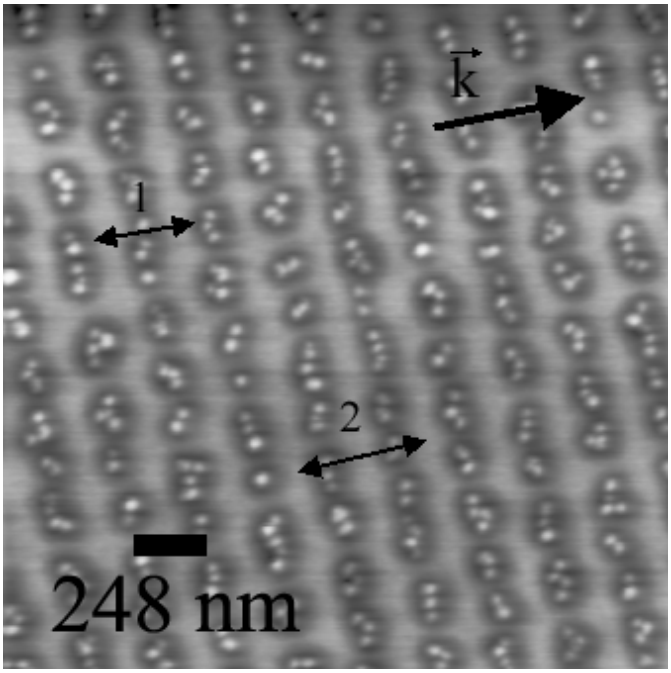

Figure 3.55 An AFM image of aligned Si nanoparticle chains is shown in the above for nanoparticles produced with 200 laser pulses in 500 mTorr UHP He (E_d = 1 J/cm^2). The wave vector of the periodic arrangement of nanoparticles is shown superimposed over the image with emphasis on the direction, the magnitude, or length, of the wave vector is not correct.

zones of clusters of nanoparticles. The wave vector of the nanoparticle lines is indicated in the figure however only the direction of this vector has meaning, the length of the vector in this image is arbitrary.

The z – axis of the image is along this surface normal and the resolution of the instrument in this direction is sub – angstrom. However, the lateral resolution is poor below roughly 50 nm. Hence, very accurate information on the *height* of the nanoparticles and the underlying surface can be extracted from these images. Figure 3.56 shows a plot of surface topography in the x – y plane of the image along the line (1) superimposed on the image in figure 3.55. The cross – section splits a particle in half exactly through its diameter and shows the shape of the surface in the regions between nanoparticles, along the wave vector of the nanoparticle lines.

The height of the nanoparticle in figure 3.56 is 2.907 nm and the nanoparticle lies in a *depression* in the surface. The nanoparticle is sandwiched between two undulations which are 2.245 nm and 1.843 nm high, respectively moving from left – to – right in the cross – section. This surface profile is representative of the topography present over the entire surface region. Obtaining multiple AFM images of the sort shown in figure 3.55 and analyzing the nature and characteristics of the surface layer in all these images was conducted in order to sample a statistically significant and thorough number of surface sites

It was found that the nanoparticles are located in depressions in the Si surface layer that lie on the order of 2 nm below the maximum z value of the surface. Moreover, the surface lying beneath the nanoparticles is roughly a sine wave with a wave vector lying in

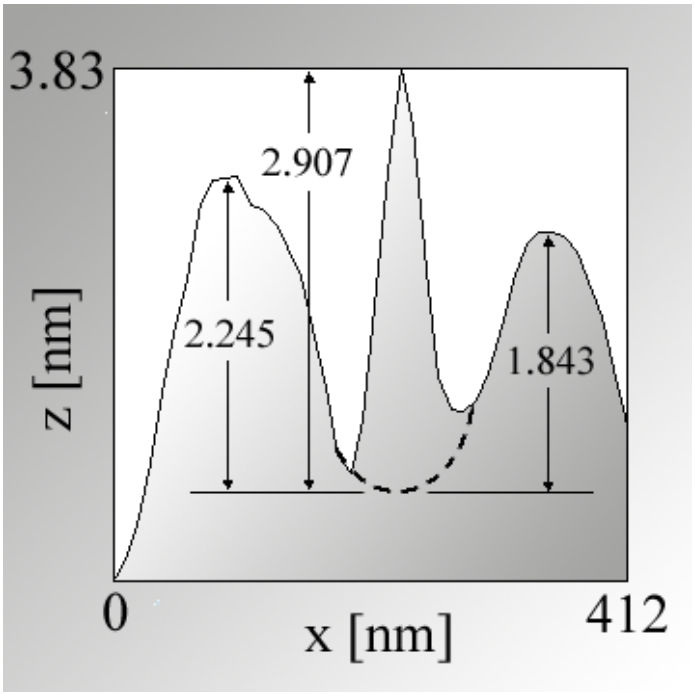

Figure 3.56 A cross – section of the surface topography in the region of nanoparticle alignment along the line indicated in figure 3.53. The cross – section is parallel to the direction of the surface structure wave vector. The nanoparticle shown rests in a trench in the surface plane and protrudes above the maximum height of the adjacent surface topography. The nanoparticle appears as a spike, rather than as a circle, in cross – section because the z – axis has been expanded x100.

the same direction as the nanoparticle lines. For example, figure 3.57 shows that the fit, Z, of a sine wave, where

$$Z = \frac{z_{\max} - z_{\min}}{2} \sin\left(\frac{2\pi x}{248nm} + \phi \right) + \frac{z_{\max} - z_{\min}}{2} \qquad 3.4$$

and x is the distance along line 2 in figure 3.55 and z_{max} and z_{min} are the maximum and minimum points of height over the line 2, respectively, closely describes the actual surface topography (extracted from an actual AFM image) also shown in figure 3.57 as the dotted line.

Si nanoparticles grow in diameter as a function of the number of laser pulses. Si nanoparticles have diameters of roughly twice the underlying LIPSS amplitude after 200 laser pulses in 100 Torr He (E_d = 1 J/cm^2, figure 3.58). The nanoparticles have diameters of ~ 4 to 6 times the amplitude of the LIPSS waves after 200 additional laser pulses (figure 3.59).

The clustering of the Si film as a function of energy density is shown clearly in the combinatorial image provided in figure 3.60. The image superposition consists of a collection of SEM images taken such that neighboring images overlap to produce an image showing a substantial portion of the surface where nanoparticle coalescence took place, namely 5 μm of surface. The superposition was taken over a region of the surface where an energy density gradient existed. The energy density in the region shown in the top – most portion of the left image was ~ 0.6 J/cm^2 and the energy density increased down the image continuing from the right – most image, down, until the maximum was reached of ~ 0.8 – 1 J/cm^2. These energy densities were estimated based on the evolved state of the film after a the number of laser pulses compared with the same surface topography produced on an independent sample of an equal number of laser pulses at various energy densities.

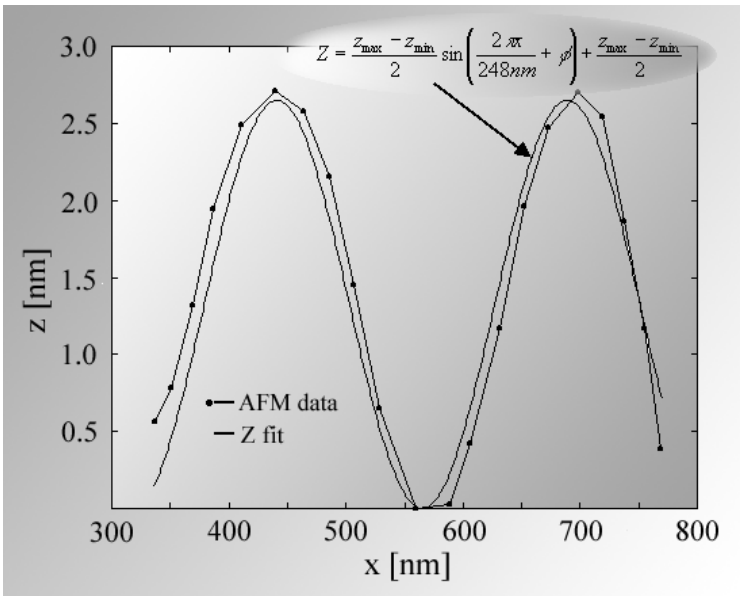

Figure 3.57 The Si surface beneath the nanoparticles has a cross – sectional spatial profile of the "sine" type as indicated in the figure above. The actual surface cross – section (shown as circular data points and derived from the AFM image in figure 3.53) is modeled closely by a sine wave of the mathematical equation superimposed in the figure.

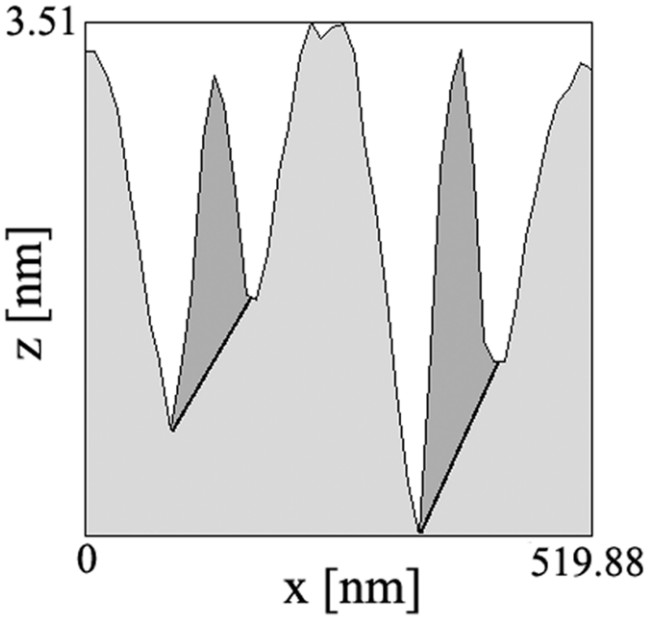

Figure 3.58 Cross – section of an AFM image showing nanoparticles (darker shade of grey) located in the LIPSS troughs. E_d = 1.1 J/cm^2, P_T = 100 Torr UHP He, 200 pulses. The LIPSS and LINO were generated with a laser incidence angle of $\theta = 0^o$.

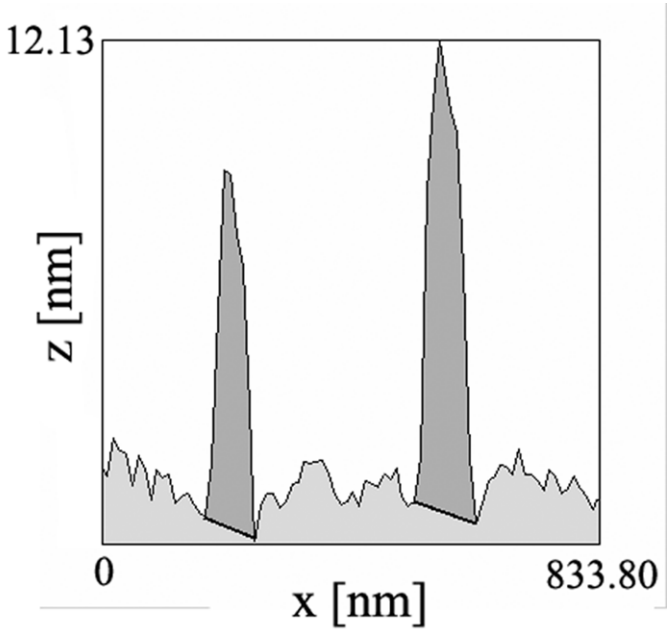

Figure 3.59 Cross – section of an AFM image showing nanoparticles (darker shade of grey) located in the LIPSS troughs. Following 200 additional pulses (refer to figure 4.21) the nanoparticles have grown in diameter such that they now protrude above the initial surface. E_d = 1.1 J/cm^2, P_T = 100 Torr UHP He, 400 pulses. The LIPSS and LINO were generated with a laser incidence angle of $\theta = 13.5^o$.

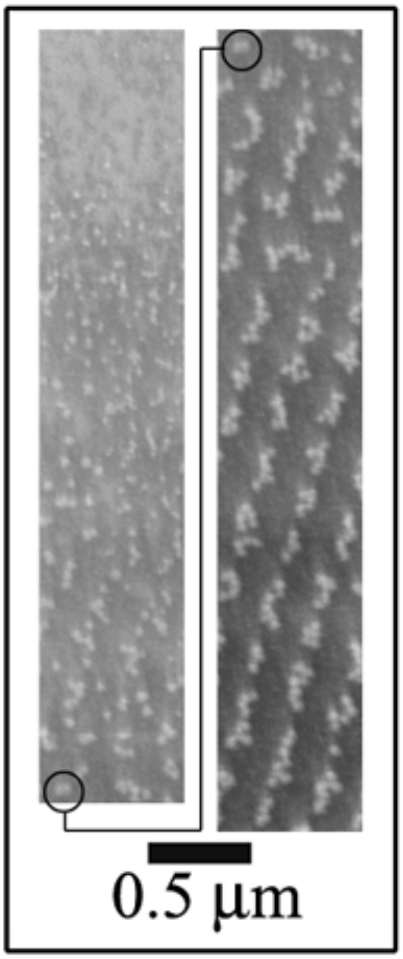

Figure 3.60 A combination of several SEM images showing the evolution of film clustering as a function of laser energy density. The gradient in fluence increases from a value ~ < 0.6 J/cm^2 in the top – left corner, and continuously increasing, down to the bottom right image where the fluence is roughly 1 J/cm^2 or thereabouts.

Moreover, the same gradient in film formation is produced as a function of the number of laser pulses. For example, region 1 in the figure is produced with the equivalent of 30 pulses , region 2, 50 – 100 laser pulses, and regions 3 & 4 after > 100 laser pulses, at a constant $E_d = 0.8$ J/cm^2. This correlation has been verified experimentally from independent samples prepared under these conditions and thus interpreting the images in figure 4.18 as a number of pulses gradient is valid based on this correlation. Moreover, it has been well established in the results portion of this work that nanoparticle clustering and nanoparticle chain motion has been directly observed, from pulse – to – pulse (figures 3.39, 3.48 – 3.52)

AFM force microscope images taken over the same region shown in figure 3.60 indicated that the LIPSS structures were detected starting at region 3 and continuing to region 4. Reiterating the point made consistently throughout this work, LIPSS and nanoparticle self – organization occur simultaneously and must be synchronized. Self – organization does not occur without LIPSS. The total self – organization process occurs as described in the following summary;

The average number of nanoparticles per cluster was determined for the surface topography shown in figure 3.55 and the data points fit nicely to a statistical Gaussian distribution of the form of equation 3.1. Figure 3.61 shows a plot of the number of nanoparticles per cluster vs. the total number of such clusters. The data was collected from several AFM images in order to derive and accurate number for the average number of nanoparticles per cluster. The Gaussian fit of the data points indicates the mean number of nanoparticles per cluster to be 2.5 for nanoparticle arrays produced with 200 pulses in 500

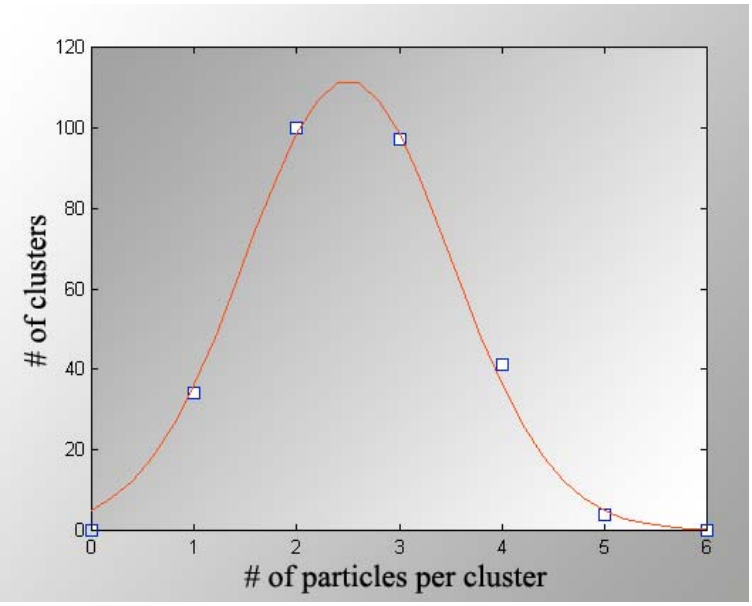

Figure 3.61 A plot of the # of clusters as a function of the number of particles per cluster derived from several sampled AFM images. The nanoparticle zones were produced with 200 laser pulses in 500 mTorr UHP He (E_d = 1 J/cm^2). The experimental data fits a Gaussian distribution providing a mean number of particles per cluster of 2.5 nm and a FWHM of ~2.5 nm.

mTorr Ar (E_d = 1 J/cm^2. The FWHM of the distribution was also 2.5, a number that indicates the deviation of the number of nanoparticles per cluster from the mean value.

In order to deduce the affect of total inert gas pressure on nanoparticle nucleation, growth, and clustering, the pressure of the inert ambient over the substrate surface during nanoparticle formation and clustering was varied over three orders of magnitude. Figure 3.62 shows the data generated at 500 mTorr, 10 Torr and 100 Torr total pressure of UHP He during similar and independent laser treatment cycles. The samples were prepared with 200 laser pulses in UHP He with 1 J/cm^2 delivered to the substrate surface per pulse.

The mean number of nanoparticles per cluster increases as the inert total pressure of gas increases. At 10 Torr UHP He the mean number of particles per cluster increases by ~ 2 times relative to the mean number at 500 mTorr UHP He. Hence, a 20 – fold increase in total He pressure increases the mean number of nanoparticles per cluster 2 – fold. Moreover, a further 10 – fold increase in total pressure to 100 Torr UHP He yields a 3.6 – fold increase in the number of nanoparticles per cluster.

Control over the deviation of the number of nanoparticles per cluster from the mean decreases as the pressure of the inert ambient increases. For example, the FWHM increases with gas pressure from 2.5 to ~ 4 to 6.8 nanoparticles per cluster for 500 mTorr, 10 Torr and 100 Torr UHP He, respectively. Thus, in order to tightly define the number of nanoparticles per cluster the total pressure of inert gas in the system should be kept low, i.e., roughly in the pressure range of 10^2 mTorr. *Si nanoparticle formation has not been observed for pressures below 250 mTorr UHP He*.

Key to the utilization of nanoparticles as semiconductor device elements, and light or electron emitters is the ability to control the mean nanoparticle diameter and the

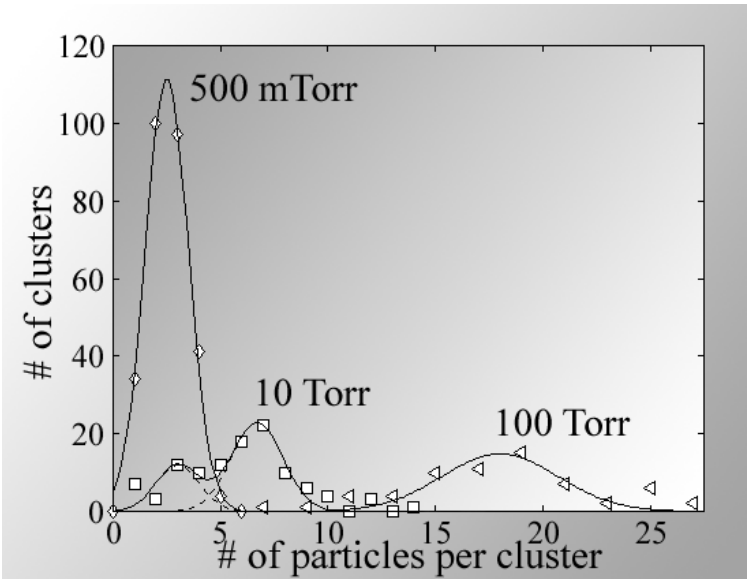

Figure 3.62 The mean number of nanoparticles per cluster increases as a function of inert gas pressure. For 500 mTorr (mean = 2.5 nm, FWHM = 2.5 nm), 10 Torr (mean = 6.7, FWHM = 3), and for 100 Torr (mean = 18, FWHM = 6.8). [E_d = 1 J/cm^2 and 200 laser pulses]

deviation of nanoparticle diameter from the mean. For example, returning to figure 1.13, if one wanted a green color emitting Si nanoparticle, the mean diameter would need to be centered around 2.3 nm corresponding to a photon energy of 2.4 eV (based on the quantum confinement theory of light emission from semiconductor nanoparticles). A blue light emitting (2.9 eV per photon) Si nanoparticle would require a mean nanoparticle diameter centered around ~ 1.8 nm. Thus, a FWHM of roughly < 2.3 nm – 1.8 nm, or 0.5 nm is required in order to have a purely "green" or "blue" light emitting region preventing the overlap into adjacent primary colors in the electromagnetic spectrum. As yet a FWHM less than this value has not been experimentally achieved.

Figure 3.63 shows the number of Si nanoparticles per nanoparticle diameter range (range, $\Delta d = 0.2$ nm) from d = 1 to 5 nm. The Si nanoparticles were prepared and collected under irradiation in 500 mTorr UHP He with 200 laser pulses ($E_d = 1$ J/cm^2). . The distribution of nanoparticle diameter for the laser driven process, over all laser generated particle diameters, falls in a range from d < 1 nm to 5 nm and is properly described by the Gaussian fit of mean diameter 2.9 nm and FWHM of 2 nm. This FWHM represents at least the best FWHM of all the Si nanoparticle formation methods reported in the literature to generate narrow size distributions in diameter.

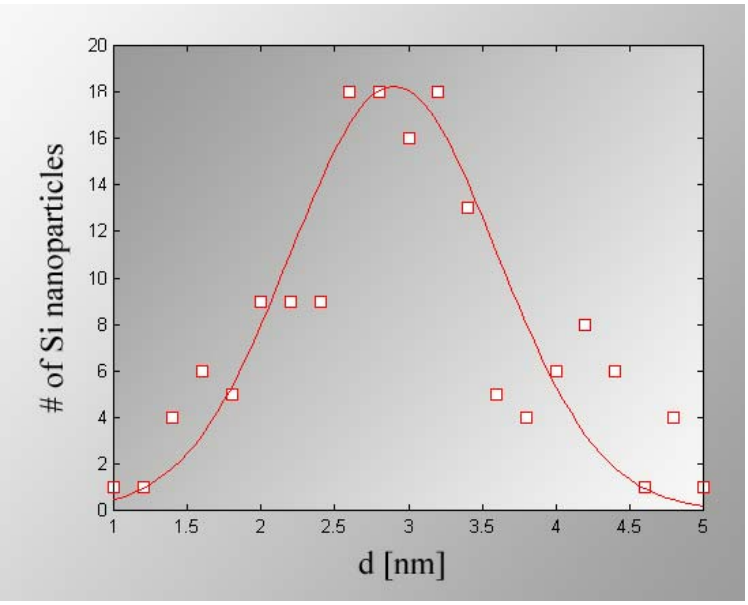

Figure 3.63 A nanoparticle diameter distribution for self – assembled nanoparticle arrays produced in 500 mTorr UHP He with 200 pulses and a per pulse fluence of 1 J/cm^2. The experimental data is shown in the figure as square points and the Gaussian fit as a solid, continuous line. The dashed lines indicate the positions of Gaussian curves used to erect the master, solid curve; mean diameter = 2.9 nm and FWHM = 2 nm.

3.4.7 Energy Density Effects on Si nanoparticles

Si nanoparticles were observed to melt at laser fluence > 1.3 J/cm^2. Figure 3.64 shows an image of a Si substrate surface irradiated in 10 Torr He with 1000 laser pulses (E_d = 1.3 J/cm^2). Arrows indicate in the figure regions where Si nanoparticles have been melted. The melted nanoparticles appear smeared out with little image contrast due to the smoothness of the melted surface. Moreover, they have flattened due to the lower value of surface tension for the liquid Si, relative to the solid phase. Hence, the nanoparticle remnants spread out over the surface and in some places connect to the liquid from other nanoparticle remnants. This gives these regions of melted nanoparticles an obscure, web – like appearance. Some nanoparticles on the surface (figure 3.64) have not melted because the sample was irradiated at the nanoparticle melting energy density (E_d = 1.3 J/cm^2) threshold and hence, some regions of the surface receive a fluence below the threshold value. Nanoparticles that form in these low fluence regions are stable and do not melt.

Figure 3.65 shows images of three Si surfaces prepared with 1000 laser pulses of 0.5, 0.8, and 1.3 J/cm^2 in 10 Torr UHP He. The decrease in nanoparticle diameter as a function of increasing the laser fluence is evident from the figure. Although quantitative measurements of the maximum nanoparticle diameter for each sample was not generated, it is clearly evident that the maximum is roughly 100 nm at 0.5 J/cm^2 and decreases below 20 nm for irradiation at 1.3 J/cm^2.

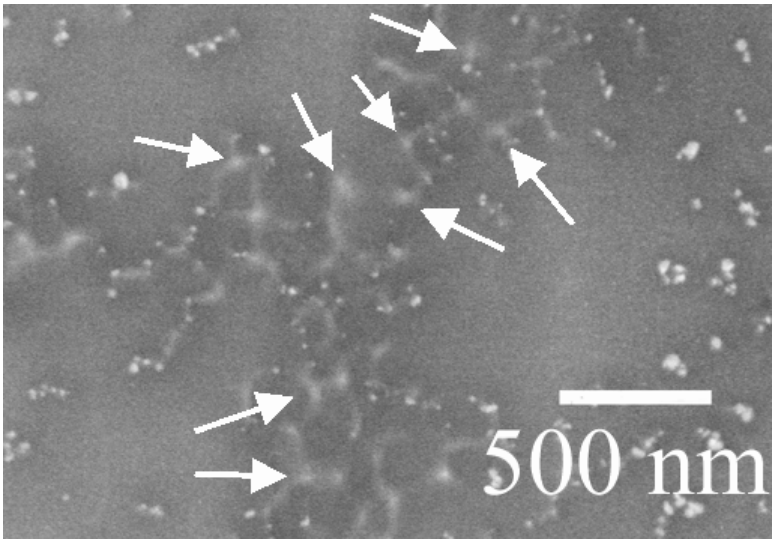

Figure 3.64 The arrows indicate regions where Si nanoparticles have been melted by the last laser pulse of E_d = 1.3 J/cm^2. This fluence is the upper threshold for stable Si nanoparticle formation; at fluences greater than this value only a thin, continuous liquid film of Si is produced on the surface during each laser pulse.

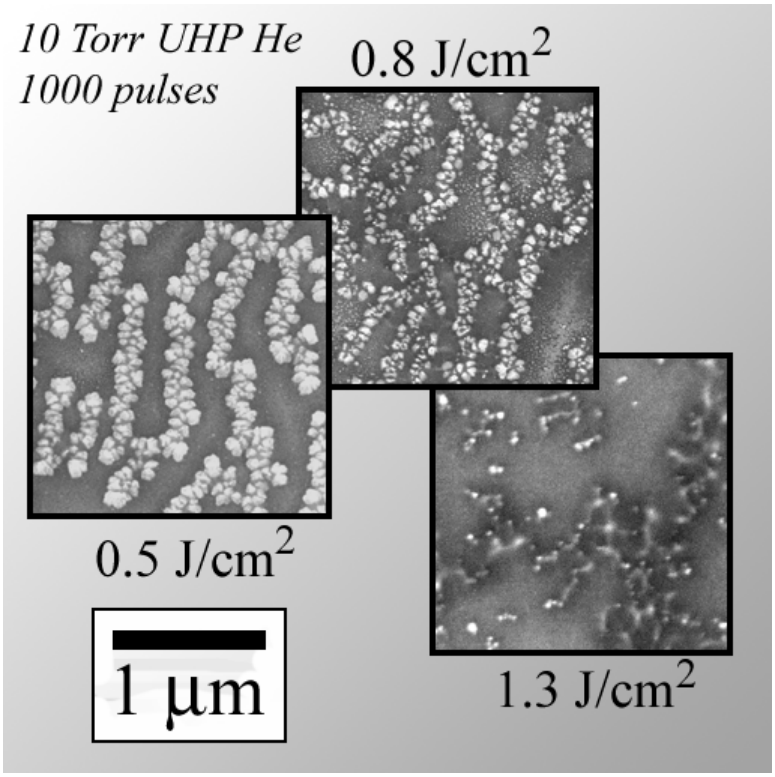

Figure 3.65 Numerical simulations, based on Maxwell's equations, that provide the local fluence a nanoparticle receives based on the average fluence the bulk sample receives, indicates that at lower laser fluences the maximum nanoparticle size on the surface should increase. The SEM images above seem to support the calculation.

3.4.8 **Nanoparticle Spacing vs. Si Substrate Tilt Angle**

Figure 3.66 shows the inter – line spacing between nanoparticle rows for a substrate irradiated at 5^{o} tilt off normal incidence. The nanoparticle lines are spaced 248 nm apart and this spacing is consistent over the entire irradiated area of the substrate. The inter – line spacing changes substantially to 357 nm (figure 3.67) and 399 nm (figure 3.68) when the substrate is irradiated at tilt angles of 13.5^{o} and 24.5^{o}, off normal incidence, respectively.

The behavior of inter – line spacing as a function of substrate tilt fits closely the relationship;

$$\Lambda = \frac{\lambda}{1 - \sin\theta} \qquad 3.5$$

as shown in figure 3.69, where Λ is the periodic grating spacing in the surface layer, λ is the laser beam wavelength, and θ is the incidence angle of the laser light with respect to the substrate surface normal. All three analytical relationships displayed as solid, curving lines in figure 3.69 describe the grating spacing induced by the laser interaction of the incident laser beam with a surface scattered component of the same beam. P – polarized light is theoretically predicted to induce grating structures of the type;

$$\Lambda = \frac{\lambda}{1 \pm \sin\theta} \qquad 3.6$$

whilest s – polarized light should induce gratings of the cos θ type.

The experimental data points generated by the author, and indicated in figure 3.69, all fit only the $\lambda/1 - \sin\theta$ grating spacing expression. 30 to 40 additional data points were generated by the author at various incidence angles between 0 and 40^{o} and all the points fell exclusively along the $\lambda/1 - \sin\theta$ expression (some points shown in figure 3.69). In

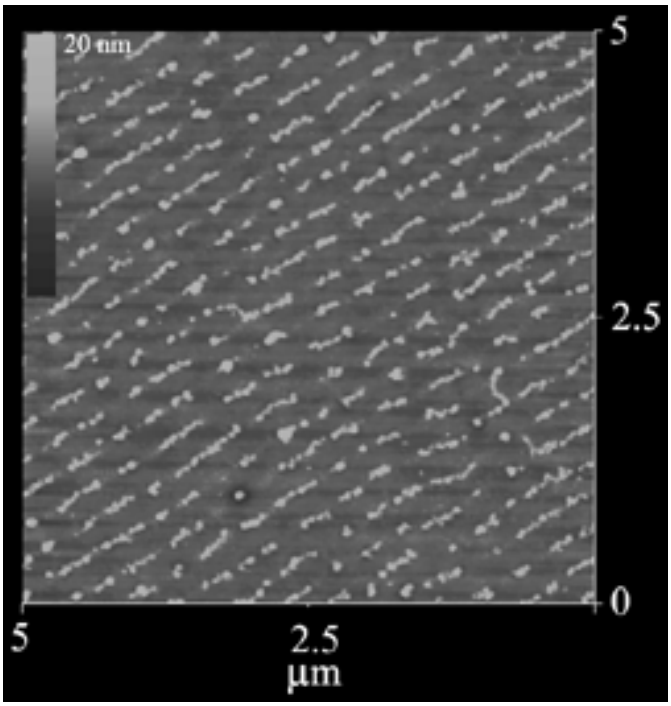

Figure 3.66 AFM image of self – organized arrays of Si nanoparticles produced by irradiation at 5^{o} tilt off normal incidence (E_d = 1 J/cm^2, 400 pulses, P_T = 100 Torr UHP He). The nanoparticle lines are spaced 248 nm apart.

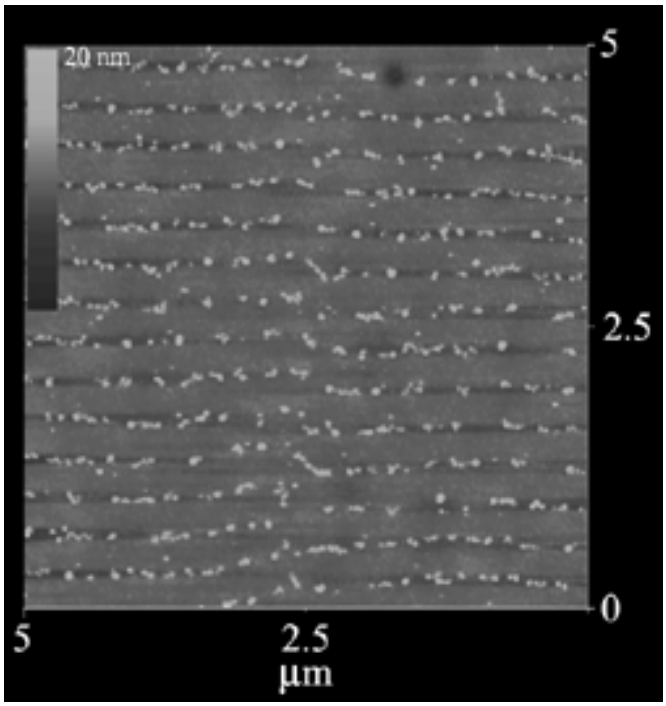

Figure 3.67 Self – organized arrays spaced 357 nm apart. The substrate was irradiated at 13.5^{o} off normal incidence (E_d = 1 J/cm^2, 400 pulses, P_T = 100 Torr UHP He).

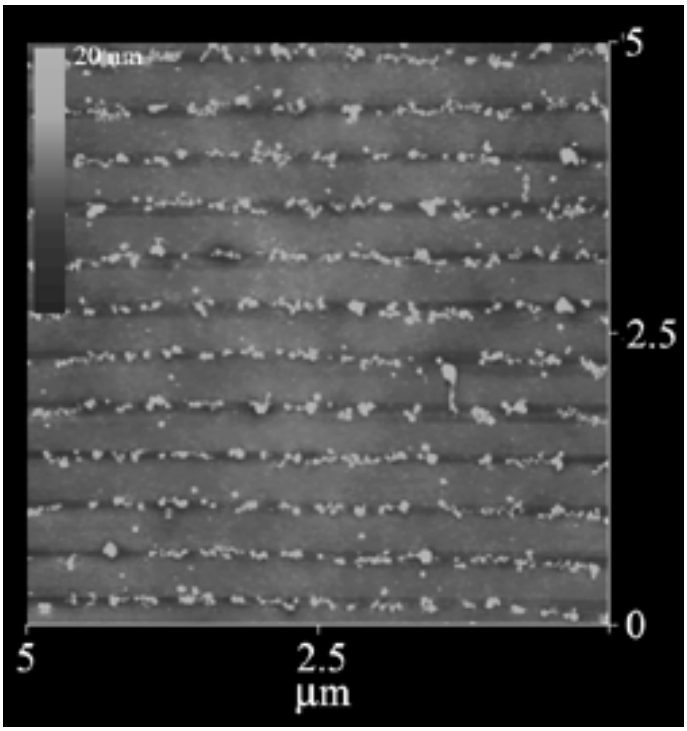

Figure 3.68 Self – organized arrays spaced 399 nm apart. The substrate was irradiated at 24.5^{o} tilt off normal incidence (E_d = 1 J/cm^2, 400 pulses, P_T = 100 Torr UHP He).

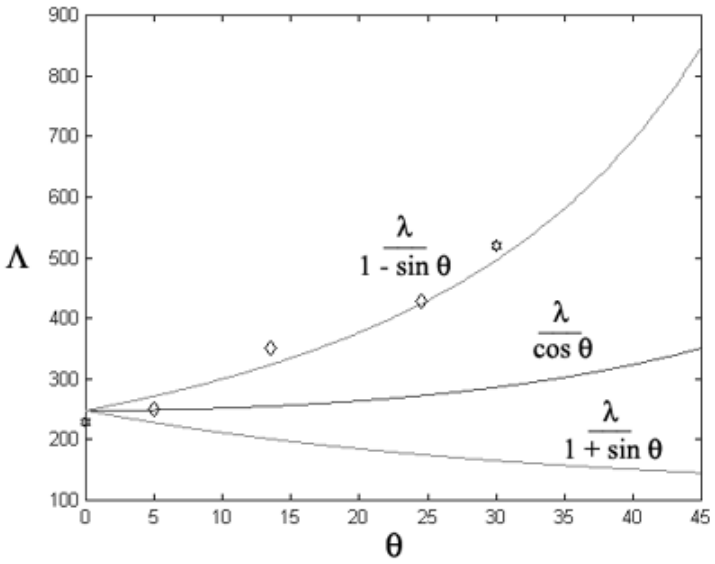

Figure 3.69 The spacing of nanoparticle arrays, as well as laser – induced periodic surface structures (LIPSS), obey the mathematical relationship $\Lambda = \lambda/1\text{-}\sin\theta$ as shown above where Λ is the LIPSS period, or nanoparticle array period, λ is the incident pulsed laser beam wavelength, and θ is the incidence angle of the beam with respect to the substrate surface normal. Experimental data points are superimposed on the figure and follow closely this indicated relationship.

addition, the wavevector of the nanoparticle line arrays were found to always lie parallel to the p – polarized component of un – polarized or p – polarized laser beam. In an un – polarized laser beam, all the light waves comprising the output beam consist of every possible electric field vector orientation in the plane orthogonal to the beam propagation direction. Each electric field vector can be broken into p – and s – components.

Figure 3.70 shows a schematic diagram of a laser beam propagating in the x – direction toward a substrate tilted at angle θ with respect to the z – axis. This is exactly the spatial experimental arrangement used to generate the nanoparticle lines shown in figures 3.66 – 3.68. An incident light wave, chosen at random from this beam, will have an E – field vector in the plane of constant phase, i.e., the z – y plane for this laser pulse, that can be split into components along the z – direction (s – polarized, this component sees no surface tilt) and the y – direction (p – polarized, this component sees the surface tilt θ). Again, for all experiments performed by the author,

1 Nanoparticle lines had always wave vectors that lie exactly parallel to the p – polarized electric field vector.

2 P – polarized, or un – polarized laser beam, was required to generate the periodic nanoparticle lines.

The use of an exclusively s – polarized laser beam induced no nanoparticle ordering, only randomly distributed nanoparticles in the substrate surface layer were formed.

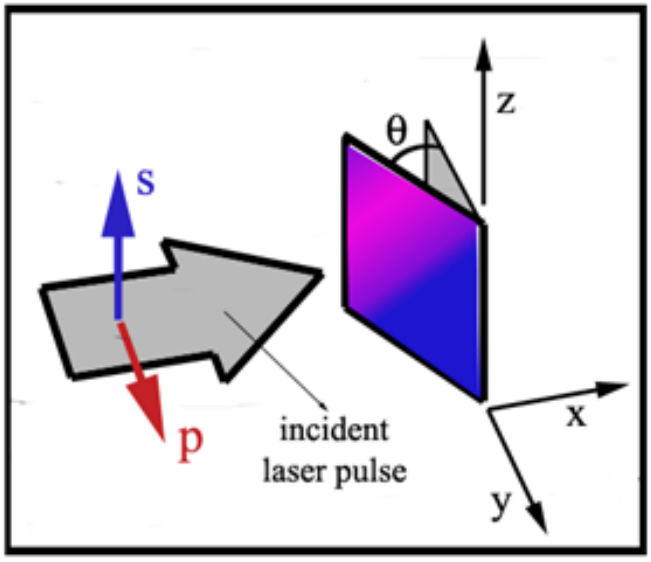

Figure 3.70 The p – polarized component of electromagnetic radiation oscillates in the plane – of – incidence with respect to the surface of interaction. The s – polarized component oscillates in a plane orthogonal to the plane – of – incidence with respect to the surface of interaction.

3.4.9 The Effect of Surface Roughness and Scattered Light on the Linear Ordering of Nanoparticles

3.4.9.1 Laser Beam Scattering by Pre – existing Micro – roughness on the Substrate Surface

The micro – roughness induces self – organization of the Si nanoparticles occurs only if the roughness protrudes above the initial substrate surface. The spatial orientation of the microcone morphology with respect to the region of self – organization is shown in figure 3.71. The top portion of figure 3.71 shows a low magnification SEM image of the edge of a region containing substantial micro – roughness, i.e., features protruding up to roughly 20 μm above the initial surface. The micro – roughness, i.e., microcones, appears as the high contrast region in the right side of the image. These features are silicon microcones and appear as sharp spikes protruding from the Si substrate, each microcone is surrounded by deep ~ 100 μm, steeply sloped microholes. *Regions a,b, and c were totally unaffected by the laser pulses to generate the micro – roughness, it is atomically flat! It is also in this region that the nucleation, growth, and linear alignment of Si nanoparticles occurs!*

Figure 3.71a – c shows the morphology produced on the Si surface when a second irradiation treatment of 200 pulses in 500 mTorr UHP He (E_d = 1 J/cm^2) was applied to the *entire* region shown in the figure. In region (a), 40 μm from the microcone morphology edge, the complete alignment of nanoparticles into discrete, 248 nm evenly spaced lines has occurred. Partial alignment is evident in region (b) located 20 μm from the microcone morphology. Most nanoparticles in figure 3.71b have yet to align into coordinated lines.

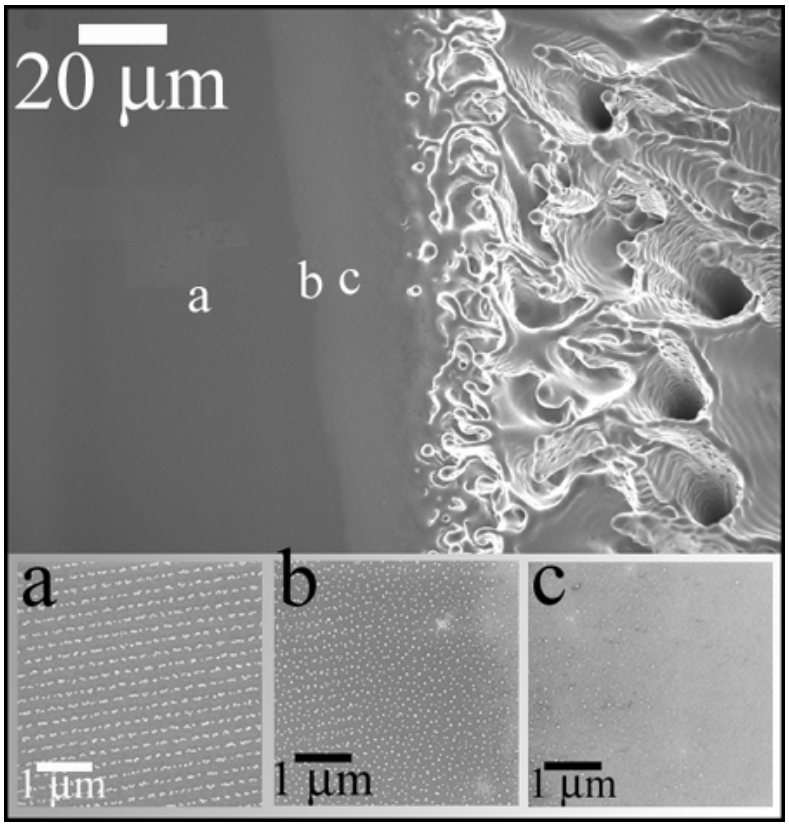

Figure 3.71 A Si microcone morphology was produced in the surface plane of a silicon substrate with 1500, E_d = 3.9 J/cm^2, in ½ atm SF_6. A second irradiation treatment of the microcones + the adjacent, flat substrate surface, with 200 pulses in 500 mTorr UHP He induces the formation of a thin Si film, the nucleation of Si nanoparticles and the eventual clustering and alignment of these nanoparticles. Shown above (top – most figure) is the irradiated region, up to 100 µm, adjacent to the microcone morphology and the stage of nanoparticle development of that specific region; a) total nanoparticle alignment (40 µm from the laser spot edge) , b) partial clustering and some film remnant (20 µm), and c) Si film.

Film clustering has taken place only sporadically in region out to 20μm from the surrounding the microcones (figure 3.71c). The substrate shown in figure 3.71 was irradiated with un – polarized laser light. The nanoparticles aligned such that the wave vector of the lines corresponds with the p – polarized component of the laser beam. The substrate was tilted at an angle of roughly 5^{o}, during irradiation.

The presence, or absence, of microcones in the irradiated region, under ~ 1 J/cm^2 laser irradiation an atmosphere of UHP He, has a drastic affect on the morphology that develops in this region. For example, a critical experiment was performed to highlight prominently the importance of the microcone morphology in triggering nanoparticle alignment. A Si substrate, 5 mm x 3 mm, containing a 2 mm x 1 mm area of microcones was prepared with the microcones located 1 mm from one edge of the substrate. A second substrate was inserted against this edge. Figure 3.72a shows a schematic illustration of the substrate containing the microcone morphology and the adjacent, un – modified Si wafer. A series of 1000 cumulative laser pulses irradiated both substrates and the microcones in 100 Torr UHP He. The complete irradiated area after the 1000 pulses is outlined by a thin, 4 mm x 3mm box in figure 3.72b.

Figure 3.73 shows a HRSEM image of the white region indicated in figure 3.72b, adjacent to the microcone morphology. Figure 3.74 shows a HRSEM image of a region on the flat substrate (figure 3.72b), irradiated only with the 1000 laser pulses in UHP He. The number of nanoparticles per cluster, the spacing between the clusters, and nanoparticle surface density are roughly the same in both of the imaged regions (figures 3.73 & 3.74). However, the nanoparticle chains located ***on the substrate*** with the microcone morphology aligned into linear arrays during the 1000 laser pulses. The nanoparticle chains on the flat

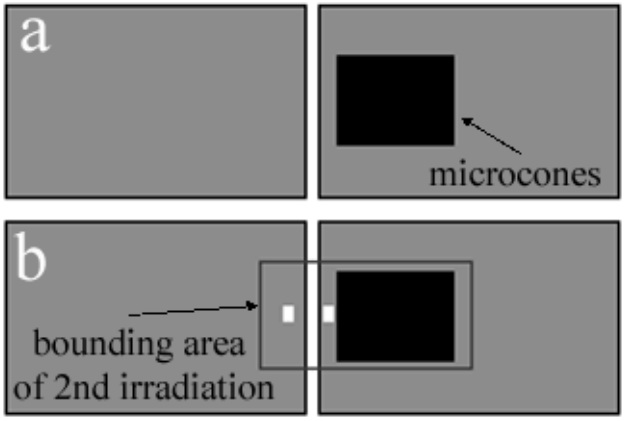

Figure 3.72 An experiment designed to discern any relationship, if any, between the nucleation of nanoparticle alignment and the presence of Si microcones in the irradiated region during nanoparticle growth. A) An atomically, smooth substrate was placed in proximity to a substrate containing Si microcones such that the substrates are mutually irradiated. B) Shown as two boxes are the regions later characterized in figure 3.66 (box lying on the substrate with microcones) and in figure 3.67 (box on initially smooth substrate) after 1000 laser pulses in 100 Torr UHP He (E_d = 1 J/cm^2). The irradiated region on the left, smooth substrate, should be independent of the microcone effect whilst the irradiated region on the microcone substrate should feel any interaction with the microcones.

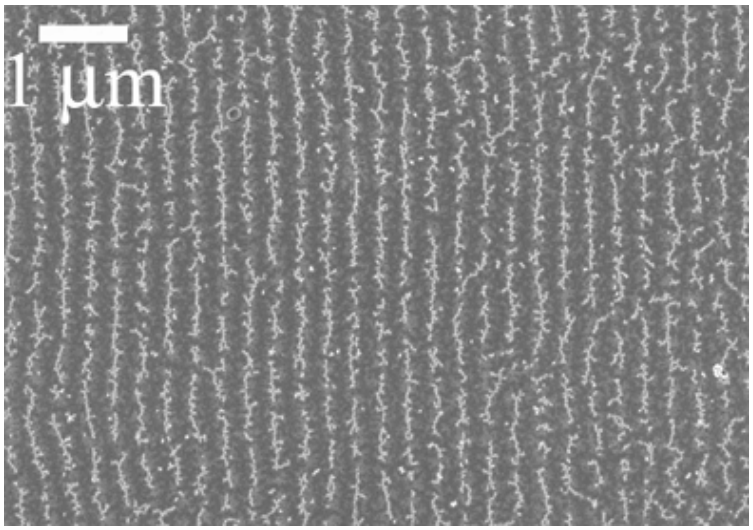

Figure 3.73 Self – organization of Si nanoparticles occurred on the substrate in figure 3.65 that had microcones present in the irradiated region.

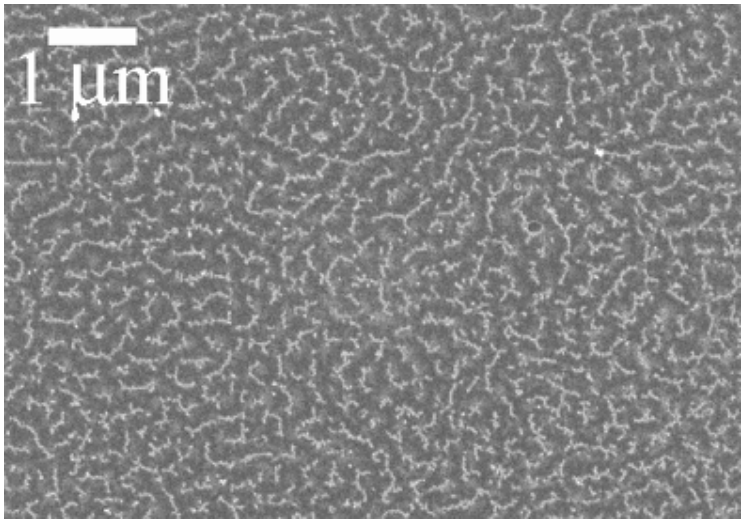

Figure 3.74 A random spatial distribution of nanoparticle chains is produced on an substrate surface with no pre – existing microcone morphology present in the irradiated region.

substrate did not self – organize but rather developed a random spatial orientation, i.e., the long axis of the nanoparticle chains have no preferred spatial orientation in the surface plane. *This experiment clearly shows that the micro surface roughness plays an important role in nanoparticle chain alignment. If it is present on the irradiated surface plane, nanoparticle alignment will occur.*

Figure 3.75 shows a dual image superposition that clearly shows the orientation relationship between the p – polarized light component of the incident laser pulse and the wave vector direction of the nanoparticle lines. A low magnification image of a microcone laser spot has been superimposed with a high magnification image of nanoparticles. The images were taken in the exact same orientation in the HRSEM so the spatial relationship of features in the images can be correlated in the plane of the page. The p – polarized light vector has been superimposed on the image as well.

Clearly, the wave vector of the nanoparticle lines aligns with the p – polarized component of the incident laser beam that generated them (figure 3.75). This same experiment was performed several times except that the wire were rotated in space with respect to the p – polarized component of the incident laser beam. This had no affect on the orientation of the nanoparticle lines. They still aligned parallel with the p – polarized E – field component.

The microcones themselves, spaced on the order of 20 μm apart, have a random spatial distribution in the surface plane for all experiments previously described in this work. A lithography technique was used to template the microcones in a microscopic, square array to determine if microcone ordering would affect nanoparticle ordering in adjacent irradiated regions. An example of patterned microcones structures is shown in

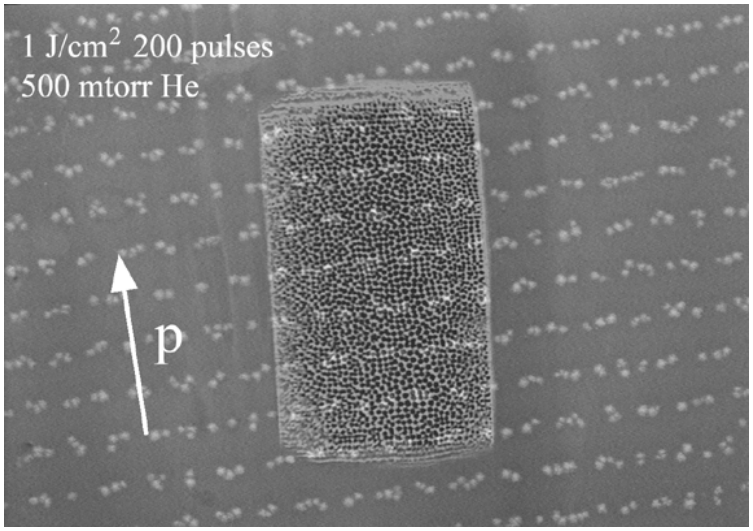

Figure 3.75 The spatial orientation of Si nanoparticle arrays is determined by the orientation of the p – polarized component of the incident, coherent electromagnetic radiation. The wave vector of the nanoparticle arrays aligns in the surface plane along the projection of the p – polarized light component. However, alignment is triggered, i.e., nucleated, by the presence of Si microcones in the surface region irradiated by the laser beam.

figure 3.76. It was found that nanoparticle alignment was unaffected by the patterned template if nanoparticles were induced to align using these structures.

3.4.9.2 Laser Beam Scattering by Obstacles in the Laser Beam Delivery Path to the Substrate

Laser – induced nanoparticle alignment is also induced on the Si surface when an opaque obstacle is placed in the path of the beam in transit to the substrate. An image of the opaque obstacle is imprinted into the film lying in the surface layer. Areas in the laser spot that were obstructed from receiving irradiation, due to the opaque obstacle, had a thin continuous film of Si there. Nanoparticle nucleation, growth, and clustering took place on the areas of the substrate that received laser irradiation. However, nanoparticle alignment occurred only in regions adjacent to the Si film, from the very edge of the film out to roughly 20 μm from the surface.

A laser light intensity modulation of the Fraunhofer – type is received on the surface with each laser pulse when an opaque obstacle obstructs the incident laser beam's path. Nanoparticle alignment into linear arrays occurs in the region adjacent to the central portion of the imaged pattern on the surface, i.e., adjacent to the film on the surface that has the shape of the object lying in the beam's path.

Figure 3.77 shows a SEM image of a Si surface following irradiation with 400 pulses by a laser beam that was obstructed in transit to the surface by two parallel wires. The right portion of the laser – induced damage is shown in the image and the two white lines running horizontal across the image with widths ~ 50 μm represent Si film lying directly behind the image of the obstruction wires. The white lines in the image listed n =

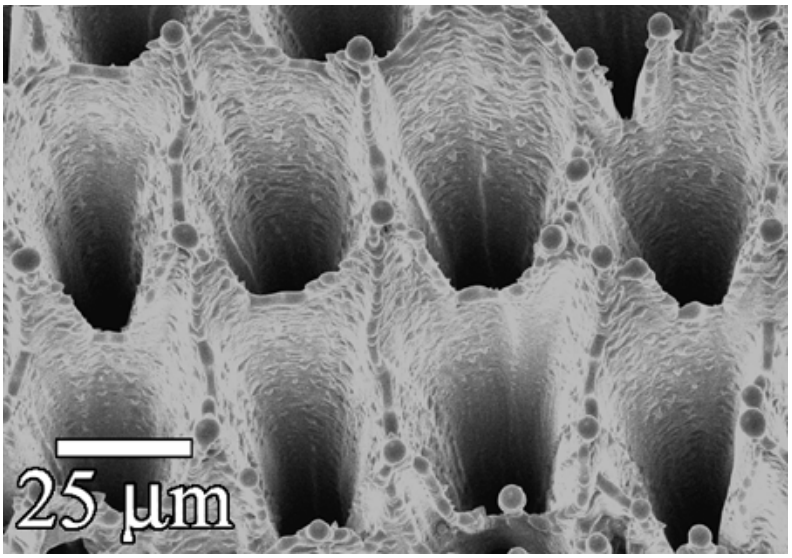

Figure 3.76 Patterned Si microcones have no affect on the alignment of Si nanoparticles in the mutually irradiated, flat Si regions in the immediate vicinity of the microcones. The Si microcones in the image above were induced to align by inserting an alignment – triggering mask in the path of the beam in route to illuminating the substrate with 2000 laser pulses in ½ atm SF_6 (E_d = 3 J/cm^2).

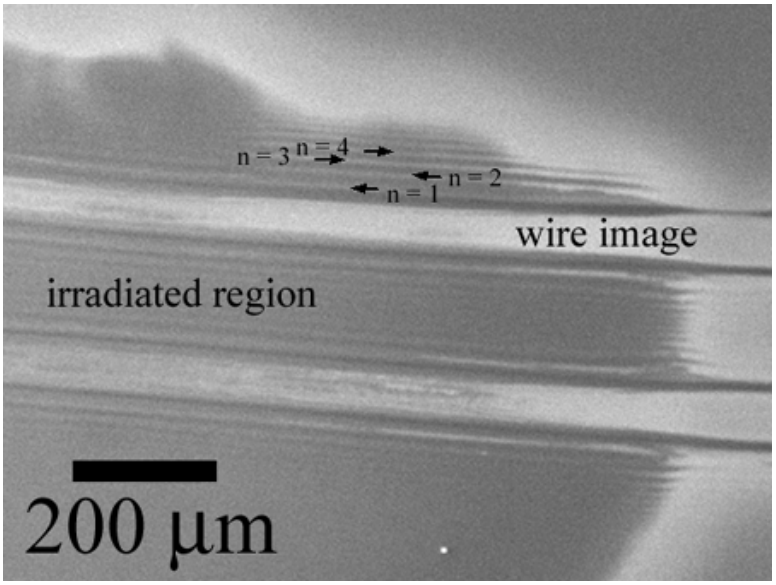

Figure 3.77 Wires placed in the path of the laser beam under irradiation conditions to induce the formation of nanoparticles produces a Fraunhofer diffraction pattern in the surface film, high intensity regions in the surface plane remove film by "re – ablation" and melting whilst film is left to cluster in the low intensity regions of the pattern; the diffraction pattern is an image of the wires in the beam path. Shown in the image above and labeled are the diffracted orders of the Fraunhofer pattern (E_d = 0.65 J/cm^2, P_T = 100 Torr He, and 400 laser pulses).

1, n = 2, etc., are first and second diffracted orders where the intensity was low and in these regions the film was only formed yet did not move and cluster! Nanoparticle alignment occurs at the region indicated in figure 3.77 by the tip of the arrow, in the region between the main strip of film and the first order, n = 1.

A higher magnification image, adjacent to the main stripe of Si film, shows the exact region where nanoparticle alignment takes place (figure 3.78). The nanoparticle aligned only in the region between the main stripe and the first diffracted order of low intensity. The stripe of aligned nanoparticles is thin, 5 μm, and the distance of this strip from the center of the imprinted Fraunhofer pattern is 12.9 μm. The image was taken after the substrate received 400 pulses in 100 Torr UHP He with an energy density of 0.65 J/cm^2.

It was found that the spatial orientation of the nanoparticle alignment has no relationship to the Fraunhofer intensity distribution. For example, in figure 3.78, the wave vector of the nanoparticle arrays lie at angle nearly orthogonal to the intensity modulation of the Fraunhofer pattern. Experiments were performed where the spatial orientation of the wires with respect to the p – polarized direction of the un – polarized beam was rotated from 0 to 90 degrees. In all cases, the wave vector of the nanoparticle arrays aligned with the direction of the p – polarized vector. These experiments indicate that the spatial orientation of the nanoparticle arrays is unaffected by the Fraunhofer intensity modulation. *Moreover, Si surfaces irradiated with laser beams under the same experimental conditions, but with the obstructing obstacle to the beam removed, the nanoparticles formed and clustered. However, the nanoparticles did not align into self – organized arrays in the surface plane!*

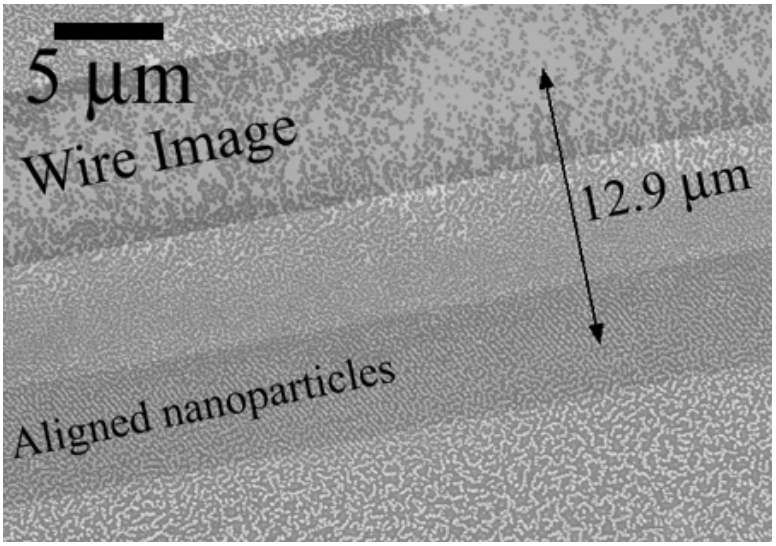

Figure 3.78 The alignment of Si nanoparticles into linear arrays occurs in regions adjacent to the main wire image of the Fraunhofer diffraction pattern.

3.5 LINO Summary

Irradiating a flat, atomically smooth Si substrate with a fluence in the range of $0.6 < E_d < 1.3$ J/cm^2, $P_{UHP\ He} > 250$ mTorr, with up to 100 – 200 laser pulses generates a thin, ~ 1 nm film of Si of the surface. With additional laser pulses, the film will begin to cluster into nanoparticles 5 – 20 nm in diameter. Moreover, the nanoparticles themselves will begin to cluster into linear chains and these chains have a random spatial orientation in the surface plane relative to one another. The motion of species on the surface saturates after roughly 400 laser pulses, little motion occurs at greater numbers of pulses. Also, the above process occurs for un – polarized light, s – polarized and p – polarized light. If a roughness is introduced in the surface plane, i.e., Si microcones, or obstructing wires in the beam path, the nanoparticles in the surface plane will self – organize into periodically spaced lines if the laser beam contains a portion of p – polarized light.

3.6 Laser – Induced Periodic Surface Structures

The self – organization mechanism of Si nanoparticles is intimately related to the formation of laser – induced periodic surface structures (LIPSS) in the Si surface layer directly beneath the nanoparticles. For example, self – organized nanoparticle lines *always* lie atop the ripple topography; no LIPSS are present in areas of the surface plane where only Si film is present or in regions where the spatial distribution of nanoparticles is random in the surface. However, the LIPSS can be generated independently on atomically flat Si surfaces on regions of the surface containing no film or nanoparticles.

A periodic grating of a discrete spatial frequency is formed on the surface of c – Si in response to 248 nm pulsed laser irradiation. Figure 3.79 shows an atomic force

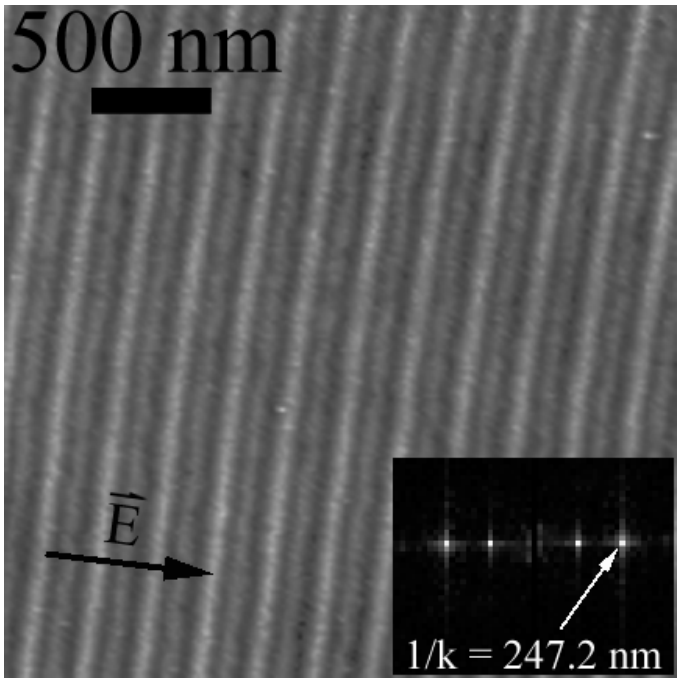

Figure 3.79 LIPSS generated at normal incidence on the surface of laser irradiated Si with 400 laser pulses of 0.8 J/cm^2 per pulse (p – polarized). The vector superimposed in the figure indicates the orientation of the p – polarized light with respect to the grating, i.e., they are parallel. The fast Fourier transform also provided in the figure gives a ripple spacing of 247.2 nm averaged over the AFM images shown above.

microscope (AFM) image of a grating surface structure (LIPSS) in Si formed using 400 laser pulses and a laser energy density per pulse of 0.8 J/cm^2. The incident laser pulse was p – polarized and the orientation of the polarization vector with respect to the grating structure is shown in figure 3.79. The p – polarized vector is parallel to the surface grating wave vector. The substrate was irradiated at < 1^o off normal incidence.

The frequency of the grating pattern was measured by taking the fast – Fourier transform (FFT) of the image in figure 3.79. The FFT is shown in the inset in figure 3.79. The intense spot in the FFT image (indicated by the arrow in the inset) corresponds to the frequency of the grating pattern in the surface region. The maximum intensity within the spot corresponds to a grating wavelength of 247.23 nm. Thus, the grating wavelength is within 0.3 % of the incident wavelength used to induce the formation of the grating structure.

A cross – section of the LIPSS morphology is shown in figure 3.80. The average peak – to – trough distance for these LIPSS was 5.30 nm ± 1.02 nm. This yields an average amplitude for the "sine – like" (refer to figure 3.57) wave of ~ 2.15 nm. The amplitude of the grating pattern is very small relative to the period of the waves. The mean amplitude of the grating pattern was measured over an AFM image of dimension 5 μm x 5 μm to sample an extensive region. The mean amplitude of the grating pattern was 2.15 nm, with a standard deviation of 0.43 nm. The maximum amplitude measured was 2.72 nm and the minimum amplitude measured was 1.50 nm.

It should be noted here that a second, frozen surface wave is embedded in the surface layer and phase shifted 180^o relative to the main, dominant sine wave in the surface. This wave has a maximum surface protrusion in the z – direction of ~ 3.5 nm

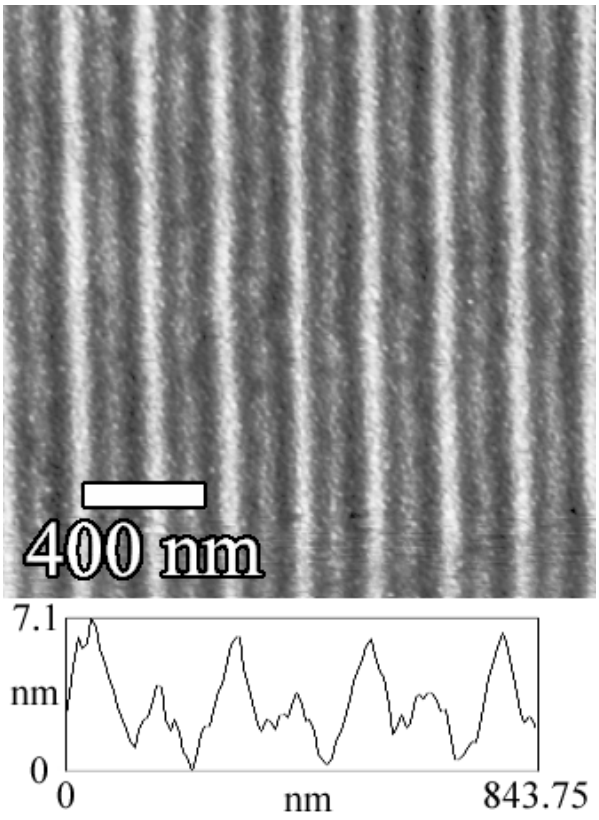

Figure 3.80 A higher magnification image of the sample shown in figure 3.72. A cross – section through the surface plane is provided in the image to better show the surface topography of the LIPSS surface. The cross – section is through the surface, parallel to the grating wave vector. The average peak – to – trough distance for these LIPSS was 5.30 nm ± 1.02 nm.

(refer to the cross – section in figure 3.80) and lies in the troughs of the dominant sine wave.

The LIPSS were generated with 400 pulses (E_d = 0.8 J/cm^2) in 100 Torr UHP He. *Moreover, only p – polarized light illuminated the substrate surface during laser processing and hence, induced the formation of the LIPSS*. LIPSS waves were not generated in the surface plane when s – polarized laser light was exclusively used to irradiate the substrate.

Figure 3.81 shows the morphology induced by s – polarized light. A roughness of RMS = 0.22 nm is produced in the surface plane, a value 24 times less than the average roughness induced using p – polarized light! Moreover, no periodic surface structure is generated from the s – polarized irradiation under constant irradiation conditions (400 pulses, E_d = 0.8 J/cm^2, P_T = 100 Torr UHP He) used to produce the LIPSS via p – polarized illumination.

An obstacle in the beam path was required to induce LIPSS formation. For example, a 500μm wire was placed in the path of the beam during irradiation. Sipe et al. also found that the grating wavelength was roughly equal to the incident laser beam wavelength under normal beam incidence [82]. Moreover, they formulated an expression to describe the relationship between the angle of incidence of the laser pulse and the induced grating spacing

$$\Lambda = \frac{\lambda}{1 \mp \sin\theta} \qquad 3.7$$

where λ is the incident laser beam wavelength and θ is the angle of incidence of the laser pulse with respect to the substrate normal [82]. The relationship was derived theoretically by Sipe et al. [82] and proven correct experimentally in a later paper by the same authors

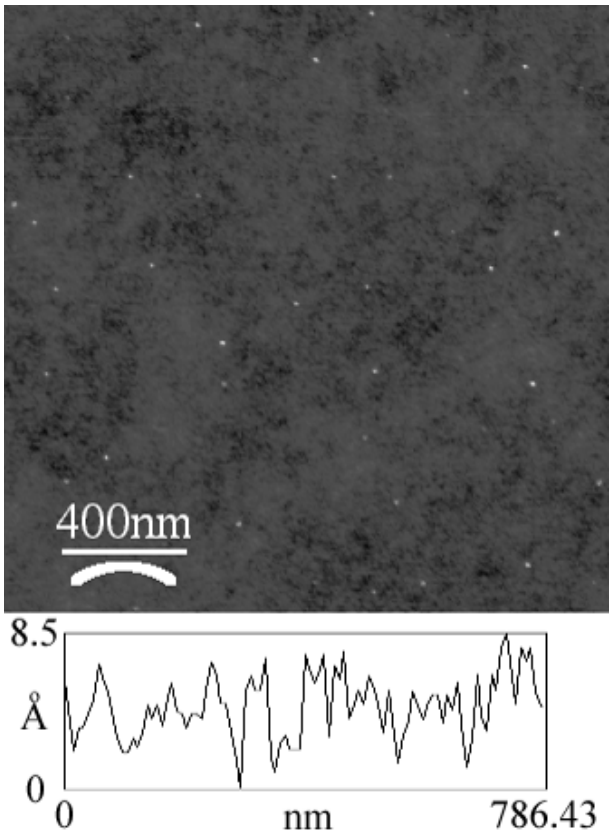

Figure 3.81 An attempt to generate LIPSS structures with **s – polarized** light with 0.8 J/cm^2 per pulse for 400 laser pulses. LIPSS waves were not generated and only a sight roughness RMS = 0.22 nm! (compare with figure 3.73)

[84]. Equation 3.7 can also be understood based on the grounds of a simple, geometrical construction of the interference pattern between incoming laser light and surface scattered laser light (section 1.6.1.4).

The grating pattern shown in figure 3.82 was formed using an irradiation angle of incidence of 38.9^{o}. Filling this angle of incidence into equation 3.6 yields two values for the grating spacing of 152.3 nm, $\lambda/(1 + \sin\theta)$ and 666.7 nm, $\lambda/(1 - \sin\theta)$. The FFT indicated a grating spacing of 149.1 nm for the LIPSS in figure 3.82. A 2% difference exists in the grating spacing between the theoretically predicted value (equation 3.6) and the experimentally determined value. The low intensity regions of the interference pattern are located exactly where the protruding molten strips are located. An explanation as to why the material accumulates in the low intensity region will be addressed in the discussion portion of the paper.

The grating pattern forms *only* in the narrow fluence range of 0.47 – 0.8 J/cm^2. The near surface region is molten over this entire fluence range. The melting threshold of silicon is roughly 0.55 J/cm^2. Thus, a molten silicon layer appears to be required for the evolution of the grating pattern. Surface grating structures have been formed at an *average* energy density as low as 0.08 J/cm^2 below the melting threshold. However, the *maximum* energy density at the center of the laser spot (0.56 J/cm^2) is roughly equal to the melting threshold.

It stands to reason that knowledge of the maximum melt depth and melting time should be important in interrupting experimental results where surface grating formation correlates with surface melting. The maximum thickness of the melted layer under 25 ns, 248 nm illumination is infinitesimally thin at the melting threshold and increases up to ~

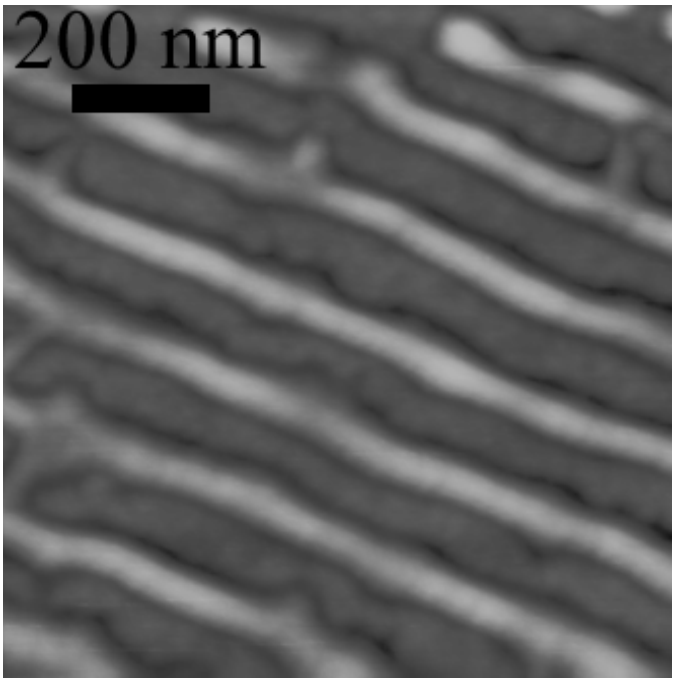

Figure 3.82 An AFM image of LIPSS structures induced in the surface plane with 500 laser pulses (E_d = 0.64 J/cm^2). Near the melting threshold of Si (E_{th} ~ 0.55 J/cm^2) the melted liquid layer is extremely thin and hence the liquid layer responds to the laser – induced and absorbed, spatially periodic temperature distribution by minimizing the surface tension in the form of liquid strips that re – solidify. Liquid transports from the hottest regions totally, leaving behind the smooth, un – melted substrate below.

100 nm at 0.8 J/cm^2 [92]. The total time the surface is molten spans from essentially nil, at the melting threshold, to ~ 30 ns for a fluence of 0.8 J/cm^2 [90].

The grating morphology produced at 0.64 J/cm^2 is significantly different from that produced at 0.8 J/cm^2. Figure 3.82 shows an AFM image of the grating morphology produced in the near surface region of silicon with a fluence of 0.64 J/cm^2. The elevated strips of silicon have the appearance of being previously melted. However, the region between the strips appears smooth and flat as if this region had not been melted. In contrast, the image shown in figure 3.79 & 3.80 appears to have been totally melted by the previous laser pulse, the surface grating has a smooth, sinuous and spatially uninterrupted appearance.

The amplitude of the grating pattern increases as the number of laser pulses increases. After 50 laser pulses the mean amplitude of the grating structures is ~ 5 nm. The mean amplitude increases to ~ 8 nm after an additional 1950 laser pulses. The energy density was kept constant for both cases such that the only variable that changed during both experiments was the number of laser pulses. These results indicate that the surface grating structure formed via a previous pulse has the affect of modifying the surface such that the next pulse cycle will produce an even more "rough" surface. Hence, surface grating formation and evolution occurs via a feedback, or non – linear, process whereby each additional surface modification is affected by previous surface structures.

The surface gratings nucleate as small, individual islands that expand in size on the surface with the number of laser pulses until they merge with other grating regions. Figure 3.83 shows an AFM image of LIPSS wave nucleation. Liquid Si appears to have migrated from initially hot circular regions to surrounding cold region. Evidence for surface flow is

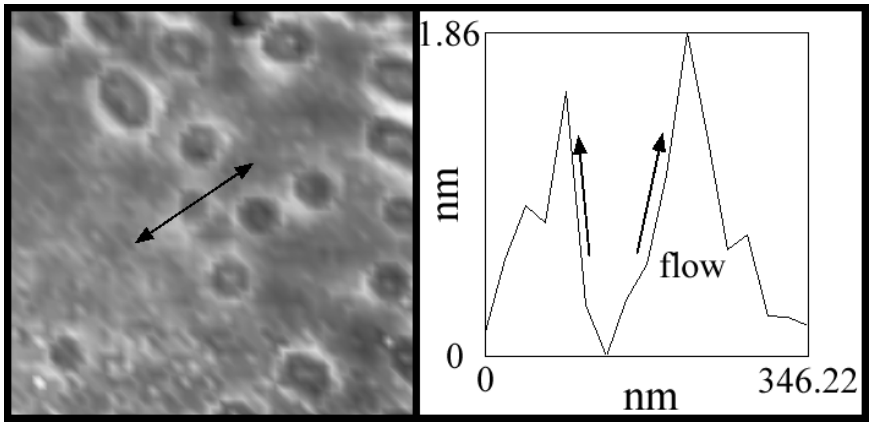

Figure 4.83 LIPSS nucleation in the surface plane of silicon. The LIPSS waves begin as localized regions of molten Si flow (the circular regions shown above). These regions eventually merge into lines forming the troughs of LIPSS structures. The cross – section shows that Si liquid has indeed migrated from points on the surface to form annular regions of raised material that surrounds the regions of localized flow.

indicated by the pile – up of material at the boundary surrounding the circular region at the expense of the inner region itself. Figure 3.84 shows an AFM of a slightly more advanced stage of LIPSS development where a wave packet of LIPSS is forming. Small, localized circles and strips can be identified in the figure where liquid Si has migrated to the boundaries of the circle, or strip, leaving a flat exposed region of the substrate surrounded by a ridge of re – solidified molten Si material. The circles represent regions of the surface where LIPSS waves are just nucleating and the strips are regions of advanced evolution. For example, in the right – side of the image shown in figure 3.84, eight strips, where localized fluid motion has taken place, feed the evolution of "high" amplitude regions between the strips. These are locations on the surface where thermal gradient driven flow initiates to develop LIPSS structures.

A substructures develops within the LIPSS wave, of the same period of the LIPSS in which they reside but phase shifted 180^{o} (figure 3.85). However, this second wave does not appear until the LIPSS wave has achieved an amplitude of ~ 3 nm. This second wave will be called the phase – shifted wave from here on to indicate the difference between this wave and the LIPSS wave. The amplitude of the phase – shifted wave is roughly half the LIPSS wavelength, or ~ 1.5 nm. The emergence of this wave, post – LIPSS development, suggests that the surface topography of the LIPSS is required for the second wave to nucleate. In fact, this substructure is also generated by the numerical simulations if a thin, initial liquid layer thickness is selected, i.e., ~ 1 nm in contrast to the 20 nm initial layer thickness selected previously.

The AFM image in figure 3.86 shows a region where the grating structures fill in the entire AFM sampled region of the substrate. In several places in the image the grating

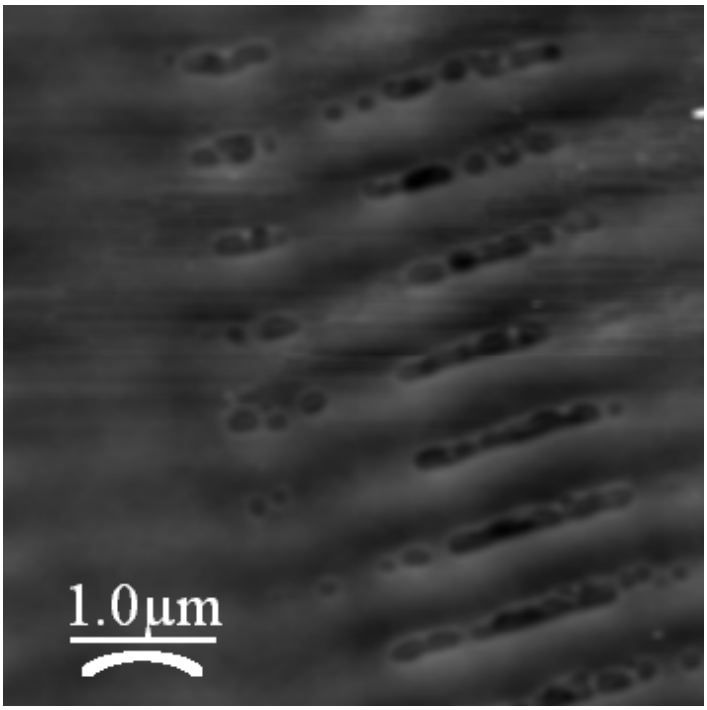

Figure 3.84 An AFM image clearly showing the merging of adjacent circular regions of localized flow. The word merging insinuates that these region move; this is incorrect. In fact, these region nucleate in lines on the surface that will later be the location of a LIPSS wave trough.

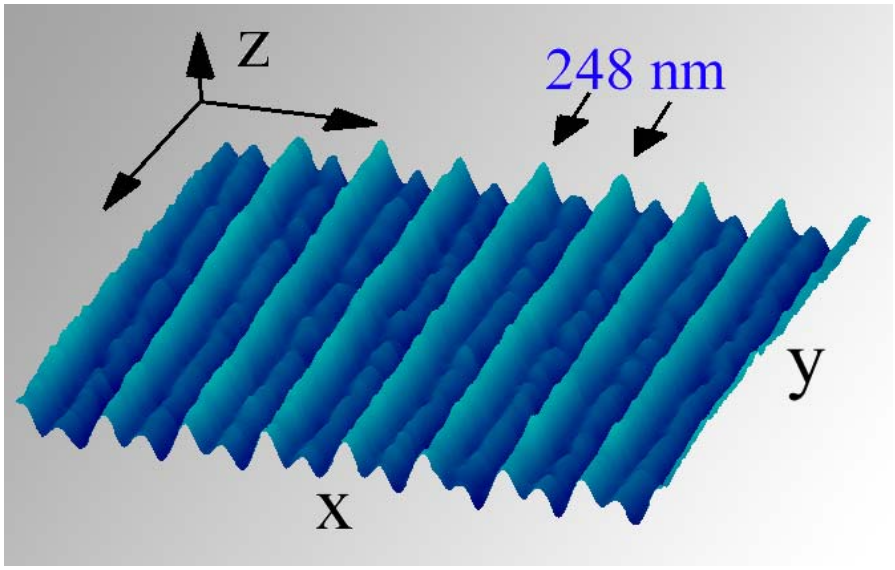

Figure 3.85 A 3D representation of an AFM image of LIPSS waves produced with p – polarized light, 400 laser pulses (E_d = 0.8 J/cm^2). The LIPSS waves were generated by normal incidence pulsed laser irradiation. The 3D representation allows for clear viewing of the phase – shifted waves, lying in the troughs of the LIPSS wave.

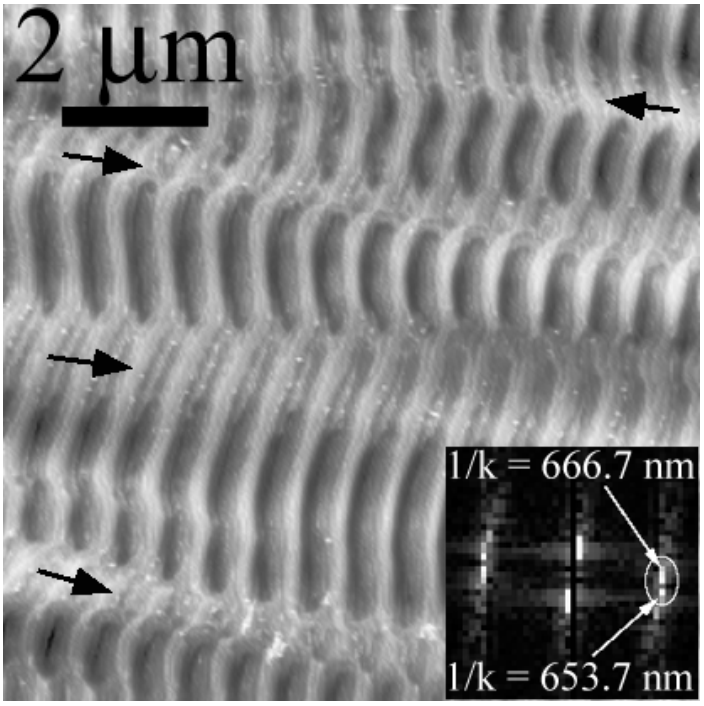

Figure 3.86 LIPSS waves nucleate as roughly points in the surface plane and appear to expand anisotropically, with propagation occurring faster along the wave vector and slower orthogonal to it. At higher number of pulses, when LIPSS waves merge, a dislocation is introduced between the region if the two LIPSS wave vectors to correspond exactly. Above, several regions of LIPSS have merged to form a continuous LIPSS wave of ~ 660 nm ($\theta = 38.9^{o}$). The diffuse ellipse in the FFT contains all the various misaligned wave vectors of all the LIPSS zones in the above image.

periodicity is interrupted. If one imagines traveling along, for example, a trough in the grating, a direction roughly orthogonal to the grating wave vector, one will encounter a boundary across which a phase shift exists in the grating morphology. The phase shift appears to be approximately 180^{o} aligning troughs from a neighboring grating to peaks in the adjacent grating. Several arrows in figure 3.86 indicate the location of boundaries between gratings of different phase.

The FFT reveals the merging gratings as a range of grating spacing values from 653.7 – 666.7 nm. This grating spacing range fits the $\lambda/(1 - \sin \theta)$ equation within 2% - 5%. Adjacent gratings must accommodate one another spatially as they come in contact. The mutual interaction shifts the respective wave vectors for the pair producing a range of grating spacing as indicated by the FFT.

Chapter 4

Discussion

4.1 The Evolution of SiO Nanostructures on Si Microcones

4.1.1 The Formation Mechanism

The SiO nanostructure is formed by the reaction of laser ablated Si species with O_2 molecules in the gas phase. The Si species are ablated from the trench pits surrounding the Si microcones. The energy density in the trench bottoms is 4 times the average, incident fluence on the bulk sample due to the focusing of laser light by multiple reflections off the trench walls [91]. An energy density in the range of 4 to 6 J/cm^2 at the trench bottoms produces a substantial flux of Si atoms that develop into a vapor plume that is confined in the trench bottoms due to the 1 atm total pressure over the substrate surface.

Si species diffuse out of the confined vapor cloud and react with O_2 in the gas atmosphere to produced SiO nanoparticles. SiO presumably does not form in the confined vapor cloud because the kinetic energy confined within the vapor itself would destabilize the SiO aggregate by dissociating it through collisions. For example, very little SiO aggregate is found attached to microcone bodies within the region of vapor cloud confinement (a region of roughly 20 – 40 micrometers extending up from the trench bottom) at the trench bottoms (figure 3.5) [91]. Moreover, nanoparticle formation by reactions taking place in the gas phase during reactive pulsed laser deposition into reactive atmospheres has been found to occur exclusively outside the vapor plume boundary [30].

The SiO nanoaggregates cluster by collisions with the high pressure background gas and other SiO species and some of these aggregates re – deposit on the microcone

walls. The laser fluence at the cones steep sides is much less than that at the cones tips and for this reason a much lower temperature during irradiation can be expected at the walls (figure 3.3). The SiO nanoaggregates deposit in an annular fashion around the steeply sloped microcone walls. On the other hand, SiO aggregate that does collide with the hot and melted microcone tip could decompose there giving,

$$2SiO_{(g)} \rightarrow 2Si_{(s)} + SiO_{2(g)}$$

As it has been observed the deposition of Si at the *molten, Si tip – solid, Si microcone bod*y interface lifting the microcone tip promotes the growth of the microcones (figure 3.7) [92].

The volume of SiO annular sheath surrounding each microcone increases as the partial pressure of O_2 is increased in the O_2 – Ar gas mixture up to at least 25% O_2 (figure 3.11). This result indicates that the reaction step between Si and O_2 is operating in the mass – transport limited regime where one can imagine that Si is "available" in the gas phase, per unit volume, to react with oxygen yet all available Si does not get consumed by the reaction.

The volume of SiO annular sheath surrounding each microcone also increases as the number of laser pulses increases (figures 3.8 & 3.9). This indicates that fresh Si is produced with each laser pulse to react with the O_2 in the ambient to form new SiO aggregate. However, after 800 laser pulses the SiO nanoaggregate annular sheath thickness begins to decrease. There are two probable causes for the reduction in SiO production at high numbers of pulses and it is possible that both processes are active simultaneously.

1 The distance between a particular location on the microcone body where SiO deposits and the trench bottom increases as the number of laser pulses increases

because material is constantly being removed from the trenches. The probability of SiO reaching this microcone body location decreases as this distance increases. Thus, at some number of laser pulses the rate of aggregate deposition per unit area should begin to decrease. The balance between deposition and ablation of SiO tilts toward the latter.

2 The attached SiO aggregate spreads out radially in space, from the axis of the microcone body as a function of the number of laser pulses, eventually shadowing the trenches adjacent to the microcone. This indicates that light that previously illuminated the microcone trenches is, at a later number of laser pulses, scattered and/or absorbed by the SiO aggregate, and hence reduces the intensity in the trenches which effectively reduces the flux of Si emerging from the trenches.

4.1.2 Room Temperature, SiO Nanoaggregate Photoluminescence

Visible, bright – to – the – eye, room temperature photoluminescence was observed from Si microcones embedded in SiO nanoaggregate sheath. Two main, prominent photoluminescence peaks located at 420 nm (3.0 eV) and 500 nm (2.5 eV) in the photoluminescence spectra provide most of the photoluminescence observed. The maximum intensity of the peak centered at 3 eV was roughly 2 times greater than the same value for the peak at 2.5 eV. However, the substantial broadening of the peak at 3 eV relative to the peak at 2.5 eV (figure 3.16) was related to the resolution of the light collection system and spectra were taken again, on a system of adequate resolution, to determine the true photoluminescence behavior of the SiO nanoaggregate sheath. Figure 4.1 shows a photoluminescence spectrum of the required resolution to identify accurately,

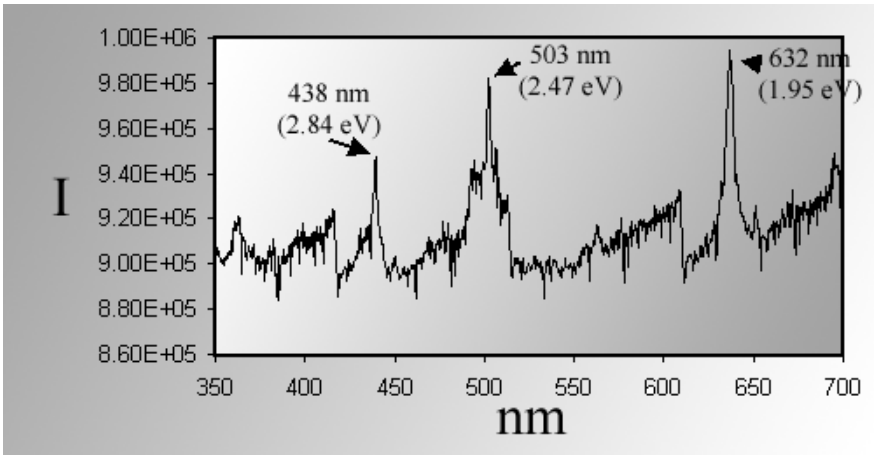

Figure 4.1 A photoluminescence spectrum from SiO nanoaggregate suspended on Si microcones. The microcones do not contribute to the photoluminescence. The SiO nanoaggregate was prepared in 25% O_2 – Ar with 1000 pulses (E_d = 2 J/cm^2).

individual peaks contributing to the photoluminescence, derived from an un – annealed sample prepared in 25% O_2 – Ar with 500 pulses.

Peaks centered at 438 nm (2.8 eV) and 503 nm (2.5 eV) *again* appear as the dominant contributors to the spectrum however an additional peak centered at 632 nm (1.95 eV) also is present in the spectrum. Moreover, the phenomenon previously observed in other spectra of both artificial peak broadening and an increase in integrated intensity, as the wavelength is decreased, have effectively been removed (figures 16, 18 - 19, & 23). This new acquisition configuration to obtain photoluminescence data consisted of a high – resolution spectrometer and intensified charge – coupled display.

The photoluminescence peaks at ~ 2 eV, 2.5 eV, and 3 eV were all attributed to the radiative recombination of electron – hole pairs at oxygen defect sites in the SiO. The type of defect per energy has been documented in the literature and is listed in detail in Table 3.2. Moreover, TEM studies on the SiO aggregate indicated a totally amorphous structure. The chemical composition of the aggregate was determined to be ~ SiO from "Quantitative" EDS spectra obtained for SiO aggregate prepared under all O_2 partial pressures. Hence, photoluminescence arises from defects in the SiO nanoaggregate structure.

Annealing of the SiO was performed under the supposition that the SiO would decompose into Si and SiO_2 thereby leaving Si nanoparticles distributed throughout, and embedded within, the SiO aggregate. Photoluminescence spectra, HRTEM imaging, and TEM diffraction studies were performed on the annealed aggregate all studies indicated that crystalline Si was not present in the SiO aggregate.

4.2 Pressure Mediated Si Nanocrystal Formation from Ablated Si Species

4.2.1 Pulsed – Laser Deposition of Si Nanoparticles

Backscattered nanoparticles were collected on the substrates they were ablated from by maintaining a pressure of $1x10^{-1}$ – $1x10^{2}$ Torr UHP Ar over the substrate surface during pulsed laser processing. The nanoparticles were formed in the gas phase as Si species, produced by ablation, collide with the Ar gas molecules thereby losing their kinetic energy, and finally condensing in the gas phase to form Si nanoparticles. These nanoparticles re - deposited, by back scattering collisions in the gas phase, over the entire substrate surface.

The re – deposited Si nanoparticles were characterized by their diameters over specific areas, dA, in the surface plane, as a function of their distance from the laser irradiated area. Also, the effect of pre – target surface roughness on the size distribution was evaluated. The optimal size distribution was one with a narrow FWHM, a minimal mean nanoparticle diameter, and a nanoparticle distribution fit to a single Gaussian peak. Size – selected nanoparticle films of this quality are attractive for potential device applications where the nanoparticles would be deposited at a specific location and their collective operation would require them all to be of a specific size for proper device operation.

The minimum mean nanoparticle diameter and minimum FWHM were achieved by

1 Increasing the target – to – nanoparticle collection area, distance.

2 Reducing the total pressure of UHP Ar present over the surface during nanoparticle formation.

3 Irradiating a rough target surface as opposed to a flat target surface all over variables constant.

A possible explanation of why the size distribution of clusters generated from both flat and rough target surfaces decreased with distance from the laser ablated region could be as follows. Atomic species and particles are ablated from the surface with a velocity that is normal to the wafer surface. The more collisions a cluster experiences with other atoms or clusters the larger it will tend to grow. Clusters that experience many collisions will tend to become larger and will on the average have acquired a larger component of the velocity parallel to the surface.

A significant number of large clusters will form very close to surface because the vapor plume density is very high there and decreases as it expands. The very high pressure of the background gas ensures that the vapor plume above the substrate surface is strongly restrained in its expansion. Due to the multiple scattering events in the plume region, large clusters will tend to reverse their direction at low altitude from the substrate and land not very far from the laser spot.

By contrast, a cluster that experiences fewer collision events in the region of high vapor density will tend to travel a large distance from the target surface and will have a higher probability of landing further from the laser spot than a larger cluster backscattered just above the wafer surface. Large clusters could also form at a high altitude but because of their large mass they are less likely to be backscattered at large angles away from the surface normal. This fact reduces the probability that a large particle will be deposited far from the laser spot. Thus, it is possible to select nanoparticles based on their mean

diameter by collecting the particles at various distances from the laser – damaged region on the target surface.

Nanoparticles of a reduced mean nanoparticle diameter, and FWHM, are collected per area on the surface dA when the ambient pressure is lowered (figure 3.26). For example, a 5 – fold decrease in mean nanoparticle diameter is accomplished by reducing the total inert gas pressure 200 – fold. Fewer clustering events take place per unit distance traveled when the total gas pressure is lowered. Hence, the average size of the nanoparticles produced in the vapor clustering process should be reduced as the pressure is lowered.

Irradiating a rough target surface, i.e., Si microcones, yields ablated flux arising from a much higher laser energy density due to multiple reflections into the surface depressions increasing the energy density there, compared to just irradiating a flat surface. The high – density plume formed in the trenches surrounding the microcones leads to substantial clustering (as has already been observed, for example, in the case of SiO formation where not only nanoparticles of SiO were formed but also high – aspect, nano – scale clustered aggregates were formed). It is evident, by comparing figure 3.27 and figure 3.30, that the degree of clustering during the irradiation of Si microcones is substantial relative to flat surfaces.

The Gaussian tails present in all the size distributions extracted from the PLD of Si nanoparticles (that were deposited on the same surface from which they were derived, figures 3.26 & 3.28) was not present when Si nanoparticles were collected on an independent substrate placed 6 cm from the target surface, directly above and parallel to it. Figure 3.33 shows the size distribution of two Si nanoparticle films collected in this

fashion. Both films are fit by closely by one single, Gaussian distribution, making them far superior in quality relative to the mutual target/substrate deposition configuration. Moreover, the size – distributions of these films fall within the visible luminescence range for Si nanoparticles exhibiting quantum confinement effects.

The 6 cm substrate – to – target distance acts as a Si nanoparticle filter by limiting the chance that a large nanoparticle will reach the substrate with increased distance. The scattering cross – section for Si nanoparticles increases with size and hence, limits the distance the larger particles can travel before being totally scattered off course. As the substrate – to – target distance is increased the mean diameter of the Si nanoparticle film decreases [30 – 31, 33 – 34]. Only those nanoparticles of small scattering cross – section, i.e., Si nanoparticles of the minimum diameter achievable by the process, can traverse the 6 cm substrate – to – target distance and, as a result, the small Gaussian tails of large nanoparticles are removed from the distributions yielding a tighter nanoparticle size distribution.

4.3 Laser – Induced Nanoparticle Ordering

4.3.1 On The Thermal Stability of Aligned Nanoparticles relative to the Underlying, Bulk, Si Substrate

Si nanoparticles produced by low fluence, i.e., 0.5 – 1.3 J/cm^2, pulsed laser irradiation in inert atmospheres, seems to exhibit a higher melting threshold than the underlying bulk Si substrate by which they are suspended. The underlying Si substrate was observed to melt at a fluence > 0.55 J/cm^2 under 248 nm pulsed laser irradiation. This value is consistent with the melting threshold for bulk Si extrapolated from the work of Singh et al. of ~ 0.5 J/cm^2 [90].

There are several reasons why the nanoparticles may not melt under suitable irradiation to induce melting. First, it is possible that laser energy densities up to 1.3 J/cm^2 induce only partial melting; the substrate region below the nanoparticles is not melted. Second, a spherical particle receives half the fluence a flat surface receives due to its curvature. Hence, an incident, average fluence of 1.3 J/cm^2 is diluted to a value of ~ 0.65 J/cm^2 over the surface of a spherical particle. This value is close to the melting threshold reported by Singh [90].

Calculations of the scattered electromagnetic field intensity above the Si surface provided an additional possibility as to why nanoparticles exhibit such a high melting threshold. The general wave equation for a high – frequency, oscillating electric field propagating in a semiconductor medium, i.e., a medium exhibiting both dielectric and conducting behavior, was split into two components, a real and imaginary part [93]

$$\nabla^2 \vec{E}_{zr} + \frac{\omega^2}{c^2}\vec{E}_{zr} + \frac{\omega^2}{c^2}\cdot\frac{Nq^2(\omega_o^2-\omega^2)}{m\varepsilon_o\left[\left(\omega_o^2-\omega^2\right)^2+\gamma^2\omega^2\right]}\vec{E}_{zr} - \frac{\omega^2}{c^2}\cdot\frac{Nq^2\gamma\omega}{m\varepsilon_o\left[\left(\omega_o^2-\omega^2\right)^2+\gamma^2\omega^2\right]}\vec{E}_{zi} + \frac{\mu_o\sigma\omega}{1+\omega^2\tau^2}\vec{E}_{zi} + \frac{\mu_o\sigma\omega^2\tau}{1+\omega^2\tau^2}\vec{E}_{zr} = 0 \quad (4.1)$$

$$i\nabla^2\vec{E}_{zi}+i\frac{\omega^2}{c^2}\vec{E}_{zi}+i\frac{\omega^2}{c^2}\cdot\frac{Nq^2(\omega_o^2-\omega^2)}{m\varepsilon_o\left[\left(\omega_o^2-\omega^2\right)^2+\gamma^2\omega^2\right]}\vec{E}_{zi}+i\frac{\omega^2}{c^2}\cdot\frac{Nq^2\gamma\omega}{m\varepsilon_o\left[\left(\omega_o^2-\omega^2\right)^2+\gamma^2\omega^2\right]}\vec{E}_{zr}-i\frac{\mu_o\sigma\omega}{1+\omega^2\tau^2}\vec{E}_{zr}+i\frac{\mu_o\sigma\omega^2\tau}{1+\omega^2\tau^2}\vec{E}_{zi}=0 \quad 4.2$$

where E_{zr} is the real part of the solution of the time averaged electric field, E_{zi} is the imaginary part of the solution of the time averaged electric field, ω is the frequency of the laser light, c is the speed of light in vacuum, N is the volume density of electrons, m is the mass, ω_o is the resonant polarization frequency, q is the electric charge of the electron, γ is a response factor related to the polarization, σ is the frequency dependent conductivity, μ_o is the electron mobility, and τ is the mobility dependent decay constant. The electric – field was taken to oscillate in the z – direction and to propagate in the x – direction. The solution of the time independent wave equation as listed above is of the form

$$\vec{E}_{zr}=e^{-\frac{\omega\kappa}{c}x}\cos\frac{\omega n}{c}x \quad 4.3$$

$$\vec{E}_{zi}=-e^{-\frac{\omega\kappa}{c}x}\sin\frac{\omega n}{c}x \quad 4.4$$

where [93]

$$\kappa=\left\{\frac{\omega^2}{c^2}\left(1+\frac{Nq^2}{m\varepsilon_o}\left[\frac{\left(\omega_o^2-\omega^2\right)}{\left(\omega_o^2-\omega^2\right)^2+\gamma^2\omega^2}+\frac{i\gamma\omega}{\left(\omega_o^2-\omega^2\right)^2+\gamma^2\omega^2}\right]\right)-\frac{\mu_o\omega\sigma i}{1+\omega^2\tau^2}+\frac{\mu_o\sigma\omega^2\tau}{1+\omega^2\tau^2}\right\}^{\frac{1}{2}} \quad 4.5$$

and n is the real portion of the refractive index and z is the polarization orientation of the laser light electric field.

The scattered intensity modulation shown in figure 4.2a and 4.2b occurs in the free space surrounding the Si surface. The UHP He surrounding the Si has a real index, n = 1, and a complex index, κ = 0, i.e., the He gas absorbs zero intensity from the interference

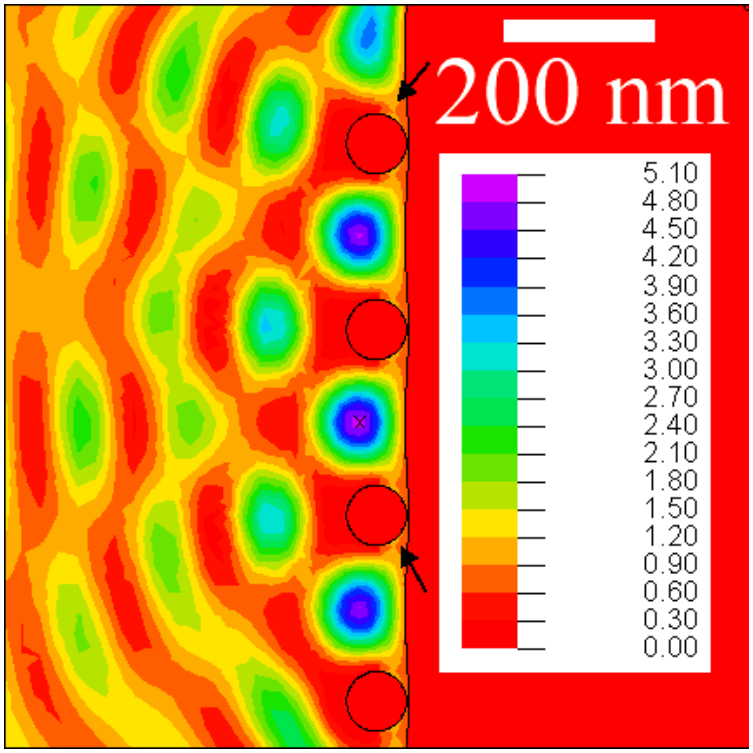

Figure 4.2 (a) The calculated time averaged, scattered intensity in the inert atmosphere region directly above a surface containing Si nanoparticles spaced 248 nm apart, each in the trough of a LIPSS structure. The LIPSS amplitude was 5 nm for the simulation. The laser pulse initiated at the left – most interface. The units above are in J/cm^2. An incident E_d = 1 J/cm^2 produces a scattered intensity touching the backsides of the nanoparticles of 1.5 J/cm^2. The arrows in the figure indicate the high intensity regions in contact with the back side of the nanoparticles. A fluence of 1.5 J/cm^2 should convert them to liquid Si.

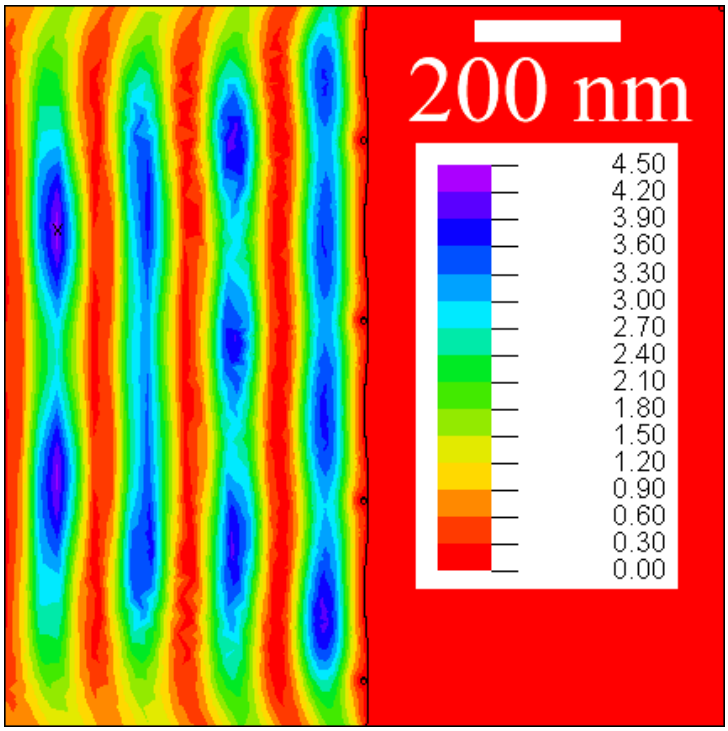

Figure 4.2 (cont'd) (b) An incident fluence of 1 J/cm^2 on Si nanoparticles 10 nm in diameter, each lying in LIPSS troughs of amplitude 5 nm, generates a time averaged intensity on the surface of the nanoparticles of 1 J/cm^2. This simulation indicates that these nanoparticles should not melt in conjuncture with the fact that Si nanoparticle melt at an incident fluence of 1.3 J/cm^2. Nanoparticles of this diameter are observed, experimentally, to be stable under 1 J/cm^2 irradiation.

pattern present within its boundaries. Under these conditions, the time – averaged electric – field in space obeys the simplified system of wave equations,

$$\nabla^2 \vec{E}_{zr} + \frac{\omega^2}{c^2} \vec{E}_{zr} = 0 \qquad 4.6$$

$$i\nabla^2 \vec{E}_{zi} + i\frac{\omega^2}{c^2} \vec{E}_{zi} = 0 \qquad 4.7$$

and the solution is of the form,

$$\vec{E}_{zr} = \cos\frac{\omega}{c} x \qquad 4.8$$

$$\vec{E}_{zi} = -\sin\frac{\omega}{c} x \qquad 4.9$$

A finite element analysis based numerical solution (FlexPDE©) was used to solve the coupled equations 4.1 and 4.2 in the silicon region and the coupled equations 4.6 and 4.7 were solved in free – space. A coherent, propagating wave, simulating a laser pulse of unit amplitude, was introduced from the left – most boundaries shown in both figure 4.2a & b;

$$E_{rp} = \cos nkx \qquad 4.10$$

$$E_{ri} = -\sin nkx \qquad 4.11$$

The wave was partially absorbed and reflected by the silicon surface. A superposition of the time averaged solutions of E_{zr} and E_{zi} in the free – space region with the propagating wave from the left produced the scattered field patterns shown in figures 4.2a and figures 4.2b. The boundary conditions;

$$E^{free}_{zr(\tan)} = E^{Si}_{zr(\tan)} \qquad 4.12$$

$$E^{free}_{zi(\tan)} = E^{Si}_{zi(\tan)} \qquad 4.13$$

$$B^{free}{}_{x,y(\tan)} = B^{Si}_{x,y(\tan)} \qquad 4.14$$

ensured that continuity of the tangential component of the electric field and magnetic field was preserved across the free – space / Si boundary on interaction of the laser beam with the interface. Moreover, phase changes due to reflection at the interface are incorporated into the model inherently when these boundary conditions are satisfied.

These coupled equations describe laser light propagation and absorption in the Si that is shown in the right portion of the images in figure 4.2a & 4.2b. Both figures seem to indicate that absorption takes place completely near the surface layers since the color coding of red throughout the Si indicates zero intensity based on the scale provided with the image. The frequency dependent absorption coefficient of Si is ~ $5x10^7$ cm^{-1} indicating that 63% of the incident 248 nm radiation is absorbed 20 nm, or $e^{-\alpha}$ (where α is the absorption coefficient) into the Si surface [14]. This high absorption rate of radiation in Si can be further understood by examining figure 4.3.

Shown in figure 4.3 is the real (n) and complex (κ) index of refraction in Si as a function of the wavelength of electromagnetic radiation penetrating the Si surface. The real portion of the refractive index can be thought of as the wavelength change (reductio) a photon experiences when penetrating a material of different index then the previous material; as Δn increases the photon is "bent" more (Snell's Law, ray optics) when it passes through the interface separating the index gradient.

Kappa is a measure of the degree of absorption of a material as a function of wavelength. As κ increases the absorption rate, at a specific wavelength increases. κ, as a function of wavelength, is a maximum of ~5.4 at roughly 380 nm indicating that light at

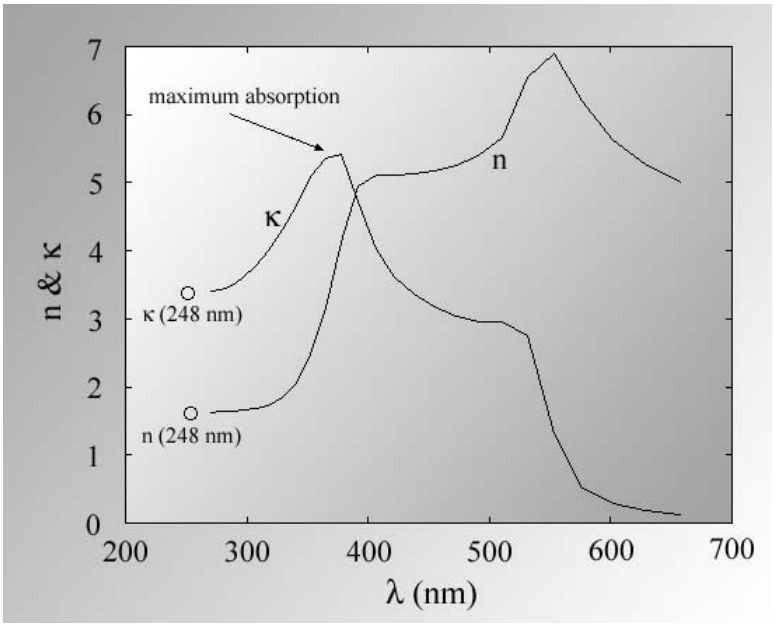

Figure 4.3 The real (n) and imaginary (κ) indices of refraction for c-Si listed as a function of wavelength.

this frequency interacts most strongly with the bonds in Si, modulating the bound charge dipole to its largest dipole moment, plus absorbing strongly with the intrinsic electron density. $\kappa = 3.2$ for 248 nm laser light suggesting strong coupling to the Si charge density, i.e., the absorption coefficient is large for Si and hence, most all of the incident intensity is absorbed within 50 nm of the surface.

The calculations showed that as the nanoparticle diameter increased in the self – organized array network, the intensity of scattered light at the Si substrate surface increased. For example, a 1 J/cm^2 laser pulse generates an intensity of 1.5 J/cm^2 on the back surfaces of Si nanoparticles 80 nm in diameter lying in LIPSS waves of maximum amplitude 5 nm (figure 4.2a). Arrows in the image in figure 4.2a indicate the high intensity (x1.5) regions contacting the Si nanoparticle surfaces. The calculations seemed to indicate that nanoparticles larger than 80 nm receive ~ x 1.5 the intensity of the incident laser pulse. The maximum amplitude of 5 nm for the LIPSS structures was selected for the simulation based on experimental observations that indicate a 5 nm LIPSS amplitude for laser irradiation with 1 J/cm^2 per pulse over many laser pulses. However, a 1 J/cm^2 laser pulse generates a negligible intensity rise on the surface of 10 nm diameter nanoparticles situated in LIPSS that have a 5 nm maximum amplitude (figure 4.2b). The details of the mathematical simulation will be shown and described in a following paragraph.

As already stated, a fluence of 1.3 J/cm^2 has been experimentally observed to melt nanoparticles of ***all sizes, at normal incidence,*** *reducing the surface to a continuous film of liquid*. Simulations indicate that a nanoparticle 80 nm in diameter would melt under irradiation at 1 J/cm^2 due to the local intensity rise at its surface to 1.5 J/cm^2; a fluence greater than the experimentally observed melting threshold for Si nanoparticles. *Hence,*

the simulation seems to suggest that nanoparticles larger than 80 nm are not stable on the surface because they will be melted locally if they form. Moreover, the simulation suggests that nanoparticles smaller than 80 nm would be stable on the surface and hence should be experimentally observed.

The calculations shown in figure 4.2a & b indicate that the self – organized nanoparticles form a grating in the surface plane that strongly modulates the incoming laser pulse. The intensity at the nanoparticles is a minimum if the nanoparticles form a grating with the distance between the particles equal to the laser wavelength. For example, in figure 4.2a, the intensity is concentrated between the nanoparticles. If the nanoparticle is much smaller than the laser wavelength, i.e., d = 5 – 10 nm (figure 4.2b), light is reflected back from the substrate in opposite phase with the incoming light producing destructive interference just over the surface. The phase change is produced because in the incident laser beam passes from a medium of lower index of refraction to the Si which has a larger refractive index [94]. This produces a phase change of 180^{o} on reflection of the scattered light relative to the incident phase. The result of this phase change is produce a thin layer over the substrate surface, with a width, $w << \lambda$, where the local light intensity is a minimum. The simulations show that Si nanoparticles of 5 – 10 nm lie within this zone and do not melt (figure 4.2b).

4.4 Laser – Induced Periodic Surface Structures

A large number of laser pulses was required to initiate the submicron ripples, or LIPSS, in silicon, in contrast with micron size LIPSS that required just a few pulses to be produced [59]. For instance, 5 nm high LIPSS were produced after 400 laser pulses (figure 3.80). Once the LIPSS were produced they tended to grow as the number of laser pulses was increased. After 2000 pulses the ripples grew to a height of 8 nm.

As it was described in section 1.6.1 one of the main assumptions in the LIPSS evolution is that the structures observed on the surface are commensurate with the intensity distribution that follows the equations described in that section. The LIPSS were observed only when the substrate was tilted off normal incidence during the laser treatment cycle. *LIPSS were experimentally observed to have a spatial periodicity exactly equal to the wavelength of the scattered wave intersecting the surface plane as predicted by equation 3.6*. Ripples of sub – micron wavelength were produced of Si substrates. The LIPSS periodicity was measured using the AFM.

The observation that the LIPSS grow in amplitude as a function of the number of laser pulses indicates a self – propagating, or feedback effect, where the absorption of the intensity distribution continuously changes the surface topography as a function of time, i.e., irradiance time. This is contrast to a "balanced" phenomenon where the laser pulse would introduce a surface topography change that would reduce the capability of the surface to absorb the next laser pulse. No such balanced phenomenon where observed over all experiments performed, but have only been mentioned here to more clearly convey the meaning of a feedback process by describing the reverse case to feedback.

The feedback process responded to p – polarized illumination only. *For example, the amplitude of LIPSS waves grew only when p – polarized light, or un – polarized light containing a p – polarized component, illuminated the substrate*. Irradiation with strictly s – polarized light, under conditions that would yield LIPSS with an amplitude of 5 nm under p – polarized irradiation, yielded no detectable LIPSS formation in the surface plane. Moreover, the p – polarized component of the laser beam had a wave vector orientation that was exactly parallel with the grating structure, i.e., the LIPSS waves, that the light induced itself. *The inhomogeneous absorption energy to promote grating formation is equal to*

$$\vec{k}_{laser} \bullet \vec{k}_{grating} = \left|\vec{k}_{laser}\right| \cdot \left|\vec{k}_{grating}\right| \cos\theta \qquad 4.15$$

where the maximum absorption into the grating is;

$$\vec{k}_{laser} \bullet \vec{k}_{grating} = \left|\vec{k}_{laser}\right| \cdot \left|\vec{k}_{grating}\right| \qquad 4.16$$

In fact, in the case here described to generate LIPSS structures, the geometry of the substrate irradiation is such that;

$$\vec{p}_{polarized} \bullet \vec{k}_{grating} = \left|\vec{p}_{polarized}\right| \cdot \left|\vec{k}_{grating}\right| \qquad 4.17$$

and that;

$$\vec{s}_{polarized} \bullet \vec{k}_{grating} = 0 \qquad 4.18$$

This indicates that the s – polarized component should not induce self – propagating LIPSS evolution because this polarized component is not absorbed efficiently into the grating and that the p – polarized component should give maximum absorption into the surface plane. *This is what is observed, p – polarized laser illumination of Si substrates induces the formation of LIPSS waves under the same experimental conditions, i.e., E_d = 0.55 – 1*

J/cm^2 and number of pulses > 20, that produced no waves with s – polarized illumination (figures 3.80 & 3.81)!

4.4.1 **Mechanism of LIPSS Formation**

The thermal induced motion of a thin silicon film, generated by pulsed laser irradiation at a fluence of 0.8 J/cm^2 (30 second melt duration) [90], 400 pulses, was calculated by a finite element based numerical solution for the single, non – linear PDE describing surface tension driven liquid flow and was compared to experimental data on the surface topography generated under these same irradiation conditions to determine if this liquid motion was responsible for the formation of the LIPSS structures. The partial differential equation to describe thermal – gradient driven liquid motion in the surface plane is the Marangoni equation [95];

$$\frac{\partial \xi}{\partial t} + \frac{1}{2\mu(T)}\left(\frac{\partial^2 \sigma(T)}{\partial x^2}\xi^2 + 2\xi\frac{\partial \sigma(T)}{\partial x}\frac{\partial \xi}{\partial x}\right) + \frac{1}{3\mu(T)}\frac{\partial}{\partial x}\left(\frac{\partial \sigma(T)}{\partial x}\frac{\partial^2 \xi}{\partial x^2}\right)\xi^3 = 0$$

4.19

where ξ is the change in the y – direction, orthogonal to the surface plane but lying in the plane of incidence, of a surface element at x, as a function of time, σ(T) is the temperature dependent surface tension, and μ(T) is the temperature dependent viscosity. An initial liquid layer thickness, ξ_t of ~ 20 nm, at a constant temperature of 1687 K (the melting temperature of silicon) was used as the initial condition to simulate the very first laser pulse. The final surface topography present on the surface after the first pulse was fed back into the program as the initial liquid layer thickness for the next pulse and this procedure was repeated to accumulate the desired number of laser pulses. The initial

condition, ξ = 20 nm, is roughly the average, over one pulse, of the melt depth over the whole x – range for a Gaussian laser pulse and as a function of time.

A 30 ns surface melt duration was simulated where the initial surface temperature was 1687 K, rose to a maximum as a function of position at exactly half the melt duration of the liquid surface layer, and decayed back to 1687 K after 30 ns. The shape of the temperature rise as a function of time;

$$T(t) = \left(T_{\max} - T_m\right)\left|\sin\left(\frac{\pi t}{\tau}\right)\right| + T_m \qquad 4.20$$

where T_{max} is the maximum surface temperature for a specific fluence, T_m is the melting temperature of Si; 1687K, t is the time, and τ is the total surface melt duration. The temperature rise as a function of both position and time is shown as a 3D plot in figure 4.4.

For the plot generated in figure 4.4, for T(x,t), λ = 248 nm , and hence this temperature distribution is similar in spatial distribution to the expected distribution of intensity provided by a laser pulse that scatters via surface roughness producing a periodic intensity modulation on a surface irradiated at roughly normal incidence.

The temperature distribution in the surface plane, as a function of time, induces a surface tension gradient of the form shown in figure 4.5. A linear relationship exists between surface tension and temperature of the form;

$$\frac{d\sigma}{dT} < 0 \qquad 4.21$$

and the exact relationship between the two variables is provided within figure 4.5. The surface tension is a maximum in the coolest regions of the surface and a minimum in the hottest region due to equation 4.21. It is this surface tension gradient that induces the flow

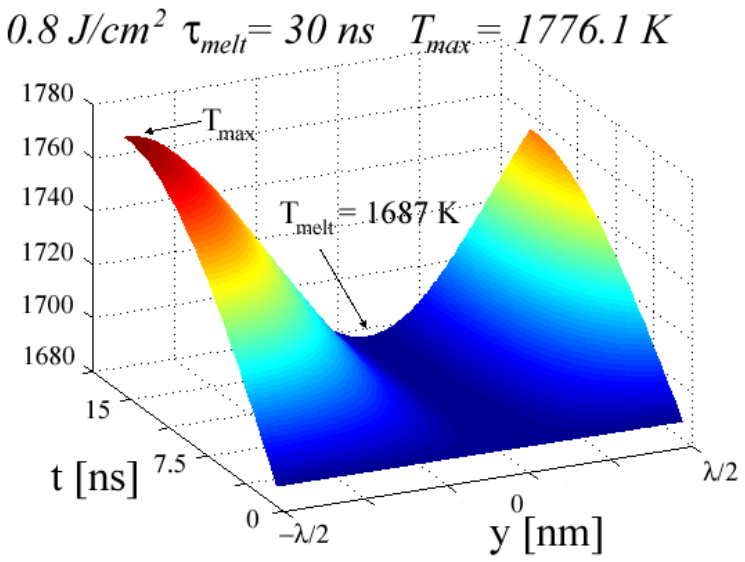

Figure 4.4 T(y,t) profile, shown over half the melt duration (τ/2), used to induce fluid motion for a simulation based on the Marangoni Flow equation. The maximum surface temperature and melt duration time, as a function of laser energy density, were extrapolated from theoretical and experimental values provided by Singh et al. [90].

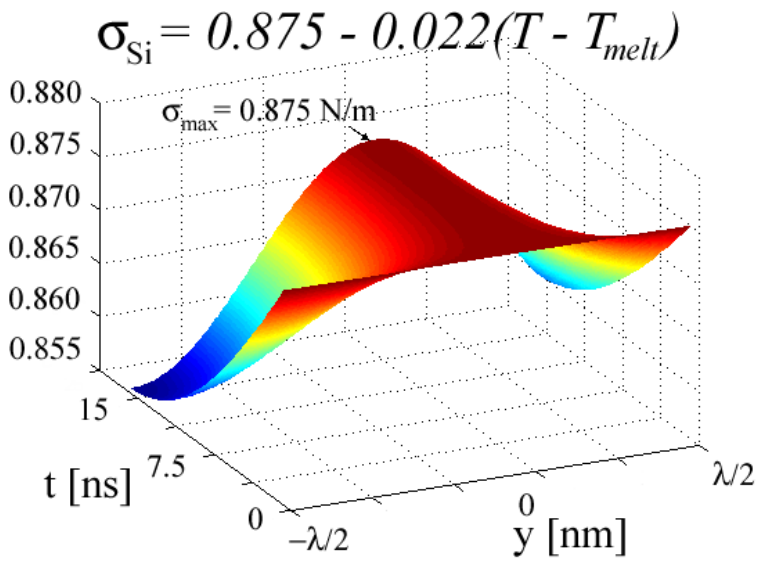

Figure 4.5 The surface tension, σ(y,t), profile in liquid Si derived from the temperature profile in the surface plane (figure 4.8) [14].

of Si in the x – direction over the duration of the laser pulse from the hottest regions (low surface tension) to cool areas, i.e., locations on the surface of high surface tension.

The melting of a thin surface layer of ~10 nm – 50 nm was induced by the absorption of the p – polarized light component of the incident laser beam for E_d = 0.47 – 0.8 J/cm^2, respectively. It appears that the total surface layer in the irradiated surface region was melted for a laser fluence of 0.8 J/cm^2 (figure 3.79). At a lower fluence of 0.6 J/cm^2 the surface was only partially melted, strips of re – solidified silicon are present in the surface layer (figure 3.82) separated by atomically smooth, flat regions between the strips, regions indicative of no prior melting. However, model calculations show that this morphology can also evolve from an initially, completely molten surface, but significantly thin, such that the motion of liquid in the surface plane due to thermal gradients could draw molten Si into the cooler regions of the surface depleting the warm regions of the thin ~ 20 nm, Si film.

A physical interpretation of the process can be obtained with the help of equation 4.19. The first term in equation 4.19;

$$\frac{\partial^2 \sigma}{\partial x^2} \xi^2 \qquad 4.22$$

acts as a resistance to the motion of liquid if the surface has areas of both positive and negative curvature, i.e., the situation when one has a sinusoidal surface topography running along the surface in the x – direction. The second term is a fluid motion driving term;

$$\xi \frac{\partial \sigma}{\partial x} \frac{\partial \xi}{\partial x} \qquad 4.23$$

this is positive and hence a large surface tension gradient dσ/dx acts to increase the flux of liquid at the location of surface slope of dξ/dx driving the surface morphology

rearrangement. The last term in equation 4.19 is also a resistance term but has little affect because the term contains ξ^3 that is on the order of $1x10^{-27}$ and is of little resistance due to the extremely small value of this cubed term.

Figure 4.6 shows both the calculated and experimental data for LIPSS waves generated with 400 laser pulses (E_d = 0.8 J/cm^2). The amplitude of the experimentally generated LIPSS waves is 2.7 nm a value of exactly half the calculated value of 5.5 nm. However, the mutual periodicity of the two waves has been preserved through the calculation, both have a wavelength of roughly 248 nm.

The 50% difference between the experimentally observed LIPSS amplitude and the calculated value is promising since calculations most often yield differences on the order of magnitudes and also, considering that the two other plausible mechanisms for LIPSS wave formation, surface polariton mode absorption and capillary wave oscillations, are not the modes of formation. For example, surface polariton mode oscillations follow a dispersion type relationship of the form;

$$\Lambda_{SEW} = \frac{\lambda}{\frac{c}{v_{phase}} \pm \sin\theta} \qquad 4.24$$

where v_{phase} is the phase velocity, c is the speed of light in vacuum, θ is the angle of incidence of the driving laser beam, λ is the driving wavelength, and Λ is the surface polarition mode wavelength [77 – 79]. For illumination of Si at 248 nm, Λ_{SEW} = 155 nm and this is clearly not the wavelength of LIPSS, formed at ~ normal incidence Λ = 248 nm, as experimentally determined (figure 4.6). The wavelength of the active mode for polariton propagation is much less because the wave is assumed to travel in the silicon, essentially just below the surface. However, solutions to Maxwell's equations yield that it

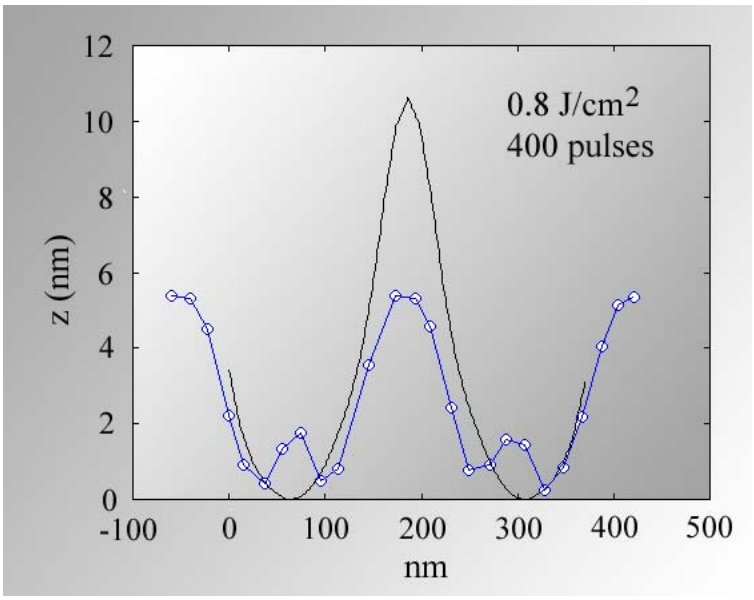

Figure 4.6 The surface morphology on Si after exposure to 400 laser pulses (E_d = 0.8 J/cm^2); each laser pulse having T(y,t) of the form shown in figure 4.8. The simulation is shown as the continuous line and the actual experimental data is listed with data points and a smooth line connected these data points.

is forbidden for light to propagate along, and within, the surface of a second medium of higher index of refraction than the first medium from which the light came [94]. For example, in the case presented here, laser light propagates in free space (n = 1) and scatters from roughness at the interface of silicon (n = 3.4). In this case, the polariton would have to propagate in the Si and this is forbidden.

4.5 Si Film Evolution, Clustering, and LINO

A silicon film forms on the surface of laser – irradiated Si by first, the backscattering of this film by the inert gas present over the substrate surface, and lastly by the re – deposition of the Si species on this surface (figure 4.7). As direct evidence for this model of deposition, for He gas pressures less than 100 mTorr, an undetectable quantity of film is re – deposited on the surface and hence no source for nanoparticle clustering is present. Indeed, subsequent irradiation does not lead to the development of Si nanoparticles. It seems at least 1 nm thick Si film is required for Si species clustering to form nanoparticles and a film of this thickness is not generated at gas pressures less than 100 mTorr He.

The vaporized flux induced by a pulsed laser can be estimated using the following expression for the vaporized depth per pulse [96];

$$\Gamma_{pulse} = \frac{P_o}{n_s\sqrt{2\pi M k_b}} \int_0^\infty T^{-\frac{1}{2}} e^{-\frac{\Delta H_v}{k_b T} dt} \qquad 4.25$$

where P_o is the equilibrium vapor pressure of the surface at temperature T, n_s is the atomic density, M is the molecular weight, ΔH_v is the heat of vaporization and k_b is Boltzmann's constant. The equilibrium vapor pressure of Si at 1800 K (~ 0.8 J/cm^2) is ~ 10 mTorr and

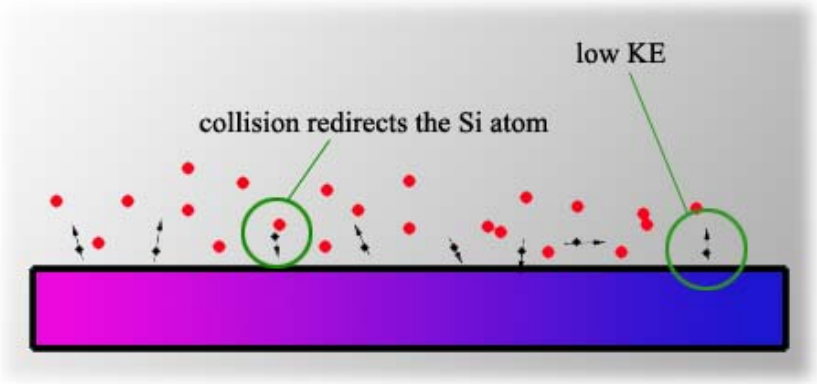

Figure 4.7 A schematic illustration of the ejection, collision, and re – deposition of Si species (black spheres) with the He background gas to produce a thin, Si film on the laser irradiated substrate. The Si species are ejected with inappropriate kinetic energy to traverse through the high pressure, inert ambient and end up back – scattered back toward the target/substrate surface where they re – deposit.

assuming this vapor pressure is achieved (even with 100 mTorr He present over the surface) a thermally – induced vaporization rate per pulse of 0.10 – 0.50 nm/pulse is achieved and remarkably this value is on the order of the value observed experimentally by measuring the thickness of the deposited film using the AFM (on average roughly 1 nm). With this vaporization rate one could expect a build – up of 1 nm of film after 30 laser pulses (figure 3.39)

It has been observed that backscattered and recollected Si, after 4000 laser pulses, resides on the surface only in the previously irradiated region, i.e, little Si aggregate is collected outside the laser irradiated region (figure 3.41). This indicates a substantial fraction of Si is recollected on the surface because if the Si vapor transferred far from the initially irradiated region one would expect to find Si species re - deposited outside the irradiated region. This is not observed experimentally.

The re – deposited film begins to cluster into detectable (~ 1 nm) nanoparticles after 30 laser pulses (figure 3.39). The clustering is most probably driven by the thermal gradient present on the surface that also drives the formation of LIPSS structures. For example, Si nano – pillars of the same size and distribution as the Si nanoparticles generated in this work were produced with by thermal evaporation of an Si source, 30 cm distant from a Si substrate at room temperature [97]. The evaporated Si species had sufficient energy once deposited on the surface to migrate and find the minimum surface configuration which, in this case, was randomly oriented Si nanocrystals [98]. In their case, the evaporation source pointed towards the substrate forcing the formation of nano – pillars as opposed to nanocrystals. This is known because Si clusters nucleated on the surface in this referenced work [97].

It has been found conclusively that the self – organization of Si nanoparticles into linear arrays must be accompanied by an underlying LIPSS nanostructure (figure 3.60). Moreover, the Si nanoparticles always lie in the troughs of the LIPSS structures. Therefore it is plausible that the Si film tends to aggregate and cluster in the regions of high intensity where liquid Si depletes during the molten cycle, assuming the surface reconstructs during irradiation by the thermally – induced motion of liquid Si in the surface plane. However, electrophoresis or thermophoresis processes could be responsible for the observed clustering process [99]. Si migration and clustering would be expected to increase in hotter surface regions for a thermally activated, diffusion process. Experiments seem to indicate that Si nanoparticle formation occurs in the trenches of the LIPSS structures with no Si nanoparticles located on the tops of the areas of maximum amplitudes midway between the trenches.

The Si film probably re – deposits after the molten Si surface has re – solidified. The mean free path of Si species in 100 mTorr He is ~ 50 μm with an average velocity of ~ $8x10^4$ cm/s. These values yield a collision frequency of vaporized Si atoms with the background gas of $16x10^6$ Hz, or a collision roughly every 60 ns. If it is assumed a vaporized Si atom were to re – deposit following one collision, which redirected it back to the surface, the Si would re – deposit after ~ 2 x 60ns. The surface is molten for ~ 30 ns during a 0.8 J/cm^2, 25 ns laser pulse and hence, re – deposition would take place after the surface had re – solidified! However, the next laser pulse is experimentally observed to induce clustering, but one would instead expect the underlying substrate to melt.

1. An intensity modulated, incident laser beam is required to nucleate LIPSS formation and nanoparticle alignment.

Figure 4.8 summarizes the active intensity modulators that have been used to induce these processes. The orientation of the microcones, their spatial arrangement in the surface plane, i.e., either random or periodic or the orientation of the laser spot relative to the LIPSS*, have no effect on the LIPSS other than to nucleate their existence*, they are always aligned orthogonal to the p – polarized component. Neither matters the crystallinity of the irradiated Si substrate!

A wire placed in the path of the laser beam in route to the surface also nucleates LIPSS formation and nanoparticle self – organization. The wire can be rotated with respect to the LIPSS with no affect on their orientation. In summary, Si microcones and wires act solely as a nucleating agents.

2. Nanoparticle clustering is triggered by the intensity modulation in the surface plane.

Any roughness present on the surface produces intensity modulations. Self – organization takes place when both, a) wires and/or microcones provide scattered p – polarized light to be absorbed by the surface and b) when the simultaneous clustering in the surface plane produces a nanoparticle of diameter > 1 nm. The nanoparticle appears to couple with the scattered and/or incident p – polarized light, enhancing absorption into the near surface region of the nanoparticle. A nanoparticle spacing of ~ Λ (the LIPSS grating spacing) is produced that indicates a strong correlation between nanoparticle formation and LIPSS evolution.

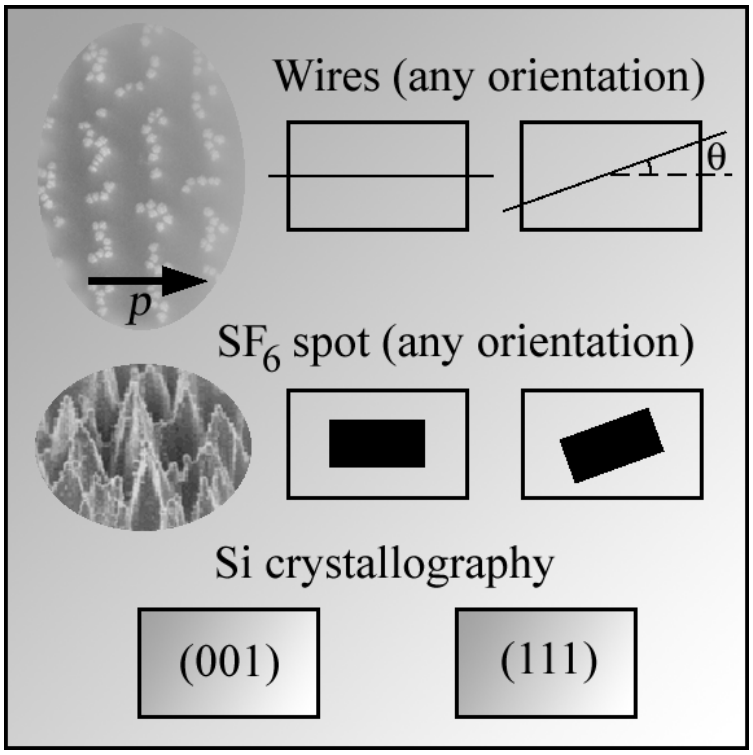

Figure 4.8 LINO is ***nucleated*** by 1) the presence of a wire in the laser beam path, regardless of the wire's orientation, 2) the presence of microcones in the laser beam spot during irradiation to produced nanoparticles, regardless of the periodicity of the microcones within the laser irradiated region or the orientation of the small laser spot containing the microcones and 3) the nucleation is totally independent of crystallography. Moreover, the ***orientation*** of the nanoparticles is orthogonal to the p – polarized light projection on the surface regardless of any of the factors listed above! ***Roughness nucleates and p – polarized light aligns!***

Point b) is a speculation based on several experimental observations. The self – organization process begins at a point on the surface and spreads outward radially, consuming Si film as a function of the number of laser pulses (figure 3.49). The spacing between nanoparticles is ~ 248 nm, the expected LIPSS spacing for a Si surface irradiated with 248 nm light at near normal incidence. Nanoparticle alignment, i.e., LIPSS formation, has not yet taken place though (figure 3.49); probably because the critical number of nanoparticles has not evolved to provide a "resonant cavity" strong enough in intensity to drive LIPSS formation.

3. Nanoparticle alignment completes and the surface intensity modulation is phase shifted because the nanoparticles become the dominant light scattering centers.

The nanoparticles continue to grow at the expense of the neighboring film until they reach a particular, maximum size. The production of Si film does not limit the maximum size of the nanoparticles because this film has been found to continuously form up to 4000 laser pulses, well after the nanoparticles have begun to decrease in diameter.

Si nanoparticles have diameters of roughly twice the underlying LIPSS amplitude after 200 laser pulses in 100 Torr He (E_d = 1 J/cm^2, figure 3.58). The nanoparticles have diameters of ~ 4 to 6 times the amplitude of the LIPSS waves after 200 additional laser pulses (figure 3.59). The laser light scattered from a surface containing 248 nm LIPSS waves is concentrated over the troughs of the LIPSS as shown by the computational simulation provided in figure 4.9. Returning to figure 4.2b, we see that the nanoparticles begin to substantially dominate the light modulation once they develop in the surface plane, relative to the underlying LIPSS, thereby shifting the maximum intensity by 180^O

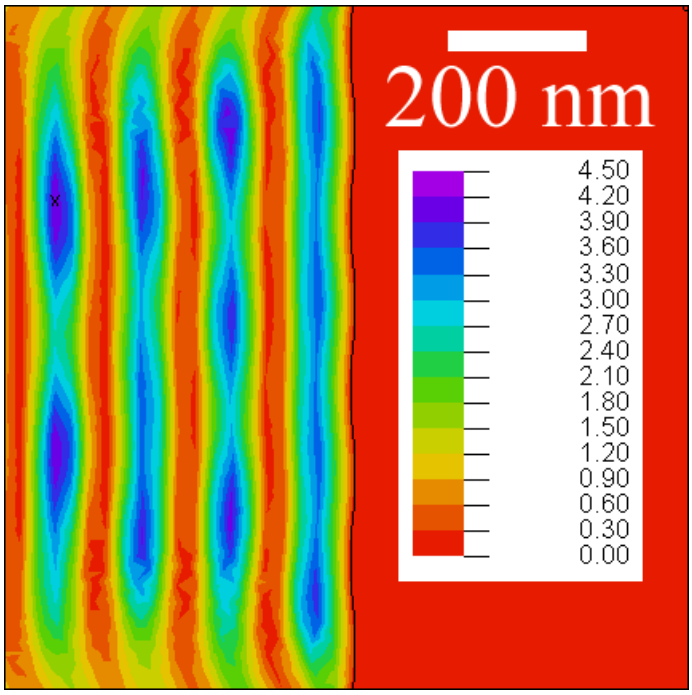

Figure 4.9 Calculation of the time averaged intensity distribution in the inert gas phase modulated by the interference between the incoming laser light and the scattered laser light from a LIPSS grating of amplitude 5 nm. The maxima are located ~ 30 nm above the surface, over the troughs in the LIPSS grating.

relative to the position shown in figure 4.9 for LIPSS controlled scattering. Exactly how this modulation effects the further development of nanoparticles is unclear. It could be that nanoparticles can only grow so big (figure 4.2a) because eventually their surface receives a fluence greater than 1.3 J/cm^2 due to intense light scattering and melt. On the other hand, the nanoparticles may be stable because the collective grating that they form modulates the incoming light such that the areas of low intensity are located where the nanoparticles are.

4.5.1 Si Film Ablation by Near – Field Lithography

Near – field optical phenomenon were used to both, pattern Fourier structures in the Si film re – deposited on the Si substrate in inert atmospheres, and to determined the ablation threshold of the Si film. Figure 4.10 shows a fresnel, i.e., near – field, diffraction pattern imprinted in the re - deposited film by preferential ablation of some areas of the film. A silicon particle, 2 μm in diameter, was used as a mask to produce an intensity modulation on the Si substrate surface, where the surface acted as a "screen" intersecting the fresnel modulation at 1 μm from the particle's center. The coherent, 248 nm laser beam provided the source (located at infinity relative to the particle – to – "screen" distance) to interfere with the micro – particle.

A numerical solution based on Maxwell's equations approximating the analytical solution to the equation describing Fresnel (near – field) diffraction, specifically the Kirchoff diffraction formula [100];

$$\Psi(P_o,t) = -\frac{iA}{\lambda}\frac{1}{R_s}e^{-i\omega t}\int_{\Delta S}\left[\frac{\frac{1}{2}(\cos\theta_o + 1)}{r_o}\right]e^{i\kappa r_o}dS \qquad 4.26$$

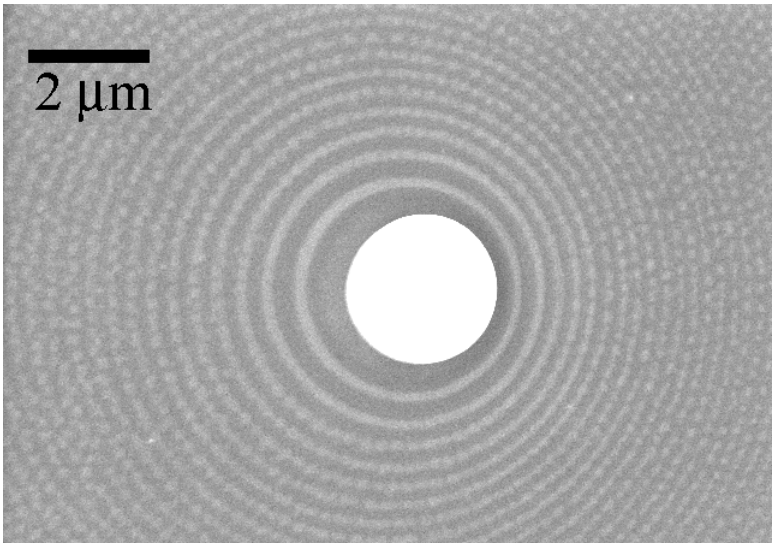

Figure 4.10 A diffraction pattern of the Fresnel variety is formed in the Si film where the pattern is permanently imprinted into the surface plane because in high intensity regions of the pattern Si film is ablated away, i.e., a $E_d > \sim 1.3$ J/cm^2, leaving behind rings of Si film. The diffraction pattern was produced by the interference of incoming beam and the diffracted beam (by the particle). $E_d = 1$ J/cm^2.

where Ψ is the electric field amplitude at the screen at position P_o and time, A is the maximum electric field amplitude of the incident laser beam, R_s is the source to particle distance which is assumed to be constant since the laser beam is located at infinity relative to the object – to – screen distance, ω is the frequency of the incident light, δS is the infinitesimal component of the diffracting object contributing to the image at some position P on the screen, θ_o is the angle between the wave vector of the incident light at an infinitesimal element dS of the diffracting object and the wave vector of the diffracted light from that element, and r_o is the distance from the element dS at the diffracting object to the point on the screen of interest. The integral is over all elements dS at the diffracting object that each contributes to all points P on the screen. The superposition of contributions from all dS gives the total electric field at the point P on the screen, i.e., the substrate.

The simulated intensity of the diffraction pattern has been superimposed over the actual pattern imprinted in the film in the composite image shown in figure 4.11. The y and x – axis labels are not provided in figure 4.11 in order to reduce clutter and are provided in figure 4.12 on the following page. Drawing a line from the film edges, at each dot, parallel to the y – axis, and intersecting the superimposed intensity profile allows for determining the fluence at the boundary between the film – denuded regions and the film itself. The film is stable at fluences < 1.1 – 1.3 J/cm^2 based on extrapolations from this figure. This result is in close agreement with the simulation shown in figure 4.2a that indicates a melting threshold for the Si nanoparticles of ~ 1.3 J/cm^2. Apparently, the Si film also melts at fluences greater than ~ 1.3 J/cm^2 giving an upper limit on the stable fluence of Si nanostructures on an underlying Si substrate.

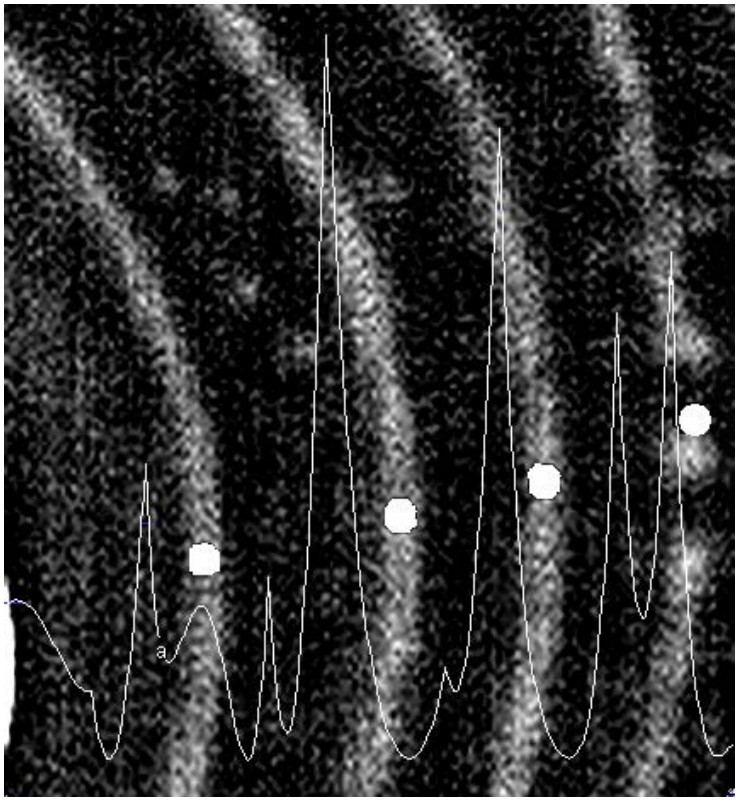

Figure 4.11 The film remained in regions of the surface plane that received a fluence < 1.1 – 1.3 J/cm^2, the calculated intensity pattern has been superimposed over the actual region on the surface, where the pattern is located. The units of the calculated intensity pattern are provided in figure 4.26.

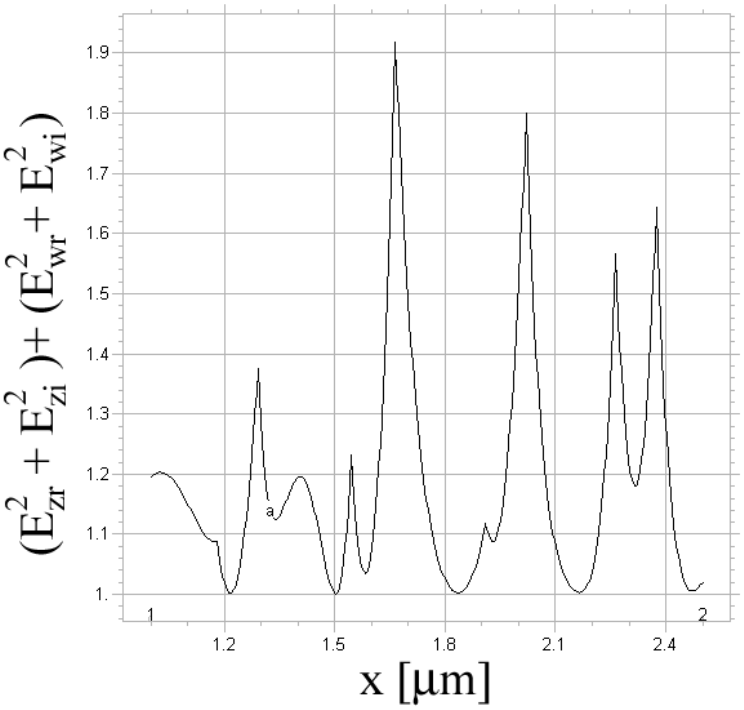

Figure 4.12 The calculated intensity distribution produced on the Si surface by the interference between the scattered light, onto the surface, from a spherical, Si microparticle (d = 2 μm) located there, and the incoming laser 248 nm laser beam. The calculated intensity pattern is a cross – section through the fresnel pattern imprinted in the surface (figure 4.24) and the region of the surface where the pattern was calculated is shown in figure 4.25.

Chapter 5

Conclusions

5.1 Laser – Induce Nanoparticle Ordering (LINO)

Irradiating a flat Si substrate produces ablated Si species that are backscattered by the ambient gas and re – deposited onto the surface. If the background pressure is lower than 250 mTorr of UHP He not enough material is backscattered to form a continuous surface film. The laser fluence must be larger than 0.6 J/cm^2 to produce enough ablated material, but lower than 1.3 J/cm^2 to avoid the fusion of the film with the substrate.

The Si film has a steady – state thickness of ~ 1 nm, even as the number of laser pulses increases, i.e., each laser pulse introduces fresh film to the surface region. However, the film is continuously consumed because part of it clusters into Si nanoparticles that remain on the surface after irradiation and a portion may be ablated during irradiation.

The Si film clusters on the surface to form Si nanoparticles. These nanoparticles scatter light in the surface plane. The superposition of the incoming light from the laser pulse plus the scattered component produces an interference pattern at the substrate surface. The clustering process is influenced by this intensity pattern and individual clusters have spacings on the surface a distance λ apart, where λ is the incident laser beam wavelength.

The diameters of the nanoparticles that can be produced by this process fall in the range of 2 – 80 nm, the larger size has been obtained at the lower energy densities used in this study. Using numerical simulations coupled with experimental results, it was found that as the laser fluence is increased, over the range 0.6 – 1.3 J/cm^2, the maximum, stable

Si nanoparticle diameter decreases, in agreement with experimental results. Larger nanoparticles scatter the incoming radiation more strongly into the surface plane causing larger local intensity maxima on the surface close to themselves.

A Gaussian, statistical distribution best represents the distribution of diameters for nanoparticle films produced by the LINO process. The minimum FWHM observed over all the LINO produced nanoparticle films was 2 nm.

The nanoparticles themselves begin to cluster into linear chains as a function of the number of laser pulses; these chains are randomly distributed on the surface. They move on the surface and orient spatially such that they are spaced by roughly λ from all their neighboring chains. The motion of species on the surface seems to saturate after roughly 400 laser pulses, little motion occurs at greater numbers of pulses.

The nanoparticles in the surface plane will self – organize into periodically spaced lines, if a periodic or quasi – periodic, microstructure is present at the surface. The two microstructures used to initiate order were Si microcones and thin wires placed in the beam path during irradiation. The purpose of the surface roughness and/or obstructing wires appears to be related to light scattering that promotes inhomogeneous energy deposition that facilitates the nanoparticle ordering.

LIPSS were found to lie beneath the nanoparticles only when they were self – organized. LIPSS formation and nanoparticle alignment seems to be intimately related. P – polarized was required to induce the formation of LIPSS and the self – organization of Si nanoparticles. The beam need be only partially polarized but it must contain a substantial portion, at least 50%, p – polarized light.

The nanoparticle chains orient themselves into lines spaced Λ apart

$$\Lambda = \frac{1}{1 - \sin\theta}$$

where Λ is the wavelength of the interference pattern, λ is the laser beam wavelength, and θ is the angle – of – incidence. The underlying LIPSS structures had a spatial of Λ also.

LIPSS formation was induced, without the presence of Si nanoparticles, when a Si substrate was irradiated with p – polarized laser light. The presence of an inhomogeneous energy distribution was required to nucleate LIPSS. A second, periodic structure was formed with a spacing also equal to Λ but phase shifted by $\Lambda/2$ with respect to the major LIPSS.

5.2 SiO Nanoaggregate Coated Si Microcones

Bright, visible and very intense, room temperature photoluminescence was observed from these SiO nanostructures. The photoluminescence spectrum consists mainly of two peaks, centered at 2.5 and 3.0 eV. These two peaks are characteristic of radiative, oxygen defects in SiO.

SiO nanoaggregates were formed by the ablation of a microstructured target in the presence of a O_2 – Ar ambient gas. The microstructure that consists of Si microcones induces strong ablation and clustering of Si. The SiO nanoaggregates are produced in the gas phase and re – deposits on the Si microcone surface forming the observed SiO sheathed microcones.

5.3 Pulsed Laser Deposition of Si Nanoparticles

Backscattered nanoparticles were collected on the substrates that they were ablated from by maintaining a pressure of $1x10^{-1}$ – $1x10^{-2}$ Torr UHP Ar over the substrate surface

during pulsed laser processing. The nanoparticles were formed in the gas phase as Si species, produced by ablation, collide with the Ar gas molecules thereby losing their kinetic energy, and finally condensing in the gas phase to form Si nanoparticles. These nanoparticles re – deposited, via back scattering collisions in the gas phase, over the entire substrate surface. The minimum mean nanoparticle diameter and minimum FWHM for the Si nanoparticle films were achieved by

1 Increasing the distance from the laser spot that the nanoparticle films were collected.
2 Reducing the total pressure of UHP Ar present over the surface during nanoparticle formation.
3 Irradiating a microstructured target surface as opposed to an atomically flat target surface.

5.4 Future Work

5.4.1 LINO coupled with Pulsed Laser Deposition to produce Multi – material Nanoparticle – Substrate Systems

A very important result of this work was the achievement of a system capable of ordering nanoparticles on substrates using a separate target. Preliminary experiments were performed in our laboratory to implement this process and the results indicated pronounced success. Si nanoparticles were deposited on Si substrates in a similar fashion to the aforementioned LINO process, the difference being the flux of Si was provided, not by the same substrate the alignment takes place on, but from a different Si target altogether.

Figure 5.1 shows an AFM image of the linear alignment of Si nanoparticles (d ~ 2 – 5 nm), spaced roughly 200 nm apart. The alignment of nanoparticles into lines is apparent in the figure however nanoparticles have also been deposited in between the lines in contrast to the LINO process. This is a direct result of the Si flux emerging from a separate vapor source. Figure 5.2 shows a schematic diagram of the experimental procedure used to prepare the sample shown in figure 5.1. A full description of the experimental procedure is provided in the figure legend.

5.4.2 Laser – Induced Ordering of Si Nanoparticles produced by Chemical Vapor Deposition

Si nanoparticles were deposited in a self – organized fashion by laser – induced chemical vapor deposition (LICVD) on a pre – existing LIPSS surface topography. The LIPSS surface topography, prior to the LICVD treatment, is shown in figure 3.80 & 3.85. Following LIPSS formation a gas mixture of SiH_4 gas and Ar was introduced into the irradiation chamber (P_{SiH4} = 0.1 Torr, P_T = 10 Torr). The substrate was irradiated with 1000 laser pulses (E_d = 0.5 J/cm^2) to induce the laser – assisted, thermal decomposition of SiH_4 at the surface plane. The LIPSS grating ensured unequal absorption of laser beam intensity establishing a temperature gradient in the surface plane. The thermal decomposition of silane,

$$SiH_4 \xrightarrow{thermal} Si + 2H_2$$

was expected to occur at locations on the surface of sufficient temperature to induce the above reaction. Figure 5.3 shows a HRSEM image of the LIPSS structures following the laser – induced, thermal decomposition of SiH_4. Si spherical, nanoparticles were formed

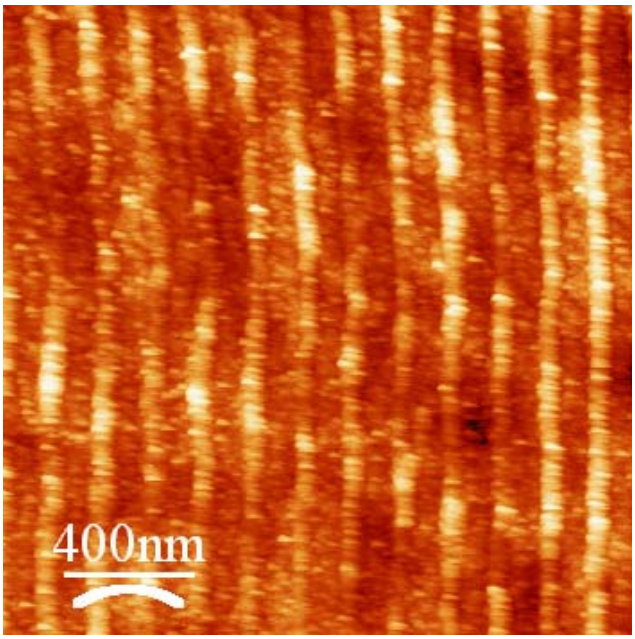

Figure 5.1 A flux of Si nanoparticles was provided to the substrate (shown above) by laser – irradiating a Si target, 6 cm distant from the substrate, with E_d = 2.5 J/cm^2 in an ambient of 100 mTorr UHP Ar with 2000 laser pulses. The substrate was simultaneously irradiated with 2000 laser pulses, p – polarized (E_d = 0.75 J/cm^2), to induce the self – organization of the deposited nanoparticles into linear arrays. The experimental configuration to generate this experiment is shown in figure 5.2.

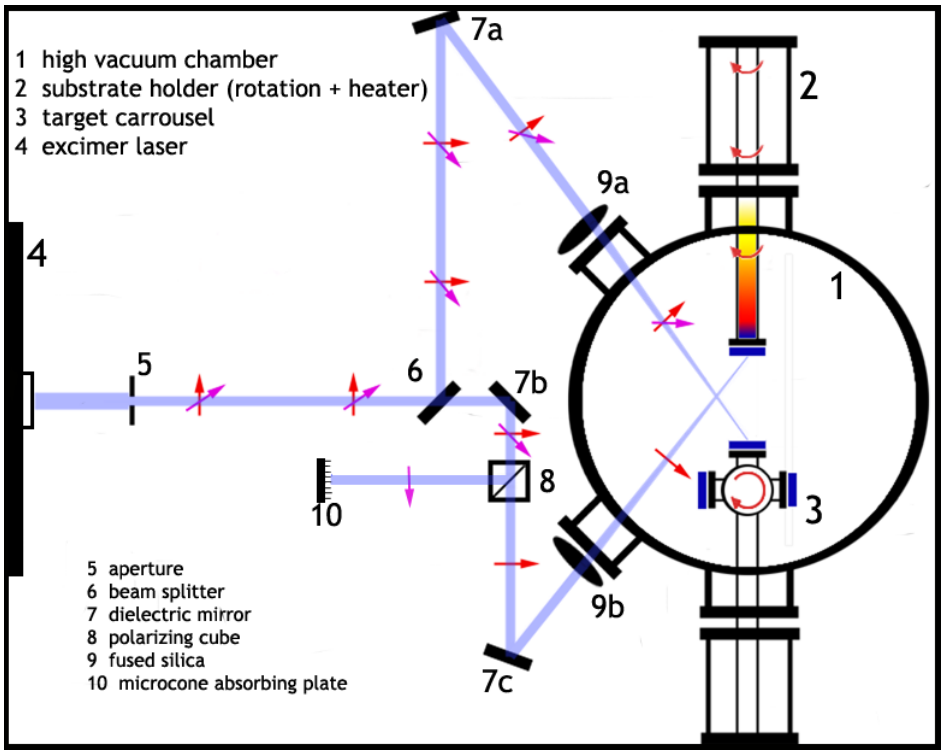

Figure 5.2 A Si target (3) was irradiated with $E_d \sim 2.5$ J/cm^2 in 100 mTorr UHP Ar (1) to produce a flux of Si nanoparticles at the substrate with a diameter distribution of roughly 2 – 5 nm. The laser used to irradiate the target was a 248 nm excimer laser. The pulse emanated from the laser (4), passed through an aperture (to clip the low energy Gaussian tails from the beam, 5) and was reflected off two mirrors (6 & 7a) to a fused silica focusing optic (9a) that focused the beam at the target surface to generate the 2.5 J/cm^2 pulse. The substrate was simultaneously irradiated with the same laser beam by using a beam – splitter (6). The beam, in route to the substrate holder, was totally p – polarized after passing through a uv – polarizing cube. The beam was then focused onto the substrate surface ($E_d = 0.75$ J/cm^2) to induce LIPSS formation and nanoparticle alignment. The pulses were not synchronized.

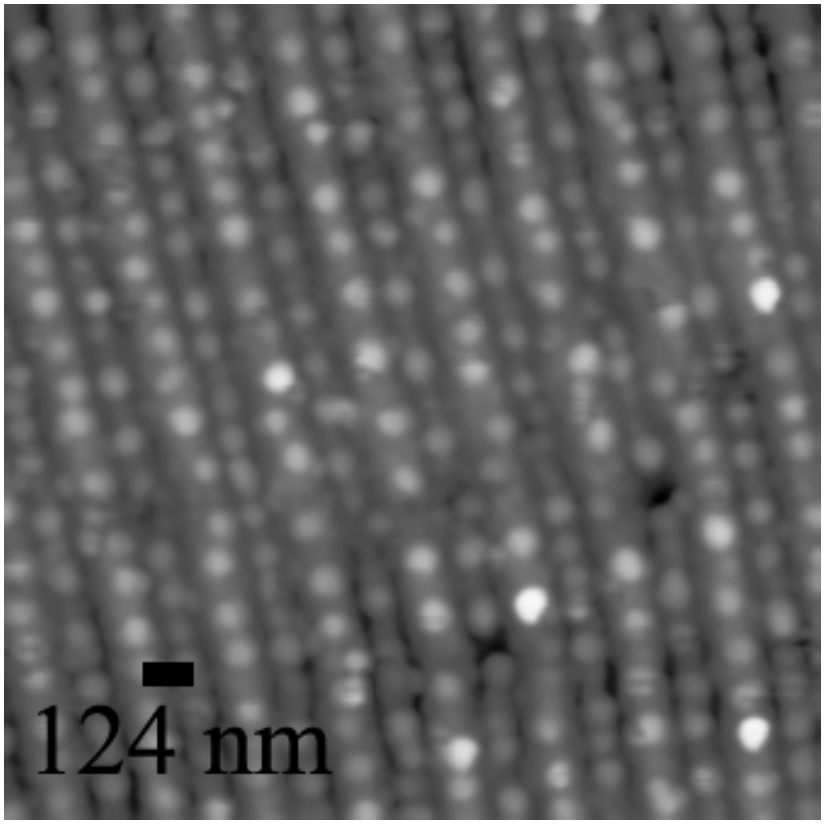

Figure 5.3 Si nanoparticles d ~ 20 – 30 nm, deposited on an underlying, pre – existing LIPSS template. The spacing between nanoparticle lines is ~ 124 nm. The nanoparticle deposition was induced via a laser – induced chemical vapor deposition technique (E_d = 0.5 J/cm^2) with 1000 pulses in $P_{SiH4\ mix}$ = 1 Torr SiH_4 10% - Ar in P_T = 10 Torr. The LIPSS template was produced with 400 laser pulses (E_d = 0.8 J/cm^2) with p – polarized light.

along the pre – existing surface protrusions, at points of zero surface slope and of negative surface curvature, of the LIPSS nanostructure. For example, the 3D AFM profile shown in figure 3.85 shows the surface topography prior to SiH_4 decomposition. Figure 5.4 shows the same sample following the decomposition treatment. The Si nanoparticle appear as the conical protrusions atop the surface maxima of the LIPSS substructure. The nanoparticles have diameters, on average, between 20 – 30 nanometers. Moreover, the nanoparticle lines are spaced 124 nm apart, exactly half the wavelength used to irradiated the substrate and induced both LIPSS formation and silane decomposition.

The ability to induce the alignment of nanostructures at sub – 157 nm wavelengths in a remarkable achievement considering no lithography mask was required for the alignment and that the spacing between nanoparticle lines is comparable to the minimum spacing achievable with standard lithography techniques to minimize inter – device spacing in high surface density, electronic device structures. The technique is also simple requiring only a pulsed, excimer laser source, high – vacuum chamber, appropriate beam steering optics, and a clean Si, single crystal substrate. Figure 5.5 shows a 3D AFM image of the clearly defined, highly self – organized, Si nanoparticle arrays with a 124 nm interline spacing.

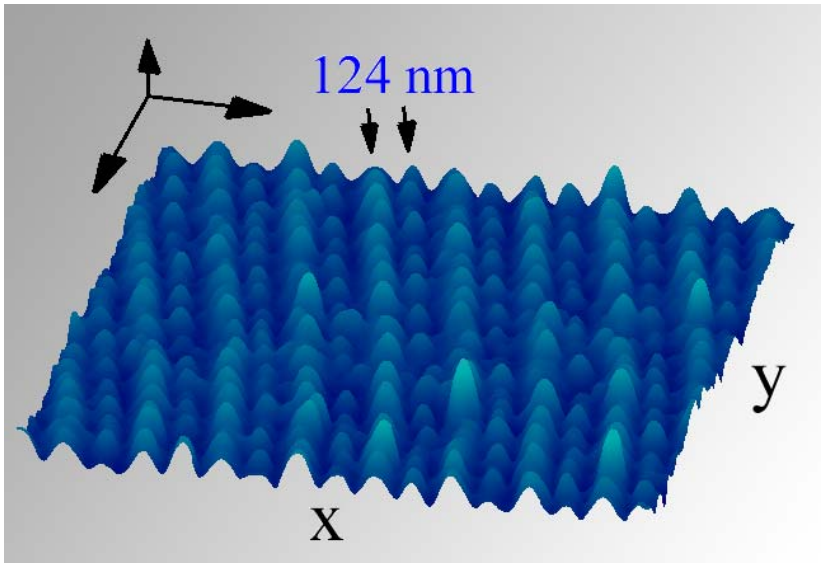

Figure 5.4 A 3D AFM image of the Si nanoparticles deposited by the LICVD technique. Figure 4.13 shows the substrate surface prior to the LICVD treatment.

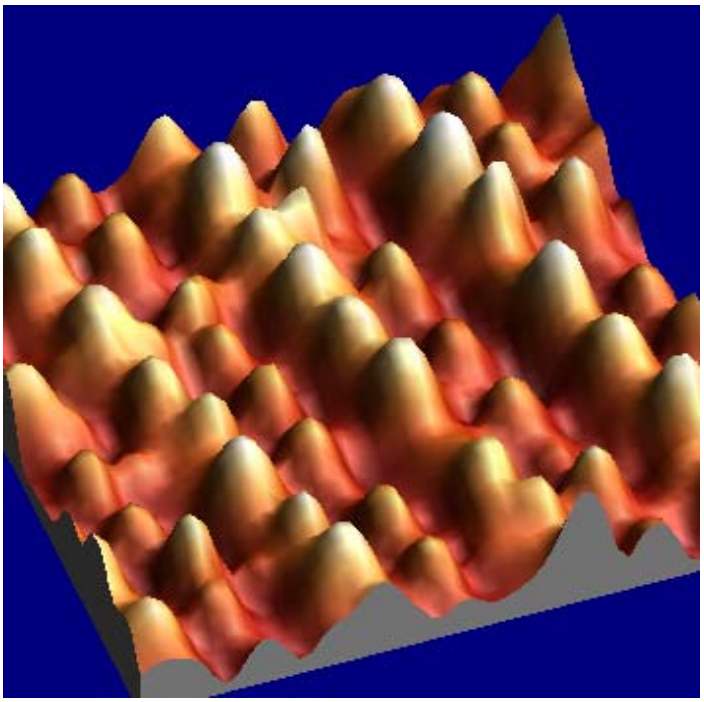

Figure 5.5 A high – resolution 3D AFM image of the nanoparticle lines deposited by LICVD. The conical structures are the Si nanoparticles; the distortion of the Si nanoparticles from their true form as spheres to the cones shown above, is an inherent product of

References

References

1. W. W. Duley, p. 6 and 36 in UV Lasers : Effects and Applications in Materials Science, Cambridge University Press, 1996.
2. D. J. Elliot, p. 48 in Ultraviolet Laser Technology and Applications, Academic Press, Inc., San Diego, 1995.
3. C. Kittel, p. 307 in Introduction to Solid State Physics, John Wiley & Sons, Inc., New York, 1996.
4. M. VonAllmen, p. 6 – 19 in Laser Beam and Electron Beam Processing of Materials, Academic Press, Inc., 1980.
5. G. E. Jellison Jr., D. H. Lowndes, D. N. Mashburn, and R. F. Wood, *Phys. Rev. B* **34**(4), 2408 (1986)
6. D. E. Aspnes and A. A. Studna, *Phys. Rev. B* **27**, 985 (1985)
7. C. W. White and M. J. Aziz, "Energy Deposition, Heat Flow, and Rapid Solidification during Pulsed – Laser – and Electron Beam Irradiation of Metals" p. 21 – 22 in Surface Alloying by Ion, Electron, and Laser Beams, ASM International, Metals Park, Ohio, 1987
8. W. L. Brown, Laser and Electron Beam Processing of Materials, (C. W. White and P. S. Peercy, eds.) Academic Press, New York, 1980.
9. D. Bauerle, p. 226 – 230 in Laser Processing and Chemistry, Springer, 2000.
10. G. B. Shinn, F. Steigerwald, H. Stiegler, R. Sauerbrey, F. K. Tittel, and W. L. Wilson Jr., *J. Vac. Sci. Technol. B* **4**(6), 1273 (1986)

11. R. F. Wood and G. E. Jellision Jr., "Melting Model of Pulsed Laser Processing", p. 204 in Semiconductors and Semimetals, Vol. 23, Pulsed Laser Processing of Semiconductors (R. F. Wood, C. W. White, and R. T. Young, eds.) Academic Press Inc., Orlando, 1984.

12. S. DeUnamuno and E. Fogarassy, *Appl. Sur. Sci.* **36**, 1 (1989)

13. W-. S. Kim, "Pulsed-Laser Deposition of TiN and Si_3N_3 films", MS Thesis (1998)

14. D. E. Aspnes, p. 683 in The Properties of Silicon, IEE, United Kingdom, 1999 (1998)

15. D. B. Geohegan, "Diagnostics and Characteristics of Pulsed Laser Deposition Laser Plasmas" p. 115 – 165 in Pulsed Laser Deposition of Thin Films (D. B. Chrisey and G. K. Hubler, eds.) Wiley – Interscience, New York, 1994.

16. S. I. Anisimov, D. Bauerle, B. S. Luk' yanchuk, *Phys. Rev. B* **48**, 12076 (1993)

17. Ya. B. Zel dovich and Yu. P. Raizer, p. 94 in Physics of Shock Waves and High Temperature Phenomena, vol. 1, Academic Press, New York

18. D. B. Geohegan, A. A. Puretzky, G. Duscher, and S. J. Pennycook, *Appl. Phys. Lett.* **73**(4), 439 (1998)

19. L. Patrone, D. Nelson, V. I. Safarov, M. Sentis, W. Marine, and S. Giorgio, *J. Appl. Phys.* **87**(8), 3829 (2000)

20. H. –P. Wu, A. Okano, and K. Takayanagi, *Appl. Phys. A* **71**, 643 (2000)

21. G. Ledoux, O. Guillois, D. Porterat, C. R. Reynaud, F. Huisken, B. Kohn, and V. Paillard, *Phys. Rev. B* **62**(23), 15942 (2000)

22. H. Morisaki, F. W. Ping, H. Ono, and K. Yazawa, *J. Appl. Phys.* **70**(3), 1869 (1991)

23. W. L. Wilson, P. F. Szajowski, and L. E. Brus, *Science* **262**, 1242 (1993)

24. C. Delerue, G. Allan, and M. Lannoo, *Phys. Rev. B* **48**, 11024 (1993)

25. A. G. Cullis, L. T. Canham, *Nature* **353**, 335 (1991)

26. D.B. Geohegan, A.A. Puretzky, G. Duscher, and S.J. Pennycook, *Appl. Phys. Lett.* **72**(23), 2987 (1998)

27. T. Makimura, T. Mizuta, and K. Murakami, *Appl. Phys. A* **69**[Suppl], S213 (1999)

28. T. Makimura, Y. Kunii, and K. Murakami, *Jpn. J. Appl. Phys.* **35**, 4780 (1996)

29. M. H. Wu, R. Mu, A. Ueda, and D. O. Henderson, *Mater. Res. Soc. Symp. Proc.* **638**, F13.2.1 (2001)

30. D. H. Lowndes, C. M. Rouleau, T. G. Thundat, G. Duscher, E. A. Kenik, and S. J. Pennycook, *J. Mater. Res.* **14**(2), 359 (1999)

31. L. Patrone, D. Nelson, V. I. Safarov, S. Giorgio, M. Sentis, and W. Marine, *Appl. Phys. A* **69**[Suppl], S217 (1999)

32. M. H. Wu, R. Mu, A. Ueda, and D. O. Henderson, *Mater. Res. Soc. Symp. Proc.* **638**, F13.2.1 (2001)

33. G. Ledoux, O. Guillois, D. Porterat, C. Reynaud, F. Huisken, B. Kohn, and V. Paillard, *Phys. Rev. B* **62**(23), 15942 (2000)

34. G. Ledoux, D. Amans, J. Gong, F. Huisken, F. Cichos, and J. Martin, *Mater. Sci. Eng. C* **19**, 215 (2002)

35. T. Makino, N. Suzuki, Y. Yamada, T. Yoshida, T. Seto, and N. Aya, *Appl. Phys. A* **69**[Suppl], S243 (1999)

36. L. E. Brus and J. K. Trautman, *Phil. Trans. R. Soc. Lond. A* **353**, 313 (1995)

37. S. S. Iyer and Y. –H. Xie, *Science* **260**, 40 (1993)

38. U. Gnutzmann and K. Clausecker, *Appl. Phys.* **3**, 9 (1974)

39. T. Takagahara and K. Takeda, *Phys. Rev. B* **46**, 15578 (1992)

40. S. Gardelis, J. S. Rimmer, P. Dawson, B. Hamilton, R. A. Kubiak, T. E. Whall, and E. H. C. Partker, *Appl. Phys. Lett.* **59**, 2118 (1991)

41. *Light Emission from Silicon*, eds. S. S. Iyer, R. T. Collins, and L. T. Canham, MRS Symposia Proceedings No. 256, Materials Research Society, 1991

42. C. Delerue, G. Allan, and M. Lannoo, *Phys. Rev. B* **48**, 11024 (1993)

43. M. V. Wolkin, J. Jorne, P. M. Fauchet, G. Allan, C. Delerue, *Phys. Rev. Lett.* **82**, 197 (1999)

44. T. Makimura, Y. Kunii, and K. Murakami, *Jpn. J. Appl. Phys.* **35**, 4780 (1996)

45. S. Botti, R. Coppola, F. Gourbilleau, and R. Risk, *J. Apl. Phys.* **88**(6), 3396 (2000)

46. X. J. Li and Y. H. Zhang, *Phys. Rev. B* **61**(19), 12605 (2000)

47. L. Patrone, D. Nelson, V. I. Safarov, M. Sentis, and W. Marine, *J. Appl. Phys.* **87**(8), 3829 (2000)

48. V. Yu. Timoshenko, A. B. Petrenko, Th. Dittrich, W. Fussel, and J. Rappich, *Thin Solid Films* **364**, 196 (2000)

49. L. Patrone, D. Nelson, V. Safarov, M. Sentis, and W. Marine, *J. Lumines.* **80**, 217 (1999)

50. H. Morisaki, H. Hashimoto, F. W. Ping, H. Nozawa, and H. Ono, *J. Appl. Phys.* **74**(4), 2977 (1993)

51. S. Sato, H. Ono, S. Nozaki, and H. Morisaki, *Nanostruc. Mater.* **5**, 589 (1995)

52. H. J. Chang, Y. F. Chen, H. P. Lin, and C. Y. Mou, *Appl. Phys. Lett.* **78**(24), 3791 (2001)

53. L. N. Skuga, A. N. Streleisky, and A. B. Pakovich, *Solid State Commun.* **50**, 1069 (1984)

54. R. Tohman, Y. Shimogaichi, H. Mizuno, and Y. Ohki, *Phys. Rev. Lett.* **62**, 1388 (1989)

55. L. Tsybeskov, K. L. Moore, S. P. Duttagupta, K. D. Hirschman, D. G. Hall, and P. M. Fauchet, *Appl. Phys. Lett.* **69**(22), 3411 (1996)

56. A. G. Nassiopoulos, S. Grigoropoulos, and D. Papadimitriou, *Appl. Phys. Lett.* **69**(15), 2267 (1996)

57. B. H. Choi, S. W. Hwang, I. G. Kim, H. C. Shin, Y. Kim, and E. K. Kim, *Appl. Phys. Lett.* **73**(21), 3129 (1998)

58. S. Tiwari, F. Rana, H. Hanafi, A. Hartstein, E. F. Crabbe', and K. Chan, *Appl. Phys. Lett.* **68**(10), 1377 (1996)

59. J. Jersch and K. Dickmann, *Appl. Phys. Lett.* **68**(6), 868 (1996)

60. D. J. Lockwood, G. F. Grom, L. Tsybeskov, P. M. Fauchet, H. J. Labbe, J. P. McCaffrey, and B. White Jr., *Physica E* **11**, 99 (2001)

61. Z. Wang, J. Li, X. Huang, L. Wang, J. Xu, and K. Chen, *Solid State Commun*. **117**, 383 (2001)

62. M. Birnbaum, *J. Appl. Phys.* **36**, 3688 (1965).

63. S. E. Clark, N. C. Kerr, and D. C. Emmony, *J. Phys. D: Appl. Phys.* **22**, 527 (1989)

64. G. N. Maracas, G. L. Harris, C. A. Lee, and R. A. McFarlane, *Appl. Phys. Lett.* **33**(5), 453 (1978)

65. N. R. Isenor, *Appl. Phys. Lett.* **31**, 148 (1977)

66. A. K. Jain, V. N. Kulkarni, D. K. Sood, and J. C. Uppal, *J. Appl. Phys.* **52**, 4882 (1981)

67. V. N. Anisimov, V. Yu. Baranov, L. A. Bol' shov, A. M. Dykhne, D. D. Malyuta, V. D. Pis' mennyi, A. Yu. Sbrant, and M. A. Stepanva, *Poverkhnost* **7**, 138 (1983)

68. A. M. Bonch – Bruevich, M. K. Kochengina, M. N. Libenson, S. D. Pudkov, and V. V. Trubaev, *Izv. Akad. Nauk SSR,* **46**, 1186 (1982)

69. A. M. Prokhorov, V. A. Sychugov, A. V. Tishchenko, and A. A. Khakimov, *Pis'ma Zh. Tekh.* **8**, 961 (1982)

70. P. A. Temple and M. J. Soleau, *IEEE J.* **QE-17**, 2067 (1981)

71. P. E. Dyer, R. J. Farley, R. Giedl, and D. M. Karnakis, *Appl. Surf. Sci.* **96 – 98**, 537 (1996)

72. P. E. Dyer and R. J. Farley, *J. Appl. Phys.* **74**(2), 1442 (1993)

73. M. Csete and Zs. Bor, *Appl. Surf. Sci.* **133**, 5 (1998)

74. M. Bolle, S. Lazare, M. Le Blanc, and A. Wilmes, *Appl. Phys. Lett.* **60**(6), 674 (1992)

75. H. Hiraoka and M. Sendova, *Appl. Phys. Lett.* **64**(5), 563 (1994)

76. P. A. Temple and M. J. Soileau, *NBS.,* **462**, 371 (1976)

77. S. R. J. Brueck and D. J. Ehrlich, *Phys. Rev. Lett.,* **48**(24), 1678 (1982)

78. F. Keilmann and Y. H. Bai, *Appl. Phys. A* **29**, 9 (1982)

79. D. J. Ehrlich, S. R. J. Brueck, and J. Y. Tsao, *Appl. Phys. Lett.* **41**(7), 630 (1982)

80. G. N. Maracas, G. L. Harris, C. A. Lee, and R. A. McFarlane, *Appl. Phys. Lett.* **33**(5), 453 (1978)

81. Z. Guosheng, P. M. Fauchet, and A. E. Siegman, *Phys. Rev. B* **26**(10), 5366 (1982)

82. J. F. Young, J. E. Sipe, J. S. Preston, H. M. vanDriel, *Appl. Phys. Lett.* **41**(3), 261 (1982)

83. J. E. Sipe, J. F. Young, J. S. Preston, and H. M. vanDriel, *Phys. Rev. B* **27**(2), 1141 (1983)

84. J. F. Young, J. S. Preston, H. M. vanDriel, and J. E. Sipe, *Phys. Rev. B* **27**(2), 1155 (1983)

85. J. F. Young, J. E. Sipe, and H. M. vanDriel, *Phys. Rev. B* **30**(4), 2001 (1984)

86. S. A. Akhmanov, V. I. Emel'yanov, N. I. Koroteev, and V. N. Seminogov, *Sov. Phys.Usp.* **28**(12), 1084 (1985)

87. J. –H. Klein – Wiele, G. Marowsky, and P. Simon, *Appl. Phys. A* **69**[Suppl], S187 (1999)

88. J. D. Fowlkes, "Growth of Silicon Microcone/Microcolumn Arrays by Nanosecond Pulsed Laser Irradiation", MS Thesis, 1999

89. Communications with Dr. C. Barnes, Professor of Chemistry, Department of Chemistry, The University of Tennessee, Knoxville

90. R. K. Singh, D. R. Gilbert, and J. Viatella, *Mater. Sci. Eng.* **B40**, 89 (1996)

91. S. Jesse, A. J. Pedraza, J. D. Fowlkes, J. D. Budai, and D. H. Lowndes, *Mater. Res. Soc. Symp. Proc. Vol.* **638**, F14.39.1 (2001)

92. K. Ohkubo, Y. Igari, S. Tomoda, and I. Kusunoki, *Sur. Sci.* **260**, 44 (1992)

93. G. R. Fownes, p. 155 in Introduction to Modern Optics, 2nd, Dover Pub. Inc., 1975

94. S. O. Kasap, p. 20 in Optoelectronics and Photonics, Principles and Practices, Prentice Hall, 2001

95. Communications with Adela Bin-Yakar, adela@stanford.edu

96. M. Ohring, p. 133 in Materials Science of Thin Films, Deposition & Structure, Academic Press, 2002

97. K. N. Shrivastava, *Nanoletters* **2(5)**, 519 (2002)

98. G. Ge and L. E. Brus, *Nanoletters* **1(4)**, 219 (2001)

99. A. Ashkin, *Optics Letters* **24(21)**, 6 (2000)

100. W. C. Elmore and M. A. Heald, p. 331 in Physics of Waves, Dover Pub. Inc., 1969

Vita

Jason Fowlkes was born in Wytheville, Virginia on August 10, 1974. He graduated from George Wythe High School in Wytheville in 1992 and entered the engineering program at the University of Alabama, Tuscaloosa that same year. After two years in the Metallurgical Engineering department at U.A. he transferred to The University of Tennessee, Knoxville where he completed the requirements for his Bachelor of Science degree in Materials Science and Engineering. In 1999, he completed his Masters of Science degree at the same school. The thesis was entitled, "Growth of Silicon Microcone/Microcolumn Arrays by Nanosecond Pulsed Laser Irradiation." At present Jason is a post – doctorial student at The University of Tennessee, Knoxville under Dr. Philip Rack.